X-ray diffraction measurements for breast tissue analysis

Jennifer Ann Griffiths

UNIVERSITY COLLEGE LONDON

Submitted for The Degree of Doctor of Philosophy
University of London
May 2005

ProQuest LLC
789 East Eisenhower Parkway
P.O. Box 1346
Ann Arbor, MI 48106-1346

Abstract

Biological tissues exhibit elastic x-ray scatter properties unique to individual tissue types. It has been suggested that these properties could be exploited in the discrimination of tissues in diagnostic radiology, particularly in mammographic imaging. The work in this thesis investigates the elastic scatter from human breast tissues with a view to moving the Diffraction Enhanced Breast Imaging (DEBI) technique towards the clinical domain.

Instrumentation was considered in terms of a suitable scatter detector and its associated collimation. A phosphor coated low-light-level CCD in conjunction with a parallel hole array collimator was introduced as a possible angular dispersive diffraction detector, and conically collimated HPGe was found to be a suitable detector for energy dispersive diffraction.

Diffraction imaging was achieved using both planar and tomographic imaging techniques. The planar imaging considered the spatial resolution needed for clinically useful results and showed that depth information of the order of 1 cm can easily be obtained using diffraction imaging techniques.

A micro-tomographic diffraction imaging technique was used to further present knowledge of the 'scatter signatures' of human breast tissue. The tissue is naturally inhomogeneous, so precise knowledge of a sample's composition is needed in order to accurately classify its scatter signature. A total of twenty seven breast tissue samples were examined, covering a range of tissue types, with nineteen of these samples being extensively studied. The microCT produced diffraction images of the inhomogeneous tissue samples and their diffraction signatures were related to the results of conventional histopathological analysis. A correlation was observed between the predominant tissue type in a sample and the ratio of the intensity of the sample's scatter at momentum transfers of 1.1 and 1.5 nm^{-1}. A Student's *t*-test performed on these results gave the probability of a null hypothesis for correlation of less than 1%.

Table Of Contents

Chapter 2

Materials and instrumentation considerations for diffraction imaging

Chapter 3

Planar diffraction imaging

Chapter 4

Micro-Computed-Tomography and diffraction signatures of small tissue sections

Figures

Chapter 1

Introduction to Diffraction Enhanced Breast Imaging

Chapter 2

Materials and instrumentation considerations for diffraction imaging

Chapter 3

Planar diffraction imaging

Chapter 4

Micro-Computed-Tomography and diffraction signatures of small tissue sections

Tables

Chapter 1

Introduction to Diffraction Enhanced Breast Imaging

Chapter 2

Materials and instrumentation considerations for diffraction imaging

Chapter 3

Planar diffraction imaging

Chapter 4

Micro-Computed-Tomography and diffraction signatures of small tissue sections

Acknowledgements

I would like to say thank you to everyone who has been involved in this work in any way, and also to my family and everyone that has helped me to achieve my goals in life.

A huge thank you must be said to my supervisors, Professor Robert Speller and Doctor Gary Royle for all of their guidance, help and near endless patience.

Many thanks to Professor Andy Hanby, the consultant pathologist for all of this work, and to the Department of Histopathology at UCL who allowed me to use their facilities. Many thanks also to the UCL Medical Physics Mechanical Workshop, especially Stewart Morrison, for constructing the experimental apparatus and teaching me invaluable workshop skills.

Thank you to Doctor Emma Harris for helping me to understand the L3Vision camera and giving me complete access to all her results, and also to Doctor Silvia Pani for the second set of L3CCD microCT images.

This PhD has been funded jointly by e2v technologies ltd. and by an EPSRC studentship awarded by the Department of Medical Physics and Bioengineering at UCL. Work carried out at the Elettra Synchrotron Radiation Source was funded by the Human Potential Programme – Transnational Access to Major Research Infrastructures of the European Community.

CHAPTER 1

Introduction to Diffraction Enhanced Breast Imaging

Biological tissues exhibit elastic x-ray scatter properties unique to individual tissue types and it has been suggested that these properties could be exploited to aid the discrimination of tissues in diagnostic radiology, particularly in mammographic imaging of cancerous lesions. This thesis investigates the elastic scatter from human breast tissues with a view to incorporating a scatter detector into a standard mammographic unit or creating an x-ray diffraction imaging biopsy tool in the future. This first chapter will give a basic outline of breast tissue pathology and mammography techniques, followed by the physical reasoning for using the elastic scatter properties of tissues to form images of them.

1.1 Anatomy and pathology of the human breast

The human breast is an organ that in its normal form varies in size, composition and structure from person to person, depending on gender, age and hormone levels, with some changes even occurring during the menstrual cycle. Childhood breast growth is isometric and many of the structures that are seen in the adult female breast do not appear until puberty when the thelarche occurs in females and the growth becomes allometric. The adult male breast closely resembles that of a prepubertal female.

1.1.1 Normal anatomy and architecture of the adult female breast

The essential components of the breast are fat, which is radiolucent, connective tissue and epithelium. Since the latter, which is where carcinoma occurs, is generally

associated with the connective tissue, it is the denser collagen rich regions of the breast which are of more interest with regards to functional biology and pathobiology.

The tissue of the breast is contained within the superficial fascia of the anterior chest wall and extends from the second to the sixth or seventh intercostal space. It is supplied with blood by branches of the axillary artery and the anterior and lateral perforating branches of the intercostal artery (figure 1.1 [Sloane, 2001]). The nerve supply is derived from the anterior and lateral cutaneous branches of the fourth, fifth and sixth thoracic nerves. The position of the breasts on the outer chest wall means that it is possible to image just these organs without having to take account of other organs being present in the image.

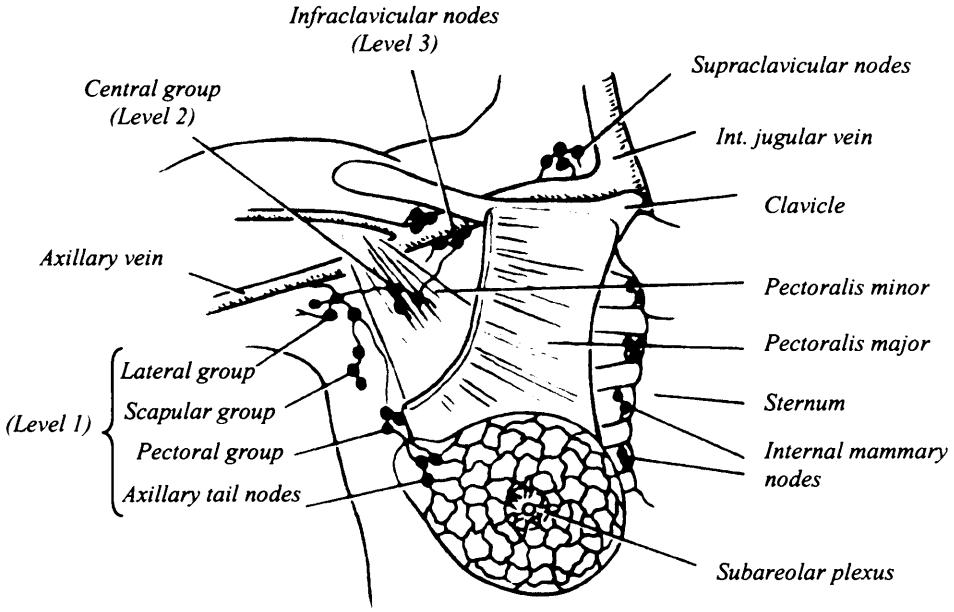

Figure 1.1 *Anatomy of the normal mature female breast [Sloane, 2001].*

The lymphatic drainage system of the breast is thought to play a key role in the metastasis of breast carcinoma [Carter *et. al.*, 1989], hence the lymph nodes are examined during mastectomy procedures in order to ascertain whether a cancer has metastasised. The lymph mainly drains to the axillary and internal mammary nodes, as well as to a posterior paravertebral group [Spratt, 1979]. The axillary lymph nodes are usually reported in three groups [McDivett *et al.*, 1968]:

Level 1 nodes lie lateral and inferior to the pectoralis minor and include the lateral, scapular and pectoral groups and the axillary tail of the breast.

Level 2 nodes lie posterior to the pectoralis minor and are essentially the central axillary group.
Level 3 nodes lie medial and superior to the pectoralis minor and form part of the infraclavicular group.

The epidermis of the breast is histologically different from the nipple and areola; these have no hair follicles and their subcutaneous tissue contains numerous irregularly arranged smooth muscle bundles. Around 15 to 20 collecting ducts emerge from the breast at the nipple surface, each through a separate orifice. The epithelium of the proximal portions of these ducts is continuous with the skin's epithelium, however further along the duct there is an abrupt change to the two-layer epithelium characteristic of the rest of the glandular tree. The collecting ducts are continuous with the lactiferous sinuses, which have a papillary appearance when in their resting state due to a marked infolding of their walls. The lactiferous sinuses receive the segmental and sub-segmental ducts leading from the terminal duct-lobular units (TDLU) (figure 1.2 [Sloane, 2001]). Each lobule is formed from a number (ranging from less than 10 to more than 100) of acini embedded within vascular tissue. It is thought that most carcinomas originate in the epithelium of the TDLU [Wellings *et. al.*, 1975].

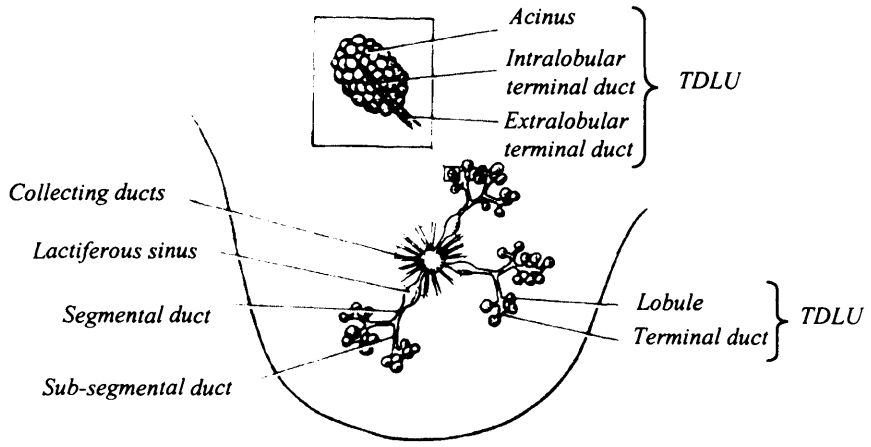

Figure 1.2 *Diagram of the ductal and lobular system in the adult female breast [Sloane, 2001].*

1.1.2 Disease of the breast

Diseases of the breast fit into three broad categories; they may be considered benign, malignant or pre-cancerous. Malignant lesions, which are the primary target of this

work, have unchecked cell growth mechanisms and may metastasise. They include carcinomas derived from epithelial tissue and less commonly sarcomas, which occur in the connective stroma of the breast. Benign lesions are also of some importance as some may be precursor lesions of malignancy or, more commonly, because they may clinically, radiologically or pathologically mimic carcinoma. Many breast lesions do not show clearly on radiographs and radiologists may often make a diagnosis of disease based purely on the presence of calcifications within the epithelium or stroma. These are small particles of either hydroxyapatite or, less commonly, the crystalline structured weddelite. Calcification is heavily associated with ductal carcinoma *in situ* (DCIS) and is much less common in invasive tumours.

1.1.2.1 Benign lesions and pre-cancerous conditions

Many benign, or non-neoplastic, changes in the breast are most commonly treated clinically either to exclude malignancy or if they become detrimental to the patient's quality of life, for example, if they become very large or cause anxiety about the possibility of cancer. Some benign lesions may mimic cancers in diagnostic images.

Table 1.1 lists the most common benign and pre-cancerous changes seen in the breast. The benign lesions (cysts, duct ectasia, fibrosis and adenosis) have not been shown to increase the risk of developing carcinoma in the future, whilst the pre-cancerous lesions (pseudo-infiltrative lesions, fibroadenoma, intraduct papilloma and phyllodes tumour) all have a statistical association with cancer. These pre-cancerous conditions are a complex and debated series of lesions where some may truly be precursor lesions whilst others may represent wholly benign lesions which share an aetiology with carcinomas – most commonly lifetime oestrogen exposure. A link to an increase in the risk of developing breast cancer in the future has been found with some of these lesions and others may resemble carcinoma either cytologically or architecturally. It is worth noting that, with the exception of phyllodes tumours, none of these lesions has been shown to metastasise.

Fibrosis, pseudo-infiltrative lesions (including radial scar and sclerosing adenosis) and fibroadenoma can all mimic carcinoma in radiographs and radial scar can also be mistaken for carcinoma in histopathological analysis. There are cases of carcinoma co-existing with pseudo-infiltrative lesions, intraduct papilloma and fibroadenoma,

although it is extremely rare in the latter. An associated carcinoma, usually of the intraductal type, is found in approximately a quarter to a third of cases of multiple intraduct papilloma.

Table 1.1 *Benign and pre-cancerous lesions.*

Type	*Occurrence*	*Risk to patient*	*Formation and location*	*Comments on diagnosis*
Cysts *[Frantz et. al., 1951; Dupont & Page, 1985]*	*35 years to menopause, but normally small and not palpable.*	*Usually cured in the act of performing needle biopsy. Slightly elevates risk of breast cancer if there is a family history of breast disease.*	*Formed by dilation and coalescence of acini in the TDLU.*	*Sometimes clustered. Radiologically similar to non-calcified Fibroadenoma, but may occasionally contain calcified material.*
Duct Ectasia *[Rees et. al., 1977]*	*Women reaching menopause.*	*May be accompanied by some inflammation.*	*Formed by dilation of the ducts.*	*May form lump with occasional discharge. Can be mistaken clinically for carcinoma. Calcification seen in 30% of images.*
Fibrosis *[Sloane, 2001]*	*Commonly seen in benign breast biopsies during involution.*	*No risk, aside from mimicking carcinoma.*	*An increase in the fibrous stroma.*	*May form a palpable lump and possibly be mistaken for infiltrating lobular carcinoma.*
Adenosis *[Sloane, 2001]*	*Women reaching menopause.*	*No evidence of association with breast cancer, but further studies are needed.*	*Enlargement of lobules with no other abnormalities.*	*Some calcification may be seen in the lumina.*
Pseudo-Infiltrative Lesions *[Jensen et al 1989]*	*35 years and above.*	*Do not metastasise, but infiltrate locally. Risk of developing cancer approximately doubles.*	*A lobular proliferation.*	*May be mistaken for infiltrating carcinoma both radiologically and histopathologically, especially radial scar.*
Fibroadenoma *[Carter et al., 1989; McDivett et al., 1992]*	*Young women.*	*May (very rarely) contain carcinoma. Increases risk of carcinoma by 1.5–3 x.*	*Lobular in origin.*	*Usually < 30 mm in size.*
Intraduct Papilloma *[Murad et. al., 1981; Sandison, 1958]*	*Solitary – women reaching menopause Multiple – very uncommon, occuring in younger women.*	*Associated carcinoma (usually intraductal) in 1/4 – 1/3 of multiple IP, with 50% recurrence after local excision .*	*Solitary - interlobular ducts Multiple - TDLU.*	*Rarely > 30 mm. Can form palpable mass, but often not clinically manifest.*
Phyllodes Tumour *[Norris & Taylor, 1967; Rosen & Urban, 1975]*	*Median age 45. Median size 60 mm.*	*Can locally recur and metastasise. Increased risk of lobular b.c.*	*Lobular in origin.*	*Same architecture as fibroadenoma.*

1.1.2.2 Carcinoma

Carcinomas are malignant lesions originating from epithelial cells. Their growth regulation mechanisms are unchecked and, given enough time, they will grow to a large size. There is also a significant chance of metastasis to other parts of the body. Cytologically, carcinoma samples show large numbers of the same type of cells (monomorphism), but within this one type, the cells may greatly vary (cellular pleomorphism). The cells also tend to have a large size and show a lack of cohesion. Carcinomas are classified as either ductal or lobular; however this classification has little bearing on where the lesions specifically originate from and defines a more qualitative attribute determined by the characteristic abnormal molecular profile of the tumour. It is thought that all tumours originate within the TDLU. Carcinomas are also classified as either *in situ* or infiltrative, depending on whether or not the basement layer and the myoepithelial layer of cells beneath the epithelium have been breached by the lesion. This classification has a temporal basis as all carcinomas will have an *in situ* period before they become invasive. *In situ* carcinomas have not spread beyond the structures from which they have arisen and therefore can not spread outside the breast, meaning that they can not metastasise. If all carcinomas could be diagnosed and eradicated whilst in their *in situ* stage, rather than reaching the invasive portion of their growth, then the risk of metastasis would be greatly reduced.

The main types of carcinoma are summarised in Table 1.2. There are two types of *in situ* carcinoma, ductal (DCIS) and the much less common lobular (LCIS), but many types of infiltrative carcinoma, the two most common, no specific type (nst) and lobular, being highlighted in the table.

Radiographic screening does not successfully detect LCIS, but has proved a success in the detection of DCIS. This type accounts for 18% of all screen detected cancers, but just 5% of cancers presenting in symptomatic women [Moss *et. al.*, 1995]. DCIS represents a non-invasive early form of carcinoma and so detection may mean that the cancer is caught earlier than it would be otherwise. Part of the success of diagnosis of DCIS from x-ray mammograms is the frequent presence of microcalcifications within the lesions. Nevertheless, despite this success, the technique frequently underestimates the extent of the lesion. Low grade DCIS (and also some benign lesions) can contain sand-like microcalcifications which may aggregate in stagnant secretions, whilst some

higher grade DCIS may contain central necrosis with the dead cells taking up calcium ions to form a crystallisation nidus, giving a comedonecrosis microcalcification pattern.

Table 1.2 *Common types of breast carcinoma.*

Type	*Occurrence*	*Risk to patient*	*Formation and location*	*Comments on diagnosis*
DCIS *[Moss, et. al., 1995; Sloane, 2001; Page et. al., 1982]*	*18% of all screen detected. 5% of all symptomatic.*	*1-2% will metastasise and 50% of residual DCIS after surgery will become invasive.*	*Originates in TDLU.*	*Microcalcifications often present. Radiographs frequently underestimate extent of lesions.*
LCIS *[Rosen et. al, 1978; Page et. al., 1991]*	*Makes up just a few % of all breast cancers and occurs predominantly pre-menopausal women.*	*Relative risk of developing invasive carcinoma increases by a factor of 7.2 – 12.*	*Originates in TDLU.*	*Difficult to detect.*
Infiltrative ductal (nst) *[Ellis et. al., 1992]*	*Most common type of infiltrative.*	*Prognosis poorer than other invasive types. 47% 10 year survival rate.*	*Originates in TDLU.*	*Appears as radiodense stellate mass on radiographs.*
Infiltrative lobular *[Sloane, 2001; Ellis et. al., 1992]*	*1-15% of all infiltrative.*	*54% 10 year survival rate.*	*Originates in TDLU.*	*Extremely variable appearance on mammograms.*

Infiltrative carcinomas are classed as those where the myoepithelial cell layer has been breached by the cancerous cells. There are many types of infiltrating carcinoma, most of which are rare; all can be graded using the modified Bloom and Richardson grading system [Elston and Ellis, 1991]. When an invasive carcinoma is detected by screening, as opposed to being symptomatic, on average, the carcinoma is smaller and of a lower grade and there is less necrosis and vascular and perineural invasion. However there is evidence to suggest that tumours of different grades are qualitatively different and that grade I tumours will not evolve into higher grade lesions [Roylance *et. al.*, 1999]. Most invasive carcinomas fall into the no specific type category. This is a morphologically and biologically diverse group which contains invasive carcinomas whose characteristics have not yet been defined enough to fit into a more informative taxonomy. The neoplastic cells grow in nests, cords or large masses. Infiltrative lobular carcinomas make up between 1 and 15% of all infiltrating carcinomas. In this type, the neoplastic cells are widely dispersed, occurring as single cells or in columns one cell wide known as 'Indian files' (invasive lobular carcinoma). Mammograms of infiltrative carcinomas have a variable appearance, ranging from ill-defined architectural distortions and densities to denser, more confluent tumour masses whose borders are often indistinct and wispy.

1.1.3 Histopathological analysis techniques

The overall aim of the work covered in this thesis is to characterise breast tissue samples using x-ray diffraction techniques. In order to fully assess the findings, the tissues being measured must be accurately correlated with the diffraction data. This means that individual tissue types within the samples must be identified along with their positions within the samples. This identification was undertaken by Professor A. Hanby at St. James' University Hospital, Leeds using pathology techniques to analyse the tissue samples after measurements were carried out at UCL.

Pathology techniques are used in hospitals both to diagnose disease through biopsy and to analyse tissues removed during surgery. Biopsy (non-operative diagnosis) normally takes the form of needling, either by fine needle aspiration cytology (FNAC) or by a needle core biopsy (NCB) [Sloane, 2001]. All biopsies are compared with clinical and radiological findings in order to ensure that the sample is representative of the lesion under examination. NCB takes a larger, more structured tissue sample than FNAC and must be done under local anaesthetic. The technique can be used to distinguish *in situ* from invasive carcinomas and to make specific diagnoses of benign conditions.

The analysis of the tissues used in the experiments detailed in this thesis followed the procedures normally used for tissues removed during surgery. They underwent gross examination and were then blocked, stained and placed under a microscope for examination. The orientation of the samples constantly changed throughout these procedures, therefore following through the portion of the sample that data was obtained from in the laboratory became imperative.

1.1.3.1 Gross examination

Specimens removed during surgery are clearly marked by coloured dyes on six sides in a quasi-cubic formation for orientation purposes and then cut into thin (5 mm) slices and visually inspected and palpated. The larger samples used in this work were treated in a similar way, whilst the smaller samples were not sliced at this point. On macroscopic examination, the size and weight of each sample was recorded along with the contour, consistency and location of masses. Tumour excision margins would also be assessed in the case of surgical samples.

Tissue taken from surgical samples that is considered surplus to diagnostic requirements may be reserved for tissue banking subject to the correct consent procedures having been followed. The work undertaken in this thesis made use of banked tissue from St. James' University Hospital, Leeds, U.K. The unfixed tissue was placed into air-tight plastic containers for the experiments and then returned to the pathologist who placed it in neutral buffered formalin for a minimum of 24 hours for fixation before further pathological examination took place. Fixing the tissue causes cross links between the proteins to be formed, resulting in the tissue no longer degrading in air, but altering the structures in ways that would affect x-ray diffraction data if the experiments were to be carried out on fixed tissues [Kidane, 2000].

1.1.3.2 Blocking

Blocks consist of a small portion of a tissue sample embedded in paraffin wax which can then be stained to indicate many different properties. A microtome is used to cut the block into 3-4 μm thick slices which are then placed on glass slides. These slides are positioned under a microscope in order to examine the specimen in more detail. Several blocks were taken from areas throughout the larger samples used in this thesis, whilst blocks were taken from just the thin slice of the sample that had been imaged for the small samples used in the later microCT work.

Paraffin wax is immiscible with aqueous solutions such as the formol saline used to fix samples. This means that the fixed samples must be dehydrated prior to blocking. This is done by using intermediate solvents in a processing machine [St. James's University Hospital, 2002]; alcohol replaces the fixative then xylene replaces the alcohol, and being miscible with paraffin wax, allows the tissue to become impregnated with the wax. This waxing process can take over a day for large tissue blocks, but small urgent samples can be processed in an hour or two if necessary. It is at this stage of the procedure that the orientation of the samples may be lost unless great care is taken in their positioning in the processing machine.

1.1.3.3 Microscopic examination

Samples to be viewed under a microscope are stained to exhibit many different features and properties. The most common stain, and the one used for analysis of the samples in this thesis, is Haemotoxylin and Eosin (H&E). The Haemotoxylin is attracted to the

acidic cell nuclei and stains them blue, whilst the Eosin is attracted to the alkaline cell cytoplasm, staining it pink.

Other stains can be used to highlight mucin and specific molecules made by tumours which can contribute to a molecular profile to help identify difficult tumours or show whether a tumour is *in situ* or invasive.

1.2 Detection of breast cancer *in vivo*

Current statistics show that 1 in 9 women in the United Kingdom will develop breast cancer at some point in their lives [Quinn *et. al.*, 2001], equating to around 35,000 diagnoses per year. All women in the U.K. aged between 50 and 70 years (70+ may also opt in if they wish to do so) are given the opportunity to have a mammogram every 2-3 years as part of the National Breast Cancer Screening Programme. It is estimated that this program has saved at least 300 lives per year since its inception and that this will rise to 1250 lives per year by 2010 [Blanks *et. al.*, 2000]. This is a result of the radiological examinations detecting certain breast cancers, especially DCIS, at a far earlier stage than that at which they clinically present. Women having mammographic examinations under the National Breast Cancer Screening Programme have the opportunity to be part of the Million Woman Study, the largest cohort study on mammography ever undertaken. The study aims to give definitive statistics on mammography based on the participants in the UK Programme [Banks *et. al.*, 2004]. Routine mammograms are not offered to younger women as the probability of detecting breast cancer in these women is not considered to be significant enough to outweigh the risk of developing cancer later in life as a result of the dose of ionising radiation received when undergoing the procedure. The probability of detecting breast cancer in younger women is low for two reasons; the first being that the risk of developing breast cancer is lower in pre-menopausal women – 4 in 5 new cases are reported in women over 50 [Quinn *et. al.*, 2004]. Nevertheless, if a malignancy does occur in a younger woman it tends to be far more aggressive than in an older woman. The second reason is that the breasts of pre-menopausal women are usually radiologically dense, giving extremely poor contrast in the mammograph which can lead to inaccurate and uncertain diagnoses.

1.2.1 Required properties of an imaging system for detection of breast cancer

The most obvious requirement for a system to detect breast cancer *in vivo* is that it can do this task with an acceptable reliability. This reliability can be defined by the sensitivity and specificity of the system. A perfect system would detect all cancers all of the time (100% sensitivity), whilst rejecting all patients who do not have cancer (100% specificity). Other factors affecting the choice of imaging system are patient discomfort, the availability of the system and the risk to the patient of developing cancer in the future due to any ionising radiation dose received during the procedure. The availability becomes of particular importance in the case of whole population screening programmes such as the UK National Breast Screening Programme.

Table 1.3 lists some imaging modalities, along with their quoted sensitivities and specificities and a report on their current status with respect to regular diagnostic use. X-ray mammography is by far the most common form of imaging of the breast, however other modalities are also able to produce diagnostically useful images and may become more common in the future if they can provide higher values of diagnostically useful soft tissue contrast than radiographic images at similar levels of spatial resolution.

Table 1.3 *Breast imaging techniques.*

Modality	***Sensitivity (%)***	***Specificity (%)***	***Current Status***
X-ray mammography *[Banks et. al., 2004]*	*86.6*	*96.8*	*Used in regular breast screening.*
Scintimammography *[Libermann, 2003]*	*85.2*	*86.6*	*Some clinical trials in progress.*
MRI *[Hendrick, 2005]*	*>90*	*37 - 90*	*Adjuvant imaging due to cost.*
Ultrasonography *[Houssami, 2002]*	*81.7*	*88*	*Adjuvant imaging for suspicious lesions in young women.*
	Women attending symptomatic clinic.		
IR/ Optical Spectroscopy *[Cheng et. al., 2003]*	*92*	*67*	*Still at early trial stage.*
	X-ray mammographically positive patients.		
EIT *[Malich et. al., 2003]*	*80.5*	*64.7*	*Still at early trial stage.*
	Ultrasound & x-ray previously shown suspicious findings.		

1.2.1.1 X-ray mammography

The most important requirement of any radiographic procedure is that that the benefit of undergoing the procedure will outweigh the risk of cancer associated with the patient dose. In mammography a useful image must be obtained using as small a dose to the patient as possible. An image can be considered useful if the spatial resolution is such that microcalcifications, usually of the order of 100 μm in size, can be observed and also if the contrast has reached a level where the necessary diagnostic features can be resolved. The contrast, C, between two areas of an image is given by:

$$C = \left| \frac{G_1 - G_2}{G_1 + G_2} \right| \qquad (1.1)$$

G_1 and G_2 are the grey level values of the two areas. The measured grey level of a point in an image is a function of the number of x-rays that have interacted with the image receptor at that point; therefore contrast in a transmission x-ray image is a function of the difference in the number of x-rays that reach the detector after passing through the object being imaged. This difference occurs due to x-rays undergoing attenuation by the object. Attenuation occurs principally via the photoelectric effect at diagnostic energies and thus the object receives a radiation dose. This means that there is always a compromise between the contrast of a transmission x-ray image and the dose to the patient. These two points mean that a good mammographic imaging system will have a spatial resolution of 100 μm or better and a high sensitivity to mammographic energy x-rays in order to achieve the highest possible contrast.

The main restriction of a mammographic x-ray system is the need for compression of the breast in order to obtain a reliable image. The median compression force is around 200 N [Chevalier *et. al.*, 2004] and this puts a limit on the time for which compression can be endured. On average, an x-ray mammographic procedure takes 10 seconds from beginning to compress the breast to release of the compression plates. This places an upper limit on the amount of time available to obtain the image, which becomes of high significance if a line-scan digital imaging system is used.

X-ray mammography usually uses film placed in a cassette containing a phosphor layer on the side of the film furthest from the patient as the image receptor; however, as in

many areas of radiology, digital detectors are starting to replace film. This transition has been slower than in other radiological examinations due to the high spatial resolution needed. Commonly used detector systems are large area flat panel amorphous silicon arrays (Senographe, G.E. Medical) and slot-scan demagnified CCDs (Senoscan, Fischer Imaging). Both systems retain the phosphor screen to convert x-rays into visible light photons before detection. Digital systems allow hard disk storage of images and their acquisition parameters, along with the ability to use processing software to manipulate the images to highlight important features.

1.2.1.2 Scintimammography

Scintimammography is a relatively new nuclear medicine procedure whereby a radiopharmaceutical that uptakes preferentially in tumours and the lymph drainage systems of the breast is administered to the patient [Rahusen *et. al.*, 2000]. Some uptake has also been shown in fibroadenomas and areas of fibrocystic change [Scoparino *et. al.*, 1997]. The accumulation of the radiation is imaged using either a conventional gamma camera or a hand held probe and the technique has so far been shown to be successful in imaging tumours down to 1 cm in size [Scoparino *et. al.*, 1997]. Monte Carlo simulation work has indicated that the use of a Compton camera could improve the current spatial resolution by a factor of 2 or 3 [Zhang *et. al.*, 2004]. Scintimammography gives functional, as well as positional, information about lesions and the procedure may also be used during surgery to locate lymph nodes to be removed from the patient; however the patient does receive a radiation dose, and anxiety may be raised during the administering of the pharmaceutical. The technique may prove useful in the diagnosis of breast cancer in younger women with dense breasts and those with implants as it is not affected by density and is permeable to implants [Libermann *et. al.*, 2003].

1.2.1.3 Magnetic Resonance Imaging

MR imaging works by analysing the spin of atomic nuclei. Hydrogen gives the largest signal due to its single half integer spin and hence the modality is excellent at imaging the water content of the body, giving high contrast images of soft tissues. The best results in MR breast imaging have been obtained using contrast enhanced techniques where the patient is injected with Gd-DTPA and a dedicated breast coil is used [Hendrick, 2005]. This technique offers the potential to separate malignant and benign

tumours and outperforms x-ray mammography in the successful diagnosis of women with a high risk of invasive breast cancer due to familial or genetic predisposition [Kriege *et. al.*, 2004]. MRI has the advantage of using non-ionising radiation, but the equipment needed is expensive (~£1 million) and the procedure can be stressful to the patients as it is noisy and claustrophobic. These factors mean that it is used as an adjunct diagnosis technique to mammography and ultrasonography.

1.2.1.4 Ultrasonography

Ultrasonic imaging works by directing high frequency acoustic waves into a body and then detecting the reflections that occur at interfaces between materials with differing acoustic properties within the object. Some depth information may be gained, but the spatial resolution is of the order of millimetres. The technique excels at detecting fluid filled cysts and voids within the breast, but has limited use for malignant breast tumour detection. The modality is considered to be mainly adjunct to x-ray mammography, although some research does suggest that ultrasound has the potential to replace x-ray mammography in screening selected populations [Irwig *et. al.*, 2004]; there has been a higher success rate when the technique is used on Oriental and younger women with denser breasts, and an increase in overall diagnostic sensitivity, but a slight fall in specificity, has been shown in symptomatic women aged 55 or under when both x-ray mammography and ultrasonography have been used [Houssami *et. al.*, 2002]. Ultrasound equipment is relatively cheap and the procedure causes minimal stress to the patient, but has been found to be operator dependant.

1.2.1.5 Infra-red/optical spectroscopy

IR spectroscopy is a technique that images the blood volume and oxygenation within a body. IR spectroscopic 3-D imaging has been used regularly to look at the brains of neo-nates [Hebden *et. al.*, 2004; Hintz *et. al.*, 2001], but is still in the early stages with regard to mammographic work [Hebden *et. al.*, 2001, Choe *et. al.*, 2005]. The technique may use partial compression of the breast or no compression at all and uses non-ionising radiation; however, the available spatial resolution is currently of the order of a few centimetres and it can only detect variations in blood flow within a body. This means that the modality will only detect lesions with a blood flow that is different from the surrounding tissues, most notably if angiogenesis or vascularisation have occurred.

1.2.1.6 Electrical Impedance Tomography

This imaging technique uses changes in the electrical conductance and capacitance of the body to create images of it and works on the principle that cancer cells have different dielectric properties compared to normal cells [Surowiec *et. al*, 1988]. An array of transmitting and detecting sensors is placed around the organ of interest and an image is built up by measuring the current, voltage and signal frequency between pairs of sensors. The equipment is cheap, but the technique is only capable of detecting lesions with a size greater than 15% of the object diameter [Holder *et. al.*, 2005] and has been shown to be unreliable for tumours less than 2-3 cm in size [Malich *et. al.*, 2003].

1.3 X-ray diffraction and coherent scatter

When diagnostic energy x-rays pass through a material, one of three interactions: inelastic scatter, elastic scatter or the photoelectric effect, may take place. The probabilities of these interactions taking place are governed by the x-ray energy and the density and atomic number of the material. Figure 1.3 shows the probabilities of these interactions occurring in Lead, Perspex, and human breast tissue (ICRU-44) at diagnostic energies [Berger *et. al.*, 1999]. The bulk of the x-rays will undergo a photoelectric interaction and deposit all of their energy in the material, some of which, particularly in materials with a high atomic number, may be converted to fluorescent x-rays, which may then escape from the material. At lower energies, there is also a significant amount of scatter in the lower atomic number materials.

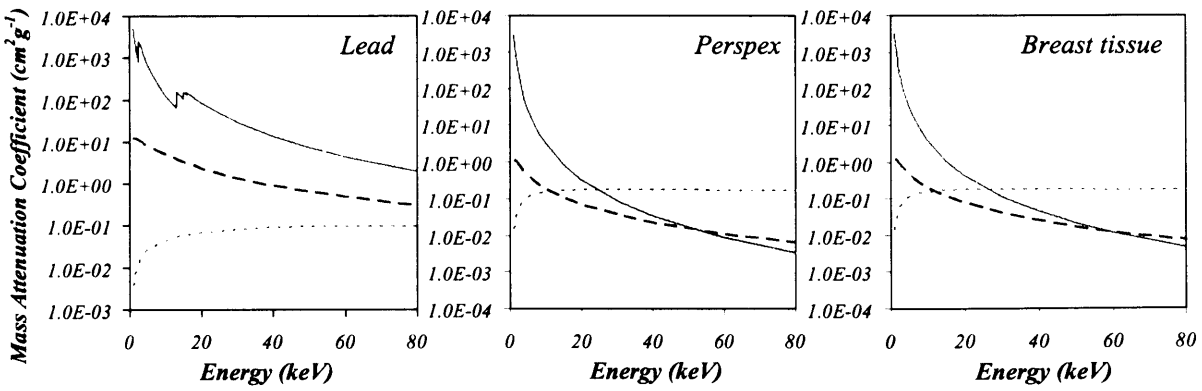

Figure 1.3 *Mass Attenuation coefficients for lead, Perspex and breast tissue; solid line, photoelectric interaction; dotted line, Compton scatter; dashed line, coherent scatter.*

In an inelastic, or Compton, scatter interaction the incoming x-ray interacts with an atomic electron and transfers some of its energy and momentum to that electron, leaving with less energy than it originally had. The probability of this type of scatter occurring in a material is almost uniform at the energies under consideration and the angular distribution of the Compton scattered x-rays is proportional to the differential cross-section per unit solid angle $d\sigma_{inc}/d\Omega$ given by [Hubbell *et. al.*, 1975]:

$$\frac{d\sigma_{inc}}{d\Omega} = [S(\chi, Z)]\frac{d\sigma_{KN}}{d\Omega} \qquad (1.2)$$

Where the first term, $S(\chi,Z)$, is the incoherent scatter function, which is zero in the forward direction and approaches Z as momentum transfer, χ, defined by equation 1.3, increases.

$$\chi = \frac{E}{hc}\sin\left(\frac{\theta}{2}\right) \qquad (1.3)$$

E is the energy of the incoming x-ray photon and θ is the photon scatter angle. The second term in equation 1.2 is the Klein-Nishina equation:

$$\frac{d\sigma_{KN}}{d\Omega} = \frac{r_0^2}{2}\left(1+\cos^2\theta\right)\left(\frac{1}{1+\alpha(1-\cos\theta)}\right)^2\left(1+\frac{\alpha^2(1-\cos\theta)^2}{[1+\alpha(1-\cos\theta)](1+\cos^2\theta)}\right) \qquad (1.4)$$

r_0 is the classical electron radius and α is the ratio of the photon energy to the rest mass of an electron.

Elastic scatter, also known as coherent or Rayleigh scatter, occurs when an x-ray interacts with an electron and its direction of travel changes, but it leaves the interaction with the same energy as it entered with. The differential cross-section per unit solid angle of the exiting radiation is given by [Johns & Cunningham, 1983]:

$$\frac{d\sigma_{coh}}{d\Omega} = \frac{r_0^2}{2}\left(1+\cos^2\theta\right)[F(\chi, Z)]^2 \qquad (1.5)$$

$F(\chi,Z)$ is the coherent scatter form factor. Conversely to the incoherent scatter form factor, the coherent scatter form factor approaches Z at small values of θ, and for large values it tends towards zero. The atomic coherent and incoherent scatter form factor can be found in tabulated form in Hubbell *et. al.* [1975] and the molecular coherent form factor for various plastics, along with beef, pork, water and human breast tissue

fixed in formalin can be found in Peplow and Verghese [1998]. Equation 1.5 indicates that at diagnostic energies the scattered x-rays predominantly follow paths at a small angle to the original direction of travel. It is thought that this type of scatter is a result of interference effects between the x-ray and the interatomic structures within the scattering material. A simple model of this situation is seen in the theory of Bragg scatter in regular crystals and a more complex treatment occurs in semi-regular structures, such as biological tissues.

1.3.1 Bragg scatter in crystals

Crystalline materials have chemical bonds that form regular lattice structures throughout. These bonds have both uniform lengths and constant angles between them. The bonds are often of a similar length to the wavelength of x-rays and hence x-rays passing through these materials exhibit interference or diffraction effects (figure 1.4).

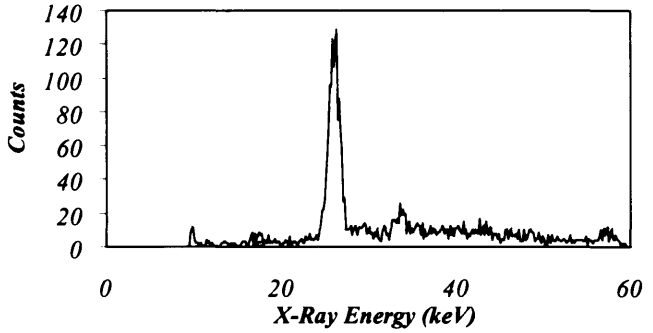

Figure 1.4 *Diffraction pattern from sugar crystals taken using the UCL Radiation Physics diffractometer system at a scatter angle of 6°. A tungsten x-ray tube operating at 70 kV was used.*

For a given material at a known lattice orientation, the interference effects seen in the exiting x-ray beam are always constant and may be used to identify constituent components of unknown materials. They follow Bragg's law which states that for constructive interference to occur, the difference in the path length between x-rays scattered by different crystal planes must be equal to an integer number n of wavelengths λ:

$$n\lambda = 2d\sin\left(\frac{\theta}{2}\right) \qquad (1.6)$$

d is the crystal lattice spacing and θ is the angle through which the incoming x-ray scatters, as illustrated by figure 1.5.

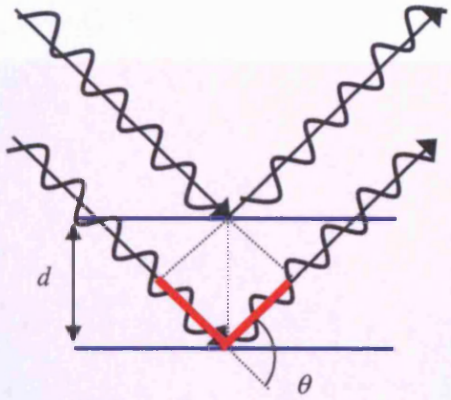

Figure 1.5 *Illustration of the path length difference used in the Bragg equation. The bold line indicates the difference in path length.*

1.3.2 Scatter in biological tissues

Figure 1.4 showed the x-ray diffraction pattern for a crystalline material. Sharp peaks occur at x-ray energy and scatter angle combinations that fulfil equation 1.6. It has been found that materials that are non-crystalline but still exhibit some short range order, such as plastics, also have diffraction patterns unique to the individual material composition. Figure 1.6 shows some of these patterns for Perspex, Nylon and PTFE taken with the same system used for the sugar pattern in figure 1.4. They do not take the sharp peaked regular structures of the crystal patterns but they still show some structure and are unique to the materials being investigated.

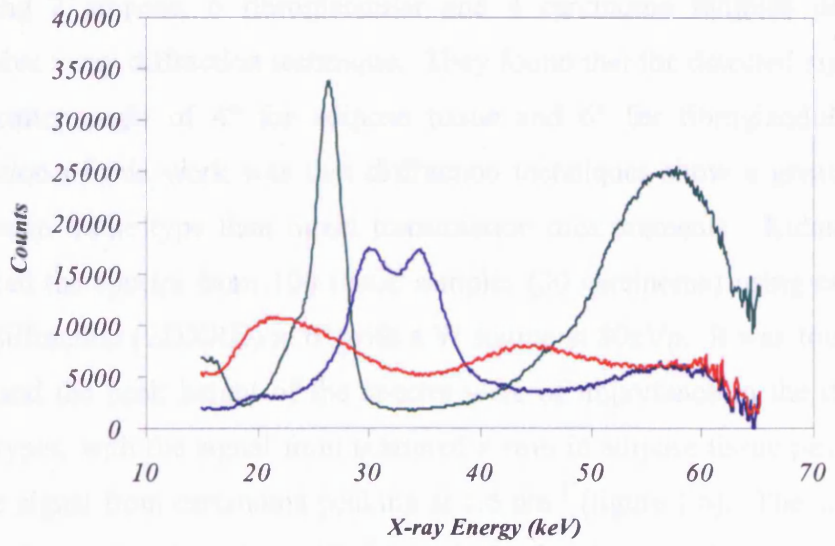

Figure 1.6 *Diffraction signatures of PTFE (green line), Nylon (blue line) and Perspex (red line) taken with a tungsten x-ray source operating at 70 kV at a scatter angle of 6°.*

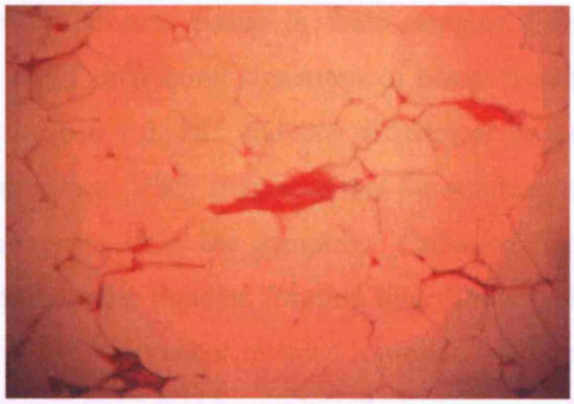

Figure 1.7 *Fat cells, as seen under a microscope. The median size of a fat cell has been measured by Sjöström et. al. [1971] and is of the order of 90 microns.*

Certain biological tissues exhibit short range order by virtue of the fact that cells of a particular type will all have similar orientations and dimensions (e.g. fat cells, figure 1.7). This means that some biological tissues also have diffraction signatures similar to those for non-crystalline, semi-regular materials. These patterns have been investigated for several different tissue types, such as brain and prostate [Lazarev *et. al.*, 2000], lyophilised blood [Desouky *et. al.*, 2001], bone [Royle & Speller, 1995], hair [James, 1999] and in particular, breast tissue.

Evans *et. al.* [1991] used a 60kVp Cu anode and filter x-ray source and a position sensitive detector to measure the scattered spectra from 19 breast tissue samples including 2 adipose, 6 fibroglandular and 4 carcinoma samples using an angular dispersive x-ray diffraction technique. They found that the detected signal was highest at a scatter angle of 4° for adipose tissue and 6° for fibroglandular tissue. The conclusion of this work was that diffraction techniques show a greater sensitivity to changes in tissue type than direct transmission measurements. Kidane *et. al.* [1999] measured the spectra from 100 tissue samples (30 carcinoma) using energy dispersive x-ray diffraction (EDXRD) at 6° with a W source at 80kVp. It was found that both the shape and the peak height of the spectra were of importance in the differentiation of tissue types, with the signal from scattered x-rays in adipose tissue peaking at 1.1 nm^{-1} and the signal from carcinoma peaking at 1.6 nm^{-1} (figure 1.8). The authors suggested that carcinoma is primarily typified by a lack of isolated pockets of fat throughout the sample. Poletti *et. al.* [2002] measured 4 adipose and 3 glandular samples and came to

similar conclusions and Geraki *et. al.* [2004] used the EDXRD technique to quantify the amount of adipose and fibrous tissue in their samples. Fernández *et. al.* [2002] measured the small angle diffraction signatures of breast tissue, looking at momentum transfer values of less than 1.0 nm^{-1} and saw differences in the recorded spectra from healthy and diseased tissues. They suggested that the resulting signatures may be due to the structure of collagen within the samples. Collagen fibres in breast tissue are arranged into 70 nm diameter bundles forming long fibrils with a 65 nm axial period, which increases by 0.3 nm in cancer invaded regions. Lewis *et. al.* [2000] also found that changes in the signatures could be explained by changes in the collagen structures.

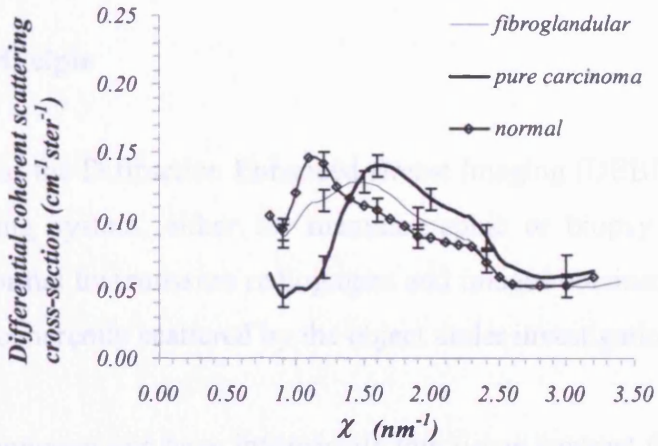

Figure 1.8 *Differential coherent scattering cross-section for breast tissues [Kidane et. al., 1999]. The error bars represent values one standard deviation from the mean. Normal tissue is assumed to be 50% fat 50% fibroglandular.*

Figure 1.8 shows the differential coherent scattering cross-section plotted against momentum transfer, χ. Comparison of equations 1.3 and 1.6 shows that χ is analogous to the inverse of *d*, the crystal lattice spacing, in the Bragg equation; both are functions of the x-ray energy and the photon scatter angle. The use of χ makes comparison between diffraction systems with varying scatter angles and x-ray energies easier. If a range of momentum transfer values are to be investigated by a system, then two ways of taking the measurements can be employed; either the scatter angle under investigation can be fixed and a range of x-ray energies can be considered, or the energy can be fixed and a range of scatter angles used, as tends to be done traditionally in x-ray crystallography.

1.4 Diffraction Enhanced Breast Imaging

Figure 1.8 shows the diffraction signatures for normal and cancerous breast tissue obtained by Kidane *et. al.* [1999]. It can be seen that the differential coherent scattering cross-section for normal tissue is around three times that of carcinoma at a momentum transfer value of 1.1 nm^{-1} and at 1.6 nm^{-1} it is approximately 1.5 times larger for carcinoma than for normal tissue. It is of a similar magnitude for both tissues at 1.4 nm^{-1}. The figure also shows that there is a difference in the signatures of mixed 'normal' and 100% fibroglandular tissues, implying that the signature from adipose tissue is different to that of fibroglandular tissue.

1.4.1 DEBI principle

The prime goal of the Diffraction Enhanced Breast Imaging (DEBI) project is to create a clinical imaging system, either for mammographic or biopsy purposes, that will combine both normal transmission radiographs and images obtained by detecting the x-radiation that is coherently scattered by the object under investigation.

Transmission mammograms have intrinsically low tissue contrast due to the uniformity of the total attenuation coefficient for different breast tissues; nevertheless they offer a high spatial resolution and are able to visualise microcalcifications of the order of 100 μm in size. Diffraction images, as will be shown in this thesis, have a much poorer spatial resolution – presently no better than 500 μm with the UCL systems – but achieve significantly higher contrast between normal and cancerous breast tissues than transmission images. The apparent opposing strengths and weaknesses of these two imaging techniques led to the suggestion of using a combination of them for imaging breast tissues [Kidane, 2000].

1.4.2 Towards a pre-clinical system

The eventual aim of this project is to create a clinical system utilising the DEBI technique. A mammography system could be built, or a system could be constructed to be used on small samples as a biopsy aid during surgery. A fully functional pre-clinical system must be constructed before the possibility of clinical trials can be considered.

The construction of this system will take several different parallel paths of research. Firstly there is the system instrumentation and engineering; suitable transmission and diffraction detectors need to be found, along with an x-ray source and collimation that suit the dose restrictions and detector requirements. Secondly the image construction, viewing and analysis algorithms must be considered. The raw diffraction images will be affected by the attenuation properties of the materials being imaged, and so corrections to the raw data may be needed. A diagnostically useful, user friendly way of viewing the final composite transmission and diffraction data must also be devised. Finally, the use of the diffraction information for tissue type discrimination must be fully investigated.

It was shown in section 1.3 that different materials, including breast tissues, have different diffraction signatures. A high quality database of these must be constructed so that they can be compared to clarify whether the signatures can be used to identify individual tissues types in a clinical setting. For homogeneous samples, such as crystals or uniform plastics, this is a fairly simple procedure using a powder diffractometer; however it becomes more complex when the purity of the materials can not be guaranteed, such as with biological samples. The nature of breast tissue means that it is a mixture of mainly fibrous, glandular and adipose tissues with small amounts of vascular tissue, and carcinoma or other lesions if diseased. These tissues intermingle with each other to a certain extent, creating ill defined boundaries on a macroscopic level meaning that any sample greater than a few millimetres in size will almost certainly contain at least two different tissue types. In this case, the composition of the sample must be analysed as accurately as possible.

It has been decided that the ideal mechanism for assessing the composition of tissue samples is to image small tissue sections using a micro-computed-tomography (microCT) system operating in transmission and diffraction imaging modes. Using small sections will hopefully mean that the chance of having several tissue types within one sample is minimised, and it also aids the process of correlating the images with the histopathologist's analysis of the samples. High spatial resolution transmission microCT will provide a map of the different structures within the slice of interest, allowing a good estimate of the proportion of each material within the slice to be acquired. The diffraction microCT will provide both diffractometer information about

the gross sample at the CT slice under consideration and high contrast, but low spatial resolution images of the samples which can be used to assess the contrast enhancement available when using diffraction techniques in CT.

1.5 Scope of this PhD thesis

The work covered in this thesis will investigate the elastic scatter from human breast tissues with a view to either incorporating a scatter detector into a standard mammographic unit or creating an x-ray diffraction imaging biopsy tool in the future. A possible detector for this purpose is also considered.

This chapter has briefly discussed breast anatomy and histopathological analysis techniques, an overview of mammography has been given, and the principles behind Diffraction Enhanced Breast Imaging (DEBI) were introduced. Chapter 2 will consider more fully the properties required from an imaging system to be used for DEBI and will introduce the collimation and detectors used in the work in the following chapters. A phosphor coated low-light-level charge-coupled-device (L3CCD) will be offered as a spatially resolving detector solution to the problems associated with detecting the scattered x-rays, and theoretical and experimental aspects of the energy resolution characterisation of this detector will be presented.

Chapters 3 and 4 will move on to examine the scatter properties of human breast tissue. Chapter 3 concentrates on using the L3CCD for DEBI measurements. It looks at the spatial resolution and collimation requirements needed for clinically useful results, shows how some depth information can be obtained by this technique and considers the attenuation corrections necessary for a final clinical imaging system. Chapter 4 presents work done to further our present knowledge of the 'scatter signatures' of human breast tissue. The tissue is naturally inhomogeneous, so precise knowledge of a sample's composition is needed in order to accurately classify its scatter signature. A microCT system has been used to image small samples so that more information can be obtained about their precise composition; the samples' scatter signatures were then classified using this information. The microCT images also allow an estimate to be made of the achievable contrast enhancement available using DEBI.

CHAPTER 2

Materials and instrumentation considerations for diffraction imaging

The previous chapter of this thesis introduced the basic premise behind the use of DEBI for either diagnostic mammography or as a biopsy tool. The development of suitable instrumentation to place the DEBI technique in the clinical environment was highlighted to be a pivotal aspect of the research, and as such this chapter considers the collimation requirements and detector properties needed to create a successful laboratory diffraction imaging system.

2.1 Diffraction imaging system geometries

As shown in chapter 1, the diffraction signal from a sample is often measured as a function of momentum transfer, which is itself a function of both the energy and scattering angle of the x-ray undergoing coherent scatter (equation 1.3). This dual energy and angle dependence of momentum transfer means that there are two usual ways of obtaining a full diffraction signature for a sample; either an angular dispersive technique may be used where the energy of the x-rays is held at a fixed value and the angle through which the x-rays are scattered is investigated, or an energy dispersive technique can by used whereby polyenergetic x-rays are detected at a single scatter angle with an energy resolving detector.

2.1.1 Angular dispersive diffraction imaging

This technique is commonly used in powder diffraction and crystallography [Alexander and Klug, 1948; Desouky *et. al.*, 2001]. A monoenergetic pencil beam of x-rays is incident on a thin sample and photons are preferentially scattered to certain angles

dependent on the internal structure of the sample. For powdered crystalline samples, 'diffraction rings' are created by the scattered beam. These are imaged either 2-dimensionally by an area detector or 1-dimensionally by scanning a detector along one of the pattern's axes. The rings adhere to Bragg's law (equation 1.4), creating well defined annuli of high and low intensities whose radii can be measured to obtain accurate information on the structures of the samples.

If the sample takes a regular fibril form, rather than a powdered crystal form, then the periodic molecular repetition within the sample varies between the sample axes. This leads to a diffraction pattern that shows a variation between the x- and y-axes. For samples with short range order, such as plastics and biological tissues, a less defined ring pattern is seen, but it still contains information unique to the structure of the sample [James *et. al.*, 1999; Evans *et. al.*, 1991, Kosanetzky *et. al.*, 1987].

The angular dispersive technique requires collimation primarily to restrict the incoming radiation beam to a parallel pencil beam. The size of this beam will affect the achievable momentum transfer resolution of the system, with a larger beam leading to an increased spatial blurring of the diffraction pattern. For a thin sample, where no further collimation needs to be used, a beam stop also needs to be placed between the sample and detector. This stops the intense primary transmitted x-ray beam from saturating the detector, which could lead to a loss of the diffraction signal. The stop must cover an area at least equal to the size of the primary pencil beam and be made of a suitable material such that the transmitted beam through it is effectively zero whilst minimal scatter is produced by the stop that could create background noise in the detected signal.

If a thick sample is placed in the system with no collimation after it, a loss in the momentum transfer resolution of the system will be seen due to photons scattering at a range of angles along the beam axis all interacting at the same point in the detector. Collimation placed such that it is focussed onto a small portion of the sample can correct this problem, however the use of collimation will reduce the flux incident on the detector and also create difficulties when trying to acquire data for all possible scatter angles.

Two types of detector are suitable for angular dispersive diffraction imaging: detectors covering the entire area of the rings, or detectors that can be scanned across the rings. An area detector needs a pixel size that will give adequate spatial resolution of the rings whilst usually needing to cover an area of 400 cm^2 in order to be able to image them without any translation of the detector [Lewis *et. al.*, 2000]. A scanning detector requires either good spatial resolution and exact positioning from a known datum point or, if the spatial resolution is poor, needs to be collimated so that the scatter signal is only obtained for one small portion of the axial translation at a time.

The reliance of the angular dispersion technique on the monochromaticity of the x-ray beam makes it unsuitable for measurements with normal polyenergetic x-ray units, but highly suited to synchrotron use [Lewis *et. al.*, 2000; Meek *et. al.*, 2001; Barroso *et. al.*, 2001].

2.1.2 Energy dispersive diffraction imaging

Energy dispersive x-ray diffraction (EDXRD) techniques rely on detecting scatter from a sample at a fixed angle whilst using a polyenergetic source to obtain data relating to a range of momentum transfer values. The momentum transfer resolution of the system depends both on the collimation used to define the scatter angle and on the energy resolution of the detector used.

Once again, using a parallel pencil beam of incoming radiation gives the best results as the angle of scatter will be better defined. The ideal collimation for the exiting scattered radiation is a circularly symmetrical system defining the solid angle within which the scatter must fall into in order to reach the detector, ensuring that as much as possible of the radiation that is scattered into the solid angle of interest is collected by the detector.

A spatially resolving detector is not required for this technique unless several scatter angles are under investigation simultaneously, however good energy resolution is of paramount importance in order to obtain adequate momentum transfer resolution.

2.2 Collimation for measurements on breast tissues

The aim of this work is to create images of breast tissue phantoms using diffraction imaging techniques. Diffraction imaging is reliant on being able to pick off photons that have been scattered to a certain angle by the sample. A collimator is always required between the sample and detector for energy dispersive diffraction techniques and one will be needed for angular dispersive techniques when collecting the scatter from samples of the thicknesses that will be used for this work. The limiting factor in the momentum transfer resolution of a diffraction imaging system is almost certainly going to be the angular resolution of the collimation as there is always going to be a trade off between the acceptance angle and the number of photons that will pass through the collimation to the detector.

The geometry of the collimator will depend on the diffraction technique used, the detector used and the final aim of the diffraction set up. Two sets of diffraction apparatus were used in the work described in this thesis; the first, based on a collimated angular dispersive technique, was used at a synchrotron source for planar imaging of life-size phantoms and for micro-computed-tomography (microCT) of small biopsy sized samples. The second system, for microCT work, was used to investigate translating this approach to a laboratory based x-ray unit using EDXRD techniques.

2.2.1 Collimated angular dispersive diffraction imaging

The use of a parallel, monoenergetic synchrotron radiation beam allowed angular dispersive diffraction techniques to be employed in imaging breast tissue samples. Barroso *et. al.* [2001] showed that diffraction microCT of small crystalline samples embedded in plastic was possible and previous experiments by Harris [2000] successfully imaged a life-size breast tissue phantom using diffracted synchrotron radiation. In the work of Harris, (a previous PhD student on this project at UCL), a low-light-level CCD (L3CCD) placed behind a parallel hole collimator was scanned across the phantom in conjunction with a full field beam in order to create a large area image. The collimator consisted of a single row of 500 μm square holes separated by 500 μm thick septa placed 1.5 cm away from the centre of the 3 cm thick phantom at a

scatter angle of 9°. It allowed x-rays scattered from a 1.3 cm thick slice of the phantom to be collected (figure 2.1(a)). The angular resolution of this collimator gave a momentum transfer value spread of 0.19 nm^{-1} when a beamline energy of 17.4 keV and a scatter angle of 9° were used (χ = 1.1 nm^{-1}). This approach was continued in chapter 3 of this thesis.

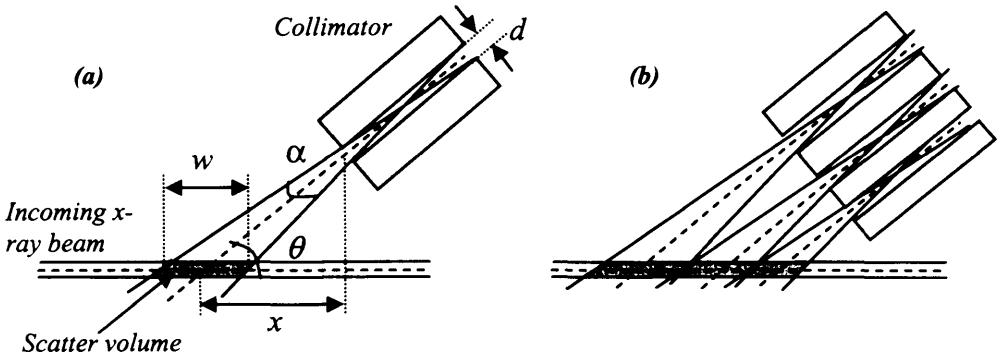

Figure 2.1 *Schematic of the scatter volume in the sample subtended by the collimation; (a) dimensions used in the calculation of the width of the volume subtended by one collimator hole; (b) the entire sample may be covered using multiple collimator holes.*

An attempt was made in this thesis to improve the efficiency of the system and thereby decrease imaging time. To achieve this, work focussed on the design of the collimation. In order to make maximum diagnostic use of the DEBI technique, the entire breast thickness must be sampled, rather than just one slice. This was done using a series of rows of holes in the diffraction collimator placed alongside each other, as shown in figure 2.1(b). The information gained from each row of holes was used to form an image of an individual slice of the phantom, giving some depth information [Harding, 1999]. The width, w, of each slice is dependent on the collimation's acceptance angle, α, the angle of the collimation to the incident x-ray beam, θ, the width of the collimator hole, d, and the distance, x, between the front face of the collimator and the centre of the scatter volume in the phantom:

$$w = \left(\frac{2x\tan\left(\frac{\alpha}{2}\right)}{\cos\theta} + d \right) \left(\frac{\sin\left(90-\frac{\alpha}{2}\right)}{\sin\left(\theta+\frac{\alpha}{2}\right)} + \frac{\sin\left(90+\frac{\alpha}{2}\right)}{\sin\left(\theta-\frac{\alpha}{2}\right)} \right) \qquad (2.1)$$

This means that a 3 cm long collimator containing three rows of 500 μm holes separated by 500 μm septa placed at a scatter angle of 9° will satisfactorily cover a volume encompassing the entirety of the first 3 cm of a 4 cm thick breast tissue phantom; 4 cm

is the average thickness of a breast under compression. This is the collimation designed for the synchrotron work in this thesis; it achieves a spatial resolution in the image of 500 μm in both the *x*- and *y*- directions and ~ 1 cm in the depth plane.

The depth information available using this collimation will never compete with that available from clinical CT systems due to the compromise that must take place between x-ray flux incident on the detector and the collimation's acceptance angle; however, it is worth considering that the only depth information currently available from normal transmission mammography is limited to what can be obtained by comparing the two views (cranio-caudal and medio-lateral-oblique) customarily taken of the patient.

2.2.2 Collimation for energy dispersive x-ray diffraction imaging

As mentioned earlier, angular dispersive techniques are ideally suited to the parallel monoenergetic radiation produced by a synchrotron, however they are not suitable for use in the laboratory with standard polyenergetic x-ray units. If an image of an object is to be formed using polyenergetic radiation scattered from the object then an energy dispersive technique, where the scatter angle is held constant must be used. In this technique, the angular resolution of the collimator becomes important and a compromise must be made between the collimation acceptance angle and the acceptable level of x-ray flux reaching the detector. A focussed conical collimator will allow the maximum amount of flux to reach the detector for a given scatter angle.

Figure 2.2 shows the collimator designed for the laboratory based diffraction work in this thesis; it consists of a primary 1 mm pin hole placed before the sample to provide a pencil beam and a diffraction collimator behind the sample set to 6° with a nut on a spindle allowing acceptance angle adjustment [Speller, 2003]. The cell has been formed from 0.5 cm brass plate, securely bolted together to ensure that the three vertical plates are parallel. This collimator can be used to collect diffraction spectra of phantoms or, if the phantoms are translated and rotated through the pencil beam, the data for a complete diffraction microCT image of the phantom can be acquired.

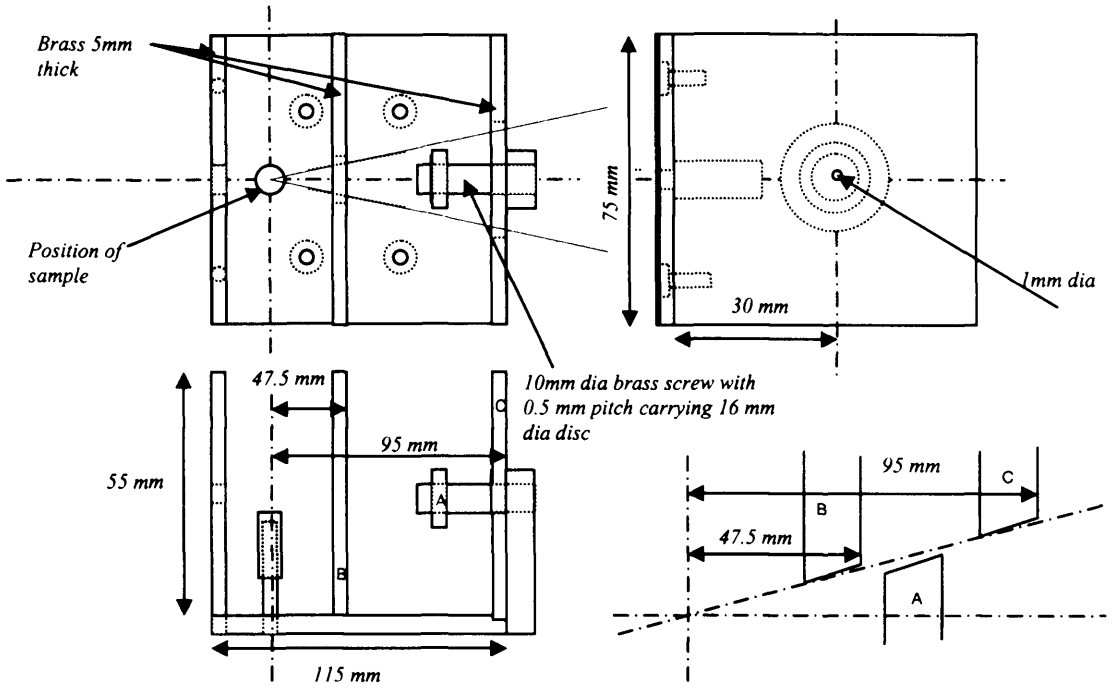

Figure 2.2 *Schematic of the UCL laboratory EDXRD collimator [Speller, 2003].*

The primary aim of the laboratory diffraction work was to produce microCT images of small tissue samples approximately 8 mm in diameter. This meant that the angular spread of the collimator needed to be sufficient to allow the scatter signal from the entire depth of the sample to be collected in one spectral acquisition. Calculations based on equation 2.1 showed that this was possible with the acceptance angle is set to 0.35°; this angle gave an error on the momentum transfer value of 3% at 1.1 nm^{-1} – the preferred momentum transfer value for this work.

2.3 Requirements of a scatter detector

The main criterion for a detector to be suitable for acquiring signals from x-rays scattering in a phantom is that it is able to clearly observe that signal above the background noise that will be present, both from stray radiation and the noise intrinsic to the detection system. The number of coherently scattered x-rays reaching the detector in a diffraction system will be small compared to the number of x-rays being produced at the source. This is due to two reasons, the first being that the probability of a coherent scatter taking place is less than one in ten and the second that the diagnostically useful coherent scatter signal, as defined by the system collimation, makes up only around a third of the total coherent scatter taking place.

The number of photons interacting via coherent scatter, I_{INT}, in the scatter volume is given by the product of the number of photons incident on the volume, $I_{INCIDENT}$, and the probability of interaction by coherent scatter within the volume, P_{INT}:

$$I_{INT} = I_{INCIDENT} \times P_{INT} = I_o e^{-\mu_T x_1}\left(1 - e^{-\mu_T x_2}\right)\frac{\mu_{COH}}{\mu_T} \qquad (2.2)$$

I_o is the number of x-rays incident on the phantom, μ_T is the phantom's total attenuation coefficient (0.968 cm^{-1} at 17.4 keV for breast tissue), x_1 is the distance traversed across the phantom before the photons enter the scatter volume, μ_{COH} is the attenuation coefficient due to just coherent scatter (0.0975 cm^{-1} at 17.4 keV for breast tissue) and x_2 is the length of the scatter volume. The attenuation coefficients have been calculated by inserting the *ICRU-44* [1989] values for breast tissue into *XCOM* [Berger *et. al.*, 1999]. 17.4 keV corresponds to the K_α lines of Molybdenum. This energy was chosen as it was used in previous diffraction imaging work at a synchrotron beamline [Harris *et. al.*, 2003] and will be used later in this thesis for further work at the same beamline.

For a 1 cm long scatter volume lying 2 cm into a 3 cm thick breast tissue phantom, equation 2.2 gives a value of $0.0089I_o$ for I_{INT}, i.e., just 0.89% of the x-rays incident on the photon will coherently scatter within the voxel of interest.

To be of diagnostic use, these coherently scattered photons must now reach the detector, which lies behind collimation. Therefore the useful coherently scattered x-ray intensity incident on the detector face, I_{Det}, is given by:

$$I_{Det} = I_{INT} \times P_{COL} \qquad (2.3)$$

P_{COL} is the probability of a scattered photon successfully passing through the collimation to the detector face. Taibi *et. al.* [2000] showed that at 20 keV, coherently scattered x-rays will fall predominantly into a conical volume centred on the original direction of travel with a half angle of 15°, with a peak lying between 6° and 8°. The data also indicated that approximately 30% of the coherently scattered photons can be assumed to have a scatter angle lying between 6° and 8°. Assuming that a collimator with a relatively wide acceptance angle of 2° is centred on this region, then P_{COL} will be 0.3, therefore I_{Det} has a value of $0.003I_o$.

It should be noted that this calculation assumes that the collimation is circularly symmetric and centred on the point of interaction and is therefore able to accept all photons scattering at angles between 6° and 8° within the voxel; this is a highly unlikely situation for many experiments, and thus the proportion of x-rays originally incident on the phantom that coherently scatter within the scatter voxel of interest and then travel along a path that will allow them to be incident on the face of the detector will be significantly less than 0.3%. The calculation also only considers total attenuation of the photons prior to the scatter voxel and does not consider any other forms of attenuation within the voxel other than coherent scatter.

This ballpark calculation indicates that only a small fraction of the incoming photons are useful for diffraction imaging purposes at any given time. This tiny useful photon fraction means that every photon detected becomes of statistical significance in the data, implying that the detection of as many as possible of the diagnostically useful coherently scattered photons becomes paramount when considering the instrumentation of the system. Therefore a detector with high sensitivity, ideally a photon counting detector, should be used in order to maximise the system sensitivity.

The total useful signal in the diffraction system comes from just a small number of x-ray photons. Thus the scatter detector must have high quantum efficiency in order to physically capture the signal from as many of the photons that reach it as possible. Once a photon has interacted with the detector, then its signal must compete with the signal due to the noise within the detector and its associated electronics, therefore a detector with intrinsic noise statistics significantly less than the signal generated by an x-ray photon is needed for detection of individual x-rays. Spatial resolving capabilities also play a part in detector choice. If the detector has no spatial resolution then scatter data can be recorded from just one collimation defined voxel at a time. This is adequate for small samples, but is not a satisfactory situation when wishing to cover a large area phantom in a reasonable time. Current large area diffraction imaging techniques have used a diffraction image pixel size of 500 μm [Harris *et. al*, 2003], however it is hoped that in the future the size could be decreased to 150 μm or 200 μm [Griffiths *et. al.*, 2003]. A detector that is used for collimated angular dispersive diffraction imaging should have spatial resolution capabilities at least of a similar order of magnitude to the collimation so that data is not lost. A large imaging area/field of view would obviously

also be an advantage for the detector such that a large area phantom can be imaged quickly, however, providing that a number of the individual detectors could be tiled, this is not such an important issue.

Energy resolution is a negligible requirement for a detector used for angular dispersive imaging with synchrotron radiation as the x-ray beam used is highly monochromatic (bandwidth is typically 10 eV at 20 keV [Arfelli *et. al.*, 1995]) and the contribution to the scatter from the Compton effect is small at low angles and x-ray energies. However energy resolution is essential for a detector for EDXRD as no momentum transfer resolution will be achieved without this capability.

2.3.1 Possible scatter detectors

The relevant characteristics for a good scatter detector have been compared for various devices in table 2.1. The detectors include Avalanche Photodiodes (APDs), Charge Coupled Devices (CCDs), Electron Bombarded CCDs (EBCCDs), Intensified CCDs (ICCDs), Position Sensitive Photo-multiplier Tubes (PSPMTs) [all found in Arisaka, 2000], Active Matrix Flat Panel Imagers (AMFPIs) [Antonuk *et. al.*, 2000; Maolinbay *et. al.*, 2000], Cadmium Zinc Telluride (CdZnTe) [Giakos *et. al.*, 2004; Ramsey *et. al.*, 2001; Kastis *et. al.*, 2000], Controlled Drift Devices (CDDs) [Castoldi *et. al.*, 1999, 2001, 2003, 2004], Low-Light-Level CCDs (L3CCDs) [Harris, 2002], CMOS Active Pixel Sensors (APSs) [Prydderch *et. al.*, 2003], Mercuric Iodide (HgI_2) [Baciak and He, 2004, Alexiev *et. al.*, 2004; Owens *et. al.*, 2002], High Purity Germanium (HPGe) [Knoll, 1999], Silicon PADs [Mainprize *et. al.*, 2002; Studen *et. al.*, 2004] and Silicon Microstrips [Beuville *et. al.*, 1998; Royle *et. al.*, 2002; Scannavini *et. al.*, 2000].

The table contains a column labelled 'Detection Type'. This is because ionising radiation is generally detected by one of two methods; it is detected either directly within the device, or indirectly where the device detects optical wavelengths emitted by a phosphor that the radiation has interacted with. Some detectors, for instance CCDs or CMOS devices, are more suited to indirect detection and some, such as HPGe, operate using direct detection.

Table 2.1 Comparison of the characteristics of possible scatter detectors for DEBI. NA means not applicable for that particular device.

Detector	Detection type	(D)QE	Gain	Dynamic range	Noise (e- r.m.s).	Noise Factor	G/N	Energy resolution †	Minimum Pixel size (μm)	Field size (cm^2)
AMFPI	Direct	>0.9	10^4	10^4	~2500	NA	NA	NA	100	1600
APD	Indirect	0.8	500	10^{11}	~100	2-5	5	Dependent on phosphor choice	200	Pixel size
CCD	Indirect	0.25	1	10^4	~100	NA	NA	NA	7	1
CDD	Direct	0.9 @ 10 keV 0.09 @ 30 keV	1	10^5	<100	NA	NA	~300 ev @ 5.9 keV	50 x 120	0.01
CdZnTe	Direct	0.1	1	Photon counting	large	NA	NA	1.2 keV @ 60 keV	330	1
EBCCD	Indirect	0.25	10^3	10^4	~100	1.1	10	NA	15	1
ICCD	Indirect	0.2	10^4	10^4	~100	2-4	10^2	NA	15	1
L3CCD	Indirect	0.25	10^4	10^3	~100	0.8	10^2	Unknown	20	1
CMOS	Indirect	0.35	8	10^3	50	NA	NA	NA	25	1.7
HgI_2	Direct	0.16	1	Photon counting	large	NA	NA	1.2 keV @ 59.5 keV	1000	1
HPGe	Direct	~1	NA	Photon counting	v. low	NA	NA	~600 eV @ 60 keV	4000	Pixel size
Si PAD	Direct	<0.3	1	10^5	620	NA	NA	1.82 keV @122 keV	50	5
Microstrip	Direct	0.8	1	10^4	450	NA	NA	6 keV @ 100 keV	52	16
PSPMT	Indirect	0.4	10^5	10^7	~100	<0.1	10^3	Dependent on phosphor choice	1000	4

† *Detectors must operate in photon counting mode in order to achieve energy resolution*

The detective quantum efficiency (DQE), has been quoted at zero frequency, and, unless otherwise stated, has been quoted at 50 keV for direct detection devices to take into account signal losses specific to the individual devices. The quantum efficiency (QE) of the device to the optical wavelengths emitted by a phosphor has been quoted for indirect detectors. This is because phosphor thicknesses and types can be specifically tailored for individual devices and applications, leading to potentially high values of DQE for all indirect detection systems. It should be noted, however, that in order to achieve a high level of DQE, the phosphor thickness may be such that a decrease in spatial resolution is inevitable [Taibi *et. al.*, 1997].

The approximate dynamic range and gain of each device has been quoted in the table. APDs, EBCCDs, ICCDs, L3CCDs and PSPMTs apply gain to the signal before readout and use electron avalanche processes. Applying gain in this way introduces Poisson distributed noise statistics into the signal as the process takes place [Hynecek, 2001]. The excess noise factor has been quoted for these avalanche gain devices. A lower factor indicates a better signal to noise ratio, implying that the detector will have advantages for low flux applications.

The quoted value for the devices' noise refers to either the readout electronic noise or the leakage current noise, depending on which is the limiting noise feature for the detector in question. The value G/N attempts to give a concept of the SNR available for detectors where gain is added to the signal prior to the limiting noise section of the device.

On the whole, silicon based indirect detection devices such as CCDs and CMOS devices do not tend to have x-ray energy resolution capabilities. They are originally pixellated area imaging optical devices where integration of a signal over time is necessary and photon counting is considered impossible. However, as will be discussed later in this chapter, measurements using a phosphor covered L3CCD have indicated that some energy resolution may be possible with this device. APDs and PSPMTs are also indirect detection devices, nevertheless they are photon counting devices and are capable of energy resolution, which has been found to be highly dependent on the thickness and type of the phosphor used with the device. Direct detection devices are often photon counting and have energy resolution capabilities. Silicon devices can have

energy resolutions of the order of 5-10% FWHM for diagnostic energy x-rays, CdZnTe and HgI_2 are capable of ~ 2% FWHM and HPGe devices will achieve <1% resolution.

The spatial resolution given in Table 2.1 has been shown as the size of the pixels of the device. Where square pixels are not possible, both dimensions of the pixel have been given. For indirect detectors it must be noted, as mentioned above, that the addition of a phosphor will lead to poorer spatial resolution. A rule of thumb is that the resolution is approximately equal to the depth of the phosphor. Most commonly used phosphors are of the order of 100 μm thick, and so the practical resolution of most of the indirect detector systems will be around 100 μm.

The field size of the device has been given in square centimetres. For APDs and HPGe detectors, which often have no intrinsic spatial resolution capabilities, the field size is equivalent to the size of a pixel and thus fields that are centimetres in size are possible provided that spatial resolution is not required.

Table 2.1 has emphasised the fact that excellent spatial and energy resolution are often mutually exclusive characteristics. HPGe detectors have by far a superior x-ray energy resolution when compared to any of the other detectors but have poor spatial resolution, whereas CCDs have the best spatial resolution - although this is limited by the addition of a phosphor - but negligible energy resolution. An ideal scatter detector would have low noise characteristics, removing the AMPFI, Si PAD, HgI_2, CdZnTe and microstrip detectors from the running, and it also needs either good energy resolution or a spatial resolution of 100 μm or better, depending on whether the diffraction signal is to be obtained by angle dispersive or energy dispersive techniques.

All types of CCD have a suitable spatial resolution for angular dispersive imaging, along with CMOS devices and the CDD; however the normal CCD, with no additional gain mechanism, may not prove sensitive enough for the requirements of good counting statistics. APDs may possibly have the required spatial resolution in the near future. Both the CDD and HPGe have good energy resolution characteristics, as do the APD and PSPMT, provided that a good phosphor choice is made. Only the CDD shows both the required spatial and energy resolutions for both diffraction imaging techniques, although APDs may soon also fit the requirements. The CDD has a drawback with

regards to its field size though, and is currently still at its prototype stage and so not yet commercially available.

2.3.2 Detector choices for diffraction imaging

The most likely detectors for EDXRD are HPGe, CDDs and APDs, provided that a suitable phosphor is used. The detectors most suitable for collimated angular dispersive imaging are CMOS, CCDs with gain mechanisms, such as the L3CCD, and possibly APDs and CDDs in the future.

2.3.2.1 APD

Normal photodiodes produce a small amount of charge (normally 2-3 electrons [Knoll, 1999]) when an optical photon interacts in their depleted region, resulting in a few thousand electrons at best being produced for a single scintillation event in the phosphor. Avalanche photodiodes utilise a high voltage region to create an avalanche of impact ionisation to turn this relatively small signal into a much larger signal, allowing additional sensitivity to be achieved with these devices. Good energy resolution can also be achieved provided that the incoming x-rays deposit all of their energy in the phosphor coupled to the device. The devices are manufactured individually, so the detector field size is the same as the pixel size. This is currently 200 μm and would be on the large side for an angular dispersive diffraction system. APDs also have the highest excess noise factor of all of the electron multiplication gain devices considered in table 2.1, leading to a poor signal-to-noise ratio.

2.3.2.2 CDD

The CDD is a device which combines the pixellated structure of a CCD with the ease of charge transfer of a silicon microstrip detector, potentially allowing chip read-out times of 2-5 μs for a 1 cm long device. It works by applying a sinusoidal potential down a silicon strip to form a pixellated structure by the creation of potential wells; these pixels are then readout by replacing this potential structure with a gradient field which moves the captured charge in packets along the strip to readout electronics. The concept was arrived at in the mid-1990s [Castoldi, 1997] and several prototypes have since been constructed. The values in table 2.1 are based on the results of the characteristion of a 1

mm^2 prototype consisting of 50 μm wide channels on a 300 μm thick substrate with a pixel length of 120 μm. The size of this prototype severely limits its use in diffraction imaging, however a 36 mm^2 prototype on the same thicknéss substrate has since been constructed [Castoldi, 2004]. Although the DQE of these devices is only 9% at 30 keV, it has been predicted that using a 500 μm thick substrate would increase this value to 14% [Castoldi, 2002]. This device could prove to be a suitable scatter detector for both angular and energy dispersive diffraction in the future as it has adequate spatial resolution, good energy resolution due to the lack of a phosphor and a low noise fast readout mechanism. The potential is also there for an increase in DQE due to an increase in substrate thickness and an increased field of view in the future. The device can not presently be considered as a detector for diffraction imaging due to current limits on its size and availability.

2.3.2.3 HPGe

High purity Germanium detectors are commonly used for x-ray spectroscopy due to their extremely high energy resolution capabilities (~ 1% FWHM at 60 keV). Their main disadvantage is their small bandgap of 0.7 eV, meaning that the detectors have to operate at liquid nitrogen temperatures; thus they must be enclosed in a vacuum filled cryostat [Knoll, 1999]. A further disadvantage is the considerable costs associated with pixellisation to create spatially resolving devices. These detectors are ideal for energy dispersive diffraction as long as the acquisition procedure and time allows for the data for each scatter voxel of the phantom to be collected individually. This condition is unfeasible for creating diffraction images of large area phantoms, but can be fulfilled for micro-computed-tomography samples. The excellent energy resolution of these detectors means that the achievable momentum transfer resolution of an energy dispersive diffraction system becomes limited purely by the angular resolution of the system collimation. A large area single crystal HPGe detector was chosen as the detector in the laboratory based EDXRD microCT system described later in this thesis.

2.3.2.4 CMOS

CMOS Active Pixel Sensors have come to the forefront of digital optical imaging in the past 10 years; they are now used in many digital cameras and are also used as the detector in some particle physics experiments [Takayanagi *et. al.*, 2003]. They are also being strongly considered for space science [Prydderch *et. al.*, 2003] and earth

observation satellites [Morrissey *et. al.*, 2003]. They have relatively low read noise and dark noise provided they are cooled. The sensors are monolithic, thereby avoiding problems related to bump-bonding or other types of read-out chip connections. They also operate with column parallel readout, like CDDs, and pixel parallel readout is possible, although it necessitates an increased number of transistors on the chip and so reduces the fill factor; nevertheless, this can be overcome in N-well, P-epi chips where the entire epitaxial layer may be used as a sensitive layer for optical radiation. These sensors look promising for angle dispersive diffractometry due to their sensitivity, field of view and spatial resolution.

2.3.2.5 L3CCD

The low-light-level CCD is a CCD device with an additional gain register added to the chip before readout. The register works using avalanche impact ionisation similar to the APD, but the L3CCD has a much lower excess noise factor. The electronic noise associated with chip read out is often the limiting noise source of a CCD camera. The L3CCD has the ability to increase the signal acquired in the chip well above the read noise, thus making this noise source negligible compared to either the quantum noise on the incoming signal or the dark noise of the device. Aside from the added advantage of the gain mechanism, L3CCDs have the same properties as standard CCDs and so could be manufactured with small pixel sizes. They have already proved their usefulness for angular dispersive diffraction imaging when coupled to a phosphor [Royle *et. al.*, 2002], but a lack of information on their energy resolution means that they are yet to be considered for EDXRD.

L3CCDs, and normal CCDs, are most suited for detection of photons in the visible region of the electromagnetic spectrum with their response usually skewed towards the longer (red) wavelengths. They can detect x-rays directly, but with a very low efficiency due to the low x-ray attenuation coefficient of silicon. The usual way for x-rays to be detected using CCDs is via a phosphor screen either placed in front of the chip, or coated directly onto the chip's surface. CCDs coupled to phosphors are regularly used in digital radiography and have been particularly successful in dental x-ray imaging [van der Stelt, 2001]. Phosphors directly coated onto the front of a CCD give 1:1 magnification and a high coupling coefficient. Those placed in front of the chip are usually in the form of a large screen, whose visible light image is focused onto

the CCD surface either by a lens system or by a fibre optic bundle. These screen systems enable large area x-ray images to be collected using a small CCD chip by employing significant demagnification in the imaging system. This demagnification results in both a loss of spatial resolution and a strong decrease in the coupling coefficient between the phosphor and the CCD.

An L3CCD/phosphor coupled system has been chosen for work in this thesis due to its proven track record in diffraction imaging, the availability of a device and the demands of the project sponsor (e2v technologies ltd.). A description of the device and its characterisation follows.

2.4 L3CCD architecture and design

A perfect radiographic imaging device should be purely quantum limited; i.e., the noise on the output should be dominated by the Poisson statistics of the incoming photons. Generally CCDs do not meet this criterion as their noise properties are often limited by the read noise sources in the device, in particular the noise due to the output amplifier. This noise is a function of the pixel readout speed and thus can be suppressed by keeping the readout rate low (~kHz, [Jerram *et al.*, 2001]). These low readout rates, however, are not practicable with the demands of imaging using megapixel devices. If the amplifier noise is to be kept low for CCDs of these sizes, then the result is a slow system with large integration times, resulting in an increase in dark current and impractical time resolution properties if used for real time imaging. CCDs are thus used with readout rates of MHz and operate with the associated higher amplifier noise.

There have been several different approaches used to overcome these issues of compromising the noise properties of a CCD imaging system for a practical integration time. The most common is to amplify the input signal from the radiation source before it enters the CCD by using either electron bombarded CCDs (EBCCDs) or Intensified CCDs (ICCDs). An alternative method for amplifying the signal is used in the L3CCD chip (e2v technologies ltd, U.K.) [Jerram *et. al.*, 2001]. The L3CCD applies gain to the signal after interaction in the CCD chip, but prior to the readout mechanisms of the device. This technique reduces the magnitude of the read noise with respect to the

signal from the chip, resulting in reduced added noise whilst making any pre-CCD intensification redundant.

2.4.1 The L3CCD architecture

The architecture of the L3CCD chip is shown in Figure 2.3. It is a front illuminated, non-anti-bloomed device that is essentially a conventional interlaced, frame transfer, TV format CCD with an additional gain register section added before the readout node. This register has the same number of gates as the readout register, thereby delaying the signal from the chip by one whole row when compared to a chip without the extra register. When reading out, charge is clocked in the conventional manner, quickly from the image section into the store section and then sequentially through the readout register. The charge then is passed through sixteen 'corner' elements and into the gain register, where it is multiplied by an impact ionisation process as it is clocked through to the readout node.

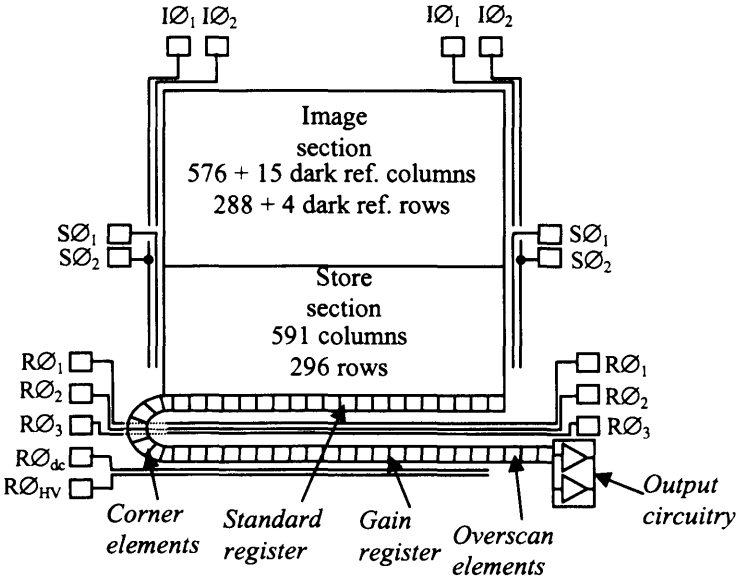

Figure 2.3 *Schematic of the L3CCD architecture [e2v technologies, 2003].*

2.4.1.1 The L3CCD gain register

Charge moves through the L3CCD using a conventional three-phase charge transfer technique (figure 2.4). Charge that has collected in a single potential well (the second electrode in figure 2.4(a)) is transferred along the electrode chain by applying a positive bias to the next electrode in the chain (figure 2.4(b)), causing the accumulated charge to be shared between the two wells. The potential on the first well is now dropped (figure

2.4(c)) and all the charge accumulates under the new electrode (figure 2.4(d)). This charge coupling mechanism is then applied to the next pair of electrodes and thus the signal in every pixel is 'clocked' through the device.

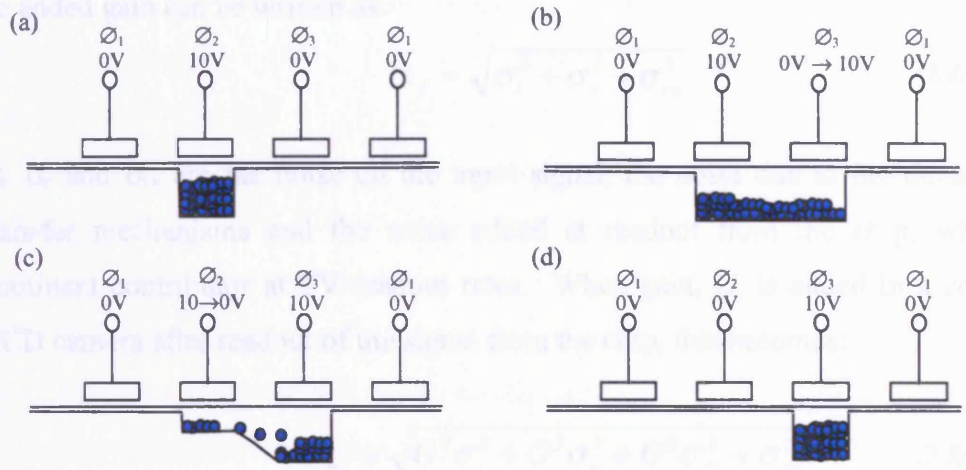

Figure 2.4 *Schematic showing the principle of a three-phase charge transfer CCD [Harris, 2002].*

When the charge reaches the L3CCD gain register a similar clocking mechanism is maintained, but one of the electrode potentials is replaced by a high voltage that causes an impact ionisation process to occur as the electrons pass into it, thus adding gain to the signal (figure 2.5). Phases $Ø_1$ and $Ø_3$ of the gain register operate at standard CCD readout register voltages, typically around 10V. The second phase, $Ø_2$HV, is clocked at a far higher voltage, usually 40-50V, and it is when the signal electrons are passing through this phase that impact ionisation occurs. An additional phase, $Ø_{dc}$, held at a low d.c. voltage (~2V), is added before the high voltage phase. [Jerram *et al.*, 2001]. This d.c. electrode creates a momentary barrier to prevent the charge entering the high field region until the high voltage has reached its maximum value. As the electrons travel from $Ø_{dc}$ to $Ø_2$HV they are subject to a large potential difference. This causes the electrons to accelerate and rapidly gain significant kinetic energy. This newly acquired energy enables impact ionisation when the electrons collide with the silicon lattice.

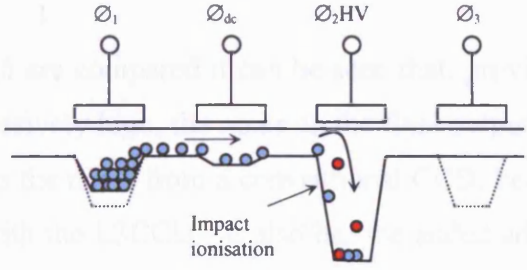

Figure 2.5 *Schematic of the potential well profile of the L3CCD gain register [Harris, 2002].*

2.4.2 L3CCD noise properties

The noise, σ_f, on the final output signal from a CCD camera (conventional or L3) with no added gain can be written as:

$$\sigma_f = \sqrt{\sigma_i^2 + \sigma_c^2 + \sigma_{rn}^2} \qquad (2.4)$$

σ_i, σ_c and σ_{rn} are the noise on the input signal, the noise due to the device's charge transfer mechanisms and the noise added at readout from the chip, which is the dominant contributor at TV readout rates. When gain, G, is added in a conventional CCD camera after readout of the signal from the chip, this becomes:

$$\sigma_{fG} = \sqrt{G^2\sigma_i^2 + G^2\sigma_c^2 + G^2\sigma_{rn}^2 + \sigma_{re}^2} \qquad (2.5)$$

σ_{re} is the noise associated with the camera's external electronic amplifiers, which usually becomes the dominant factor in a TV rate camera when gain is added.

Gain is added in the L3CCD before readout, so the readout noise is not multiplied by it. Adding the gain at this point also means that electronic amplifiers in the camera external to the chip are not required. This means that the noise on the final output signal from the L3CCD with gain, G, added is given by:

$$\sigma_{fL3} = \sqrt{G^2\sigma_i^2 + G^2\sigma_c^2 + \sigma_{rn}^2 + \sigma_e^2} \qquad (2.6)$$

σ_e is a parameter called the excess noise. This factor is due to the gain being created by impact ionisation, which is a random mechanism and so has a noise distribution associated with it. The excess noise depends primarily on the level of multiplication gain used [Harris, 2002].

If equations 2.5 and 2.6 are compared it can be seen that, provided the excess noise in the L3CCD is not excessively high, the noise on the final output of the L3CCD must be significantly lower than the noise from a conventional CCD, because external amplifier noise is not an issue with the L3CCD. It also has the added advantage that the gain is applied prior to the read out node meaning that any readout node reset noise is not multiplied by the gain.

2.4.3 L3CCDs used for diffraction imaging and microCT

The ability of the L3CCD to apply high levels of gain to a signal whilst maintaining low amounts of noise makes it sensitive enough to use as the scattered x-ray detector in a diffraction imaging system. This was successfully proven by using a Europium doped Gadolinium Oxysulphide (Gd_2O_2S:Eu) coated L3CCD to collect a coherent scatter image of a life-sized breast tissue phantom containing cancerous inserts [Royle *et. al.*, 2002]. This camera (CCD65-02) had previously been characterised by Harris [2002] with respect to its spatial resolution and noise properties and was used for the planar diffraction imaging work and some microCT later in this thesis. The camera is housed in a back-pumped borosilicate glass casing incorporating a low attenuation 50 μm thick Mylar window, and was Peltier cooled to -7°C in order to reduce the dark current, thus reducing the noise in the chip [Harris, 2002].

A second L3CCD camera (CCD65-01) was also used for some of the microCT covered later in this thesis. This chip has a fused fibre-optic faceplate bonded to it with optical adhesive so that the phosphor can be changed. This causes a reduction in the phosphor-chip coupling, but allows a range of application-tailored phosphors to be used with the camera and also reduces the amount of direct x-ray interactions in the chip. The chip is sealed into a box of dry nitrogen and so can be Peltier cooled well below dew point [Nishibayashi, 2004].

The CCD65-02 camera has a 160 μm thick layer (the standard thickness for a dental phosphor) of Gd_2O_2S:Eu coated directly on to the chip (figure 2.6); the spectral emission of this phosphor is found to be well matched with the L3CCD's spectral response and the thickness provides 100% absorption for photons up to 20 keV.

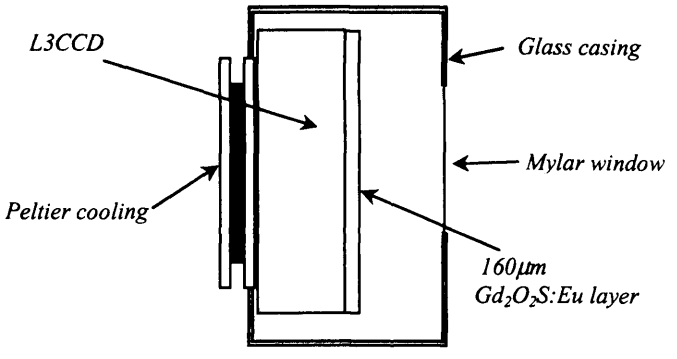

Figure 2.6 *An illustration of the CCD65-02 x-ray sensor design.*

2.4.3.1 On-camera acquisition variables

Both L3CCD cameras are interlaced TV format sensors (568 x 568 pixels). Each camera has four on-camera parameters that can be altered externally by the user. These are binning, temperature, gain and dark level offset.

Binning - The cameras have the option of one pixel, two pixel or four (2 x 2) pixel binning. Using the binning option reduces the output image file size and quantum mottle, but also reduces the spatial resolution of the detector.

Temperature - The cameras are Peltier cooled and the current to the cooling pack, and thus the chip temperature, can be controlled externally to the camera. CCD65-02 runs at -7°C, whilst CCD65-01 is limited to just above 0°C. The initial characterisation of the cameras by Harris [2002] indicated that the dark noise in a cooled camera is greatly reduced compared to operation at room temperature. There is no automatic cooler feedback loop, so the stability of the camera's temperature must be monitored regularly throughout every experiment as the chip's avalanche gain is temperature dependent, changing by approximately 10% for every degree Centigrade change in sensor temperature [Harris, 2002].

Gain – The high voltage of the avalanche gain can be altered by the user by means of a 0 – 5 V potentiometer on the camera. The potentiometer setting can be correlated to the high voltage applied using data in Harris [2002]. Increasing the gain increases the sensitivity of the camera, but also adds gain to the dark noise in the chip. Equation 2.4 shows the noise on the final output of the L3CCD camera. At low gain the system noise is dominated by the read noise, whilst at higher gains it is dominated by the input noise, the largest contribution of which tends to be the thermal dark noise.

Dark level offset – This parameter is a pedestal on which the signals from the camera sit. It is normally set such that no cut-off is seen in an image's grey level distribution.

2.5 Characteristics of the L3CCD

Both of the UCL L3CCDs have previously been characterised for general use by Harris [2002]. A full study of their spatial resolution, signal to noise properties and gain mechanisms was undertaken and the results indicated that a phosphor coupled L3CCD would be a suitable detector of diffracted x-rays. Particular attention was paid to measurements of the sensitivity of the devices with respect to their minimum detectable signal and the excess noise introduced into the signal by the avalanche gain mechanism.

2.5.1 L3CCD x-ray sensitivity

It is commonly held that, due to the high amounts of read electronics noise usually associated with them (typically of the order of 150 electrons r.m.s. per pixel per frame), CCD-phosphor coupled systems do not exhibit the capability to detect individual x-ray photons. A 50 keV x-ray photon will produce 300 light photons in a red emitting Gadox phosphor. These photons give a signal in the CCD of around 45 electrons. This means that phosphor coupled CCD detectors are not photon counting systems and therefore can not be used to obtain the energy of individual incoming x-ray photons. However, it has been found that this is not true for the L3CCD-phosphor coupled system at UCL.

Every detector has a minimum detectable signal (*MDS*), usually defined using the Rose criterion [Rose, 1948]. This is effectively a cut off value, below which a signal can not be discriminated from the noise in the detector. Harris [2002] calculated this to be 2.1 photoelectrons per pixel per frame for the CCD65-02. This can be converted into the number of light photons needed to hit a pixel N using:

$$N = \frac{MDS \times W}{E_{ph} \times QE} \qquad (2.7)$$

QE is the quantum efficiency of the CCD (assumed to be ~25% at the wavelengths emitted by the Gd_2O_2S:Eu phosphor, which peak at 625 nm [Spencer and Catlett, 2000]), W is the amount of energy needed to create one photoelectron in silicon (3.65eV [Knoll, 1999]) and E_{ph} is the average energy of one light photon (~2eV at 625nm). This

gives a value of just over 15 for N. This implies that at least 16 light photons need to reach a single pixel in the time taken to integrate one field in order for that signal to be observed above the background noise of the imaging system. This indicates that, if an x-ray interacting in the phosphor produces more than 16 photons, then there is the potential for individual x-rays to be imaged with the system.

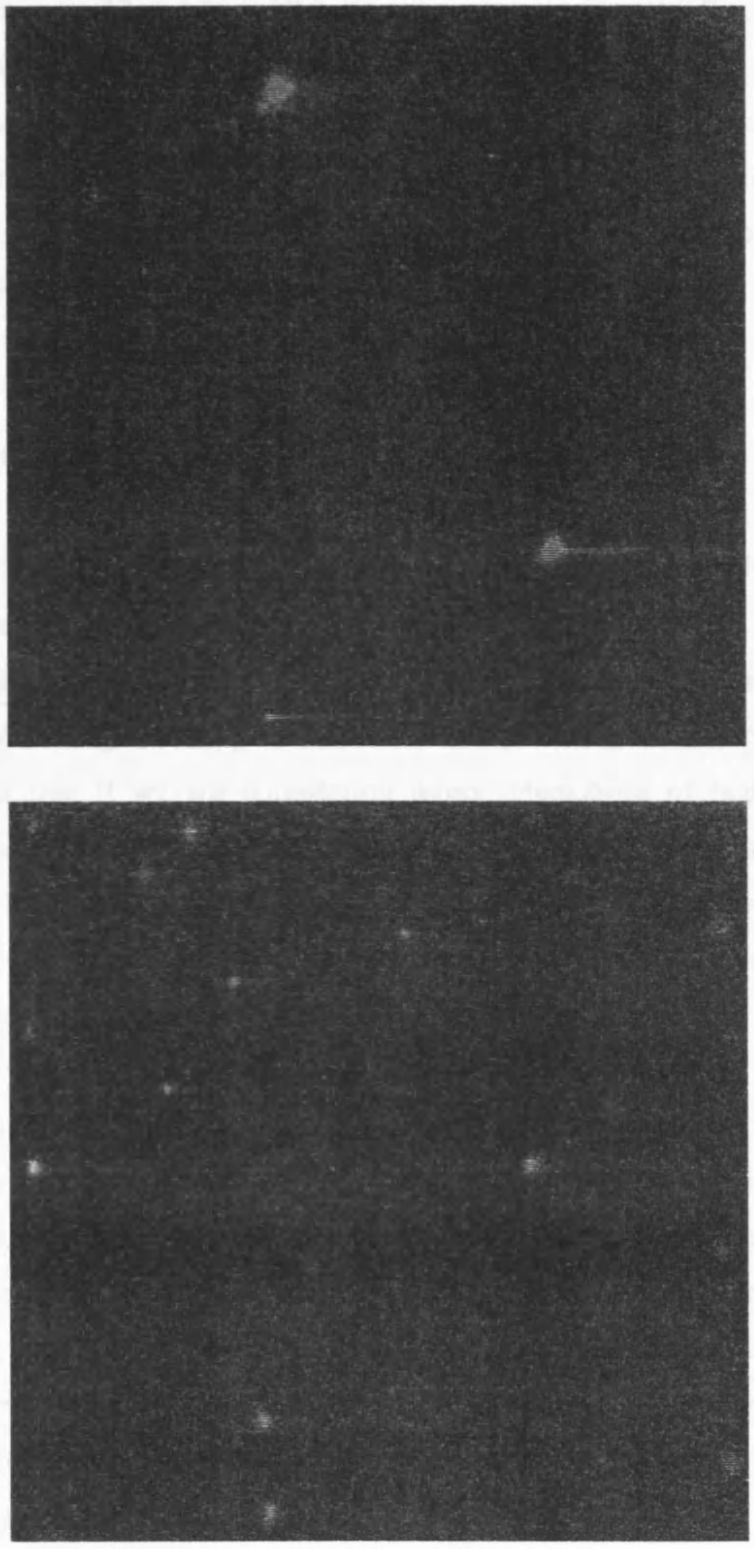

Figure 2.7 *Images of individual (a) ^{137}Cs and (b) ^{241}Am gamma photons taken with the CCD65-02.*

In this thesis, the characterisation of the L3CCD has been extended to study the energy resolving properties of the device. The hypothesis that the Gd_2O_2S:Eu coated CCD65-02 could be photon counting was tested in the laboratory using ^{241}Am (59.5 keV with lower energies filtered out by shielding) and ^{137}Cs (82% of photons at 662 keV and 8% of photons between 32 and 38 keV) calibration sources. Figure 2.7 shows images from the camera of single integration fields (20 ms) taken with the sources placed directly in the field of view. Photon 'hits' on the phosphor have produced approximately circular areas of charge deposition in the L3CCD chip which appear to vary in size for the two sources. These areas of deposition have been named 'blobs' for ease of reference by the workers at UCL.

2.5.2 L3CCD energy resolution

The energy of an x-ray photon is significantly higher than photons with wavelengths in the visible region. The typical well depth of a CCD pixel is around 150,000 electrons and the work function of n-type silicon is approximately 3 eV, meaning that an energy deposition in the region of 450 keV would be large enough to saturate a pixel. This factor means that if we are considering direct interactions of higher energy x-ray photons then one single photon may saturate a pixel, leading to smearing in the image. When using lower energy x-ray photons this saturating deposition value of 450 keV will severely limit the dynamic range of the pixels, requiring the incident flux onto the detector to be very low in order to avoid saturation.

Pixel saturation will produce an inaccurate measurement of the total charge deposited by the x-ray interaction, also in an integrating device it is not possible to know how many photons have contributed to the charge in the pixel. Therefore the energy of an incoming directly interacting photon cannot usually be ascertained in a practical manner from CCDs. So far there has been limited work done in this CCD direct interaction x-ray energy resolution [Ott *et al.*, 2000, Livet *et al.*, 2000, Burke *et. al.*, 2004], and successes have only occurred when using either extremely deeply depleted devices (~300 μm) or low x-ray energies (<1 keV).

The blobs in figure 2.7 taken using the ^{137}Cs source are visibly larger in area than those taken with the ^{241}Am source. The clear visual difference between these two images has given a motivation for attempting to quantify the energy of the incoming x-ray photons. Although it is likely that any energy resolution using the L3CCD-phosphor system will be poor, it will be of significance as this would be an entirely novel energy resolving x-ray detection system. It may also prove useful for diffraction imaging as dual energy systems allowing more than one momentum transfer value to be simultaneously obtained could become a viable option.

A data set of blobs taken at different x-ray energies was obtained and an algorithm [Speller, 2002] used to firstly process these images and then to quantify the blobs in terms of both their area in pixels and the total signal associated with each blob.

2.5.2.1 Experimental set up

The radiation sources chosen for the images were a high activity ^{241}Am (59.5 keV) and a ^{137}Cs (32-38 keV and 662 keV) source. These were placed in the field of view of the CCD65-02 and images were taken using the camera settings shown in Table 2.2 (for further explanation of settings the reader is referred to §2.4.3.1). Calibration tables [Harris, 2002] were used to find the temperature of the camera and the value of multiplication gain added to the signal. The SNR was measured to be 3, which was found to be adequate for this work. Binning was not used as it would blur the signal at the edge of the blobs by integrating it with neighbouring dark pixels.

Table 2.2 *L3CCD experimental parameters.*

Parameter	***Value***
L3CCD chip gain	*4.36 V = gain of ~200*
L3CCD chip offset	*4.30 V*
L3CCD chip temperature	*12.3 kΩ = -5.2°C*
Binning	*off*
Number of images taken	*5 buffers of 50 images*

In order to achieve energy resolution, individual x-ray photons must be imaged; this means that the signals from individual hits must not overlap spatially within a CCD field (20 ms). The ^{137}Cs source was placed just 2 cm from the camera to maximise the flux hitting the imaging area (calculated to be ~ 90 photons per field incident on the

phosphor), whilst the highly active ^{241}Am source was placed at a distance of several metres from the camera in order to reduce the flux hitting the imaging area (calculated to be ~295 photons per field incident on the phosphor).

2.5.2.2 Scintillator response calculations

Two radioactive sources were used in the experiment: ^{241}Am and ^{137}Cs. A simple model of the response of the detector system was formed to predict the signals that could be expected when using each of the sources with the camera. The model takes into account the proportion of photons emitted by the source at a given energy and the attenuation coefficient of the Gd_2O_2S:Eu phosphor at that energy.

The detector response model uses equation 2.8 to give a value, R, proportional to the number of visible light photons produced by the gadox phosphor for each energy, E, emitted by the sources assuming that the total activity of each source is the same:

$$R(E) = A(E) \times P(E) \qquad (2.8)$$

A is the percentage of the source's total activity at energy E and P is the 160 μm thick phosphor layer's efficiency at energy E.

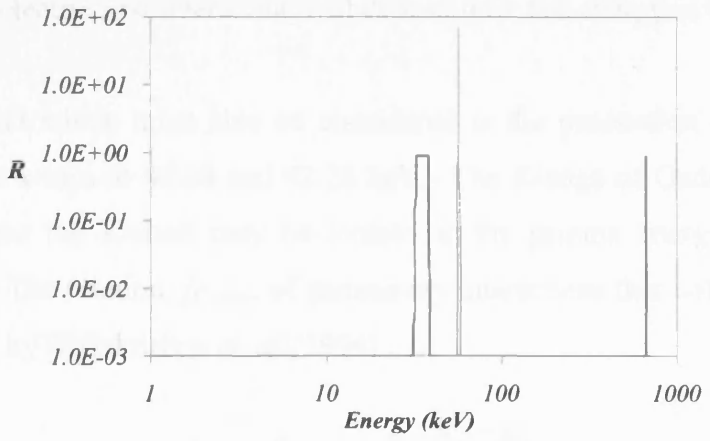

Figure 2.8 *Plot of R against photon energy for the gamma sources; light line is ^{241}Am and dark line ^{137}Cs.*

A plot of R against gamma ray energy for the radiation sources is shown in Figure 2.8. It shows that despite the 662 keV line of ^{137}Cs being approximately 10 times more active than the lines around 32-38 keV, the value of R for these two sets of lines is

similar due to the phosphor having a much lower x-ray attenuation coefficient, and thus absorption efficiency, at the higher energy.

It was assumed for energy resolution purposes that all of the energy from an x-ray photon is transferred to the phosphor at one single point, i.e. a photoelectric interaction takes place. This assumption holds for the ^{241}Am source and the lower energies of the ^{137}Cs source where the ratios of the attenuation due to the photoelectric effect and Compton scatter are 45:1 and 51:1 respectively. The assumption does not hold so well for the 662 keV line of ^{137}Cs where the ratio is only 0.25:1. These ratios mean that the probability of the first photon interaction being photoelectric is 98% for both the 59.5 keV ^{241}Am photons and the lower energy ^{137}Cs photons, but only 20% for the 662 keV photons. It must also be remembered that these probabilities are for this interaction to occur; they are not the probabilities of full energy deposition in the phosphor. The photoelectric effect produces a photoelectron which then deposits the energy from the photon interaction in the surrounding medium. Energy deposition by the electron is efficient at the lower energies where its path length remains small in comparison to the 160 μm phosphor thickness (6 μm at 35 keV and 15 μm at 59.5 keV), but is extremely inefficient when 662 keV of energy is deposited by the ^{137}Cs photons (510 μm CSDA path length). This means that very few of the small number of 662 keV photons that have a photoelectric first interaction will deposit their full energy in the phosphor.

Another effect which must also be considered is the production of Gadolinium K_α-characteristic x-rays at 42.98 and 42.28 keV. The K-edge of Gadolinium lies at 50.2 keV, and thus the K-shell may be ionised at the gamma energies chosen for this experiment. The fraction, $f_{K\text{-}char}$, of gamma-ray interactions that will produce Gd K_α x-rays is given by [Balakrishna *et. al.*, 1994] :

$$f_{K-char} = Y \times \frac{\mu_+ - \mu_-}{\mu_+} \qquad (2.9)$$

where Y is the K fluorescent yield of Gd (0.992 [Balakrishna *et. al.*, 1994]) and μ_+ and μ_- are the attenuation coefficients of Gd immediately above and below the K-edge respectively (18.64 and 3.812 cm^{-1} [Berger *et. al.*, 1999]). Therefore, $f_{K\text{-}char}$ has a value of 73% for Gd, meaning that the majority of gamma-ray interactions in the phosphor will produce Gd K_α characteristic x-rays. The production of these x-rays means that the

incident gamma-ray energy is not deposited at a single point in the phosphor, and moreover, these x-rays may also exit the phosphor, resulting in a complete loss of the 42.5 keV that they are carrying.

A second assumption made in this model which does not entirely hold for the Gadox phosphor used in this experiment is that all light photons produced by the phosphor will exit the phosphor. Gadox is slightly opaque to its own wavelengths of emission, meaning that light photons produced at a point in the phosphor close to the CCD have a higher probability of reaching it than photons produced at a point further away from the CCD.

2.5.2.3 'Blobfinder' algorithm

The image processing and blob data collection algorithm was written using IDL (Interaction Data Language, Kodak Ltd.) [Speller, 2002]. A block diagram depicting the main features of the algorithm is shown in Figure 2.9. Explanations of the physics and image processing decisions used in the writing of the algorithm follow.

The image files were exported from the L3CCD data acquisition software (LabWindows CVI) as 16-bit binary files. Each file contained the pixel information for 50 consecutive frames of the L3CCD, i.e. two seconds worth of data. These were then read into a 3-D array in the IDL program, creating a stack of 2-D images, each 568 x 568 pixels in size. A dark noise image was then subtracted from all 50 images in the array in order to remove pixel thermal noise non-uniformities.

The L3CCD has an interlaced architecture, meaning that the odd numbered rows read out whilst the even numbered ones integrate and vice versa. One x-ray photon takes only a fraction of the field integration time to interact with the phosphor and the visible phosphor afterglow is short. These facts mean that the total duration of signal production for a single x-ray photon is much less than the time taken to acquire one field of the L3CCD. This resulted in each blob appearing in either the odd or the even rows only, accounting for the striped appearance of the blobs in Figure 2.7. This can be seen more clearly in Figure 2.10.

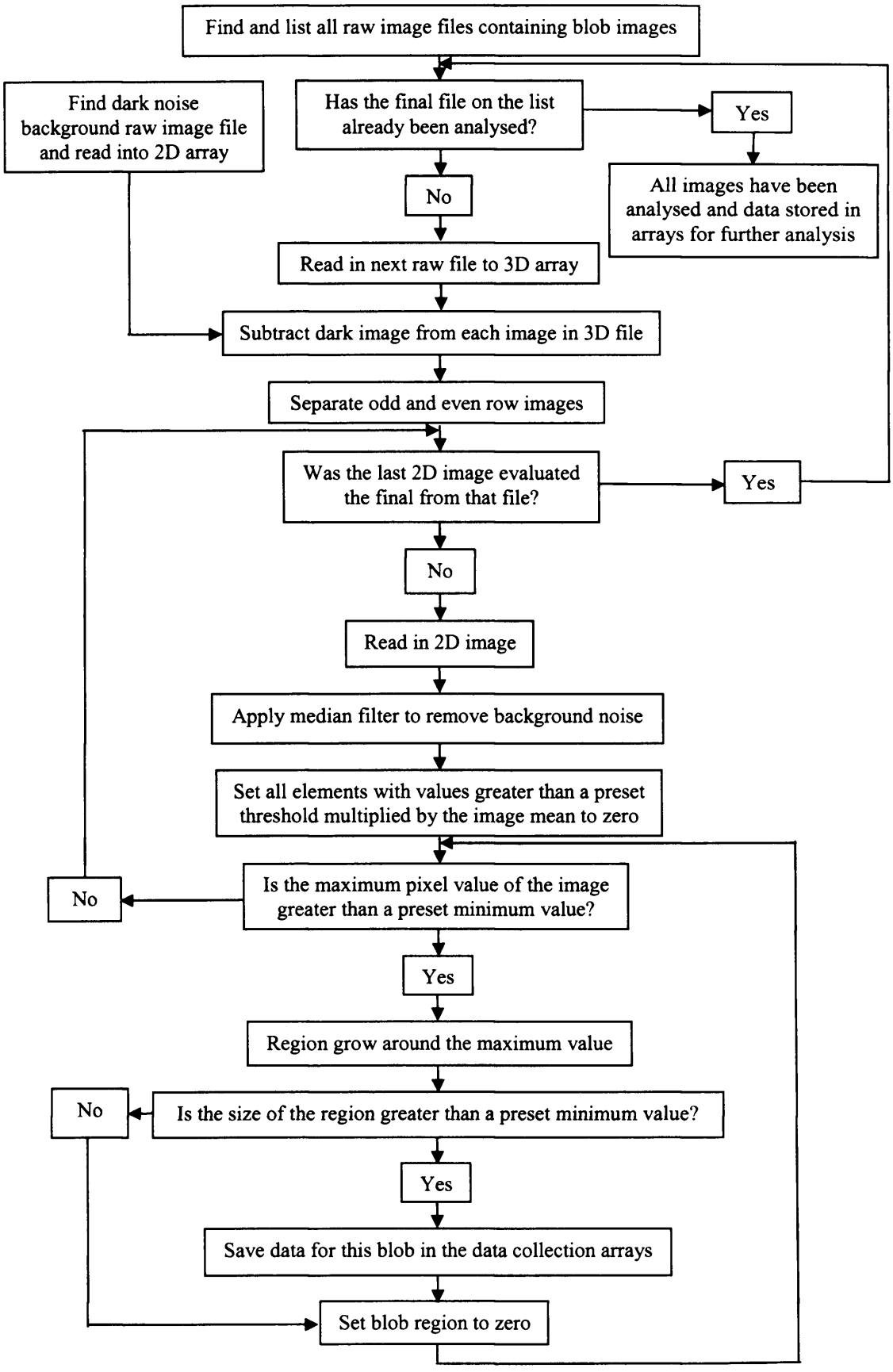

Figure 2.9 *Flow chart depicting the main features of the 'blobfinder' IDL program.*

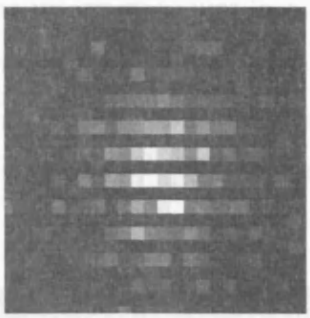

Figure 2.10 *Magnified image of a blob. The striped appearance is due to the L3CCD's interlacing.*

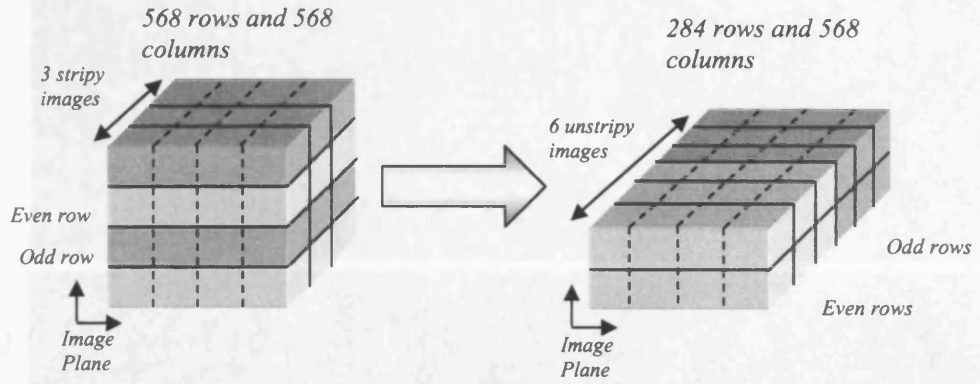

Figure 2.11 *Illustration of the image array manipulation to compensate for the striped appearance of the blobs.*

The program compensated for the camera interlacing by manipulating the image array. The odd rows for each image were extracted and placed contiguously in a new array, then the even rows were extracted and placed contiguously at an offset position in this array (Figure 2.11). The original array contained 50 images consisting of 568 rows and 568 columns and the new array contained 100 images of 284 rows and 568 columns. This array manipulation effectively compresses the blobs in one dimension, resulting in an ovoid shape with an area equal to half the actual blob area, as can be seen in figure 2.12. This means that any blob area sizes measured using these compressed images must be doubled to obtain the true area of the original charge deposition.

The random background noise in the image was then removed by the algorithm using a median filter operating with a window of 3 x 3 pixels. The filter used was the standard one in the IDL package; it uses a nearest neighbour approach when operating on the array's edges. After this filtering, all pixels with a value less than the product of the mean image pixel value and a manually set threshold variable (*thresh*) were set to zero.

This re-setting meant that some information was lost around the edges of the individual blobs, but this problem was more than compensated for by the fact that the re-setting also removed the last of the random noise in the image. A raw image and the same image after the noise removal procedure has taken place are shown in Figure 2.12.

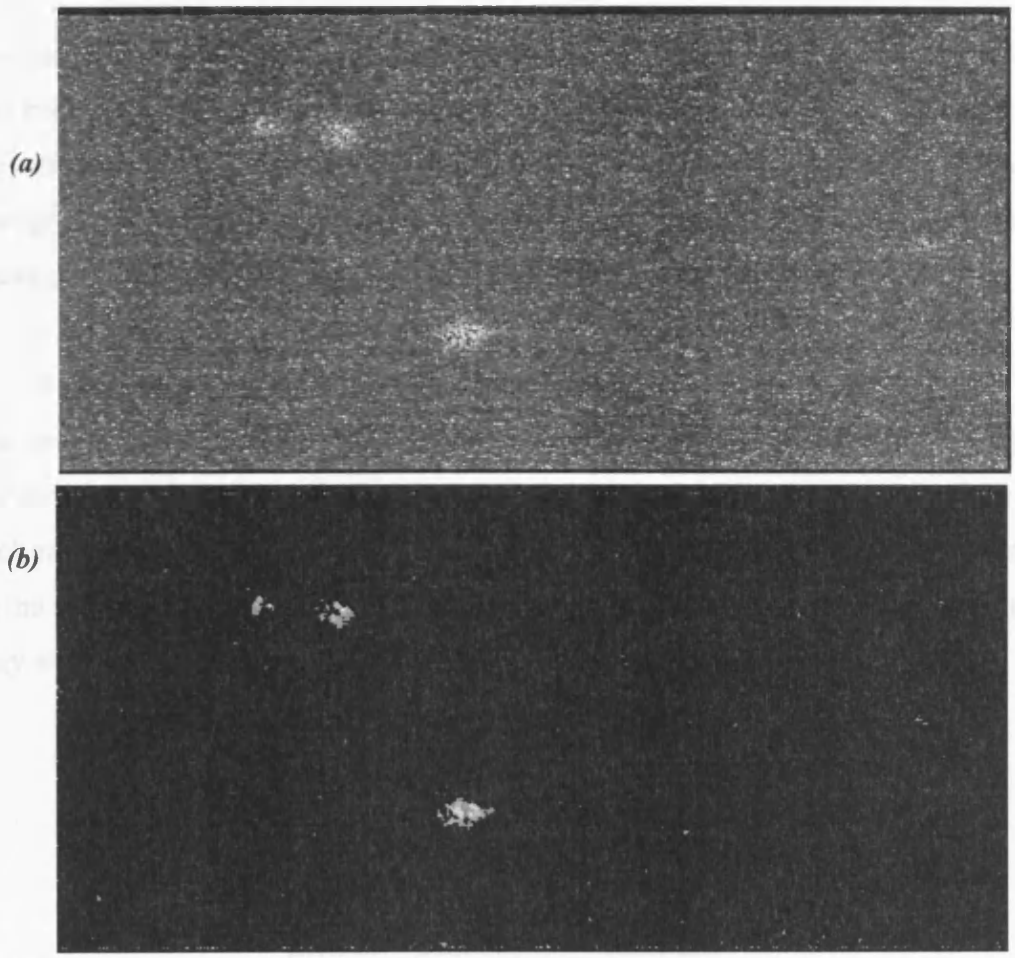

Figure 2.12 *(a) An unprocessed raw image of blob data; (b) a processed image.*

The program now analysed the image to find individual blobs. It then collated information about them in storage arrays for later use.

The first blob in the image was found by looking for the image's maximum pixel value. So long as this value was larger than a pre-set minimum, the program then grew a region of interest around the position of this maximum using a function from the standard IDL package (search_2D). Once the region had been identified it was then analysed and if its area was found to be greater than a pre-set minimum area, then the size of the area (in pixels) and the total signal within the region (in digital units, *D.U.*)

were stored for later analysis. All values within the identified blob region were then set to zero and the program found the new maximum value of the image. The program continued in a loop, finding the maximum, region growing, collecting data and setting the blob region to zero until the last maximum found was less than the preset minimum value allowed. At this point the program moved on to analysing the next image.

The blob data was stored in two arrays for analysis after all the blobs in all the images had been found; one array stored the number of pixels in each blob and the other stored the total signal associated with each blob. These results were then plotted in a histogram for each data set. The raw numbers can also be exported into other software packages as text files.

2.5.2.4 L3CCD Energy resolution results and discussion

The analysis of the data sets obtained by taking images of individual gamma-ray photon interactions with the CCD65-02 sensor resulted in two histograms being produced for each radiation source used. The first histogram examined the size of the blobs in terms of the number of pixels they contain. Due to the thickness of the x-ray phosphor, there may well be some variation in this size (Figure 2.13).

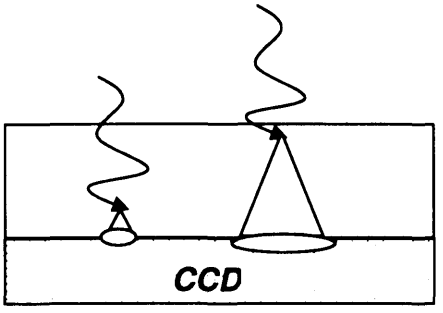

Figure 2.13 *Illustration of the dependence of light spread at the CCD surface due to x-ray interaction position in the phosphor.*

In section 2.5.2.2 it was indicated that for low x-ray photon energies it can be assumed that the photon effectively gives its energy up at a single point in the phosphor by photoelectric interaction. At this point, visible light photons are produced with a yield proportional to the energy of the interacting x-ray. The light photons then spread isotropically until they interact with the CCD sensor. This means that they project a circle of light onto the CCD, the radius of which depends on how far the light photons have travelled, and therefore on the depth of interaction of the x-ray in the phosphor.

An x-ray depositing its energy in the top of the phosphor will project a larger circle onto the CCD surface than one interacting lower down; nevertheless, both circles will contain the same number of light photons as the solid angle of projection is the same for both cases. This means that the mean intensity of the larger circle is comparatively lower than that of the smaller although they both have comparable amounts of total signal in them. The second histogram aims to take this into consideration and investigates the total amount of signal associated with a blob. This approach attempts to solve simply what appears to be a simple problem at first, nevertheless the approach may not be sufficient as the situation is slightly more complicated due to the opacity of the phosphor (see §2.5.2.2) and there being a minimum signal that the sensor is capable of detecting, which has been estimated at 16 light photons per pixel per field (see §2.5.1).

Assuming that an x-ray interacts with a phosphor by giving up all its energy at one point in that phosphor, then n light photons are produced at that point where:

$$n = Y_{op} \times E \qquad (2.10)$$

Y_{op} is the optical photon light yield of the phosphor per MeV of interaction x-ray energy, E. For Gd_2O_2S:Eu, Y_{op} is approximately 6000 MeV^{-1} [e2v technologies, 2002]. At a distance d from the interaction point, these n photons can be assumed to be distributed isotropically over the surface of a sphere of radius d centred on the point of interaction. If we assume that d is the distance between the interaction point and the surface of the CCD and that the phosphor is transparent to the wavelengths under consideration, then the number of photons reaching a single pixel, n_p, is given by:

$$n_p = n \times \frac{1}{4\pi d^2} \times pixelarea \qquad (2.11)$$

The pixel area of the CCD65 is 20 μm x 30 μm = 600 μm. If Equation 2.11 is rearranged and n_p is set to the *MDS* value, N, then the maximum allowable distance from the interaction point to the CCD that gives a resolvable signal, d_m, can be found:

$$d_m = \sqrt{\frac{pixelarea \times Y_{op} \times E}{N \times 4\pi}} \qquad (2.12)$$

Table 2.3 shows the values of d_m for the gamma sources used in this experiment. It should be noted that this calculation assumes that the phosphor is perfectly transparent; however it is probably the case that the Gadox is self-absorbing, which will be discussed later, and thus the tabulated values of d_m will be higher than the true maximum interaction distances. The small values of d_m for the lower energies imply that only x-ray photons depositing their energy in the region of the phosphor closest to the CCD will be seen reliably.

Table 2.3 *The maximum allowable distance from the interaction point to the CCD, dm.*

Source	*Energy (keV)*	*dm (μm)*
Americium-241	*59.5*	*33*
Caesium-137	*32-38*	*24-26*
	662	*109*

Figure 2.7 showed images of photon hits from ^{241}Am and ^{137}Cs sources on an L3CCD coated with a 160 μm Gd_2O_2S:Eu phosphor. It was seen from these images that the 'blobs' produced by the ^{137}Cs photons (32-38 keV and 662 keV) were larger in area than those produced by the ^{241}Am photons (59.5 keV). This observation has lead to the hypothesis that either blob area or the total signal in each blob may be considered to be measures of the energy of the incoming gamma photons.

Figure 2.14 shows histograms of the areas of the Americium and Caesium blobs in terms of the number of pixels counted in each image processed blob. Both histograms show a peak at low values. This peak may be due to 'noise' that has not fully been removed in the image processing, and may have even been turned into a blob like shape by the processing. Both histograms exhibit a shoulder off this peak, extending into the higher values of blob area. This shoulder has tailed off for the lower energy plot (^{241}Am) at an area size of 200 pixels, but continues up to 400 pixels for the higher energy (^{137}Cs) plot, giving a difference in the maximum blob area of a factor of 2. The L3CCD pixel area is 600 μm^2; this gives the cut off areas as 120,000 μm^2 and 240,000 μm^2, which translate into circles of radii 195 μm (~8 pixels) and 276 μm (~11 pixels). The mean blob areas for the two sources are 56.4 pixels (area = 33,840 μm^2, radius = 103.8 μm, ≈ 4 pixels) for the ^{241}Am blobs and 97.8 pixels (area = 58,680μm^2, radius = 136.6μm, ≈ 5.5 pixels) for the ^{137}Cs blobs.

The energy of the higher energy ^{137}Cs photons (662 keV) is 11 times larger than that of the ^{241}Am photons (59.5 keV); however, as previously described in section 2.5.2.2, only one fifth of the higher energy photons will have a photoelectric interaction as their first interaction and photoelectrons produced by these photons will have a high energy and thus a large range. Therefore very few of these photoelectrons will deposit the full amount of gamma ray energy that was transferred to them by the photoelectric interaction. This lack of full energy deposition in the phosphor, as well as the phosphor's opacity to its own wavelengths, will lead to a reduction in blob size and goes part way to explaining why, although the maximum energies of the photons vary by a factor of 11, the maximum blob areas only vary by a factor of 2 and the mean areas by a factor of 1.7.

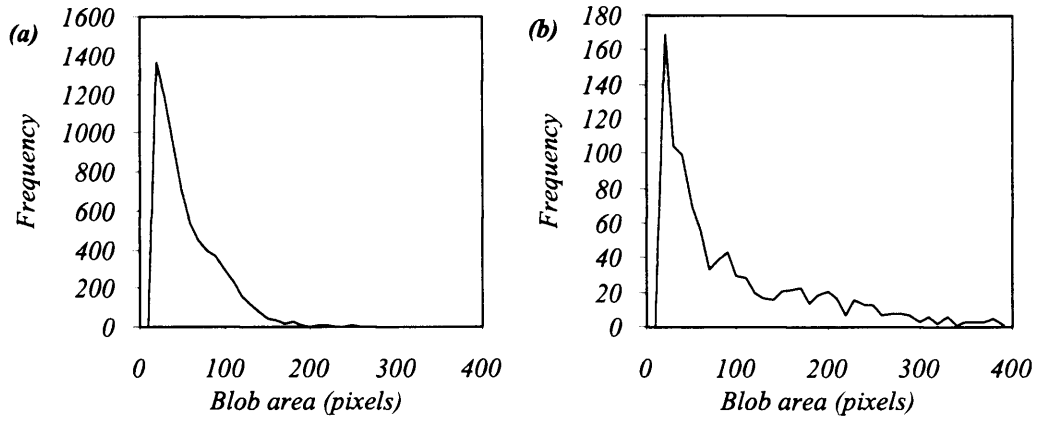

Figure 2.14 *Histograms of blob area for the (a) ^{241}Am and (b) ^{137}Cs gamma ray sources.*

The results in figure 2.14 indicate that the quantification of blob area alone is not a good measure of incoming photon energy. This is due to there being many unaccountable variables along the chain of events from the gamma photon first entering the phosphor to the light photons being detected by the L3CCD sensor. The blob area is sensitive to a combination of the gamma photon energy, the depth and type of interaction (which are also partially dependent on the photon energy) and the phosphor's opacity to its own wavelengths of emission (which is dependent on the depth of interaction in the phosphor).

The observation that the blob area is dependent on too many unaccountable variables then lead to the use of a more conventional approach to energy resolution; it is usual to measure photon energy by measuring the amount of charge deposited in the detector.

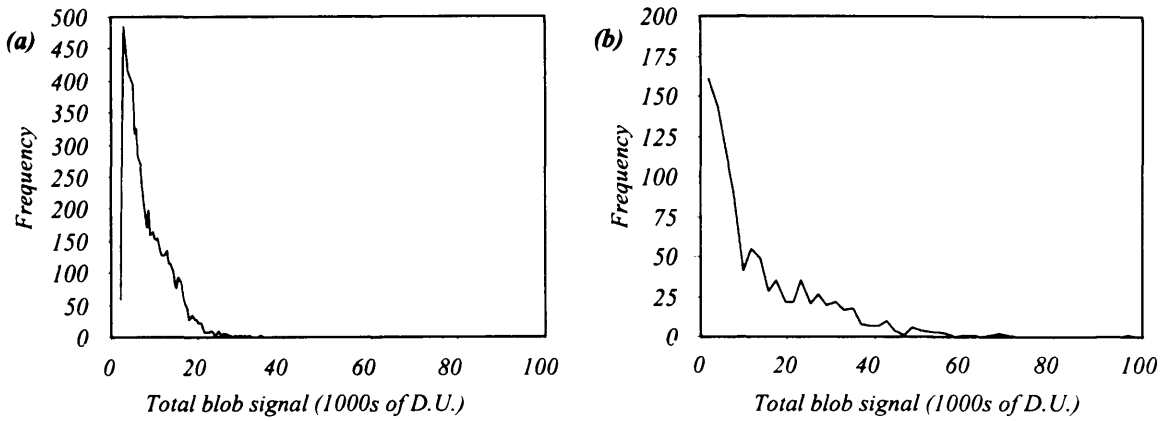

Figure 2.15 *Histograms of the total signal associated with each blob for the (a) ^{241}Am and (b) ^{137}Cs gamma ray sources.*

Figure 2.15 shows histograms of the total signal in Digital Units (*D.U.*) associated with each image processed blob for the two gamma sources. These plots again show a maximum at the lower end leading to a shoulder at higher values. The signal size is found by summing all the 16-bit grey-level values of all the pixels identified as being in a blob. Ignoring any noise added by the system and assuming that all processes are linear, a pixel's grey-level value, V, can be approximately calibrated against the number of light photons n_l interacting within it by:

$$n_l = \frac{VCW}{GE_l} \qquad (2.13)$$

C is the calibration factor of the camera's *ADC* which gives the number of electrons needed to produce one Digital Unit (measured to be 256 ± 5 [Harris, 2002]), W is the work factor of silicon (3.6 eV [Knoll, 1999]), G is the gain applied to the pixel's signal by the L3CCD on-chip gain mechanism (~200 for this work) and E_l is the average energy of a light photon (~2 eV for Gadox photons).

The maximum signals lie at around 25,000 *D.U.* for the ^{241}Am source and 70,000 *D.U.* for the ^{137}Cs source. This offers a difference between the values of a factor of almost 3. The mean signals are 8,092 for the ^{241}Am photons and 13,695 for the ^{137}Cs photons. Using equation 2.13, the maximum signal values correspond to 57,600 and 161,280 light photons interacting with the L3CCD and the mean signals to 18,644 and 31,553 light photons. These numbers of photons seem rather high, suggesting that some of the values used in equation 2.13 may not be accurate.

Nevertheless this signal summing technique appears to give better results than merely finding the areas of the blobs, as suggested previously, as it removes some of the variations due to the height of x-ray interaction in the phosphor.

2.5.2.5 Analysis and verification of L3CCD energy resolution results

Section 2.5.2.2 briefly analysed the interactions that will occur between the gamma photons and the gadox phosphor. It was highlighted that the ^{241}Am source is effectively monoenergetic, with an energy of 59.5 keV, whilst the ^{137}Cs source has photons at 32-38 keV and 662 keV. The lower energy photons will mainly interact via the photoelectric effect, thus transferring their energy in a single interaction. The photoelectrons produced by these photons have short ranges and so will deposit the energy given to them within the phosphor. However, due to the incoming photon energy being greater than the energy of the Gadolinium K-shell binding energy, many of these photoelectric interactions will go on to produce characteristic x-rays. These x-rays have energies around 42.5 keV and thus they will deposit their energy some distance away from the original interaction site, and may even escape the phosphor. The 662 keV photons will have a much more complicated energy deposition history due to the probability of photoelectric interactions at this energy being much smaller than the probability of Compton interactions.

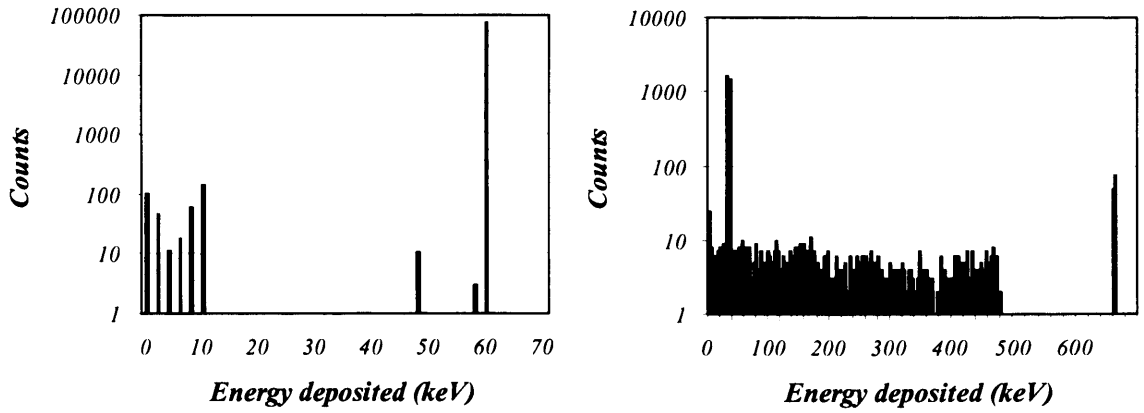

Figure 2.16 *Plots showing the results of a Monte Carlo simulation to investigate the deposition of energy in a 160 μm gadox phosphor by (a) ^{241}Am and (b) ^{137}Cs gamma rays.*

An EGS4 Monte Carlo simulation for 100,000 photons was run in order to model the energy depositions of the two sources' photons within the phosphor [Royle, 2002]. The simulation includes photoelectric, Compton and coherent scatter interactions, as well as

K-fluorescent photons. The results of the simulations are shown in Figure 2.16 and Table 2.4. The code simulated a 1 mm^2 beam of photons incident on a 160 μm thick, semi-infinite slab of Gd_2O_2S in a vacuum. This geometry means that the simulation does not allow for loss of energy at the edge of the phosphor, as will happen in the experimental set-up; nor does it include any interactions that may occur at the boundary between the phosphor and the silicon L3CCD.

The simulation gives the energy deposition within the phosphor, but does not then go on to consider the conversion of that energy to visible light photons by the phosphor and their subsequent propagation through to the L3CCD. The propagation of the light photons will be impeded by the opacity of the phosphor to its own emission wavelengths. This means that signals that have to travel significant distances through the phosphor to reach the CCD will appear smaller than they actually are.

Table 2.4 *Results of a Monte Carlo simulation to investigate the deposition of energy in a 160 μm gadox phosphor.*

Source	***^{241}Am***	***^{137}Cs***
Number of energy depositions for 100,000 photons	*75,685 ± 275*	*6,952 ± 83*
Number of depositions at gamma ray energies of interest(% of total)	*59.5 keV 75,278 ± 274 (99%)*	*32-38 keV 5,806 ± 76 (84%)* *662 keV 73 ± 9 (1%)*
Modal energy deposited	*59.5 keV*	*32 keV*
Mean energy deposited	*59.2 keV*	*71.7 keV*

The simulation shows that the lower energy photons emitted by the ^{137}Cs source cause the bulk of the energy depositions within the phosphor. Very few of the high energy ^{137}Cs photons interact via the photoelectric effect, and even fewer of these deposit their full energy in the phosphor due to the photoelectrons produced having ranges longer than the phosphor thickness. The mean energy deposited by the ^{137}Cs photons is 71.7 keV. This is significantly lower than the maximum energy emitted by the source (662 keV), but is still higher than the maximum energy emitted by the ^{241}Am source.

The results from this simulation would suggest that the majority of blobs produced by the ^{137}Cs source, being in the region of 35 keV, should have a smaller area than those produced by the ^{241}Am source, even so, by visual inspection (Figure 2.7) it has been

seen that this is not the case. The probable cause of this is the fact that the Monte Carlo simulation does not consider the propagation of the light photons produced by the gamma ray interactions. Table 2.3 gave estimates based on the detector's minimum detectable signal, of d_m, the maximum distance away from the L3CCD surface that an interaction can take place and be reliably detected. This distance is four times larger for 662 keV photons than for 32-38 keV photons. This means that the volume of phosphor that the higher energy depositions can occur in and still be seen is four times larger than the volume allowed for the lower energy depositions, increasing the probability of detecting the higher energy depositions compared to detecting the lower energy ones.

2.5.3 Conclusions on the possibility of achieving x-ray energy resolution using the CCD65-02

Images of individual x-ray photons interacting with the CCD65-02 were obtained using two gamma-ray sources with differing photon energies: ^{241}Am (59.5 keV) and ^{137}Cs (32-38 keV and 662 keV). These blob images appeared to be different under visual inspection; the area of the photon hits, and therefore maybe also the total signal, was larger for the ^{137}Cs source, which emits higher energy photons. This observation lead to the suggestion that some x-ray energy resolution may be possible with the CCD65-02. An analysis algorithm was written to test this hypothesis, the results of which have been presented as a series of histograms.

2.5.3.1 Is there any energy resolution?

The results have shown that there is a difference of a factor of 2-3 in the area of the blobs and the total signal associated with each blob for the two gamma ray sources. A Monte Carlo simulation has shown that the majority of energy depositions for the ^{137}Cs source will be at the lower end of the spectrum, with the mean deposition energy being just 21 keV higher than the mean deposition energy of the ^{241}Am photons.

The results have shown that energy differentiation could be possible using the 160 μm gadox coated CCD65-02, however, the resolution can not be accurately quantified without a more extensive study. The true energy deposition in the phosphor for the ^{137}Cs photons, as indicated by the Monte Carlo simulation, is not a good representation

of the actual energies emitted by that source. This is partially due to the phosphor being extremely thin compared to the attenuation lengths needed for 662 keV photons and also due to the fact that a range of energies are deposited by Compton scatter interactions. The predicted Monte Carlo spectrum shows large numbers of depositions around 35 keV, indicative of photoelectric interactions by the lower energy lines of the source, followed by a small continuum of energies up to around 450 keV. There is a small photopeak at 662keV. Considering this polyenergetic energy deposition spectrum and the problem of the phosphor's opacity, it can be inferred that complete energy resolution of the gamma rays emitted from a ^{137}Cs source, even with an ideal detector collecting the light photons produced by the phosphor, would not be possible with a 160 μm thick Gd_2O_2S:Eu phosphor.

This work, which was to quantify the energy resolving capabilities of the L3CCD, has been severely limited by the phosphor available. A thicker phosphor with low self-absorption properties is needed to improve the quality of the gamma photon energy collection. Indeed, it would be difficult to thoroughly optimise the analysis algorithm until more accurate images of the signals produced by full energy deposition blobs could be obtained. However, such a phosphor would significantly limit the spatial resolutions of the L3CCD required for the diffraction imaging task.

If an alternative phosphor can be used, it may be pertinent to take further images of photons at alternative energies in order to build up a greater amount of data to allow full analysis of the energy resolution available from the phosphor/L3CCD system. Ideally these photons should be from monoenergetic sources at energies sufficiently low enough to interact with the phosphor mainly via the photoelectric effect. Suitable sources may be either a range of gamma emitters with energies less than ~ 100 keV or a synchrotron radiation source.

In conclusion, these results have shown that limited energy discrimination is possible with the phosphor coated CCD65-02, but it has been impossible to quantify the energy resolution of the detector due to limitations caused by the phosphor available. Another choice of phosphor may well be needed in order to reliably quantify the potential energy resolution of the detector.

2.5.3.2 Implications of the energy resolution of the L3CCD on diffraction imaging

In this thesis, L3CCD cameras will be used for angular dispersive diffraction imaging at a synchrotron radiation source. This monoenergetic source means that the energy of the coherently scattering photons is well known and thus energy resolution is not a requirement that must be considered in the detector choice. The diffraction imaging collimator has several rows of holes such that several depths within the phantom can be imaged simultaneously (figure 2.1). With a single energy in use, the experiment is obviously limited to measuring one momentum transfer value at a time. Previous diffraction work on breast tissue has highlighted that the coherent scatter from normal tissue is greatest at 1.1 nm^{-1} whilst it is greatest in diseased tissue at 1.6 nm^{-1} (figure 1.8). At a scatter angle of 9°, these momentum transfer values correspond to energies of 18 and 26 keV. If x-rays with both of these energies could be produced simultaneously and discriminated between with a detector, then images highlighting either the normal or the diseased tissue could be produced simultaneously. In order for this to occur, the detector must be capable of discriminating between these two energies. A rule of thumb is that two signals can be considered resolvable if the difference between them is at least equal to one full-width-half-maximum (FWHM) [Knoll, 1999]. This means that the FWHM of the detector must be less than 8 keV in order to discriminate between these two energies. It is not clear from these current experiments if this is the case.

It was previously shown that an energy resolving detector would not be needed for detecting the coherently scattered x-rays in an angular dispersive DEBI system using a mammographic x-ray source [Taibi *et. al.*, 2000], so there are no direct detrimental implications that the lack of quantified energy resolution has on the planned use of the L3Vision technology.

2.6 Conclusions on collimation and detector choices for diffraction imaging

This chapter has investigated methods of measuring the diffraction signal from objects. The two techniques for this are angular dispersive diffraction and energy dispersive diffraction. Angular dispersive techniques use a monoenergetic x-ray source and collect scattered photons from a range of angles and energy dispersive techniques use a

polyenergetic source and hold the scatter angle constant whilst measuring the energy of the photons. Both techniques will be used in the work covered in this thesis.

The next chapter will consider planar diffraction imaging of life-size breast tissue phantoms. An angular dispersive technique will be used at a synchrotron to obtain images of phantoms. A collimator consisting of an array of parallel holes has been chosen for this task so that depth information about the phantom may be obtained. The detector for this work needs spatial resolution, but energy resolution is not needed. The L3CCD has been chosen as a suitable detector as it meets the spatial resolution and sensitivity requirements of the imaging modality and is available for use by the research group at UCL. A preliminary analysis of the potential x-ray energy resolution of this detector has been undertaken, but results have proved inconclusive. If the detector could discriminate between 18 and 26 keV x-rays then the two important momentum transfer values for normal and diseased breast tissue discrimination could be imaged simultaneously (provided that they could be produced simultaneously with no contamination from other energies).

Chapter four will cover transmission and diffraction microCT of breast tissue samples. The L3CCD has again been used at the synchrotron to produce some images, although the bulk of this work has used energy dispersive diffraction with a laboratory tungsten x-ray unit. An annular collimator set at 6° has been chosen for this work, along with a HPGe detector. A spatially resolving detector is not a requirement for this laboratory based work, however energy resolution is essential and HPGe fills this requirement more fully than any other detector available.

CHAPTER 3

Planar diffraction imaging

3.1 Introduction

As described in Chapter 1, it has been shown that biological tissues exhibit x-ray diffraction signatures indicative of the type of tissue being irradiated. One of the future goals of the DEBI project is to incorporate a diffraction imaging system into a standard transmission x-ray mammographic imaging system by using a slot scan method to acquire both images simultaneously. A feasibility experiment for this method was previously carried out by the UCL Radiation Physics Group [Kidane *et. al.*, 1999; Harris *et. al.*, 2003] using a life-size human breast tissue phantom. Harris *et. al.* took the L3CCD (CCD65-02) described in chapter 2 to a synchrotron radiation source and placed it behind a single row of collimation holes at an angle of 9° to the sample, which was then scanned through the beam in order to acquire the diffraction image. A transmission image was then taken using the synchrotron radiation and a photostimulable plate. These images are shown in figure 3.1. Analysis by the authors indicated that the image formed using diffracted x-rays showed contrast between normal and cancerous tissues around three times higher than that in the image formed conventionally using x-rays transmitted through the phantom. However, the spatial resolution of the diffraction image was poorer than the transmission image due to the fact that the diffraction pixel size was equivalent to the 500 μm square collimator hole size.

This preliminary experiment showed that diffraction imaging techniques could be used to form a higher contrast image of normal and cancerous breast tissue than transmission imaging and this chapter aims to build on this previous work. Harris *et. al.* used a single row of holes in their collimation, allowing information from a single slice of the phantom approximately 1 cm thick to be collected. In chapter 2 of this thesis a multiple row collimation system was described that will allow information to be collected from

all depths in a phantom, giving a third dimension to diffraction imaging. Images of two phantoms – one high contrast Perspex and air, one breast tissue – were acquired and analysed for the work in this chapter. The analysis considers further the achievable contrast of diffraction imaging and also examines the corrections necessary to form an accurate diffraction image of an entire breast.

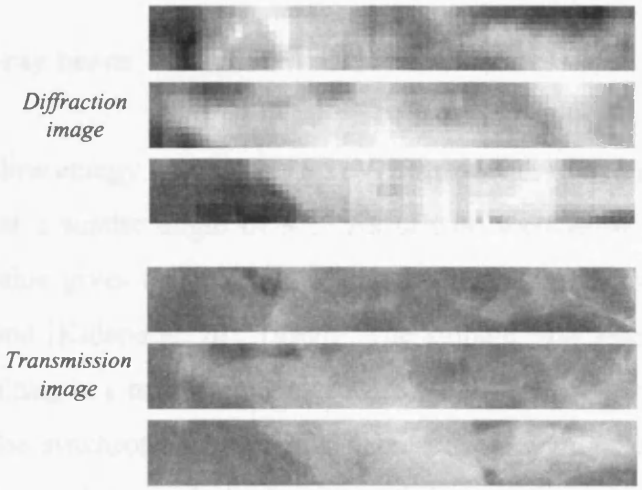

Figure 3.1 *Diffraction and transmission images of a life-size breast tissue phantom [Harris et. al., 2003]. The diffraction image was obtained by scanning down three separate strips of the phantom.*

3.2 Experimental Apparatus

The purpose of this experiment was to produce planar diffraction images of two phantoms in order to investigate the need for an attenuation correction.

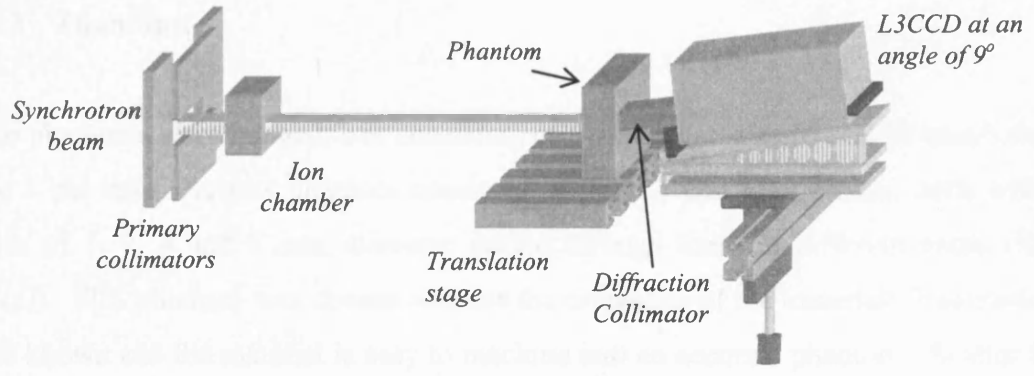

Figure 3.2 *Diagram of the experimental set up at the SYRMEP beamline, Elettra. [Griffiths et. al., 2003]*

The diffraction images used in this work were acquired using the SYRMEP (SYnchrotron Radiation for MEdical Physics) beamline [Arfelli *et. al.*, 1997] at the Elettra synchrotron radiation source in Trieste, Italy. The gadox coated L3CCD camera discussed previously in Chapter 2 was set at 9° to the beam axis and used to detect x-rays scattering in a phantom that was scanned perpendicularly through the beam (figure 3.2).

3.2.1 X-ray beam

The beamline energy was set to 18 keV, corresponding to a momentum transfer value of 1.1 nm^{-1} at a scatter angle of 9°. As can be seen from figure 1.8, this momentum transfer value gives the maximum amount of contrast between normal and cancerous breast tissue [Kidane *et. al.*, 1999]. The storage ring electron bunch energy was 2.4 GeV, resulting in a maximum flux of 2 x 10^8 photons s^{-1} mm^{-2} at the beamline [Elettra, 2005]. The synchrotron beam flux decreases throughout the day following a shallow semi-exponential curve from the time of electron injection into the storage ring. The half-life of the beam is 32 hours at injection, increasing to 50 hours 24 hours later. The ion chamber seen in figure 3.2 proved highly unreliable for obtaining an accurate measurement of the beam intensity and so was not used to correct the data for the change in intensity over the time taken to acquire it. Instead, the measurements, which took up to four hours to acquire for each phantom, were taken later in the day, once the flux had become more uniform, to minimise temporal intensity fluctuations in the data.

The beamline collimators were set for a 10 mm wide, 1 mm high primary beam incident on the phantom.

3.2.2 Phantoms

Two phantoms were imaged; one consisting of Perspex and air and one of breast tissue. The 3 cm thick Perspex phantom consisted of three 1 cm thick blocks, each with air holes of 1, 2, 4 and 8 mm diameter drilled through them in different areas (figure 3.3(a)). This phantom was chosen because the properties of the materials it contains are well known and the material is easy to machine into an accurate phantom. Scatter from Perspex at 18 keV is abundant, whilst it may be considered negligible for air. This

means that the phantom can be used both to test the validity of any attenuation correction for an extreme case and also to test the spatial resolution of the system. The premise was that such an extreme difference in scatter and attenuation properties, as found in Perspex and air, would provide a good test for the attenuation corrections. In the case of the breast tissue phantom, the differences in the attenuation properties of the components are small.

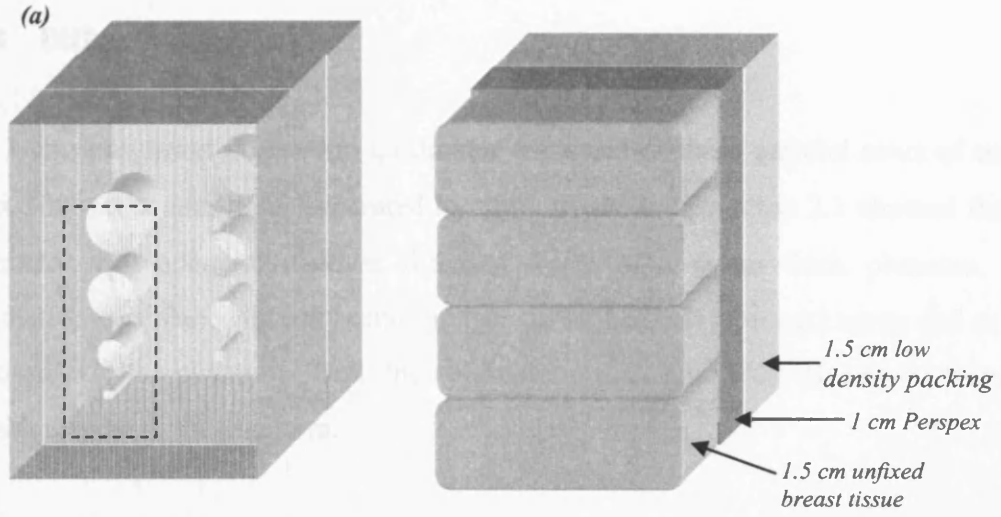

Figure 3.3 *(a) Illustration of the Perspex test phantom. The drilled hole diameters are 8 mm, 4 mm, 2 mm and 1 mm. The dotted line indicates the area imaged. (b) Schematic of the breast tissue phantom contained within a sealed Perspex container.*

The 4 cm thick breast tissue based phantom was 6 cm wide and 8 cm high. It consisted of 1.5 cm of unfixed, excised, normal and cancerous human breast tissue, 1 cm of Perspex and 1.5 cm of low density packing, all contained within a thin walled, air-tight Perspex container (figure 3.3(b)). The breast tissue layer consisted of four pieces of tissue, each wrapped in a thin protective polyethelene layer to separate it from adjacent samples and to prevent seepage of fluids into the low density packing foam. The thinness of the protective layer meant that its contribution to the scatter would be negligible. The tissue samples were collected by Professor Andrew Hanby during routine surgery at St. James' University Hospital, Leeds and were considered surplus to diagnostic requirements. They were transported in dry ice and the phantom was stored at -40°C when not in use. The phantom was warmed up fully to room temperature before the experiment commenced. Allowing the sample to remain at room temperature during the experiment prevented ice crystals from forming, which can affect the scatter from the tissues, but it did result in some loss of integrity of the cytological features used in the histopathological analysis of the composition of the samples after imaging.

3.2.3 Translation Stage

The phantoms were placed on a translation stage, whose servo motor was manually controlled and moved vertically in 1 mm steps with 0.01 mm precision. A full automation linking automatic movement of the translation stage with data acquisition by the L3CCD camera could not be achieved.

3.2.4 Diffraction Collimator

The 3 cm long brass diffraction collimator consisted of three parallel rows of ten 500 μm x 500 μm square holes separated by 500 μm septa. Equation 2.1 showed that this collimator will adequately cover the first 3 cm of a 4 cm thick phantom. The collimation was placed directly onto the face of the L3CCD chip packaging and as close as possible to the phantom. Both the collimator and camera were placed at an angle of 9° with respect to the phantom.

3.2.5 L3CCD and Data Acquisition

The L3CCD used was previously described in chapter 2. It was operated at a servo-regulated temperature of -5°C ± 0.1°C and a gain of 35, giving a SNR of >4 for this photon flux and energy [Harris, 2002]; it was controlled via a National Instruments DAQ card by a PC running LabView software which stored the acquired image as a 16-bit tiff file. In order to reduce the effects of statistical noise within the images, the software averaged 20 L3CCD fields together for each acquisition. Five white images were obtained by collecting the scatter from a large homogeneous block of Perspex; five dark images were also acquired. The averages of these two sets of images were used to correct the images of the phantoms for pixel variations.

3.2.6 Image formation algorithm

The scattered x-ray photons pass through the diffraction collimator and are detected by the L3CCD camera. An image obtained by the camera is shown in figure 3.4. The streaking seen in the image is due to saturated camera pixels being clocked through the device. This saturation will result in some signal information being lost. The pixels

were saturated mainly as a result of a direct photon interaction occurring in silicon of the L3CCD chip, with a small contribution due to bad pixels. Each bright rectangle seen in the image corresponds to a single hole in the diffraction collimator and the summed intensity of the L3CCD pixels in each rectangle provided the data for one pixel of the final diffraction image. The rectangular L3CCD pixels have been displayed as squares in the image, therefore giving the impression that the square collimator holes are rectangular. Each row of rectangles in the image corresponds to a row of collimator holes and thus a different depth within the phantom. Three collimator rows were imaged, but due to on-chip noise problems the data from one row was un-useable and so only two rows, as shown in figure 3.4, were used to form the diffraction images of the phantoms.

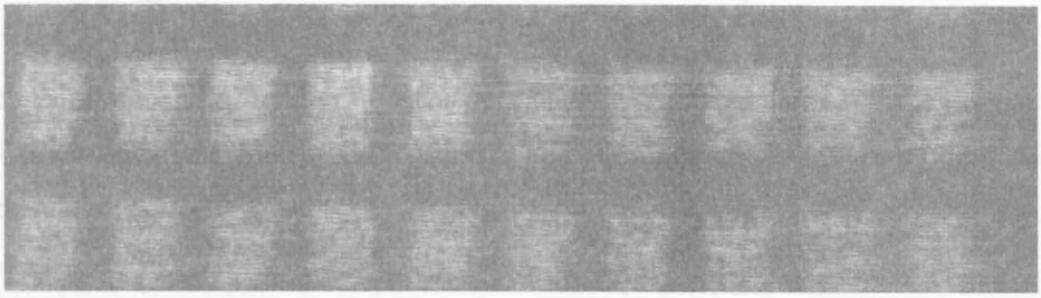

Figure 3.4 *Raw image data from the L3CCD. Each rectangle corresponds to a hole in the diffraction collimator.*

An image similar to figure 3.4 was captured for every scan position of the phantom and an algorithm [Speller and Horrocks, 2003] was written in IDL to form a diffraction image using the collimator hole data for each phantom position. The IDL algorithm read in each tiff file and applied a mask consisting of two rows of ten 25 x 26 pixel holes to each image. Each hole in the mask corresponded to a collimator hole. The mean of each of the ten regions of interest in each row in the mask was then calculated and placed into the corresponding pixel position in an array which forms the final diffraction image. This 10 element wide array was 41 elements high for the breast tissue phantom image and 72 elements high for the Perspex phantom. A region of interest was also taken in the dark area between the two rows of holes. This provided a background grey level value which was used to correct the diffraction data for any fluctuations in the camera gain. The final image arrays were scaled up to 150 x 600 pixels and their grey scales rescaled into an 8-bit image for viewing in this thesis, however all quantitative data used in this work was acquired from the raw image data.

3.2.7 Transmission Images

Transmission images of both phantoms were taken prior to the diffraction work being carried out. The images were taken using a microfocal Mo target and filter x-ray unit (X-Tek, U.K.) operating at 30 kVp. The phantom was placed directly onto the surface of an amorphous silicon array (dPix/Varian, U.S.A.) which has a pixel size of 127 μm. The array uses Flashscan software to acquire a full field image which is then saved as an 8-bit bitmap file. The edges of the image can then be cropped to select just the portions of interest.

3.3 Images

Transmission and diffraction images were taken of each phantom and then registration of the images was attempted in order to compare the contrast of the images and aid attenuation correction.

3.3.1 Transmission Images

The transmission images of the phantoms are shown in figure 3.5. The dashed lines indicate the regions later imaged using diffraction techniques; time constraints at the beamline limited the region that could be scanned for the diffraction imaging. The image of the Perspex phantom (figure 3.5(a)) shows the air holes clearly. In this phantom, the holes on the left of the image are in the middle 1 cm thickness of the phantom and the holes on the right are in the 1 cm thickness lying closest to the x-ray source and furthest from the detector.

The image of the breast tissue phantom (figure 3.5(b)) resembles a normal mammographic image, but the contrast in this image is enhanced above that usually associated with mammograms as the tissue within the phantom is thinner than a compressed breast and the dose to the tissue did not have to be kept as low as possible as this is a phantom, not a patient.

The images in figure 3.5 have the area of the phantom that was imaged using diffraction techniques highlighted. This area is 71 mm x 10 mm for the Perspex phantom and was marked on the phantom prior to the diffraction measurements for correlation with the transmission image at a later time. The area is 20 mm x 10 mm set 20 mm and 5 mm away from the edges of the Perspex holder for the breast tissue phantom. The mean grey levels and standard deviations of the entire highlighted regions of these 8-bit images are 47 ± 16 (34% of mean) for the Perspex phantom and 27 ± 2 (7% of mean) for the breast tissue phantom. The mean grey level value for the air holes in the Perspex phantom is 84 and the mean for the solid Perspex is 40.

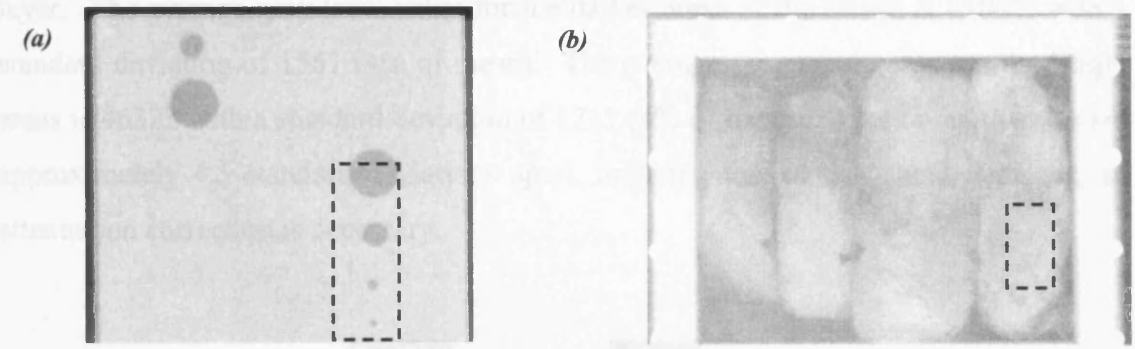

Figure 3.5 *Transmission x-ray images of (a) 3 cm thick Perspex block shown in figure 3.3; (b) phantom consisting of 1.5 cm unfixed, excised normal and cancerous human breast tissue, 1 cm Perspex and 1.5 cm of low density packing, all contained within a thin walled, air-tight Perspex box. The dashed lines show the areas of the phantoms corresponding to the diffraction images.*

3.3.2 Diffraction images

The diffraction images of the Perspex phantom are shown in figure 3.6. Data was successfully acquired for two collimator rows and thus diffraction images for two different phantom depths were constructed. In order for satisfactory display of the images in this thesis, the number of pixels in these images has been expanded and the grey levels set so that the minimum value is equivalent to 0 and the maximum to 255 for an 8-bit image, however any values quoted for the images relate to the raw 16-bit data prior to manipulation for viewing. Figure 3.6(a) shows the slice of the phantom furthest from the detector, which contained the four air holes. Despite using 0.5 mm collimation, the 1 mm diameter hole can clearly be seen, indicating a potential *x-y* spatial resolution of better than 1 mm when using this collimator. The image shows a

high scatter intensity in the Perspex (mean data value = 38876 ± 936 standard deviation (2% of mean)) and a significantly lower intensity where the holes are present (mean data value = 33046 ± 134 standard deviation (0.4% of mean)). Figure 3.6(b) is an image of the diffraction data from the slice closest to the detector. The dark line seen to run down the image is due to on chip problems with the detector affecting one of the central holes and is not an artefact due to the beam, phantom or reconstruction technique. This layer should show as a uniform slab of Perspex in the area imaged however bright 'ghost' images of the air holes in the previous layer are seen. These significantly brighter areas are the result of the incident beam on the second layer having a higher intensity where it has not been attenuated by the Perspex in the previous layer. The average grey level value for the darker areas of the image is 41007, with a standard deviation of 1561 (4% of mean). The average grey level value for the bright areas is 46323 with a standard deviation of 1711 (4% of mean). These mean values are approximately 4.5 standard deviations apart, implying that in this particular case, an attenuation correction is necessary.

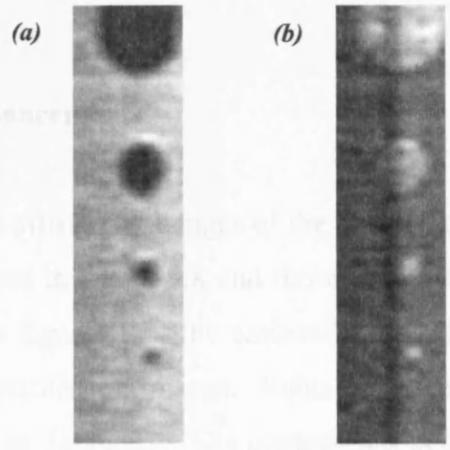

Figure 3.6 *Raw diffraction images of the Perspex phantom; (a) image of the top layer, closest to the x-ray source containing the drilled holes; (b) image of the lower, uniform layer.*

Figures 3.7(a) and (b) show the diffraction images of the layers closest to the source and closest to the detector for the composite breast tissue, Perspex and low density packing material phantom. It can be assumed that the packing and Perspex layers are homogeneous across the imaging plane of the phantom, and thus any variations across the image are due wholely to the human breast tissue in the phantom. The mean grey level value and standard deviation are 32251 and 1567 (5% of mean) for the layer

closest to the source and 31771 and 1576 (5% of mean) for layer closest to the detector. These mean values lie within one standard deviation of each other and so the difference between them is not significant, unlike the Perspex and air phantom. Thus it is possible that an attenuation correction may not be important for the tissue phantom. This will be discussed further in section 3.5.3.

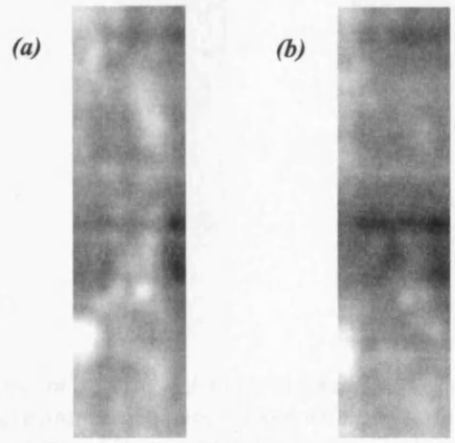

Figure 3.7 *Raw diffraction images of the breast tissue phantom; (a) image of the top layer, closest to the x-ray source; (b) image of the lower layer, closest to the detector.*

3.3.3 Contrast enhancements

The transmission and diffraction images of the layer of the Perspex phantom containing the air holes are shown in figure 3.8 and those of the tissue phantom in figure 3.9. It can be seen from the figures that the contrast in the diffraction images appears to be higher than in the transmission images. Values of contrast for the areas highlighted in the images are given in Table 3.1. The contrast has been calculated using equation 1.1 and the error on the constrast σ_C using equation 3.1 which was arrived at by propagation of errors from the contrast equation [Knoll, 1999]. σ_{G1} and σ_{G2} are the standard deviations of grey level values G_1 and G_2.

$$\sigma_C^2 = \left(\frac{2G_2}{(G_1+G_2)^2}\right)^2 \sigma_{G1}^2 + \left(\frac{2G_1}{(G_1+G_2)^2}\right)^2 \sigma_{G2}^2 \qquad (3.1)$$

Table 3.1 shows that the contrast in the diffraction image is almost 7 times the transmission image contrast for the Perspex phantom and almost 10 times the

transmission contrast for the breast tissue phantom. This is particularly encouraging for the breast tissue phantom as the higher soft tissue contrast may lead to more diagnostic information being extracted from the image.

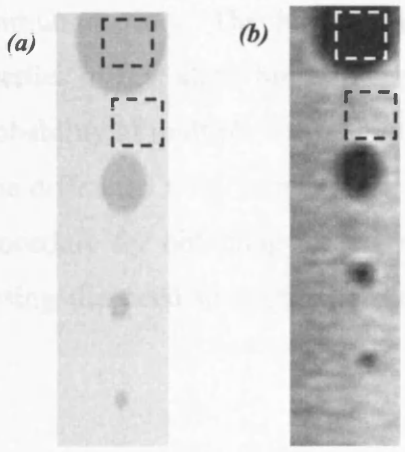

Figure 3.8 *Images of a 3 cm thick Perspex phantom containing airholes drilled 1 cm into the phantom; (a) transmission image taken with a Mo-Mo mammographic x-ray unit; (b) raw diffraction image of layer containing holes. Dashed lines indicate regions used for contrast analysis.*

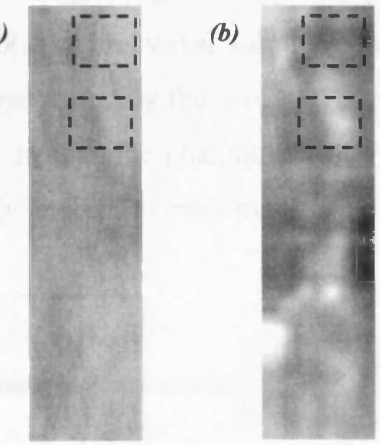

Figure 3.9 *Images of a composite Perspex, low density packing material and breast tissue phantom; (a) transmission image taken with a Mo-Mo mammographic x-ray unit; (b) raw diffraction image of layer closest to source. Dashed lines indicate regions used for contrast analysis.*

Table 3.1 *Contrast values for diffraction and transmission x-ray images of two phantoms.*

Phantom description	*Transmission image contrast*	*Diffraction image contrast*
Perspex and air	*11.5 ± 0.1%*	*78.9 ± 0.2%*
Breast tissue	*2.4 ± 0.3%*	*23.9 ± 5.4%*

3.4 Attenuation correction

The collimation used to obtain the diffraction images in this chapter was described in chapter 2 (figure 2.1). It enabled diffraction images of slices at different depths within a phantom to be imaged simultaneously. The detected signal for each slice is not purely due the diffraction properties of that slice, but also depends on other properties of the phantom, such as the probability of multiple scatter and the attenuation properties of the materials traversed by the diffracted x-ray beam. Thus, the work in this section aims to identify a correction procedure for obtaining the diffraction signal from the detected signal whilst also assessing the need to apply the correction in a clinical diagnostic system.

3.4.1 Correction procedure formulation

The information in each pixel of a transmission x-ray image of a phantom is representative of a voxel running along a straight line path from the source to the pixel in the detector (figure 3.10(a)). The voxel's dimensions, if we consider signals due to air to be negligible, are approximately the area of the pixel multiplied by the length of the straight line x-ray path through the phantom. Thus, no depth information within the phantom is achievable as the voxel traverses the entire phantom.

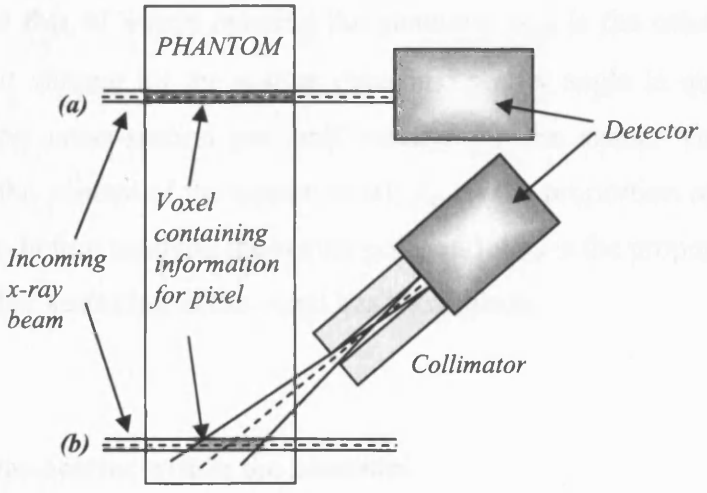

Figure 3.10 *Schematic showing the voxels that the information in an individual pixel of an image correlates to for (a) transmission imaging and (b) diffraction imaging. The angle of the detector for the diffraction imaging has been exaggerated for demonstration purposes.*

The voxel that the scatter information in a pixel of a diffraction image represents is illustrated in figure 3.10(b). It is a complex geometric shape that is formed at the point where the incoming x-ray beam and the solid angle subtended by the diffraction collimation intersect. The figure also shows that as we are only considering one portion of the phantom, the information in a pixel of raw diffraction image data is not purely due to the scatter interactions within the voxel of interest, but will also include attenuation information from interactions occurring along the entire path that the x-ray takes to reach the detector. In this way, the raw diffraction image formed consists not only of scatter effects, but also of the same attenuation effects as the transmission image, but along a slightly different path. Therefore, in order to isolate the diffraction component from the recorded signal, an attenuation correction must be performed.

The raw pixel data can be split into three different parts: (1) the scatter taking place in the voxel of interest, (2) the attenuation of the x-rays as they pass through the phantom, including Compton and coherently scattered photons and (3) a term, M, representing multiple scatter events in the phantom that contribute toward the final signal in the detector. This means that the photon flux, F_d, reaching the detector can be written as:

$$F_d = F_o\{(scatter)\times(attenuation)+M\} \qquad (3.2(a))$$

$$F_d = F_o\{(\sigma_{coh}+\sigma_{com})V(\{1-A_{pre}\}\{1-A_{post}\})+M\} \qquad (3.2(b))$$

F_o is the initial flux of x-rays entering the phantom, σ_{coh} is the coherent scatter cross-section per unit volume for the scatter voxel and scatter angle in question, σ_{com} is the Compton scatter cross-section per unit volume for the scatter voxel and angle in question, V is the volume of the scatter voxel, A_{pre} is the proportion of x-rays attenuated by the phantom before reaching the scatter point and A_{post} is the proportion attenuated by the phantom after scattering in the voxel has taken place.

3.4.2 Compton scatter within the phantom

Equation 3.2(b) has terms that take into account the Compton and multiple scatters occurring in the phantom that will contribute towards the final signal detected in the

diffraction imaging experiments. An assessment of these contributions needs to be made to assess their impact on the final detected signal.

Table 3.2 gives the attenuation coefficients for Compton and coherent scatter in breast tissue [ICRU-44, 1989] and Perspex [Hubbell & Seltzer, 2004] at 18 keV calculated using *XCOM* [Berger *et. al.*, 1999], along with the proportion of the total attenuation coefficient that they make up. It can be seen from the table that for 18 keV photons, the proportion of the total attenuation coefficients made up by the Compton attenuation coefficient is approximately twice that of coherent scatter. Thus the probability of Compton scatter is approximately twice that of coherent scatter; even so, this is just the probability of the scatter event taking place and does not take into account the direction of travel of the photon after the event.

Table 3.2 *Mass attenuation coefficients and mean free paths for Compton and coherent scatter interactions in breast tissue and Perspex at 18 keV.*

Material	***Compton***		***Coherent***	
	Mass attenuation coefficient (cm^{-1})	*% of total attenuation coefficient*	*Mass attenuation coefficient (cm^{-1})*	*% of total attenuation coefficient*
Breast tissue	1.83×10^{-1}	*20.5%*	9.28×10^{-2}	*10.4%*
Perspex	2.05×10^{-1}	*24.1%*	9.87×10^{-2}	*11.6%*

Figure 3.11 shows the normalised probability distribution of the direction of travel of 20 keV photons leaving Compton and coherent scatter interactions in breast tissue. The Compton probability has been calculated using the Klein-Nishina formula (equation 1.2) whilst the coherent scatter data is taken from a Monte Carlo simulation [Taibi *et. al.*, 2000]. The scatter from the Compton interaction is seen to be almost isotropic, whilst the distribution of the coherently scattered photons is mainly in the forward direction, distributed around a scatter angle of 8° with respect to the original direction of travel. These experiments only intend to collect scattered photons from small scatter angles, specifically at 9° ± 0.95° to the photons' original direction of travel. The isotropic nature of the Compton scatter means that only 1.11% of photons scattering via this mechanism will scatter into the acceptance angle of the collimator; however, the forward directional nature of the coherent scatter allows up to 20% of the coherently

scattered photons to pass through the collimation. This means that over 10 times more coherently scattered photons reach the detector compared to Compton scattered photons, allowing an approximation to equation 3.2 to be made where the Compton contribution is considered negligible.

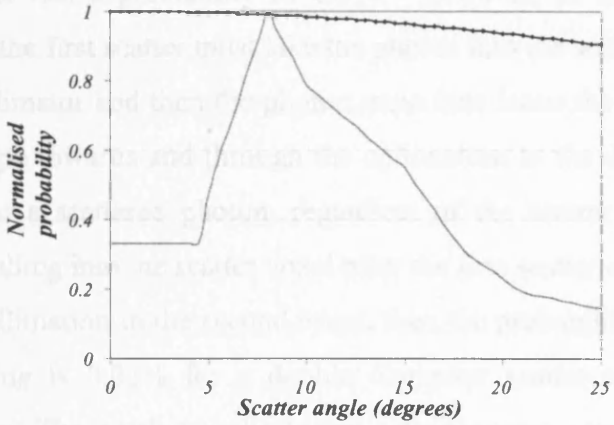

Figure 3.11 *Plot of the probability of scatter as a function of scatter angle for 20 keV x-rays in breast tissue for coherent scatter (unmarked line) [Taibi et. al., 2000] and Compton scatter (marked line).*

3.4.3 Multiple scatter within the phantom

Along with single Compton scatters, multiple scatter events contributing to the final signal must also be considered. At 18 keV, photons transfer very little of their energy to the electron during Compton scatters – the most likely energy transferred from a 20 keV photon is 0.721 keV [Johns & Cunningham, 1983] – therefore the same attenuation coefficients may be assumed for both the first and second scatters in a multiple scatter chain. The forward direction preference of coherent scatter interactions indicated in figure 3.11 means that *M*, the multiple scatter term in equation 3.2, will increase for the diffraction image slices situated furthest from the source.

M represents photons that scatter out of the geometric x-ray beam path and then scatter back into the acceptance volume of the diffraction collimator (figure 3.12). For a small sample and narrow collimation the term will be negligible compared to the coherent scatter term in equation 3.2. The probability of a single Compton scatter occurring in the first two centimetres of a breast tissue phantom is 16.2% and that of a single coherent scatter is 8.2%. If a maximum of two scatter events per photon is assumed, then four combinations of scatter interaction are possible: Compton-Compton,

Compton-coherent, coherent-Compton and coherent-coherent scatters. The combination with the maximum probability of occurrence is a double Compton scatter, with a probability of occurring in the first two centimetres of a breast tissue phantom of 2.6%, not taking into account the final direction of the scattered photon, whilst a double coherent scatter has a probability of 0.7%. However, in all four of these possible combinations, the first scatter must take the photon into the solid angle subtended by the diffraction collimator and then the photon must then leave the second scatter travelling within this angle towards and through the collimation to the detector. Assuming for a worst case that a scattered photon, regardless of the scatter mechanism, has a 50% chance of travelling into the scatter voxel after the first scatter event before scattering up through the collimation in the second event, then the probability of this required double scatter occurring is 0.02% for a double Compton scatter and 0.07% for a double coherent scatter. These values indicate that a double scatter event within the phantom is highly unlikely. Therefore M may be considered negligible for this experiment.

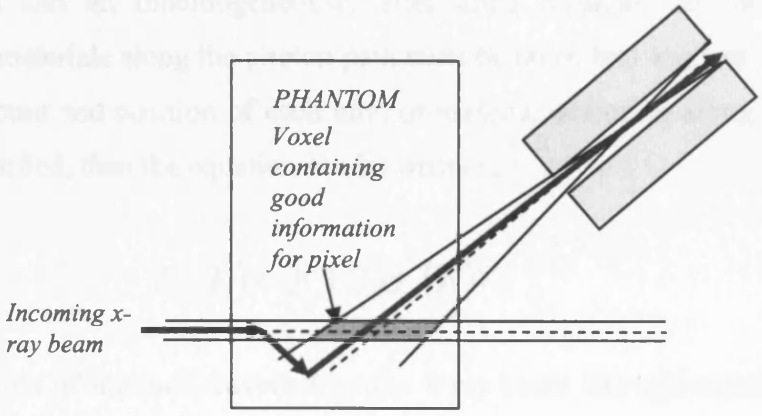

Figure 3.12 *Schematic illustrating a possible multiple scatter path (bold arrows) for a photon that may contribute to the signal for the shaded voxel in the phantom.*

3.4.4 Approximations to the attenuation procedure

The previous sections have shown that the contributions of Compton and multiple scatters to the detected scatter signal for these experiments are small compared to the contribution from the coherently scattered photons. If the negligible Compton and multiple scatter terms are removed from equation 3.2(b), it can be shown that for a monoenergetic beam traversing a homogeneously attenuating phantom, the equation

simplifies to a function consisting of just one attenuation coefficient, μ, the total attenuation coefficient of the homogeneous phantom, and the actual pathlength, x, of the x-ray beam, where x_1 is the pathlength before the coherent scatter event occurs and x_2 is the pathlength after the coherent scatter event:

$$F_{d(\text{hom})} = F_o \sigma_c V e^{(-\mu x_1)} e^{(-\mu x_2)} \qquad (3.3(a))$$

$$F_{d(\text{hom})} = F_o \sigma_c V e^{-\mu(x_1+x_2)} \qquad (3.3(b))$$

If the scatter angle, θ, is small, then it can be assumed that the x-ray pathlength, x_1+x_2, is the same for all voxels within the phantom and thus in this particular case of a homogeneously attenuating phantom, the attenuation effects across the entire image would become constant and no longer modulate the coherently scattered data across the image.

Equation 3.3 becomes more complex for the more realistic situation of a polyenergetic x-ray beam and an inhomogeneously attenuating phantom, as all the differently attenuating materials along the photon path must be taken into account. If it is assumed that the amount and position of each kind of material occurring along the x-ray's path can be quantified, then the equation can be written as:

$$F_d(E) = F_o(E)\sigma_c(E)Ve^{-\left(\sum_i \mu_i(E)x_i\right)} \qquad (3.4)$$

x_i is the length of the path travelled by the x-ray beam through material i, which has attenuation coefficient μ_i.

Breast tissues present a situation where they are inhomogeneous, yet the attenuation properties throughout the sample are usually similar; this is the fundamental reason why there is such poor soft tissue contrast seen in transmission mammography.

3.4.5 Attenuation correction theory validation

An outline of the basic premise of an attenuation correction to the diffraction images has been given above, resulting in equation 3.4 when the contributions due to Compton and

multiple scatters are ignored in the final detected signal. This simplified equation should be verified in order to show that ignoring these contributions does not seriously affect the final correction. As the transmission images of the phantoms were obtained using an almost monoenergetic mammographic x-ray source and the diffraction images were taken at a synchrotron radiation source set to a similar energy, the energy dependence of equation 3.4 can also be removed in this instance. This means than all terms in the equation can be considered constant across the diffraction images except for the coherent scatter cross-section and the summation in the exponent of the total attenuation within the beam path. The various values of μ_i and x_i are unknown for the tissue phantom used in these experiments, however, the values can be found for the Perspex and air phantom as its composition is known fully.

The validity of equation 3.4 for use in an attenuation correction procedure was tested using the diffraction data from the Perspex phantom and theoretical values for the attenuation experienced by the diffracted photons. A procedure was written in IDL to exploit the fact that the attenuation difference between the lighter and darker areas of figure 3.6(b) is due purely to x-rays passing through either 1 cm of air or 1 cm of Perspex prior to them scattering in a uniform layer of Perspex. The first step of the procedure was to locate the air holes in the phantom. This was done using the diffraction image of the layer of Perspex containing the holes (figure 3.6(a)). It was chosen to locate the holes in this way as both of the diffraction images contain the same number of pixels and the attenuating features should be positioned in the same place in the x-, y- plane for both of them. This removes spatial ambiguities that may be caused by photon path differences and image registration if using the transmission image. The holes were found by thresholding the data in figure 3.6(a). If the data value is below the threshold it is classified as being part of an air hole and the data for figure 3.6(b) is corrected for air attenuation; if the data value is above the threshold the image is left uncorrected. The grey level values classified as being 'hole' are corrected by multiplying them by a normalisation factor, n, which is defined as the ratio of the intensities, F_P and F_A, of two identical 18 keV x-ray beams after one has passed through 1 cm of Perspex and the other through 1 cm of air.

$$n = \frac{F_P}{F_A} = \frac{e^{-\mu_P x}}{e^{-\mu_A x}} = e^{(\mu_A - \mu_P)x} \qquad (3.5)$$

μ_A and μ_P are the attenuation coefficients of air and Perspex at 18 keV and x is the distance travelled by the x-ray beams (1 cm). The values of μ_A and μ_P are 1.205×10^{-3} cm^{-1} and 8.497×10^{-1} cm^{-1} respectively [Berger *et. al.*, 1999], giving a value of 0.428 for n.

Figure 3.13 shows the original uncorrected diffraction slice through the phantom and the same slice after this correction procedure has been used. The data has been converted to an 8-bit greyscale; in order to visualise the benefit of the correction, the maxima and minima of the two images' grey scales in figure 3.13 are identical, with 0 representing the minimum data value of the two images and 255 representing the maximum value. The correction appears to have worked well, aside from one bright area in the corrected image which is possibly caused by a partial volume effect due to a misalignment of the collimation holes caused by the manufacturing process. The mean grey level of the uncorrected image is 41871 and the standard deviation is 2747, which is 6.5% of the mean. The mean grey level and standard deviation of the corrected image including the bright area seen in image 3.13(b) are 41621 and 1524 (3.7% of mean value). When the bright area is ignored, the mean becomes 41159 and the standard deviation 830 (2% of the mean value). These standard deviation values indicate an approximately three-fold increase in the uniformity of the image and validate the use of a correction based on equation 3.4 to correct the diffraction data for attenuation throughout the phantom.

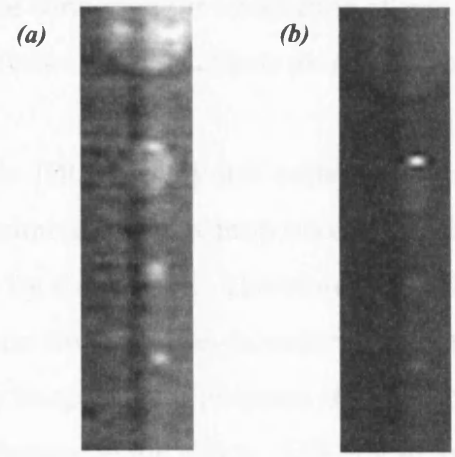

Figure 3.13 *(a) the original uncorrected diffraction image of the uniform layer of Perspex; (b) the image after correction by the procedure using database attenuation data, as outlined in section 3.4.3.*

3.4.6 Experimental application of the attenuation correction

In order for equation 3.4 to be used to correct the raw diffraction images for attenuation, the attenuation coefficients of materials along the path that the x-rays travel must be identified. As a first pass correction, assuming a small scatter angle, this correction can be done solely by assuming that the intensity reduction due to the attenuation component of the signal for each diffraction pixel is proportional to the intensity of the corresponding pixel area of a transmission image of the phantom. This correction can be applied practically by dividing the diffraction image of the phantom by the transmission image. Due to the path of the photons not being an entirely straight line through the phantom, this will lead to some discrepancies at well defined borders between differing materials, which may become apparent in the correction of the Perspex and air phantom. These discrepancies may be less important in the breast tissue phantom as the attenuation properties of the entire phantom vary less and changes in biological tissue types do not tend to be well delineated on the scale used. Over 3 cm, a photon travelling at 9° from its original direction of travel is deviated by 4.75 mm. This attenuation correction method was attempted in the laboratory in order to ascertain whether or not it would be sufficient for this work.

A future development of this correction could consider the depth positions of lightly and heavily attenuating materials within the phantom. This could be attempted by using the diffraction images acquired for different phantom depths to identify the materials' likely depths, and would allow the correction for attenuation effects to be matched to the areas of the diffraction image affected by these effects more precisely.

A procedure was written in IDL to apply this correction to experimental data. It was assumed that the transmission signal was proportional to the intensity drop caused by attenuation of the photons by the sample. Therefore the diffraction image was divided through by the transmission image. The procedure first read in both the diffraction image and a transmission image of the phantom that had been cropped using image editing software (Scion Image, Scion Corp., U.S.A.) to cover just the area of the phantom seen in the diffraction image. The images were then manipulated such that they were in identical orientations. Although the cropped transmission images showed the same area of the phantom as the diffraction image, they contained different numbers

of pixels as they were obtained using different techniques and different detectors. The IDL program resolved this issue by rebinning both images into 33 x 180 pixel arrays, thus expanding and interpolating the diffraction data whilst contracting the transmission image. The array size chosen meant that the diffraction array dimensions were multiplied up by the same factors as the transmission array dimensions were divided by (3.3 and 2.5 for the x- and y- ordinates respectively). Both images were then converted to an eight-bit grey scale, with their minima equal to 0 and their maxima equal to 255.

The attenuation correction was then finally performed by dividing the diffraction image by the transmission image. In order to visualise the corrected image, any areas of this new image affected by division by zero were set to the mean value of this image.

3.4.6.1 Perspex and air phantom

Figure 3.14(b) shows the Perspex data corrected using this technique alongside the uncorrected data for comparison. Unlike the theoretical correction data, the grey level scaling of the two images is not identical as this makes the corrected image unviewable when printed. It is clear from the figure that the registration of the transmission and diffraction images has not been entirely successful. This is partially due to non-uniformities in sensitivity over the diffraction voxel, but also due to operator error in marking the ROI on the phantom and selecting it accurately in the transmission images. This issue will need to be resolved before this technique becomes viable for correcting these images. It can also be seen that the lower portion of the corrected image has become quite noisy. The quality of the correction can be assessed by considering the contrasts of the uncorrected and corrected images, given in table 3.3. The images refer to 3.14(a) as the uncorrected image, 3.13(b) as the theory corrected image and 3.14(b) as the experiment corrected image. The contrast areas in the table refer to the positions of the small square areas marked in image 3.14(a). In a perfect image, the contrast between the middle and bottom squares should be zero within the errors of the counting statistics, as both signals should be due to x-rays passing through, and being scattered by, exactly the same amounts of material. In a perfectly corrected image, the other two contrast values in the table should also tend to zero within statistical error.

Table 3.3 shows significant contrast between all areas in the uncorrected image. This is expected when comparing the top area to the other two, but is unexpected when

comparing the middle and bottom areas and is due mainly to variations in the L3CCD camera – the left side of the images appears darker than the right – but is also due to a 10% drop in the beam intensity over the time taken to scan the phantom through the beam.

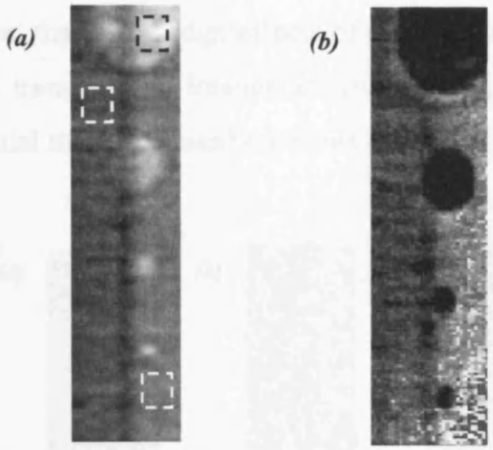

Figure 3.14 *(a) the original uncorrected diffraction image of the uniform layer of Perspex. The dashed boxes indicate the areas used for the contrast analysis; (b) the image after correction by the procedure using the transmission image data, as outlined in section 3.4.6.*

Table 3.3 *Contrast of the uncorrected Perspex diffraction image and the two corrected images. The errors were calculated using equation 3.1.*

Contrast areas	*Uncorrected image*	*Theory corrected image*	*Experiment corrected image*
Top-middle	*59.9 ± 4.8 %*	*9.5± 0.9 %*	*5.2± 2.3 %*
Top-bottom	*37.1 ± 0.7 %*	*9.7 ±1.3 %*	*37.9 ±30.4 %*
Middle-bottom	*29.3 ± 7.5 %*	*0.2 ±0.5 %*	*33.3 ±29.5 %*

The theory corrected image shows a large reduction in the contrast between the top area, where the 'hole' was seen in the uncorrected image, and the other two areas, although the contrast has not been reduced to zero, as would be expected in a perfect correction scenario. This could be due to non-linearities in the data acquisition, or to slightly incorrect values of pathlength or attenuation coefficients being used in the exponent of equation 3.3. It may also be due to the approximations made in the correction formulation that the contributions to the signal from Compton scatter, in particular, and multiple scatter events are insignificant.

The contrast between the top 'hole' area and the middle 'Perspex' area is closer to zero in the experimental correction than in the theory correction, although the error on the

value is significantly higher (42% of the contrast value, as opposed to 9% of the contrast for the theory image). The other two values of contrast can not be considered to be statistically significant as they have a very high level of error due to the noise in the bottom area of the image.

These results suggest that if the edge effects of the holes caused by poor registration of the diffraction and transmission images are overlooked, then this division technique may have the potential to be exploited once this difficulty has been overcome.

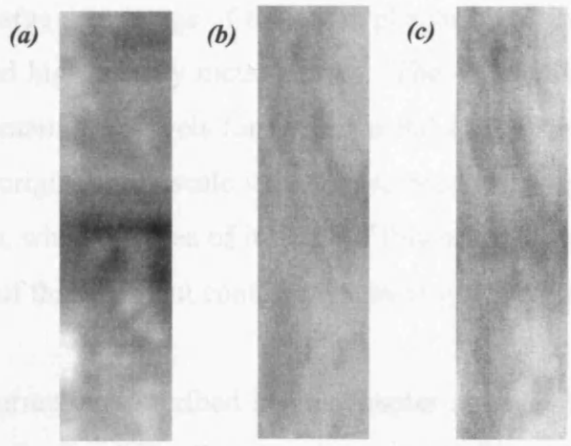

Figure 3.15 *Images of the breast tissue phantom; (a) raw diffraction image; (b) transmission image; (c) corrected diffraction image.*

3.4.6.2 Breast tissue phantom

The attenuation procedure was also used on the breast tissue phantom images, as shown in figure 3.15, but this had limited success. The figure shows the diffraction image before correction, the transmission image used for the correction and the final corrected diffraction image. It appears that the diffraction image has been 'overcorrected' using this technique, turning it into a facsimile of the transmission image. This overcorrection occurs because the grey level range of the entire raw transmission image of the region of the phantom being considered had a standard deviation equal to just 3.3% of the mean. This is a very small spread when compared to the 256 levels available to use in an 8-bit image, meaning that the section of the full transmission image used for the correction, although being originally part on an 8-bit image, contains far fewer grey levels than an 8-bit image. This small range of values means that normalising the data by dividing through by the transmission image values, as was done for the correction to the Perspex phantom data, will give very different results depending on where in the

256 available grey levels the narrow range of levels used lies; this in turn depends on the original scaling of the image by the detector. For instance, say the maximum grey level value is just five values higher than the minimum one, then if they grey level values are 250 to 255, then the ratio of the highest to the lowest is 1.02, whereas if they lie at values 2 to 7, this ratio becomes 3.5 and therefore dividing the diffraction data by these numbers results in a greater effect than dividing by the higher set.

The narrowness of the grey level range occurs due to the automatic scaling of the data collection from the transmission detector. The original transmission image, as shown in figure 3.5, was a large area image of the entire phantom and its surroundings, including low density air and high density metal screws. The acquisition system has scaled this entire image to contain grey levels for air and metal at either end of the scale and thus, only a few of the original grey scale values have been taken up by the variations in the tissues. Therefore, when the area of interest of this image is selected, it is not a true 8-bit representation of that area, but contains far fewer grey levels.

The attenuation correction described in this chapter assumes that the x-ray beam path through the tissue for the diffraction data is a straight line following the same path as the transmission image x-rays. This is obviously an approximation and leads to misregistration of the correction in the images, apart from the diffraction image of the layer of tissue closest to the detector. X-rays scattered in this layer will not be deviated from the original path by a significant amount by the time they reach the detector. For other tissue layers, the paths that the x-rays follow out of the phantom after they have passed through the scatter voxel will need to be considered more carefully for a more accurate correction to be made. Nevertheless, this is not a trivial procedure if a transmission image is to be used to obtain information for the correction, as the depth of densities that show in the image can not be found using the transmission image alone. A possible solution to this problem, requiring further work and analysis, is to use the diffraction images themselves to find the depths of the dense tissues in order to decide on the attenuation factors used throughout the final diffraction images.

3.5 Conclusions on planar diffraction imaging

This chapter has shown a diffraction imaging technique that allows several depths of a phantom to be imaged simultaneously. Diffraction images of two phantoms – one high contrast Perspex and air, and one breast tissue – were acquired and analysed for contrast enhancements compared to transmission images of the same phantoms. The corrections necessary to form an accurate diffraction image of an entire breast were also examined.

3.5.1 Collimation considerations

This work has shown that some depth information is available when imaging an object using the diffraction techniques presented here. The collimation used, as described in chapter 2 of this thesis, allowed depth information with a spatial resolution of the order of 1 cm to be collected for voxels that are approximately 1 mm square in the other two ordinates. Finer collimation would allow data to be collected from voxels that are smaller in all three spatial dimensions; for instance, reducing the collimator holes from 500 μm squares to 200 μm squares reduces the voxels to approximately 400 μm x 400 μm x 6 mm in size, giving around a ten times reduction in the voxel volume. This would reduce partial volume effects and allow more depth detail to be obtained. However, it needs to be remembered that there would also be a proportionate loss in the photon flux incident on the detector per voxel, hence a compromise between the spatial resolution of the system and the acceptable signal to noise ratio for the data needs to be considered.

A number of issues must to be considered when selecting the most suitable collimation size. Firstly, if the collimation size is reduced, this also reduces the size of the scatter voxel and therefore there are fewer scattered photons to detect. The diffraction image pixel information was formed by taking an average over 20 frames of the sum of the total signal detected in the area of the L3CCD covered by a collimation hole. This reduction in the scattered photon flux would mean that if the flux incident on the phantom remained constant, more frames would have to be averaged in order achieve the same counting statistics as previously; a 10 times reduction in the scatter voxel will result in a 10 times increase in the number of frames that should be averaged.

Secondly, reducing the size of the collimator hole also reduces the area of the L3CCD integrated over to form the diffraction image pixel data. This means that data is obtained from fewer pixels and any non-uniformity in individual pixel responses, for instance due to bad pixels or thermal noise variations, will start to play a role in the resulting data from the sensor. Reducing the hole size from 500 μm square to 200 μm square has the result of reducing the number of pixels contributing to the diffraction data point from 416 to 66. Nevertheless, this number of pixels should still be large enough for the non-uniformity factor to play just a minor role if the collimation holes are reduced to 200 μm squares.

Finally, a more practical problem associated with finer collimation is an increase in the difficulty of aligning the collimation for the experiment. These experiments were performed at a synchrotron radiation source, where access to the beamline is limited to a few days at a time. This extra alignment time, when coupled with the increase in acquisition time required when using finer collimation, may hinder the quality and quantity of the data acquired during the experimental period and therefore becomes a major consideration when analysing the optimal collimation requirements of the system.

3.5.2 Image viewing possibilities

Ideally, the imaging technique used for these experiments could eventually be modified for use in conjunction with a standard digital mammographic x-ray unit by scanning the x-ray source and detector, rather than the object being imaged [Kidane, 2000]. This combined system would allow clinicians access to high spatial resolution transmission mammograms and lower spatial resolution, but significantly higher contrast, diffraction images of the breast. The use of an array of holes in the collimation used in the experiments in this chapter has led to diffraction images of planes at different depths within phantoms to be formed. This third dimension is not available to planar transmission mammography and so may be utilised by a clinician for clearer location of lesions within the compressed breast with a view to biopsy and surgical guidance. This third dimension also brings visualisation and image viewing issues to the forefront as the clinician would need to compare a 2-D high spatial resolution conventional transmission image with several different 3-D high contrast diffraction image slices.

3.5.3 Attenuation correction

This chapter has described work done to analyse the corrections that must be carried out on the detected signal for planar diffraction imaging in order to obtain the pure diffraction signal related to the scatter volume of interest. It was shown that the Compton scatter and multiple scatter contributions to the signal were small compared to the coherent scatter signal and therefore the most significant correction is that which takes into account the attenuation of the x-ray beam as it passes through the phantom.

This correction was shown empirically on a diffraction image of a simple high contrast phantom using attenuation data obtained from a database for the materials present in the phantom. This was shown to give good results and so the correction was then implemented practically by dividing the diffraction image through by a transmission image of the phantom which was assumed to be proportional to the intensity of the x-ray beam after attenuation by the phantom. This was successful for the simple high contrast Perspex and air phantom, but highlighted some data acquisition problems when implemented for the low contrast breast tissue phantom image; mainly that the number of grey levels present in the transmission image of the area of the phantom under examination was not sufficient to allow a good correction to be obtained due to automatic scaling of grey levels by the detector system used.

Further work would be needed to ensure that the scaling of any transmission image used in future is adequate for the purpose of correcting the diffraction image for attenuation. Nevertheless, this chapter also indicated that an attenuation correction may not be necessary for good visualisation of the scatter properties of breast tissue phantoms. This is for the same reason that the grey level range in the transmission image was poor; the attenuation coefficients of different soft tissues in the breast are very similar, resulting in a near uniform intensity in the x-ray field as it passes through the breast. This means that there will be only a slight variation in the attenuation properties across the image, compared to a large variation in the scatter properties.

Although an attenuation correction is required for separating out the 'pure' diffraction signal from the detected signal, it is not clear whether it will aid clinicians in diagnosis using diffraction images, as it can both increase and decrease the resolution of a

diffraction image depending on the momentum transfer value used. Figure 1.8 showed the attenuation corrected diffraction signatures of normal and cancerous breast tissue. Normal tissue peaks at 1.1 nm^{-1} whereas carcinoma shows a peak at 1.6 nm^{-1}. Carcinoma is denser than normal, fatty breast tissue and so attenuates x-rays more strongly. This means that if the attenuation correction were to be removed from the signatures in figure 1.8 then the plot for carcinoma would be lowered, thus reducing the contrast between the two tissue types at 1.6 nm^{-1}, but raising it at 1.1 nm^{-1}. This analysis implies that a selective correction of the images at specific momentum transfer values could be beneficial, but fails to fully take into account the fact that the diffraction data forms images for several different depths within the tissue, each of which may contain different tissue types.

CHAPTER 4

Micro-Computed-Tomography and diffraction signatures of small tissue sections

4.1 Introduction

The previous chapters of this thesis have introduced the DEBI principle and presented a study to show how the technique would work in a scanning mammographic system. This demonstrated that a much higher soft tissue contrast is available using DEBI techniques than in transmission mammography techniques. One of the research tracks highlighted in the first chapter was the need for further investigation of the composition of the tissue samples used to create the diffraction signature database. Human breast tissue is inhomogeneous by nature and so large samples will almost certainly contain more than one type of tissue. Databases of diffraction signatures for breast tissue have previously been obtained by other workers [Kidane *et. al.*, 1999; Lewis *et. al.*, 2000; Kosanetzky *et. al.*, 1987]; however, due to the inhomogeneous nature of human tissue samples, it has proved difficult to guarantee that samples categorised as one particular tissue type contain only that tissue.

The work reported in this chapter intends to address this sample purity problem by fully imaging and analysing small, 8 mm diameter tissue samples using three micro-Computed-Tomography (microCT) systems. The first was based around an L3CCD camera and a monoenergetic synchrotron radiation source and was used for both diffraction and transmission imaging; two different L3CCD cameras were employed in this system at different times. The second microCT system was used purely for transmission imaging and made use of an amorphous silicon array to detect x-rays produced by a laboratory based quasi-monoenergetic molybdenum microfocal x-ray unit. The final diffraction system was based around an HPGe detector and a polyenergetic tungsten target laboratory x-ray unit; this system was capable of

producing full energy dispersive diffraction data for small samples, along with diffraction microCT images.

The intention of this work was two-fold; primarily it was hoped that using small samples would mean that they have a higher chance of being mainly one tissue type. The size of the samples also made them easier to image at high spatial resolution in order to segment any areas of differing tissue types for classification purposes in the analysis of their diffraction properties. Secondly, the work investigated the most suitable method and instrumentation for obtaining the diffraction information that will be used to construct microCT images.

4.1.1 Overview of diffraction measurement systems

MicroCT images of small tissue samples constructed either using transmitted or diffracted x-rays were obtained for this work. The diffraction images were obtained by two methods; one based on angular dispersive imaging at a synchrotron radiation source and the other on energy dispersive imaging using a laboratory polyenergetic x-ray unit. Both diffraction microCT systems used identical samples and sample holders. The aim of the diffraction measurements was to produce images containing high tissue contrast.

The higher spatial resolution transmission images were used for verification of, and comparison with, the diffraction images, meaning that registration between all images of the same sample was essential. The diffraction images have the poorest spatial resolution and thus create the outer limits of the registration criteria. The registration rotational error must be no worse than the maximum angular step used between views for the diffraction images, whilst the linear error needs to be no bigger than the spatial resolution of the final diffraction microCT images.

The first diffraction microCT system used a technique evolved from the planar imaging apparatus used in chapter 3 of this thesis. This was an angular dispersive diffraction system used in conjunction with a synchrotron radiation source built around the L3CCD and a parallel array collimator. For the microCT, this contained a single row of holes. The system was also used to obtain transmission microCT images by removing the

collimation and placing the camera in line with the primary radiation beam passing through the sample.

The second diffraction microCT system utilised energy dispersive diffraction techniques and used a tungsten x-ray unit. A single crystal HPGe detector was placed behind the conical collimation system described in chapter 2 (figure 2.2) and detected x-rays scattered by samples placed at the focus of the collimation in a translate-rotate CT geometry. High spatial resolution transmission images were also taken in the laboratory using a fan-beam molybdenum x-ray unit and a phosphor screen/amorphous silicon array.

4.1.2 Breast tissue samples

All of the tissue samples were stored in a locked -35°C freezer when not being imaged. Two batches of unfixed tissue samples were used for this work, both of which were collected by Professor A.M. Hanby at the Academic Unit of Pathology, St. James' University Hospital, Leeds, UK during mastectomy and tumour removal procedures. The first batch (Set A) contained eight samples and was imaged just with the L3CCD system. These tissue samples were approximately 1 cm long and were inserted into 8 mm diameter thin walled plastic tubes which were sealed at either end with plastic stoppers before being transported to UCL in dry ice. The second batch (Set B) contained nineteen samples of around 6 mm in diameter and 5 mm height. They were placed into thin plastic sleeves within a Perspex collecting array, as shown in figure 4.1(a). This array facilitated the collection of tissues by allowing clear marking of the sample numbers and by creating a fixed volume to fill with each sample. The array had thin windows made from OHP acetate, giving virtually unobstructed views of the samples. It was sealed using rubber gaskets and placed in dry ice for transport. In order to take microCT images of each sample separately, the samples and their sleeves were transferred to individual holders similar to the ones used for the first batch (figure 4.1(b)) at the Department of Pathology, University College London Hospital. These holders were sealed with a plastic plug at one end and a brass plug at the other; the reason for this choice of plug material is explained in the following section.

The brass plugs on sample set B had locating flats machined onto them so that they would always fit into the microCT sample holders in the same orientation, giving rotational registration between the transmission and diffraction images of each sample when taken with different imaging systems.

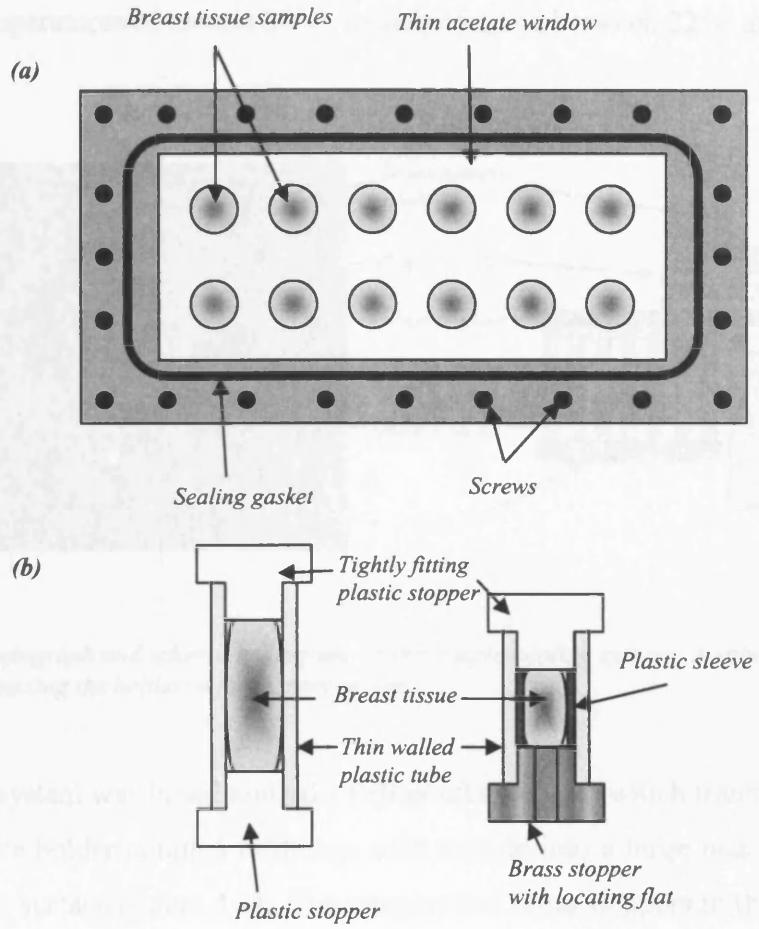

Figure 4.1 *Sample holders (a) the collecting array for set B; (b) the individual holders. Set A holders (left), Set B holders (right).*

4.1.3 Sample cooling

As mentioned in section 4.1.2, the samples in Set A were imaged before those in Set B. The imaging process meant that they were at warm room temperature (>25°C) during the imaging procedure, which took 2-3 hours in total. This step was taken in order to avoid ice crystals from being present that could alter the perceived diffraction signature from the samples. After imaging, the samples were returned to the histopathologist for examination and classification. It was noted during the pathological analysis that it was

difficult to assess the samples in detail as the cell walls and nuclei had significantly degraded during the time spent at room temperature. This fact led to the construction of a cooling system for the samples in Set B. This was especially important as Set B were to be additionally imaged using the laboratory based imaging systems. The HPGe diffraction microCT took approximately 5 hours to acquire an image and the laboratory can reach temperatures of around 30°C, usually ranging between 22°C and 27°C.

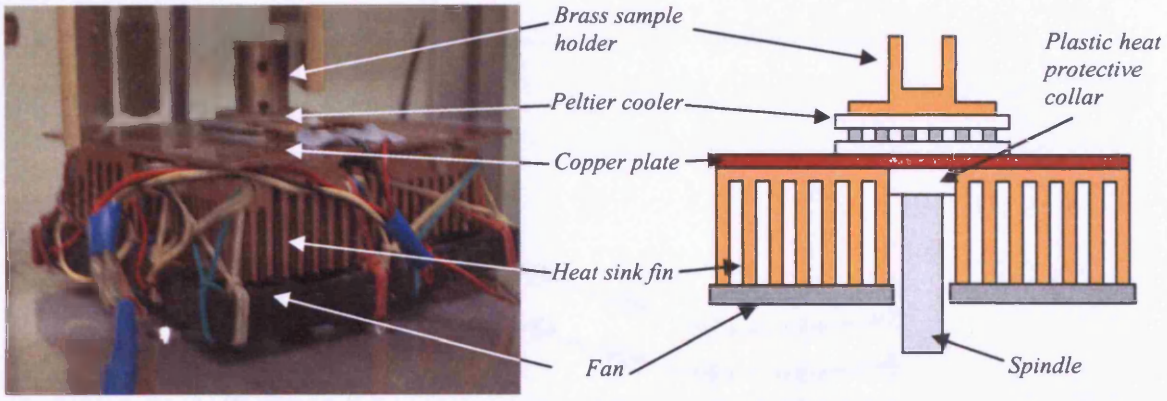

Figure 4.2 *Photograph and schematic diagram of the sample cooling system. A spindle passes through the centre connecting the holder to the stepper motor.*

The cooling system was based around a Peltier effect cooler which transferred heat from a brass sample holder coupled to its top, cold surface into a large heat sink coupled to the lower, hot surface (figure 4.2). The samples had brass stoppers in their bases (figure 4.1(b)), which fitted snugly into the brass sample holder and transferred heat away from the sample to the holder. The holder was coupled to the Peltier device (SH1.0-95-05L, Melcor Ltd. [Melcor, 2004]) using a silicone based heat sink compound. In turn, the Peltier device was thermally coupled to a forced convection air cooled heat sink. The heat sink consisted of an approximately 10 cm x 10 cm square copper sheet which had four sets of computer component heat sink fins affixed to it and coupled with heat sink compound. The heat sink fins had 12V PC fans connected to their bases which circulated air through the fins. It was found that setting up a desktop fan such that it could blow air across the entire heat sink system caused the achievable cooling temperature to rise due to the turbulence created causing warm air to pass by the cold sample holder. To ensure reliable coupling between the rotary system and the brass sample holder, the holder screwed onto an aluminium spindle which passed through the

cooling system and fixed onto the rotary system. The copper plate of the cooling system sat on a plastic collar attached to the spindle. The collar provided support for the weight of the cooling system, whilst avoiding heat conductance from the plate to the spindle and back up into the brass holder. The added weight of the cooling system meant that the microCT rotary stage stepper motor did not have the required torque to turn the system once it was in place. This resulted in a 1:25 gearbox being added between the motor and the spindle.

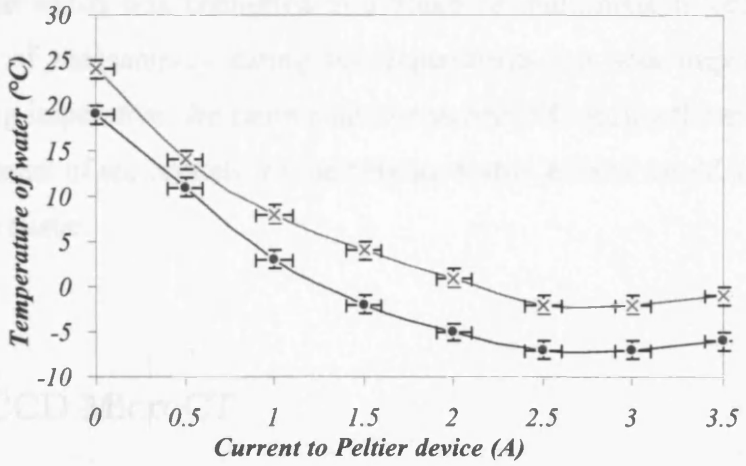

Figure 4.3 *Cooling curve of the cooling system; line marked with crosses taken at an ambient room temperature of 24°C; line marked with dots taken at an ambient of 19°C.*

The cooling system allowed stable cooling of the sample to normal refrigeration temperatures (1-4°C). Two cooling curves (Figure 4.3) were plotted by filling a sample holder, as seen in figure 4.1(b), with water and placing a thermocouple into it. The curves were measured on different days when the ambient temperature in the laboratory was different. The curve marked with the crosses was taken in an ambient of 24°C and the curve marked with the dots in an ambient of 19°C. The current to the Peltier device was raised by 0.5 Amps every five minutes and the temperature taken just before the current was adjusted for the next measurement, allowing the system five minutes to reach equilibrium for each current measurement. The curves follow a similar shape set approximately 5°C apart, which implies that the system cooling curve will always follow this shape. Therefore the expected temperature for a given amount of current to the Peltier can be found using these plots provided that the ambient temperature of the room is known. The minimum achievable temperature of the cooling system was limited by the rate of heat loss from the heat sink, which in turn was limited by the size

and cooling mechanisms of the heat sink, nevertheless it appeared adequate for the purposes of this experiment. The minimum achievable temperature occured between 2.5 and 3.0 A and for an ambient of 30°C was expected to be around 2°C. The ambient temperature of the radiation laboratory was measured to usually lie between 22°C and 27°C when the x-ray tube was in use, therefore the required temperatures of 1-2°C could be easily reached using this cooling system.

The sample holder had a small hole drilled in its side to accommodate a K-type thermocouple which was connected to a Fluke 78 multimeter in order to monitor the temperature of the samples during the experiments. It was important that, despite cooling being imperative, the sample never reached 0°C during the experiment to avoid the development of ice crystals, as their Bragg scatter effects would alter the diffraction signal of the tissue.

4.2 L3CCD MicroCT

The L3CCD system was used at the SYRMEP beamline, Elettra synchrotron radiation source, Trieste, Italy. By altering the gain of the L3CCD it was possible to use the camera to obtain both transmission and diffraction microCT images of the tissue samples.

4.2.1 Experimental Apparatus

The microCT equipment consisted of a primary collimator, rotary stage and L3CCD camera all mounted onto a 1 cm thick Dural plate for rigidity and ease of set up on arrival at the synchrotron beam (figure 4.4, [Griffiths *et. al.*, 2003]). The plate and apparatus were positioned in the radiation beam using crossed goniometers. The camera could be mounted either parallel to the radiation beam, observing it directly for transmission mode, or collimated and at an angle to the beam for the diffraction images.

4.2.1.1 X-ray source

The beamline energy was set to 18 keV, the approximate energy of a molybdenum mammographic x-ray tube, and the beamline collimators set to give a beam 2 cm wide and 2 mm high. The synchrotron radiation has a bandwidth of approximately 10 eV at 20 keV [Arfelli *et. al.*, 1995]. The storage ring electron bunch energy was 2.4 GeV, giving a maximum possible flux of 2 x 10^9 photons s^{-1} mm^{-2}. The radiation beam intensity follows an exponential decay throughout the day from the time when the electrons are injected into the storage ring and thus an ion chamber was used to monitor the beam intensity in order to be able to normalise the data within each image. As with the results in chapter 3, it was discovered that the error on the ion chamber measurements was significant. Each image acquisition took less than 30 minutes to complete, so it was decided to omit correcting the data using the ion chamber measurements.

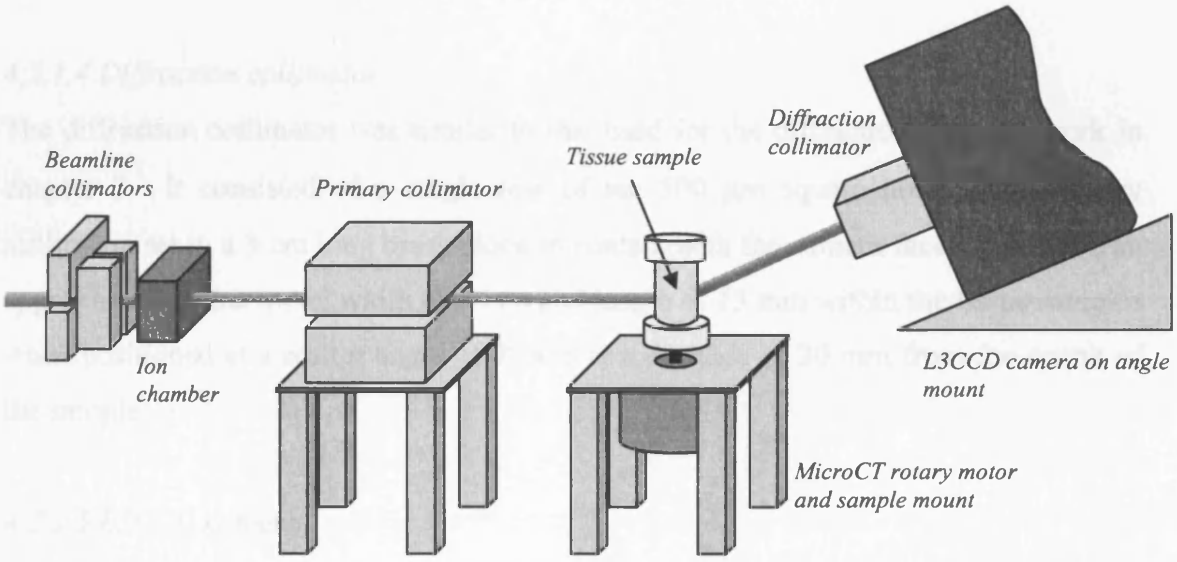

Figure 4.4 *Schematic diagram of the experimental set up. The primary collimator, rotary stage and L3CCD angled mount were all affixed to a single sheet of Dural for rigidity and ease of set-up.*

4.2.1.2 Primary collimator

The primary collimator was a 3 cm long brass block containing a 2 cm x 500 μm slit. This collimator defined the CT slice under examination by only allowing radiation to fall onto a thin section of the sample. This guaranteed correlation between the transmission and diffraction image slices provided that the sample was not removed between acquisitions.

4.2.1.3 Rotary stage

The rotary stage consisted of a stepper motor (RS product number 440-420) controlled by a PC through a compact driver card (RS 240-7920). A 25:1 gear box (RS 718-974) was also used when the sample cooling system was in place. The motor sat on a 4-screw adjustable mount that ensured alignment of the axis of rotation. The minimum step allowed by the motor was 0.9°, giving up to 400 views per 360° rotation without the gear box. The transmission microCT data sets consisted of 200 views spread over 180° taken in a direct transmission mode, whilst the diffraction CT data sets consisted of 100 views taken over 360° at a momentum transfer value of 1.1 nm^{-1}. Due to the parallel nature of the synchrotron radiation beam, the transmission images needed only to be taken over a half rotation as the images obtained between 180° and 360° would be the mirror images of those taken between 0° and 180°. The diffraction CT reconstruction technique used an emission CT treatment similar to SPECT imaging and therefore required images to be taken over a full 360° rotation.

4.2.1.4 Diffraction collimator

The diffraction collimator was similar to that used for the diffraction imaging work in chapter 3. It consisted of a single row of ten 500 μm square holes spaced every millimetre set in a 3 cm long brass block in contact with the camera face. This gave an approximate scatter voxel width of 1 mm and length of 13 mm within the tissue samples when positioned at a scatter angle of 9° and at a distance of 20 mm from the centre of the sample.

4.2.1.5 L3CCD camera

Two L3CCD cameras were used at different times for this experiment. The samples in Set A were imaged using the 160 μm Gd_2O_2S:Eu coated camera (CCD65-02 [Harris, 2002]) used in the previous chapters, whilst the samples in Set B were imaged using a camera fitted with an optical fibre stud coupled to a 95 μm thick structured CsI scintillation crystal. The reason for the use of two cameras was due to the failure of the first camera (CCD65-02). The second camera was the CCD65-01 chip previously characterised at UCL [Harris *et. al.*, 2001]. This camera was modified to allow cooling to 0°C by placing it in a dry nitrogen filled container with a thin plastic x-ray window [Nishibayashi, 2004]. The gain of both cameras was 35 for the diffraction images and 5 for the transmission images.

4.2.1.6 Camera and collimator mount

The region of momentum transfer space investigated by this apparatus could be altered by adjusting either the energy of the synchrotron radiation or the angle of the L3CCD and diffraction collimator with respect to the incoming radiation beam. The mount allowed a range of angles from 0° (transmission images) to 10°. The diffraction collimator and L3CCD camera were placed at an angle of 9° with respect to the pre-sample radiation beam. At a photon energy of 18 keV this gave a momentum transfer value of 1.1 nm^{-1}. As discussed previously in section 1.3.2, this momentum transfer provides a large difference in scatter intensity between fatty, normal and cancerous tissues. The mount and diffraction collimator could be removed without disturbing any other portion of the experimental set-up, thus allowing the camera to take either transmission or diffraction images of the same slice within the sample under investigation.

4.2.2 Experimental Procedure

The samples in Set A contained approximately 1 cm high portions of tissue in 8 mm diameter thin walled plastic cylinders. Due to time constraints at the synchrotron, it was only possible to image one 500 μm slice of this 1 cm height. Pre-selection of suitable tissue slices for the experiment was thus carried out in the laboratory at UCL. A microCT system using a microfocal x-ray source (X-Tec Systems Ltd., Hertfordshire, U.K.) and a dPix/Varian am-Si array (Kodak systems/Varian Inc., U.S.A.) was set up for this purpose [Speller and Royle, 2003]. Slices were chosen on the basis of them appearing to contain several different tissue and air components in order to fully test the capabilities of the diffraction system.

The samples in Set B were 5 mm or less in height and the pathologist stated that it is unlikely that the tissue types in the samples will vary significantly over a distance of a millimetre or so [Hanby, 2004]. These facts meant that slice selection for these samples was random, but remained constant throughout all imaging modalities as all of the sample holders had fixed dimensions.

4.2.2.1 Imaging Procedure

The L3CCD cameras operate at TV rates and were controlled via a National Instruments DAQ card by a PC running LabView which stores images as 16-bit tiff files. The bit depth is stretched for tiff format as the digital CCD65-02 is 12-bit, whilst the analogue output CCD65-01 is 8-bit. The acquisition parameters for the two experiments are given in table 4.1. The chip temperature was monitored throughout the experiments as a change in temperature results in a change in the avalanche gain of the chip of approximately 10% for every 1°C [Harris, 2002]. The diffraction image pixels are the same size as the collimator holes (500 μm x 500 μm), whilst the L3CCD pixels are 20 μm x 30 μm. This difference in size between the camera pixels and the required resolution of the image allowed on-chip pixel binning to be used which gave a higher signal to noise ratio for a fixed integration time. The transmission microCT images were formed from 200 views taken over a 180° rotation of the sample; the number of views was limited for Set A by the minimum step of the rotary stage motor. Rotation past 180° was not necessary when working at the beamline as the radiation beam is parallel. The diffraction microCT images were formed from 100 views taken over a 360° rotation. A full rotation was needed for these images as they should be considered as a type of emission CT, rather than of transmission CT. The number of frames integrated for the transmission images of Set A was high as a significant amount of filtration (3 mm Al) had to be placed in the beamline to reduce the intensity reaching the L3CCD, thus avoiding camera saturation. The filtration is an automated system, which meant that the thicknesses inserted into the beam were fixed and thus a thickness allowing a slightly shorter integration time could not be used.

Table 4.1 *L3CCD acquisition parameters for the two sets of data.*

Acquisition Parameters	***Set A***		***Set B***	
	Transmission	*Diffraction*	*Transmission*	*Diffraction*
Camera Gain	*5*	*35*	*5*	*35*
Camera Offset	*4.91 V*	*4.91 V*	*4.91 V*	*4.91 V*
Chip Temperature	*-5°C*	*-5°C*	*0°C*	*0°C*
Pixel Binning	*none*	*3 x 1*	*none*	*none*
Views Taken	*200 over 180°*	*100 over 360°*	*200 over 180°*	*100 over 360°*
Number of frames integrated	*175*	*40*	*255*	*255*

Dark and flat transmission fields were taken with the L3CCD gain set to the value to be used for the transmission microCT. Five of each field were taken and the average of these five used for the image correction procedures. The samples were then placed at the centre of rotation of the rotary table and the previously marked slices of interest for Set A lined up with the primary collimator slit using a laser. Once in place on the table, the sample was not moved (apart from by the rotary table itself) until the end of the acquisition of both the transmission and diffraction images, ensuring complete correlation of the CT slice under examination. After the diffraction CT data had been taken, the sample was removed from the apparatus and dark and flat fields obtained at the camera gain value used for the diffraction imaging. The diffraction flat field was formed using a 1 cm thick uniform sheet of Perspex as a scatterer placed on the axis of the rotary table. Five of each of these fields were also taken and the averages used in later corrections.

4.2.3 Corrections to the raw L3CCD images

As mentioned in section 4.2.1.1, due to the inaccuracy of the ion chamber measurements, the data was not corrected for the drop in beamline flux throughout the day from beam injection time. The images were acquired for each CT in less than half an hour and it was decided that the flux would not have dropped significantly within that time. Each transmission and diffraction image was corrected for pixel non uniformities by subtracting the dark field and dividing by the flat field. Beam hardening effects did not have to be considered for the transmission images as the synchrotron beam is virtually monoenergetic.

4.2.4 Reconstruction algorithms

All reconstructions were carried out using algorithms written in IDL [Speller, 2003(a); Pani, 2005]. The diffraction data raw images from the L3CCD camera resembled that in figure 3.4; they were a single row of ten collimator holes. The algorithm used a mask to select these ten regions of interest and find their mean values. An eleventh ROI was again also selected to monitor the L3CCD avalanche gain (see §2.4.1.1). The values

taken from the ten ROIs were expanded to represent 100 data points and used to create an emission CT sinogram. This was then used to form the diffraction microCT image. An attempt was made to shift the collimator by 500 μm to fill in the gaps blocked by the septa but this proved unreliable for Set A.

4.3 Laboratory Based Transmission MicroCT

Transmission x-ray microCT images of the samples in Set B were also taken using a laboratory based imaging system [Bohndiek, 2004]. These high spatial resolution images were used to correct the laboratory based diffraction images for self-attenuation of the scatter signal by the sample and also for accurate segmentation of the samples for further analysis of their diffraction signals.

4.3.1 Experimental apparatus

A microfocal molybdenum x-ray unit was used in conjunction with a PaxScan amorphous silicon array imager (Figure 4.5). The images acquired use a fan-beam magnification imaging technique to give a high spatial resolution projection of the sample onto the imager.

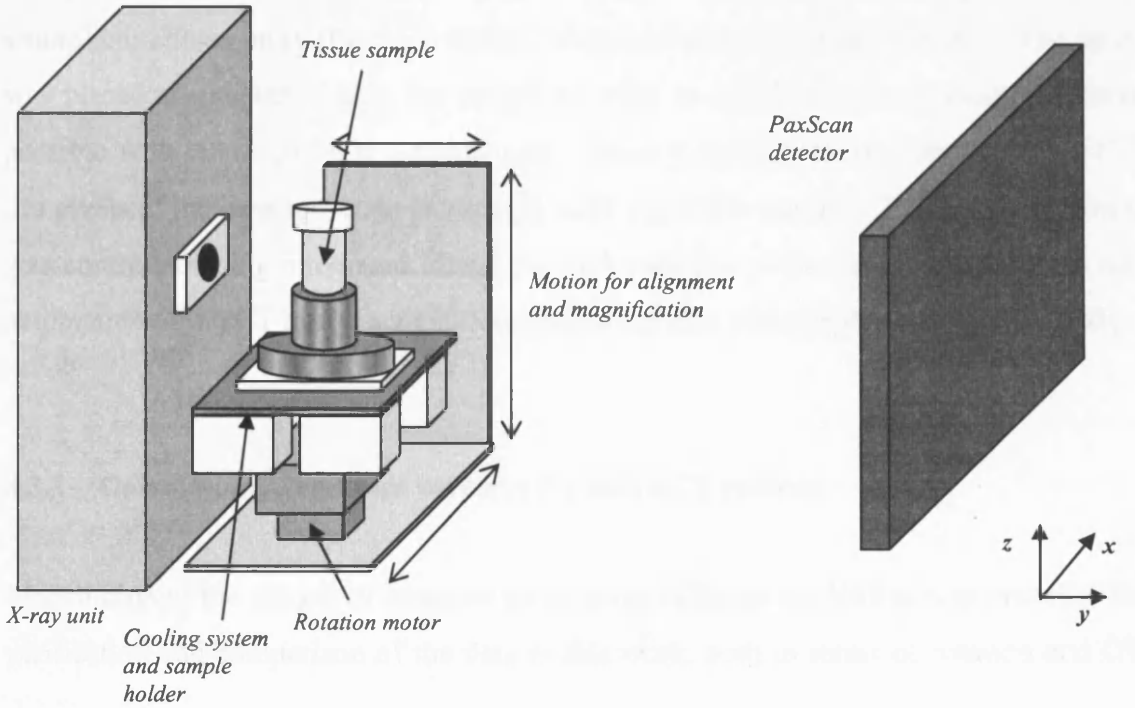

Figure 4.5 *PaxScan transmission microCT apparatus.*

4.3.1.1 X-ray source

The x-ray source used was a molybdenum target and filter, high-power, water-cooled rotating anode microfocal source (XTec systems Ltd., U.K.) operating at 30 kV and 0.2 mA. The source spectrum is quasi-monochromatic, giving an effective energy of 17.4 keV. The focal spot is 15 μm in size and the unit offers around ten times the output of other units with similar sized focal spots. The small spot size allowed high levels of magnification to be achieved with minimal penumbral effects. A magnification of approximately 6 was used for the transmission microCT.

4.3.1.2 Sample mount

The sample cooling system and holder, along with the rotational stepper motor, compact driver card and 25:1 gear box was placed on a right-angle mount that allowed movement along all three axes, giving motion across the face of the x-ray tube (x and z) and allowing variation of the magnification used (y axis). The position of the mount was set such that the slice of interest of the sample lay at the position in the x-ray beam where the beam was perpendicular to the imaging array. Images of the sample were taken at 0.9° intervals over a total rotation of 210°. This angle corresponds to a half rotation of 180° plus the 30° x-ray fan beam angle [Bohndiek, 2004].

4.3.1.3 Imaging array

The projection images of each view of the sample were collected using a pixellated amorphous silicon array (PaxScan 4030R, Varian Medical Systems., U.S.A.). The array was placed at a distance from the sample in order to exploit the magnification effects possible with the microfocal x-ray source. The 6 x magnification meant that the 127 μm pixels of the detector relate to a length of 21 μm at the sample. The data acquisition was controlled using integrated FlashScan and LabView software set up such that full automation of the CT image acquisition procedure takes place [Speller & Royle, 2003].

4.3.2 Correlation of samples between the microCT systems

Registration of the images of a sample taken using different modalities was essential for verification and comparison of the data in this work, both in terms of rotation and CT

slice height. This meant that the orientation of a sample within the experimental set-ups needed to be known at all times during the imaging procedures.

The front collimation of the L3CCD based system defined the CT slice being imaged in both the transmission and diffraction modes of the apparatus by only allowing radiation to be incident on a 500 μm high portion of the sample (Figure 4.4). Rotational registration of the L3CCD diffraction and transmission images of each sample was assured by taking the diffraction and transmission images during the same experimental session and not moving the sample between the end of one imaging procedure and the beginning of the next. Diffraction CT images required a full 360° rotation of the phantom, whilst transmission CT needs just 180° as the synchrotron beam can be considered to be parallel. The sample holder was rotated by 180° after each transmission image in order to set it in an identical rotation position for the next acquisition.

The laboratory based imaging was carried out on two separate systems and so accurate positioning of the sample when placed in both systems was necessary to ensure ease of registration of the reconstructed microCT images.

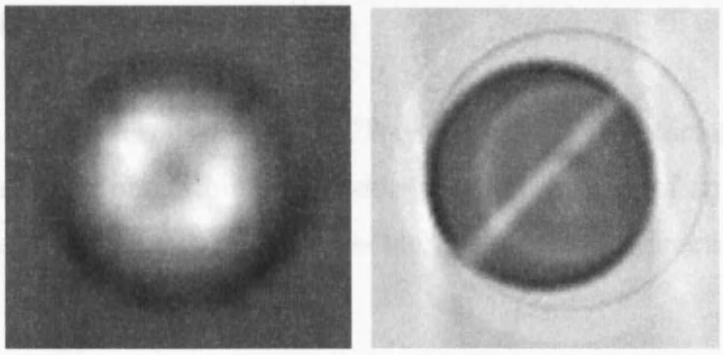

Figure 4.6 *MicroCT images of a Perspex rod with a 1 mm diameter air hole drilled through the centre; uncorrected diffraction (left); transmission (right).*

Due to its collimation, the HPGe diffraction microCT system was only capable of viewing one 1 mm slice of the sample at any one time, whilst the PaxScan transmission system acquired images of the entire sample. This meant that the CT slice of interest in the HPGe diffraction images needed to be reliably identified in the transmission image. The stoppers and sleeves of all sample Set B's individual sample holders were of identical dimensions, therefore the middle of each tissue sample was placed at the same

height from the base of the brass stopper. A Perspex rod with a 1 mm diameter hole drilled through it at the height of the required diffraction CT slice was used to verify the slice correlation between the two microCT systems. The images of the rod taken by both systems are shown in figure 5.2. The 1 mm air hole can be seen to cut all the way through the images, thus also verifying the flatness of the microCT rotary tables with respect to the plane of the x-ray beams.

An alignment pointer with a location flat machined into its base was designed to ensure rotational registration between the HPGe and dPix microCT systems. The pointer was held in position in the sample holder by a grub screw pressed tightly against the flat and the holder was then rotated until the pointer was in contact with a fiducial marker. The power to the CT rotation stepper motor was then turned on, gripping the sample holder in position to give an identical starting point for each microCT procedure. Each of Set B's sample holders had a flat machined onto its bottom stopper, allowing the sample to be imaged on both laboratory systems starting with the same view. This registration removed rotational ambiguities when aligning the laboratory transmission and diffraction images of the sample.

4.3.3 Experimental procedure

The laboratory based transmission microCT system was fully automated and used fan beam magnification to obtain high resolution microCT images of small samples. In order to achieve the best image quality possible, the system was precisely aligned prior to use.

4.3.3.1 System alignment

In order to prevent distortion of the final images, it was important that the samples were placed in the x-ray beam at the point where the beam was perpendicular to the face of the amorphous silicon array. The pixel where this perpendicular beam axis lay was found by imaging a long thin metal plate placed parallel to the y-axis of the beam. The metal was first placed horizontally and moved in the z-direction until the image of the end-on sheet was as thin as possible in the z-axis. The position of the centre of the metal in this image was then noted and the same procedure was carried out in the x- axis

with the sheet placed vertically. All further images were then centred on this identified pixel and thus were coincident with the beam centre with respect to the flat imaging array.

The flatness of the microCT rotary table was checked by rotating a pin placed at the edge of the sample holder. The table was considered to be flat in all directions when the head of the pin remained level with the height of the beam centre for a full rotation of the sample holder. The flatness was also checked by taking a microCT image of a Perspex rod with a 1 mm hole drilled through it in the plane of the beam axis (figure 4.6).

As discussed in section 4.3.2, the samples were rotationally aligned by lining up a pointer with a marker and then replacing the pointer with the samples, whose base stoppers incorporated a location flat.

4.3.3.2 Imaging procedure

The sample cooling system was switched on 5 minutes prior to the sample being placed in the holder in order for it to cool down. After rotational alignment of the sample, the LabView based automated microCT procedure was commenced. The microCT virtual interface (.vi file) controlled the rotation of the motor and the storage of the region of interest of the image acquired by the PaxScan's FlashScan software [Speller and Royle, 2003]. The region of interest selection was necessary as the 30 cm x 40 cm active imaging area of the array produced a 14 MB image file, most of which was superfluous to the needs of imaging a phantom less than 1 cm in diameter. The PaxScan averaged the signal for 3.5 s for each view of the sample and dark fields were acquired for automatic image correction by the software. Flat fields were also taken for correction during the reconstruction of the microCT images.

In a parallel x-ray beam geometry, views of the sample need only be acquired for a 180° rotation of the sample as the view at 180° is identical to the view at 0° flipped around the axis of rotation and so on for all view between 180° and 360°. This exact half rotation symmetry does not hold for a fan beam geometry. In this case, the angle of rotation is equal to 180° plus the angle of the fan beam. An interpolation method is then

used during the reconstruction process to create a virtual parallel-beam data set. This means that images need not be taken for an entire rotation of the sample. It was found for this system that a 210° rotation would be sufficient; therefore 234 views taken 0.9° apart were acquired. After each full microCT acquisition, the sample holder was rotated back to the starting position to ensure that the rotational alignment of the samples was maintained. The transmission microCT images took approximately 25 minutes to acquire for each sample.

4.3.4 Reconstruction algorithm

A filtered back-projection reconstruction algorithm was developed in IDL by the Academic Radiation Physics Group at UCL for the correction and reconstruction of the transmission CT data [Speller and Bohndiek, 2004]. Corrections for the fan-beam geometry, beam-hardening and geometric beam profile were taken into account by the algorithm.

The reconstruction software firstly read in all of the images of the microCT data set in the order in which they were acquired and divided them through by an averaged flat field formed from five flat images. Any variations in the x-ray flux collected for each image were then corrected by normalising the images using the pixel values at their edges that were associated with the air surrounding the sample. A sinogram proportional to the attenuation properties of the sample was then formed by taking the natural logarithm of the appropriate slice of the projection images. This sinogram was then modified to take account of the fan-beam geometry of the system by interpolation over a fan for the *x*- and then the *z*- axes. The region of this new sinogram that contained the image data was selected and filtered, firstly to remove ring artefacts and then with a Shepp-Logan filter to create a viewing quality CT image. A radon back-projection was then carried out, creating a 400 x 400 pixel tomographic image of the data.

4.4 HPGe Diffraction MicroCT

The HPGe diffraction microCT system allowed full diffraction signatures to be obtained at a fixed scatter angle using an Energy Dispersive X-Ray Diffraction System (EDXRDS) technique. The ability to resolve the energy of the x-ray photons meant that a full spectrum of momentum transfer values could be imaged simultaneously.

4.4.1 Experimental apparatus

The HPGe based diffraction microCT used a rotate-translate system to image the samples (figure 4.7) [Riviere, 2004; Whish, 2004]. The scattered photons were detected by a High Purity Germanium (HPGe) detector. This detector has excellent energy resolution properties, but no spatial resolution capabilities. This meant that in order to form an image of an object using this detector, the pixels in the image needed to be generated by scanning the object through a highly collimated beam of x-rays, where the collimation defined the available pixel size. The front plate of the diffraction cell created the pixel defining collimation for this experiment and the sample was moved through the collimated beam to create the image.

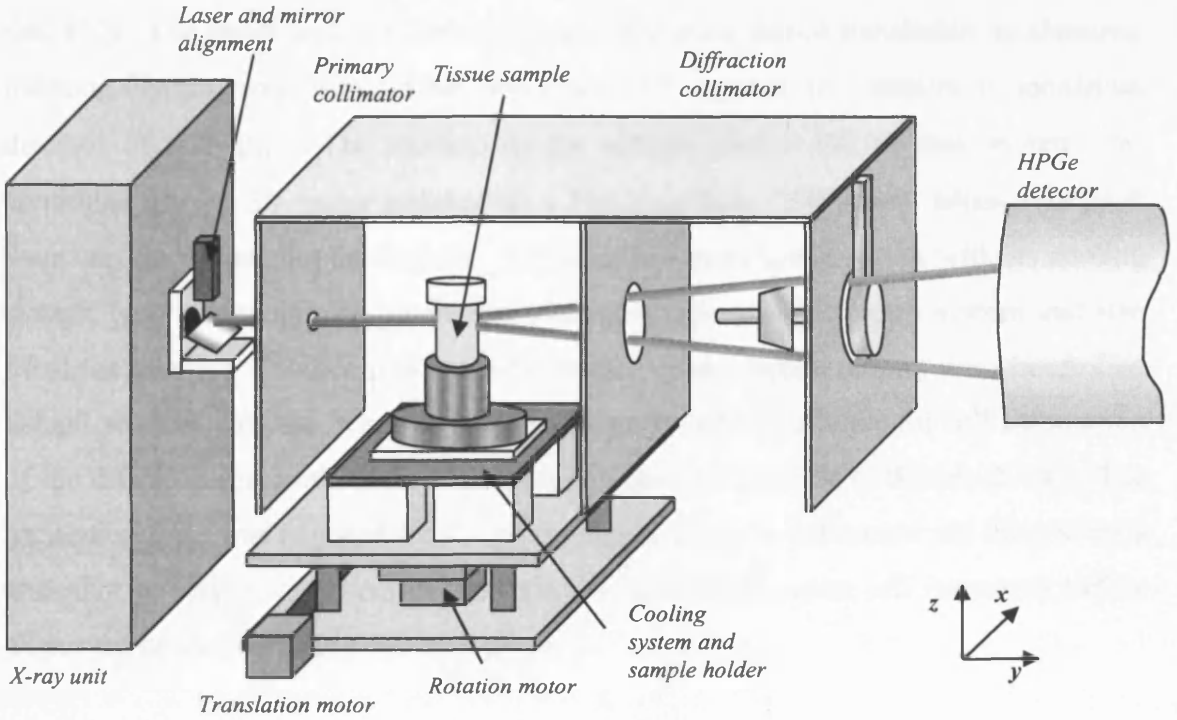

Figure 4.7 *HPGe diffraction microCT system.*

4.4.1.1 X-ray source

The x-rays were produced by a tungsten target x-ray unit (HS-MP1, AGO) operating at 70 kV and 10 mA. The focal spot size of this unit is 3 mm x 3 mm, making it unsuitable for high spatial resolution transmission measurements. The x-ray beam lay parallel to the experimental optical bench and passed through a 1 mm diameter circular collimator as it left the unit. The beam centre lay behind the collimator. A small diode laser and mirror were placed such that the laser beam was in line with the centre of the x-ray beam in order to facilitate preliminary set up of the experimental apparatus.

4.4.1.2 Diffraction Cell

The fundamental element of the experimental set-up was the diffraction cell. As described in Chapter 1, the cell defined both the volume from which the scatter signal originated and the angle at which the photons needed to scatter in order to be detected. The alignment of this cell with the incident x-ray beam and the sample position was crucial to the momentum transfer resolution and counting statistics of the experiment and will be discussed in section 4.4.2.

4.4.1.3 Automation

The sample translation was controlled using a 12 V stepper motor (RS product number 440-420). The motor was attached to the end of a screw thread translation mechanism, meaning that the motor's minimum step size of 1.8° equated to a minimum translation distance of 6.25 μm. The rotation of the sample holder and cooling system was controlled using a 5V motor attached to a 25:1 gear box. 200 views, taken over 360° were used to reconstruct the images. The sample was mounted, along with its cooling system, onto an aluminium spindle that allowed coupling to the rotary system and also lifted the required CT slice into the x-ray beam. Both stepper motors were controlled using LabView software linked to Maestro data acquisition software for full automation of the diffraction microCT data collection process [Riviere, 2004; Whish, 2004]. The translation table was adjusted for CT slice flatness using an off-centre pin imaged by a phosphor screen/CCD camera in transmission mode (diffraction cell removed) before alignment of the diffraction cell took place.

4.4.1.4 Detector

The scattered x-rays were detected by a High Purity Germanium detector (GLP 16260/13-P-S, EG&G Ortec, U.S.A.). The detector operated at -1500 V and the signals were fed through an amplifier (855 Dual Spec Amp, EG&G Ortec, U.S.A.) into a Multi-Channel Analyser (MCA) (921 Spectrum Master, EG&G Ortec, U.S.A.), which was controlled by a PC running Maestro acquisition software. The MCA had a 'handshake' facility which allowed control signals to be sent to, and received from, other equipment.

4.4.2 Diffraction cell alignment

A schematic of the diffraction cell was shown in figure 2.2. The cell consisted of three 0.5 mm thick brass plates fixed perpendicularly to a base plate. The first plate had a 1 mm diameter hole through it, which defined the pixels used to produce the views of the sample. The sample lay behind this plate, and the middle and rear plates, along with the angled nut on the spindle attached to the rear plate, defined the solid angle through which the photons needed to scatter in order to be detected by the HPGe detector placed behind the cell. The nominal angle of the diffraction collimation was 6° and it focussed to a point 5 mm behind the front plate of the cell. The angled nut on the spindle could be moved back and forth to change the acceptance angle of the scatter. The cell was mounted on micrometer gauges that allowed movement in the *x*-, *y*-, and *z*-axes (see figure 4.7 for axis orientation) and rotation parallel to the experimental bench; rotation perpendicular to the table was obtained by placing spacers between the micrometers and the cell.

4.4.2.1 Cell alignment with the x-ray beam axis

Initial rough alignment of the diffraction cell was done by moving the micrometer gauges until the laser beam that ran along the axis of the incident x-ray beam went through the hole in the front plate of the cell and hit a small well drilled into the centre of the diffraction collimator spindle. The back plate of the cell, which holds the spindle, was then removed and a CCD camera imaging a phosphor screen was placed behind it. The front plate was then removed and an image of just the hole in the centre plate was taken. The micrometer gauges in the *z*- and *x*- axes were then adjusted until the beam profile across this hole was uniform, meaning that the cell was in line with the focal

spot of the x-ray source. The front plate was then put back in place and an image of the pinhole in that plate obtained. The entire cell was then rotated both parallel and perpendicular to the experimental bench until the centres of these two images were aligned. When the centres of the images were aligned, the central axis of the cell was considered to be running parallel to the x-ray beam. The back plate, along with the spindle and nut, was then replaced and the CCD camera exchanged for the HPGe detector.

The next alignment task was to ensure that the scatter angle accepted by the collimation was uniform for all points around the subtended cone. This was done by exploiting the fact that any given value of momentum transfer has a unique energy that it corresponds to provided that the angle of scatter is constant, as we wish to be the case for these measurements (see equation 1.5). This meant that if the diffracted x-rays from a material with a well defined scatter peak are observed, the energy the peak appears at in the system should be constant, regardless of the portion of the solid angle subtended by the collimation that we are looking at. Any variation in the mean energy of the peak as parts of the collimator are masked off implies that the scatter angle varies around the collimator circumference. Variations in the peak intensity and FWHM were used to indicate variations in the acceptance angle of the collimation.

A 1 cm diameter cylindrical PTFE scatterer was placed at the approximate focal point of the diffraction collimation and the cell moved back and forth in the y- direction until the maximum scatter signal was achieved. A lead mask that allowed x-rays to pass through only one quadrant of the back plate was then placed around the collimator's spindle. PTFE scatter spectra were then obtained for four quadrants of the collimator: top, bottom, left and right. Spectra for opposing quadrants were compared and the variation of the peak energy between each pair of spectra analysed in order to find out the angle by which the collimator's spindle needed to be moved.

When the collimator was collecting scatter over all four quadrants, the PTFE spectrum was found to peak at 31.0 keV. Assuming a nominal angle of 6° for the collimation, this gives a momentum transfer value of 1.3 nm^{-1}. At this value of momentum transfer, a 0.5° change in scatter angle corresponds to an approximate change in peak energy of 2.5 keV. The collimation spindle was adjusted by placing layers of aluminium foil

between it and its mounting plate until the variation of the mean peak energy over the four quadrants was 0.34 keV, giving an angular variation of 0.05°. The precision of the machining of the collimator is 0.02 mm. It was assumed at this point in the alignment process that the collimation had been aligned as precisely as possible within the errors occurring due to the machining of the individual parts.

4.4.2.2 Defining the acceptance angle of the collimation

The scattered x-rays were collected by the detector from a volume of space defined by the concentric cones formed by the rear diffraction collimation of the cell and the 1 mm diameter hole in the front plate of the cell. The *y*-axis length of this volume, and also the acceptance angle of the collimation, could be changed by winding the angled nut along the collimator's spindle. The *y*-axis bounds of the scatter volume were found by moving a 500 μm plastic filament along the axis. It was found that the scatter volume was approximately 12 mm in length. The samples under investigation were 10 mm or less in diameter, so the volume length was more than is required, however it was used in order to maintain the counting statistics of the system; reducing the volume length would also means reducing the acceptance angle of the collimation, thus reducing the flux of scattered photons reaching the detector.

Using geometric techniques and assuming a perfect collimation system, a scatter volume length of 12 mm corresponds to an acceptance angle of 0.53°, which at a scatter angle of 6° and a momentum transfer value of 1.3 nm^{-1} gave an error on the measured energy of around 2.6 keV.

4.4.2.3 Verification of diffractometer performance with published data

Finally, the system was used as a diffractometer to collect spectra of known substances. These were compared with published data and also used to give an estimate of the resolution of the system. When grains of sugar suspended on sticky tape were placed in the system, it was found that the peaks in the spectrum moved when the crystals were moved, leading to the inference that we were looking at the scatter spectrum from individual crystals. These peaks are known to be well defined and narrow, and so were used to give an estimate of the resolution of the system. The average FWHM of the peaks was 1.55 keV; the FWHM of the HPGe detector using the 60 keV line of ^{241}Am is 0.58 keV.

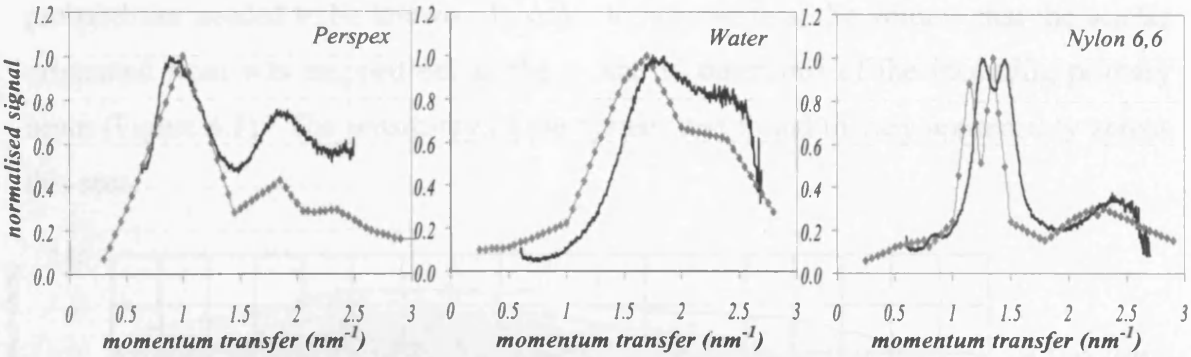

Figure 4.8 *Results from the UCL microCT system when used as a diffractometer (plain line) compared to results by Kosanetzky et. al., 1987 (marked line).*

Figure 4.8 shows the spectra obtained for Perspex, water and nylon 6,6 compared to data obtained by Kosanetzky *et. al.* [1987] using a powder diffractometer. The comparison data by Kosanetzky had been corrected by the authors to take account of the spectral shape of the beam, sample self-attenuation and other gain and conversion factors due to the apparatus used. The double peak of the nylon scatter signature could be clearly seen in the UCL microCT diffractometer results, giving confidence in the momentum transfer resolution of the system. The corrections used to obtain the final UCL spectra are explained in section 4.4.6. Both sets of results were normalised for plotting in figure 4.8 such that their maximum values were both unity. Variations in the positions of features in the plots are thought to arise mainly due to errors on accurately plotting the comparison data as it was copied from small plots in a scientific journal.

4.4.3 Sample alignment

The volume in space that the scatter was collected from was defined by the diffraction cell. The cylindrical primary beam entered the cell by passing through the 1 mm diameter opening in the front plate. The rear plates and the spindle defined a small solid acceptance angle. Only x-rays that scattered within the region where this conical angle and the cylindrical primary beam intersected, and then continued to travel within the solid acceptance angle reached the detector. The probability of a scattered photon reaching the detector also depended on where within the scatter volume it originated from. Photons from the centre of the volume had a higher probability than those near the edge of the volume. This meant that in order to achieve the highest count rates for

the experiment, the position of the scatter volume and the areas of low and high scatter probabilities needed to be known. In order to achieve this, the volume that the scatter originated from was mapped out in the *x*- and *y*- directions of the incoming primary beam (Figure 4.9). The sensitivity of the system was found to vary appreciably across this area.

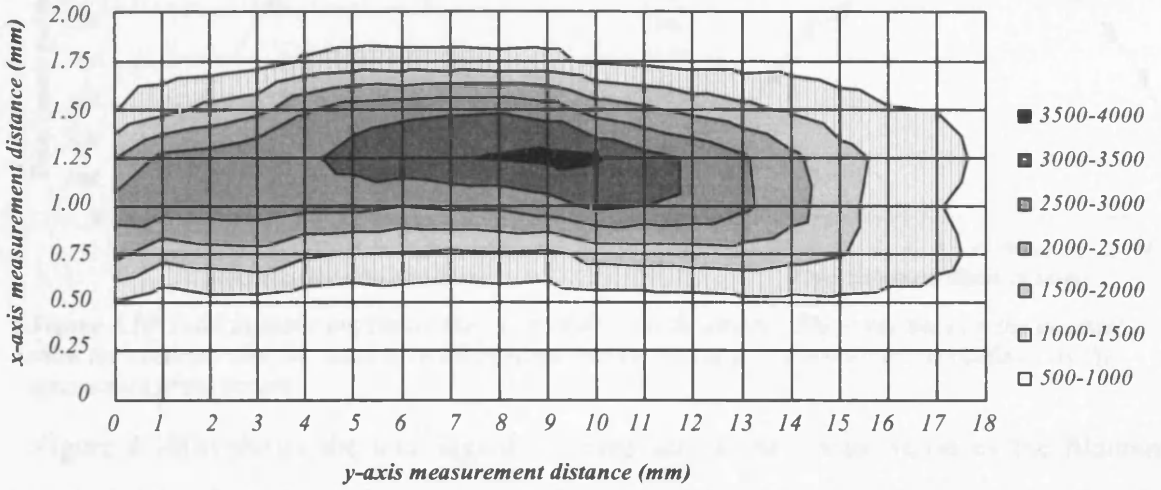

Figure 4.9 *Map showing intensity of scatter throughout the scatter voxel.*

Preliminary scatter measurements using a 500 μm diameter plastic filament were carried out to find the approximate bounds of the scatter voxel and then the sensitivity of the assumed voxel was mapped out by moving the filament around it in a grid formation. The grid was 9 measurements wide, taken 0.25 mm apart in the *x*- direction (covering 2 mm) and 19 measurements deep, taken 1 mm apart in the *y*- direction (covering 18 mm). The x-ray tube was set to 70 kVp and 10 mA and the number of x-ray counts detected by the HPGe in a 60 s live time lying within an energy range of 20 – 31 keV was noted for each position. The resulting intensity map is shown in figure 4.9; dark areas indicate high scatter intensities and lighter areas low intensities. The background measurement (no filament in place) was approximately 645 counts per minute.

The plots in figure 4.10 show the summed counts for lines taken parallel to the *x*- and *y*- axes. These indicate the co-ordinates of the maximum scatter point within the voxel in terms of measurement position. 4.10(a) shows that the maximum amount of scatter is achieved along the line where the scattering filament is at *x*- position 1.275 mm; this meant that the part of the sample that we wished to record the scatter from was placed at this point. The curve also shows that the width of the scatter volume (FWHM) is 875 μm. The sample moved through the diffraction system in 1 mm steps, and thus the

signal recorded for each translation step was mainly due to the middle 875 μm of the incident beam, with the 62.5 μm of the sample either side of this central area contributing significantly less to the signal.

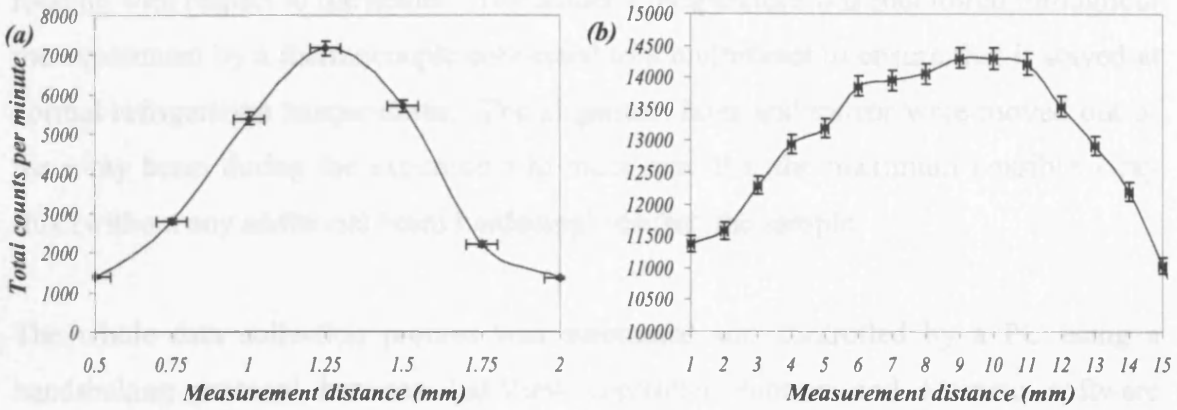

Figure 4.10 *Total intensity profiles in the –x (a) and –y (b) directions. The error bars on the abscissa show the accuracy that the position could be measured to; the bars on the ordinate are defined as the square root of the counts.*

Figure 4.10(b) shows the total signal summed across the scatter voxel as the filament moves through it along the *–y* axis. The sample lay on this axis to ensure that the maximum amount of scatter was collected from it. The sample size was measured to be 7.5 mm ± 0.5 mm, so 8 mm was assumed as a worse case. If the front of the 8 mm diameter was placed at measurement distance 4.75 mm, centred on 8.75 mm, then the scatter probability was found to be equal for both sides of the sample, with the peak scatter occurring at approximately measurement position 9 mm

Therefore the centre of the brass sample holder was positioned such that it lay at *x*-position 1.275 mm and *y*- position 8.75 mm. All micrometer measurements were noted and checked before the start of all microCT acquisitions, ensuring that the centre of rotation remained at this maximal scatter point.

4.4.4 Experimental procedure

The sample cooling system was switched on to allow the holder to cool for approximately 5 minutes before the sample was removed from the -35°C freezer and placed in the holder. The sample was then left for 2 minutes to reach equilibrium with the temperature of the holder. The translational position of the holder was checked to ensure that the alignment laser beam passed across its central axis. The system was then

aligned rotationally, as indicated in section 4.3.2 and the sample placed in the holder with the alignment flat on its bottom stopper placed behind a grub screw in the holder. The screw was then tightened and thus ensured that the sample was positioned at a fixed rotation with respect to the holder. The holder's temperature was monitored throughout the experiment by a thermocouple connected to a multimeter to ensure that it stayed at normal refrigeration temperatures. The alignment laser and mirror were moved out of the x-ray beam during the experiment to make sure that the maximum possible x-ray flux (without any additional beam hardening) reached the sample.

The whole data collection process was automated and controlled by a PC using a handshaking protocol between LabView controlled motion and Maestro software controlled spectrum acqisition. The number of views and translations per view were set in LabView and the software then controlled the movement of the sample through the x-ray beam. The x-ray spectrum acquisition parameters, such as the acquisition live time were set in a Maestro job file and this software controlled the MCA. The Maestro job file and LabView .vi file were started synchronously in order to activate the microCT acquisition. The job file instructed Maestro to loop a series of commands consisting of:

1) wait for an INCOMING sample ready signal from LabView
2) Acquire a spectrum using the MCA
3) Save the acquired spectrum
4) OUTPUT a ready to move signal to LabView.

The LabView software conversely looped a sequence of:

1) OUTPUT a sample ready signal to Maestro
2) Wait to receive an INCOMING ready to move signal from Maestro
3) Move the sample to the next position in the image.

Each full diffraction microCT sequence started and ended with the x-ray beam incident on the centre of the sample. The sample then translated out of the beam to the first measurement position and from then on the Maestro and LabView loops fitted together such that the sample translated across the x-ray beam in set distance steps with a spectrum acquisition occuring between each movement. It then translated in one move

back to the first translation position, rotated to the next view angle and then once again moved across in steps with a diffraction spectrum acquisition between each step. This process was repeated until data had been collected for all translations positions of all views. The sample was then moved back to the central starting position before the sequence ended. The acquisition parameters were set such that there was at least one clear air (or no sample) measurement at the beginning and end of the set of measurements for each view.

4.4.5 Acquisition parameters

The images shown in this work were taken using a tungsten target x-ray tube operating at 70 kVp and 10 mA. The MCA live time was set to 4 seconds, giving a total image acquisition time of approximately 5 hours for a microCT acquisition consisting of 200 views taken every 1.8° with 11 translation measurements taken 1 mm apart for each view.

4.4.5.1 Detector live time

The live time was chosen by taking images of a phantom of the same dimension as the breast tissue phantoms, but constructed from pork and lard, using live times of 2, 4 and 6 seconds. The pork phantom was used so that the breast tissue phantoms would be preserved for the full experiments. It offers a reasonable substitute for human tissue in terms of the achievable count rates of scattered x-rays. The image quality was found to be worse for the 2 second acquisitions, whilst it was good for the 4 and 6 s acquisitions, with no obvious benefit achieved when using the longer counting time (figure 4.11).

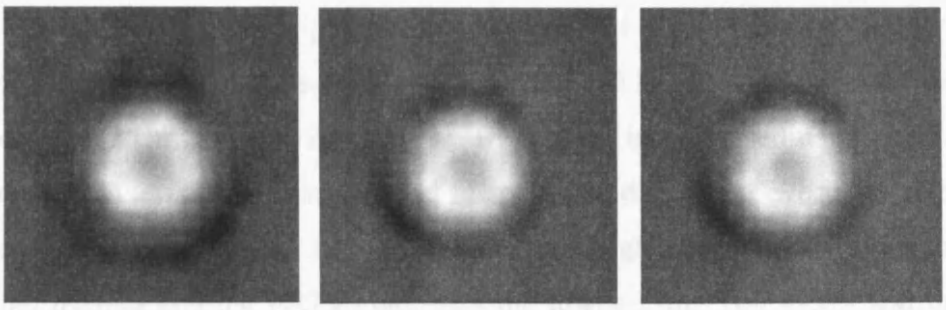

Figure 4.11 *Diffraction microCT images of a pork and lard phantom constructed at a momentum transfer of 1.1 nm^{-1} taken with 2s (left), 4s (centre) and 6s (right) acquisition live times.*

4.4.5.2 Number of measurement points

Images were taken using a plastic geometric test object to verify the optimum number of views and translation steps across the samples within the limits of the system (figure 4.12). The phantom consisted of a cylinder of Perspex the same diameter as the tissue samples containing 2 mm and 4 mm diameter Delrin inserts. The scatter signatures of Perspex and Delrin are shown in figure 4.13. Perspex has a broad signature when compared to Delrin, with a maximum value occuring at around 0.9 nm^{-1}, whereas Delrin shows a sharp peak at 1.4 nm^{-1} and a smaller peak at 2.1 nm^{-1}.

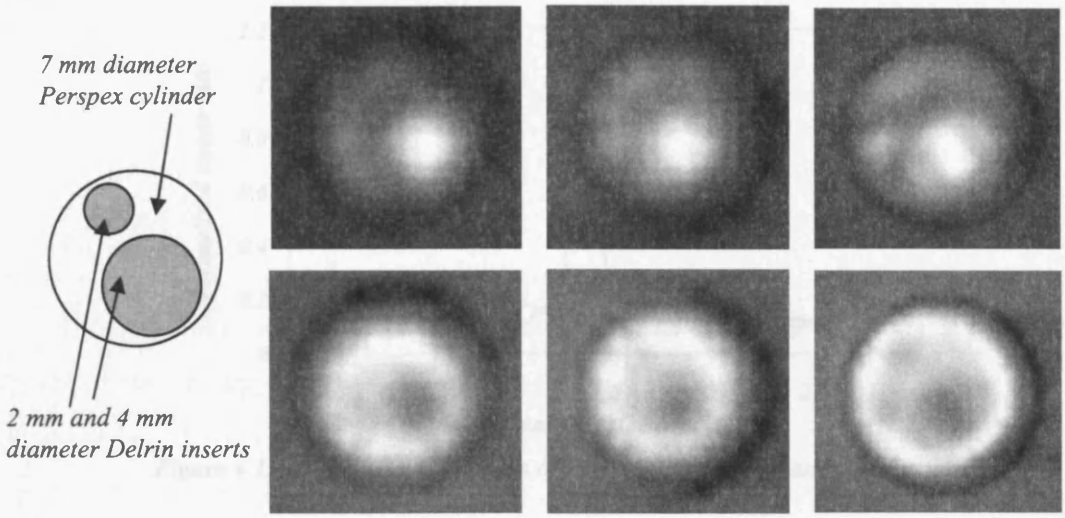

Figure 4.12 *Schematic diagram and diffraction microCT images of a Perspex phantom with Delrin inserts. The top images were taken at 1.4 nm^{-1}, highlighting the Delrin and the lower images at 0.9 nm^{-1}, highlighting the Perspex. Left hand images: 1 mm translations, 200 rotations; central images: 1 mm translations, 100 rotations; right hand images: 0.5 mm translations, 100 rotations.*

The images at the top of figure 4.12 were reconstructed by selecting a 1.66 keV wide (10 MCA channels) energy window around the Delrin peak and thus they highlight the Delrin inserts, whilst the images in the lower half of the figure were reconstructed around 0.9 nm^{-1} and so highlight the Perspex bulk of the phantom. Details of this selective reconstruction process are given later. The left hand images were formed from data taken every 1 mm across 200 views. The central images used data taken every 1 mm across 100 views and the right hand images used data taken every 0.5 mm across 100 views. The image using 200 views showed a higher contrast between the areas containing plastics and the background than the image using 100 views and the same size translation; this indicated that the final imaging procedure should acquire 200 views of the samples, rather than 100. Although giving better edge definition to the

outside of the phantom than the 1 mm translation images, the 0.5 mm translation image did not appear to give any further information. The 4 mm insert was seen in all images, whilst the 2 mm insert was not be reliably visualised in any image, indicating that the extra translation steps were not required. Also, due to sample cooling, a key factor in the imaging protocol was the measurement time, therefore fewer translations were preferable. The final parameters decided on were eleven 1 mm translations for 200 views, with an individual 4 s spectrum acquisition time. The full microCT acquisition took approximately 5 hours, with around half of this time taken up by the system automation.

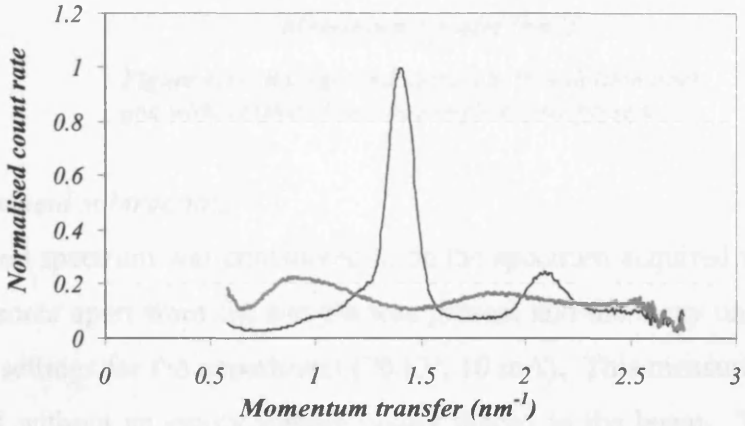

Figure 4.13 Diffraction signatures of Perspex (broad line) and Delrin (thin line).

4.4.6 Corrections to the diffraction spectra

The raw spectra acquired by this system required some corrections in order to make direct comparisons with other peoples' work and to create true images of the diffraction characteristics of the samples. A corrected spectrum *Cor(E,x)* can be defined as:

$$Cor(E,x) = [N(E,x) - (B(E,x) + M(E,x))]S(E)A(E,x) \quad (4.1)$$

Where *N(E,x)* is the raw spectrum, *B(E,x)* is the background spectrum, *M(E,x)* is the component of the raw data due to Compton and multiple scatters, *S(E)* is a correction factor due to the spectral shape of the incident x-ray beam and *A(E,x)* is a term to correct for attenuation effects in the phantom. *E* is the energy of the x-ray beam and *x* is the position of the translation measurement across the phantom. This dependence on position is due to the fact that the samples are cylindrical, and thus the x-ray beam

passed through different thicknesses of the sample depending on which translational measurement was being taken.

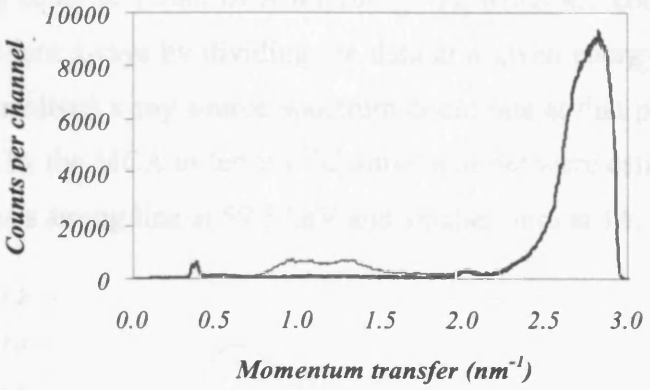

Figure 4.14 *Background spectra both with (thin line) and without (thick line) the sample holder present.*

4.4.6.1 Background subtraction

The background spectrum was considered to be the spectrum acquired when everything for the experiment apart from the sample was present and the x-ray unit was operating at the normal settings for the experiment (70 kV, 10 mA). This measurement was taken both with and without an empty sample holder placed in the beam. This allowed the background to be subtracted both for the plastic test phantoms, which do not need a sample holder, and for the tissue phantoms in the holders. A single background spectrum was used when no holder is present, but a measurement for each translation position was needed when the holder was in place as different amounts of plastic were present in the beam as the holder moved across it. Background spectra taken both without the holder and with the holder in a central position are shown in figure 4.14. The peak rising at 2.5 nm^{-1} is due to break through of the primary beam through the brass collimation. Equation 4.1 corrects for the background spectrum by subtracting it from the raw data spectrum.

4.4.6.2 Multiple and Compton scatters

Sections 3.4.2 and 3.4.3 showed that the contribution of single Compton and multiple scatters to the single coherent scatter signal from 4 cm thick Perspex and breast tissue phantoms is small. The microCT samples are less than 1 cm across, so there was even less chance of multiple scatters occuring. Therefore this term was considered to be negligible in equation 4.1.

4.4.6.3 X-ray source spectrum

The spectrum of the x-ray unit used for these experiments (figure 4.15) was obtained using reference data from Birch *et. al.* [1979] for a 70 kV Tungsten target source with inherent filtering equal to 1 mm of Aluminium. Equation 4.1 corrects for the spectral shape of the incident x-rays by dividing the data at a given energy/momentum transfer value by the normalised x-ray source spectrum count rate at that point. The diffraction spectra obtained by the MCA in terms of channel number were calibrated using a ^{241}Am source, which has a strong line at 59.5 keV and smaller ones at 14, 18, 21 and 26 keV.

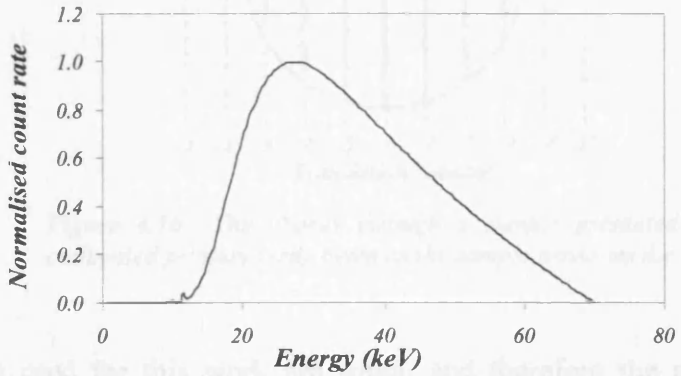

Figure 4.15 *Spectrum for a tungsten target (1 mm Al filtration) tube operating at 70 kVp. [Birch et. al., 1979]*

4.4.6.4 Attenuation

A polyenergetic x-ray beam was used for this experiment and thus beam hardening, although minimal for small, low density samples, took place. Beam hardening is due to the samples attenuating lower energy x-rays more than higher energy x-rays. The result is that the coherent scatter signal at higher photon energies will be unnaturally elevated with respect to the signal at lower energies. This phenomenon can be ignored when analysis data is obtained from diffraction images taken at the same narrow region of energy/momentum transfer values, as this can be considered to be a quasi-monochromatic situation.

As the samples pass across the primary collimated x-ray beam, the attenuation of this beam will vary due to two factors associated with the samples. The first being that the cylindrical samples present varying thicknesses to the beam as it traverses across, as can be seen in figure 4.16; the second factor is that the samples contain a mixture of tissue types, each with its own associated attenuation coefficient. The diffraction microCT images are formed from data taken in a rotate-translate CT mode. As will be elucidated

in section 4.4.7, each rotational view consists of eleven sets of data corresponding to the eleven translation positions shown in figure 4.16 for the laboratory based work and ten data points for the synchrotron based work. The attenuation by the sample of the x-ray beam is unique for each point, and thus each should be corrected individually.

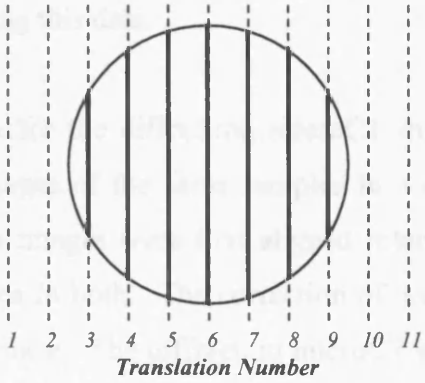

Figure 4.16 *The chords through a sample presented to the collimated primary x-ray beam as the sample traverses the beam.*

The samples used for this work are small, and therefore the attenuation differences across the sample may be small. Also, the tissues within the sample have similar attenuation coefficients. These two factors lead to the possibility that the attenuation differences across the phantom will be negligible compared to the variations in the signal due to the diffraction signal. Another point of note is that the laboratory based diffraction microCT took place at higher energies than the synchrotron based work. Therefore, as attenuation effects are more pronounced at lower energies, it can be expected that variations in the laboratory images due to beam attenuation will be less than those seen in the images obtained using the synchrotron source. Thus, in the following sections of this thesis, an attenuation correction will first be performed on the synchrotron images in order to ascertain whether the conjecture of the lack of necessity of an attenuation correction holds true for this data.

To successfully correct the diffraction microCT images for attenuation effects, the attenuation properties of the samples at the energy used to form the diffraction images must be accurately known. The synchrotron transmission and diffraction data sets were obtained using the same beamline energy. Therefore the attenuation properties of the materials are constant between the two sets, thus allowing true, rather than extrapolated attenuation coefficients to be obtained using the transmission data.

The sinogram for the transmission microCT images is formed by taking the natural logarithm of the projection data and therefore is proportional to the line integral of the attenuation coefficients across the sample along the line of view. This means that the transmission microCT image values are proportional to the attenuation coefficient per pixel for the material. An attenuation correction of the diffraction microCT sinogram can thus be performed using this data.

An attenuation correction for the diffraction microCT images based on using binned transmission microCT images of the same samples in a rotating reference frame was written in IDL. The two images were first aligned rotationally and set such that the sample filled the same area in both. The correction of the data for the first diffraction microCT view then took place. The diffraction microCT sinogram is formed using just ten acquisition data points set across the 8 mm sample and the air either side of it at 1 mm intervals, whereas the transmission sinogram effectively has several hundred data points at intervals of a single pixel width (20 μm). Therefore, in order to simulate identical acquisition conditions, the transmission image was binned into ten columns, each correlating to a single diffraction acquisition point across the phantom (Figure 4.17(a)).

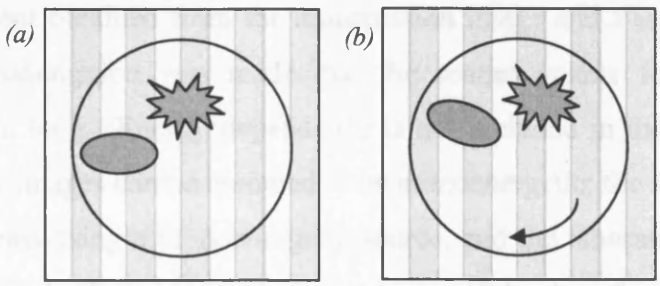

Figure 4.17 *Representation of the geometries used in the attenuation correction procedure; (a) The transmission image is binned into ten columns; (b) The original transmission image is rotated by the angle between the diffraction sinogram views and then binned again to obtain the correction data for the next view.*

The grey level values of all the pixels in each of the ten columns were then summed and divided through by the number of pixel columns in each binned column (40 in the case of the synchrotron microCT images) to obtain the mean line integral of attenuation per pixel. This mean value was then converted to units of cm^{-1} by division through by the number of pixels in one centimetre (50,000). The values for each of the ten binned columns were then stored in an array for later correction of the first view of the

diffraction microCT sinogram and the correction procedure moved onto the acquisition of the correction data for the second view of the diffraction sinogram.

To obtain the correction data for the next view of the sinogram, the transmission image was rotated by the angle between the diffraction data views and then the binning and integration procedure described above for the first view's corrections was applied again to this rotated image. This rotation, binning and attenuation coefficient collection procedure was continued until the transmission image had been rotated by 180°. There was no need to complete a full 360° rotation of the image as the data was taken using a parallel beam and thus the attenuation coefficients found for the ten columns at 0° will be the mirror image of those for 180°.

Once this full data set of attenuation coefficients had been obtained, each data point in the diffraction image sinogram could then be corrected for beam attenuation using equation 4.2.

$$A_{corr}(t,\theta) = A_{raw}(t,\theta)e^{-\mu(t,\theta)x} \qquad (4.2)$$

$A_{raw}(t,\theta)$ is the raw diffraction sinogram data, $A_{corr}(t,\theta)$ is the corrected data, t and θ are the translation and angular rotation positions of the sinogram data point, μ is the attenuation coefficient obtained from the transmission image and x is the length of the scatter voxel; an assumption was made that the scatter voxels for the diffraction microCT were 1 cm long. Energy dependence is not included in this equation, as all diffraction microCT images can be assumed to be monoenergetic; the synchrotron based images being obtained using a monoenergetic source, and the laboratory based images formed using an energy windowing technique which will be described in the following section.

4.4.7 Reconstruction algorithm

Each pixel of raw projection data was represented by one translation step of the system and therefore by one Maestro MCA spectrum channel file. These are longword binary files which contained (after a header section) the counts for the 512 channels of the MCA. Energy calibration of these files was done by inspection of the 512 channel wide spectrum for a ^{241}Am source with the MCA amplification set to the value used for the

experiments. The files were read into the IDL based reconstruction algorithm in the order in which they were acquired by the experimental apparatus, starting with translation position 1 of view 1 and ending with translation position 11 of view 200. As each file was read, an energy window of interest, and therefore a momentum transfer region of interest, was examined by selecting a range of channels. 10 channels were used, giving an ROI of approximately 1.6 keV. The summed signal of these channels was then found and stored in a unique element of an array. When all files had been read, this total value array was arranged into a conventional CT projection array, 11 elements wide and 100 elements deep, which was then used to form an emission CT sinogram. A radon transform back-projection CT reconstruction algorithm created the final diffraction microCT image which was 20 pixels wide and 20 high.

This algorithm included the corrections listed in section 4.4.6. The background spectrum was subtracted from each raw spectrum, which was then multiplied by a factor to correct for the spectrum of the x-ray unit. The attenuation correction was included by dividing the final diffraction microCT image by the binned transmission microCT image of the same sample. The energy windowing property of this reconstruction allowed images to be formed for different values and ranges of momentum transfer, highlighting different materials within the samples and maximising the available contrast between the two materials.

4.4.7.1 Construction of diffraction signatures

Each data position of the microCT acquisition consisted of a full MCA spectrum of the radiation scattered by the sample. This allowed EDXRD diffractometer spectra to be constructed for each sample.

Normally a cylindrical sample would be placed in a diffractometer with the incoming x-ray beam incident on its centre. It would then be rotated to ensure that the scatter from all parts of the sample is measured over the time taken for the signature to be acquired. The microCT data can be used to obtain this type of data set by summing the diffraction signal acquired for each of the central translation positions of the rotations.

A simple algorithm was written that read in each of the central spectra for a sample, subtracted a background spectrum from them, and then summed them to give a total

diffraction signature for the sample. This spectrum was then corrected for the spectral shape of the x-ray beam. Self attenuation of the signal by the sample can be corrected by considering the mean pathlength of the radiation for a uniform cylindrical phantom, but must be corrected at raw spectrum level and with knowledge of the position of the sample for each acquisition for an inhomogeneous sample.

4.5 MicroCT Images

Images were obtained of three different groups of phantoms: plastic, pork and lard, and human breast tissue phantoms. The L3CCD system was only used to image breast tissue, whilst all samples were imaged using the laboratory based HPGe diffraction microCT system. Some of the L3CCD images were used to assess the attenuation correction procedure described in section 4.4.6.4. The plastic phantoms were used to provide well defined test objects to characterise the HPGe diffraction microCT system and the pork phantoms were used as human tissue substitutes to evaluate and test the lab based acquisition procedures before they were used for the human breast tissue phantoms. After imaging, all of the human breast tissue samples were returned to St. James' University Hospital, Leeds for histopathological analysis.

4.5.1 MicroCT images of breast tissue taken with synchrotron radiation

Two sets of human breast tissue samples were imaged using the SYRMEP beamline at the Elettra synchrotron radiation source. The eight samples in Set A were imaged just at the beamline and not in the laboratory. These samples were not cooled during the image acquisitions, resulting in degradation of the pathological markers for classification, such as cell walls and nuclei. The images of these samples were used to assess the attenuation procedure.

There were nineteen samples in total in Set B; five of these samples were subjected to imaging with synchrotron radiation using the L3CCD after they had been imaged in the laboratory.

The transmission images of Set A were used to segment the registrated diffraction images in order to make an estimate of the proportions of different tissue types within each sample. This procedure was changed slightly for Set B, whereby comparison of tissue types was made with the aid of digital photographs of the processed samples.

4.5.1.1 L3CCD images of Set A

The primary aim of the imaging the samples in Set A was to assess the contrast achievable from diffraction microCT imaging compared to transmission microCT imaging. Figure 1.8 showed the diffraction signatures of different breast tissues acquired by Kidane [2000]. The figure indicated that the greatest contrast between normal and cancerous breast tissues should be achieved at momentum transfer values of 1.1 and 1.6 nm^{-1}, corresponding to x-ray energies of 18 and 26 keV at a scatter angle of 9°. 1.1 nm^{-1} emphasises the fat content of tissues, and therefore emphasises normal tissue, whereas 1.6 nm^{-1} focusses on the cancerous part of the spectrum. The synchrotron source's small bandwidth meant that the momentum transfer resolution of the system was limited purely by the collimation (see section 2.2.1).

The secondary function of these images was to assess the feasibility and necessity of the proposed attenuation correction procedure described in section 4.4.6.4.

The samples in Set A were approximately 1 cm in height and fitted into 8 mm diameter plastic cylinders for the experiments. The L3CCD microCT system was only capable of viewing one 500 μm thick portion of the sample at one time and the time available for the experiments at the synchrotron beamline was limited, allowing just one thin slice of each sample to be imaged. This meant that pre-selection of the tissue slices to be imaged was necessary in order to gain the maximal benefit from the experiment. The pre-selection was done by producing transmission CT images of the entire sample using the amorphous silicon imaging array described in section 4.3.1.3. Slices were then selected for further imaging if they contained minimal air pockets, along with clearly defined areas of apparently solid tissue types, preferably containing a range of structured tissue types.

The L3CCD system ensured rotational correlation between the transmission and diffraction images by taking one image after the other without removing the sample

between the acquisitions. Figure 4.18 shows transmission and diffraction images of the samples taken at 1.1 nm^{-1}, along with the diffraction image when corrected for attenuation. The grey-scales of the two imaging modalities are effectively reversed for tissue types, with normal tissue appearing darker in the transmission images and brighter in the diffraction images and diseased tissue brighter in transmission and darker in diffraction; the momentum transfer value of 1.1 nm^{-1} should highlight the normal tissue in the samples. The background air has the darkest grey level in the transmission images. The first column of figure 4.18 shows the transmission image, the second shows the uncorrected diffraction image, and the third column, the corrected diffraction image. Five of the transmission images have regions of interest marked on them; these were used to assess the contrast in the images between areas of normal (oval ROI) and diseased (rectangular ROI) tissue. Ring artefacts can be seen in the transmission images and these may affect the quality of the data obtained from them. Two of the diffraction images have outlines of the main features of their corresponding transmission image superimposed on them. These structures, although of poorer spatial resolution in the diffraction images, are visible in them, indicating rotational correlation between the images.

Sample 1

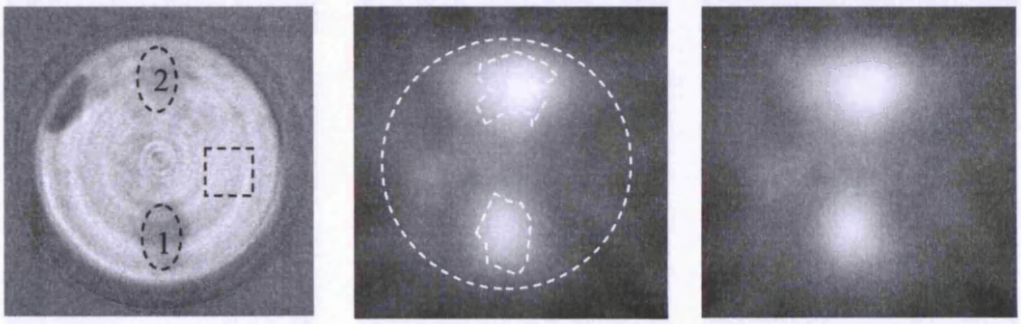

Sample 2

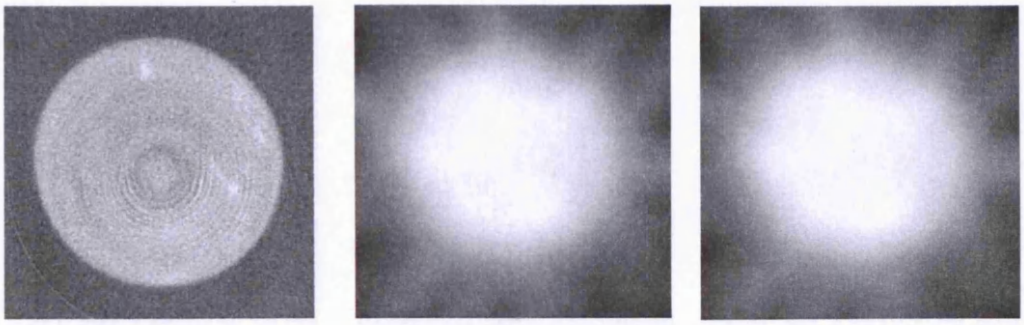

Sample 3

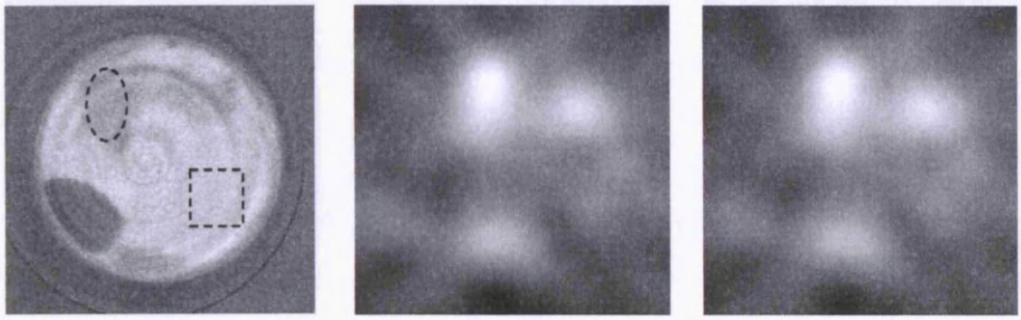

Sample 4

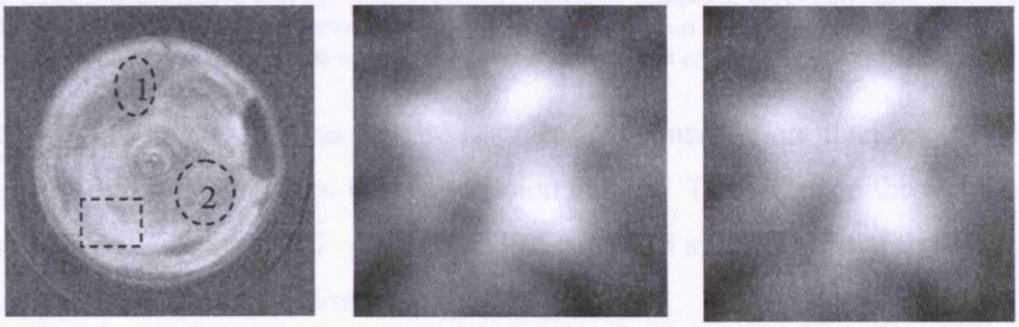

Sample 5

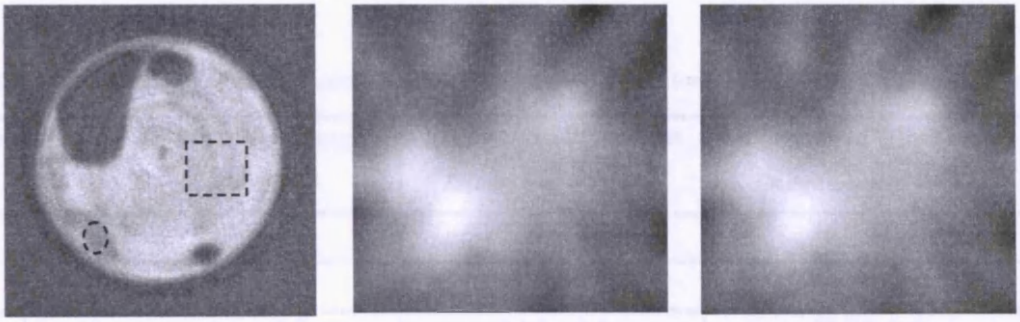

Sample 6

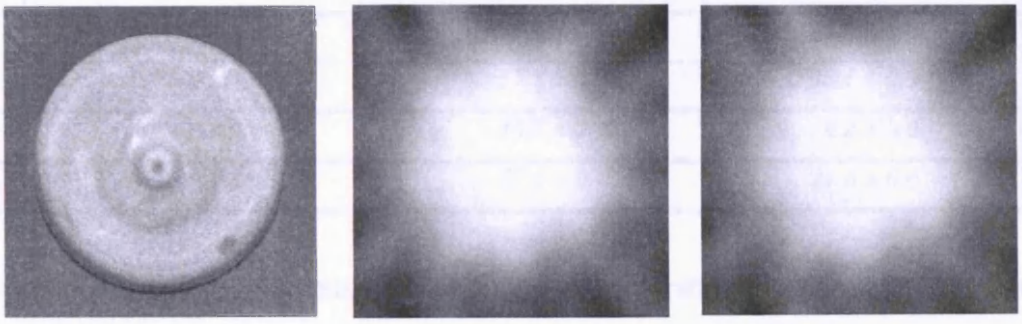

Sample 7

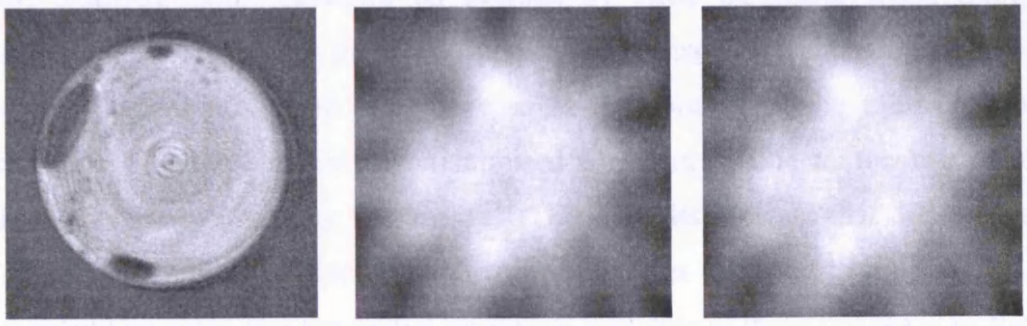

Sample 8

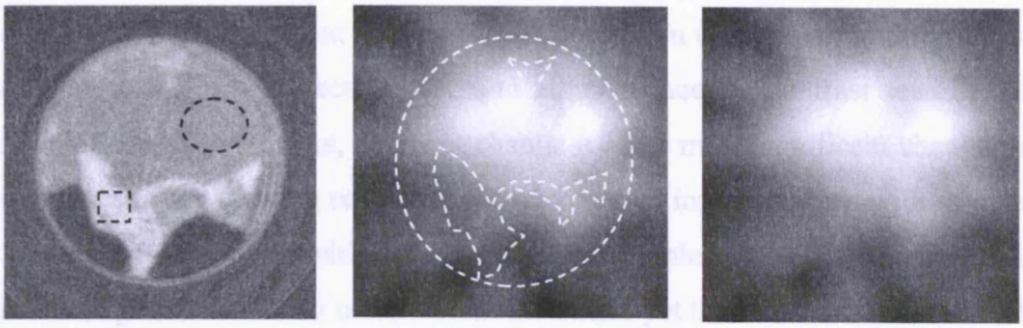

Figure 4.18 *L3CCD transmission and diffraction (1.1 nm^{-1}) microCT images of the breast tissue samples in Set A. The first column shows the transmission images, the second shows the raw diffraction images and the third shows the diffraction images after correction for attenuation effects.*

Table 4.2 gives the contrast values for the samples that contain more than one tissue type using the areas highlighted on the transmission images. The errors on the contrast were calculated using equation 3.1. Oval ROIs in figure 4.18 indicate normal tissue and rectangular ROIs indicate denser tissue.

Table 4.2 *Contrast between normal and cancerous areas in the microCT images of samples in Set A.*

Phantom	*ROI*	*Transmission Image Contrast (%)*	*UncorrectedDiffraction Image Contrast (%)*	*Corrected Diffraction Image Contrast (%)*
1	*1*	*25.5 ± 1.0*	*33.6 ± 0.4*	*36.0 ± 0.3*
	2	*16.8 ± 0.7*	*40.8 ± 0.3*	*42.5 ± 0.2*
3		*15.9 ± 0.7*	*34.3 ± 0.6*	*33.8 ± 0.6*
4	*1*	*21.5 ± 0.8*	*37.8 ± 0.5*	*39.8 ± 0.4*
	2	*13.0 ± 0.7*	*37.8 ± 0.5*	*38.1 ± 0.5*
5		*16.0 ± 0.6*	*15.7 ± 0.4*	*18.2 ± 0.6*
8		*17.5 ± 0.4*	*32.6 ± 0.7*	*29.6 ± 0.6*

Two main conclusions can be drawn from Table 4.2. Firstly, the contrast between normal and diseased tissue increases on average by close on 100% when using diffraction techniques to image them as opposed to transmission imaging. In a laboratory environment this factor may increase as the contrast of the transmission images in figure 4.27 were effectively maximised for contrast due to the use of a monoenergetic source in obtaining the images. These results indicate that diffraction microCT is a viable option for creating high contrast images of breast tissue samples, however it should be noted that the spatial resolution available in these images is of the order of 500 μm, as opposed to 50 μm in the transmission images.

The second conclusion from Table 4.2 is that the change in contrast between the diffraction images with and without the attenuation correction is minimal; in three cases out of the seven shown, the correction serves to either reduce the contrast seen in the image, or, within the quoted errors, does not change it. The most significant change in the values of contrast between the corrected and uncorrected images is seen with sample 5, which has a large insert of air within the breast tissue sample. Nevertheless, sample 8 also contains a large amount of air compared to tissue and yet the correction has not had a positive effect on this sample's diffraction data, despite there also being clear differences in the tissue densities seen in the transmission image of this sample.

The attenuation correction was carried out as set out in section 4.4.6.4. Therefore the transmission images seen in figure 4.18 were used to correct the diffraction images. The transmission images can be seen to contain significant noise and ring artefacts, both of which will lead to inaccuracies in the implementation of the attenuation correction. The transmission image with the most uniform grey levels for individual regions of data (i.e., the least ring artefacts and quantum mottle) is that for sample 8; the sample for which the correction has a negative effect. Therefore, we can not be sure whether the changes in the corrected diffraction images are due to attenuation or are mainly a result of the artefacts seen in the transmission images used to correct them. When the attenuation coefficient values for each view used in the correction were examined, it was found that they were all close to zero. The attenuation coefficients are all small as the samples are both small and constructed from low atomic number materials. Therefore the attenuation correction can be considered to have a only a small effect for this set of images.

The images of the samples in Set A were obtained using 18 keV x-rays and the application of the attenuation correction was shown to only marginally change the diffraction microCT images. The differences in the attenuation coefficients between the materials in the samples would decrease if higher energy x-rays were to be used to form the images. Therefore, it can be assumed that an attenuation correction will have an even smaller effect on diffraction microCT images of small, low atomic number samples if the energy at which they are obtained is greater than the 18 keV at which these test images were taken.

The diffraction microCT images in this thesis obtained in the laboratory were all formed using x-rays with energies significantly higher than 18 keV. Therefore an attenuation correction will not be essential for this data as it can be assumed that it would not make any significant contribution to the final results.

4.5.1.2 L3CCD microCT images of selected samples from Set B

The L3CCD microCT images of the samples in Set A indicated that diffraction microCT would produce low spatial resolution images compared to transmission microCT, but with a much higher soft tissue contrast. The work also highlighted the need to keep the samples cool whilst performing the procedure in order to maintain the cellular integrity needed for accurate histopathological analysis.

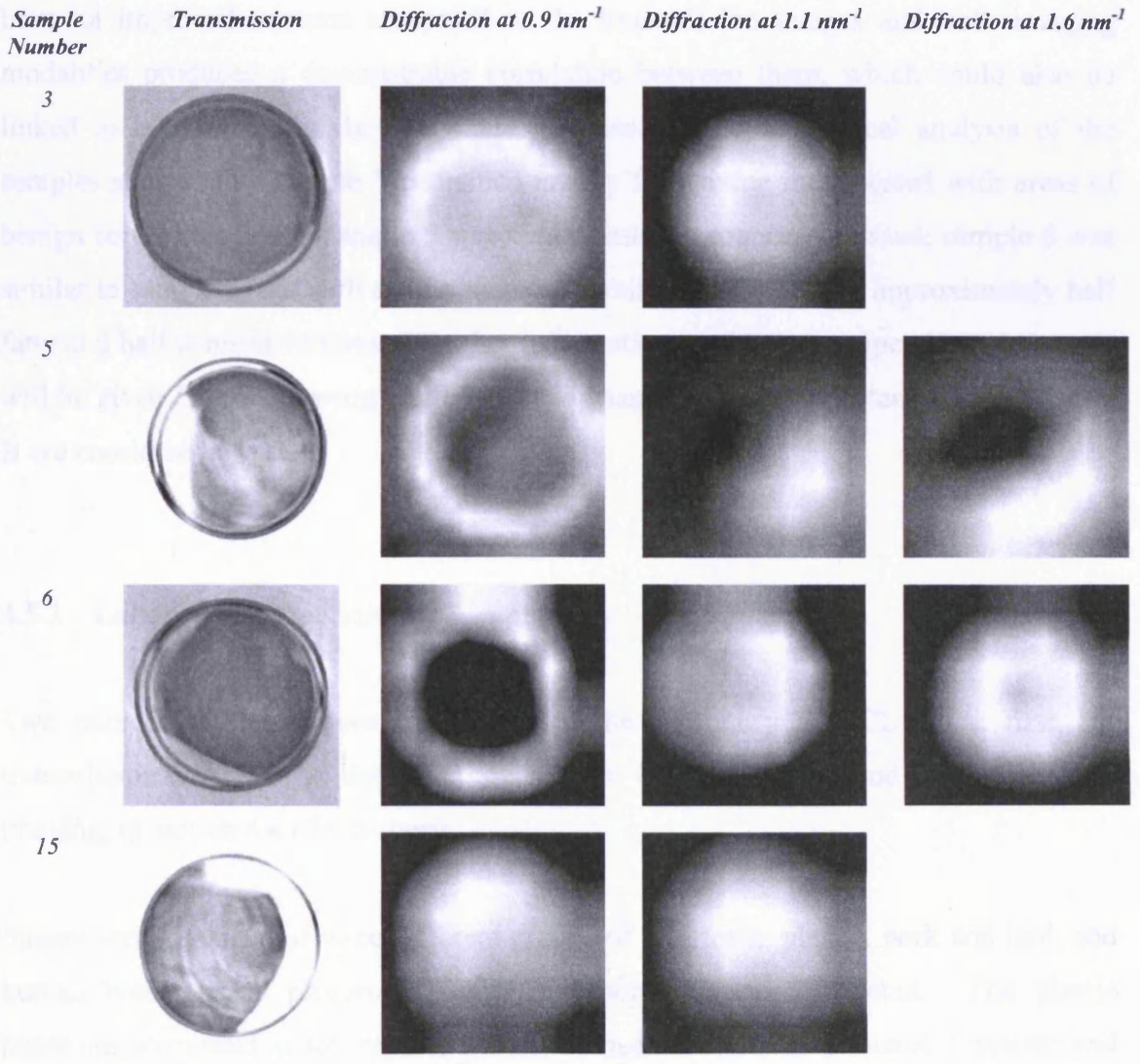

Figure 4.19 *L3CCD microCT images of samples from set B. Top row sample 3, second row sample 5, third row sample 6 and bottom row sample 15. Left hand images are transmission taken at UCL. Other images are all diffraction taken at a scatter angle of 9° at the SYRMEP beamline, Elettra, Italy.*

A new L3CCD camera was built that made use of an optical stud placed between the phosphor and the chip in order to minimise direct x-ray hits in the sensor and a sample cooling system was designed, constructed and tested. This new, modified experimental set up was once again taken to the SYRMEP beamline at the Elettra synchrotron radiation source where four of the samples in Set B were imaged [Royle *et. al.*, 2004].

Transmission microCT images were taken at UCL using the equipment described in section 4.3. Diffraction images were taken at the SYRMEP beamline using a scatter angle of 9° and photon energies of 14, 18 and 26 keV, corresponding to 0.9. 1.1, and 1.6 nm^{-1} (figure 4.19). These new diffraction microCT images showed an improvement in the localisation of the edge of the sample compared to the preliminary images. This is due to the reconstruction technique used [Pani, 2005]. Again, the diffraction images have an improved contrast compared to the transmission images and both imaging modalities produced a demonstrable correlation between them, which could also be linked to histopathology data for these samples. Histopathological analysis of the samples showed that sample 3 contained mainly fatty tissue interspersed with areas of benign connective tissue, sample 5 was almost entirely connective tissue; sample 6 was similar to sample 5, but with a little more fat, whilst sample 15 was approximately half fatty and half connective tissue. Further information on the tissue types in each sample will be given in the following sections of this chapter where all nineteen samples in Set B are considered.

4.5.2 Laboratory based microCT imaging

Two microCT systems were constructed in the laboratory at UCL. The first, for transmission imaging, is described in section 4.3 and the second, for diffraction imaging, in section 4.4 of this thesis.

Images were obtained of three different groups of phantoms: plastic, pork and lard, and human breast tissue phantoms using the laboratory based systems. The plastic phantoms were used as test objects to characterise the diffraction microCT system and the pork phantoms were used during system set up to simulate human tissues. The breast tissue samples formed Set B, part of which was imaged at the Elettra synchrotron

radiation source, as shown in the previous section. After imaging, all of the human breast tissue samples were returned to St. James' University Hospital, Leeds for histopathological analysis.

An attenuation correction was not applied to the laboratory microCT images, as it was shown in section 4.5.1.1 that the correction would have a negligible effect on the final images.

4.5.2.1 Plastic phantoms

Figure 4.20 shows diffraction signatures obtained using the HPGe microCT system for four different plastics: Nylon 6,6, Perspex (also known as PMMA and Lucite), Polytetrafluoroethane (PTFE) and Delrin (a DuPont trade plastic similar to Nylon). These plots have been corrected for background scatter, x-ray beam spectrum and sample self-attenuation. The signatures of Nylon 6,6 and Perspex have been measured previously by Poletti *et. al.*, [2002] and Kosanetzky *et. al.*, [1987]. The *y*-axis of figure 4.20 is proportional to the differential coherent scattering coefficient of the materials. It allows a comparison of the potential contrast available between two different plastics for a given value of momentum transfer. These results indicated that the maximum contrast between plastics should be achieved between Delrin and PTFE at momentum transfer values of 1.1 and 1.4 nm^{-1}.

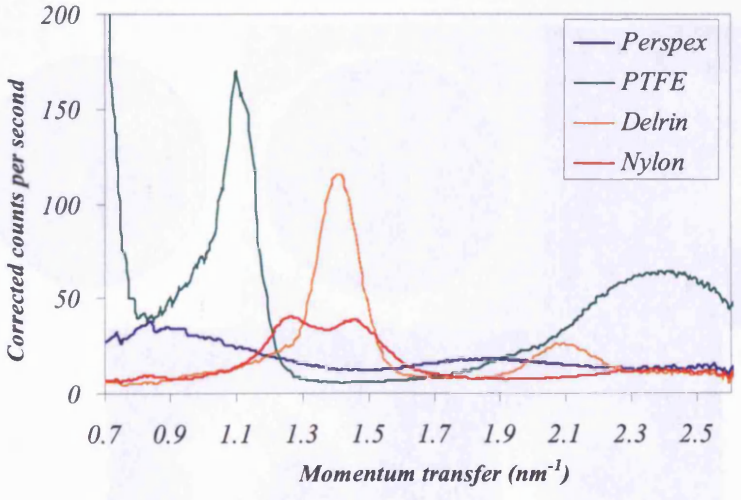

Figure 4.20 *Corrected diffraction signatures for four plastics obtained using the UCL diffraction microCT system.*

One solid phantom and five geometric phantoms, summarised in Table 4.3, were constructed from these constituent materials for use in the characterisation and analysis

of the HPGe microCT system. The solid Perspex homogeneous test phantom allowed assessment of the corrections applied by the reconstruction algorithm, whilst the geometric phantoms give an indication of the momentum transfer and spatial resolutions of, and the achievable contrast enhancements from the diffraction imaging system. Phantom 2 was imaged and analysed in order to assess the number of measurement points needed for diffraction microCT (figure 4.12, §4.4.5.2) and phantom 5 was also used in the alignment of the systems and also to indicate the position registration between the two systems.

Table 4.3 *Composition of the plastic phantoms and the momentum transfer values used.*

Phantom Number	***Main body (7 mm diameter)***	***Inserts***	***Momentum transfer values of diffraction images (nm^{-1})***
1	*Nylon*	*2 mm and 4 mm diameter Perspex*	*Perspex peak – 0.85* *Nylon peaks – 1.25 & 1.45*
2	*Perspex*	*2 mm and 4 mm diameter Delrin*	*Perspex peak – 0.85* *Delrin peak – 1.4*
3	*PTFE*	*2 mm and 4 mm diameter Delrin*	*PTFE peak – 1.1* *Delrin peak – 1.4*
4	*Delrin*	*6 mm diameter Perspex*	*Perspex peak – 0.85* *Delrin peak – 1.4*
5	*Perspex*	*1 mm air hole parallel to beam*	*Perspex peak – 0.85*

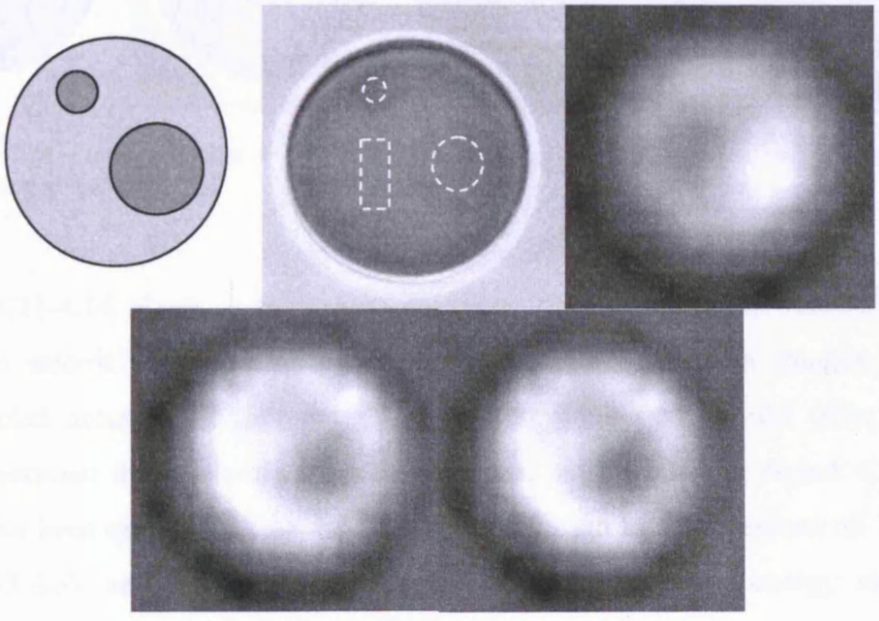

Figure 4.21 *Images of plastic phantom 1. Top row (l-r) schematic diagram, transmission, diffraction at 0.85 nm^{-1}. Bottom row (l-r) diffraction at 1.25 nm^{-1}, diffraction at 1.45 nm^{-1}.*

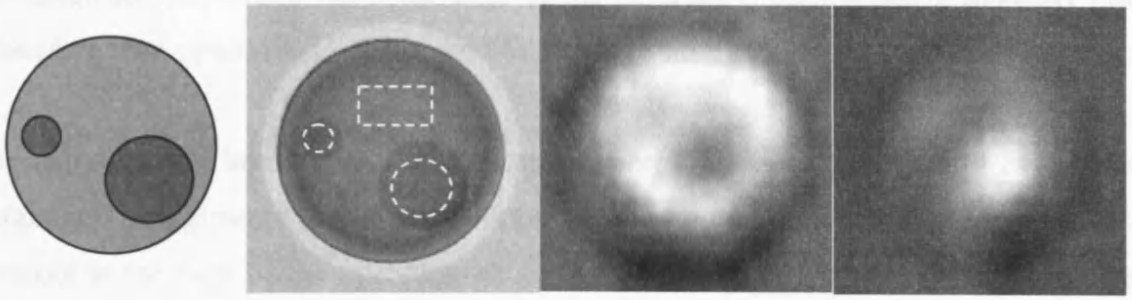

Figure 4.22 *Plastic phantom 2. (l-r) Schematic diagram, transmission, diffraction at 0.85 nm^{-1}, diffraction at 1.4 nm^{-1}.*

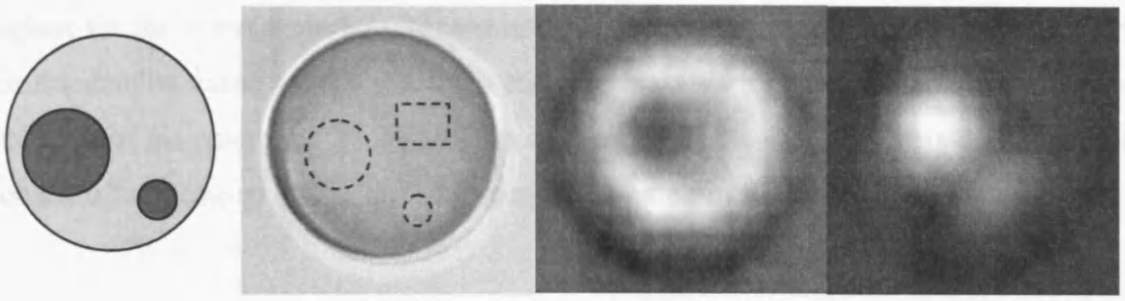

Figure 4.23 *Plastic phantom 3. (l-r) Schematic diagram, transmission, diffraction at 1.1 nm^{-1}, diffraction at 1.4 nm^{-1}.*

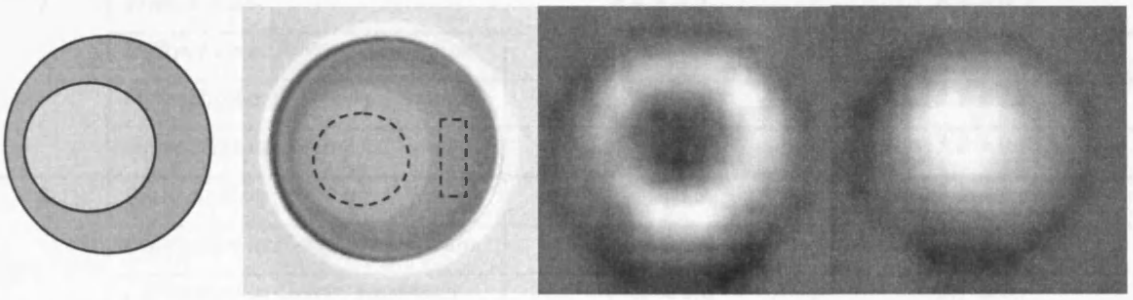

Figure 4.24 *Plastic phantom 4. (l-r) Schematic diagram, transmission, diffraction at 1.4 nm^{-1}, diffraction at 0.85 nm^{-1}.*

Figures 4.21-4.24 show a schematic diagram, the transmission microCT and the diffraction microCT images of phantoms 1-4. The diffraction images have been reconstructed around the momentum transfer regions that should offer maximum contrast between the materials in each phantom, as indicated in figure 4.20. These values have been quoted in table 4.3. These momentum transfer regions all lie between 20 and 35 keV and so are slightly higher than the effective energy used for the transmission images. Nevertheless, this has no significant impact on the results as it can

be assumed that, within the constraints of the laboratory, each imaging modality has therefore been optimised to obtain the best possible contrast.

Several ROI have been marked on the transmission images in figures 4.21-4.24. These highlight the regions of the image used to assess the image contrast for the inserts with respect to the bulk of the phantom, as given in Table 4.4. The table shows that the contrast in the transmission images is consistently lower for the big insert than that in the diffraction images, and that the insert contrast is consistently highest in the diffraction images constructed around the momentum transfer region where the signal is highest for the insert material. Nevertheless, these statements do not necessarily hold for the smaller insert where the diffraction contrast varies greatly depending on the materials of the phantom. This variation in contrast of the small insert is due to partial volume effects caused by the limiting spatial resolution of the system.

Table 4.4 *Contrast of the inserts compared to the background phantom. The error on the contrast has been calculated using equation 3.1.*

Phantom	***Image***	***Big Insert Contrast (%)***	***Small Insert Contrast (%)***
1	*Transmission*	*3.1 ± 0.2*	*6.5 ± 0.2*
	Diffraction at Perspex maximum	*19.0 ± 0.5*	*1.2 ± 0.6*
	Diffraction at Nylon maximum 1	*32.3 ± 0.3*	*2.3 ± 0.3*
	Diffraction at Nylon maximum 2	*39.1 ± 0.4*	*3.2 ± 0.3*
2	*Transmission*	*8.2 ± 0.2*	*9.2 ± 0.1*
	Diffraction at Perspex maximum	*33.6 ± 0.4*	*7.3 ± 0.2*
	Diffraction at Delrin maximum	*47.3 ± 0.6*	*0.5 ± 0.7*
3	*Transmission*	*7.6 ± 0.3*	*1.0 ± 0.4*
	Diffraction at PTFE maximum	*51.7 ± 0.7*	*7.6 ± 0.4*
	Diffraction at Delrin maximum	*78.5 ± 0.5*	*55.6 ± 0.9*
4	*Transmission*	*16.7 ± 0.4*	-
	Diffraction at Perspex maximum	*31.3 ± 0.4*	-
	Diffraction at Delrin maximum	*74.1 ± 0.6*	-

Visual observation of figures 4.21-4.26 have suggested that the small insert can not be seen in the diffraction images of phantom 1. It is only barely visible in the Perspex maximum image for phantom 2. It is clearly visible in the Delrin maximum image of

phantom 3, but not the PTFE maximum image. These observations link with the values of contrast seen in table 4.4. The large 4 mm diameter inserts are seen in all images.

The microCT acquisition procedure used 1 mm translation steps between data points with an incoming beam diameter of 1 mm. As can be seen from figure 4.9, these factors will create a partial volume effect that becomes significant at the 2 mm diameter scale of the small inserts. These results indicate that the limiting spatial resolution of the HPGe diffraction microCT system is presently of the order of 2 mm.

4.5.2.2 Breast tissue phantoms

All nineteen samples in Set B were imaged in the laboratory at UCL using the HPGe diffraction and amorphous silicon transmission microCT systems with a sample cooling system (Figure 4.2) in operation. Five of these samples were then subjected to further imaging with synchrotron radiation using the L3CCD (§4.5.1.2). After imaging, all of the samples were classified according to tissue type by histopathological analysis at St. James' University Hospital, Leeds. After this analysis, comparison of the tissue types within the samples was made with the aid of digital photographs of the processed samples.

The L3CCD microCT work showed that the diffraction microCT technique was feasible and could be used to create high contrast images of breast tissue samples that correlate with transmission images. The work was carried out using synchrotron radiation. The use of a synchrotron source meant that a parallel beam of monoenergetic x-rays was used for the experiment, but also meant that the amount of experimentation that could be done was limited due to the time allocated on the beamline. Translation of the microCT work into a laboratory environment removed the time constraints associated with synchrotron work, allowing more images to be obtained at times convenient to the research group.

As described in sections 4.3 and 4.4, two laboratory based microCT systems, one for transmission and one for diffraction, were built. All nineteen of the breast tissue samples in Set B were imaged on these two systems; a detailed set of images for one sample can be seen in figure 4.25 and images of all the other samples in an identical format are shown in figure 4.26. The diffraction images, taken at 1.1 and 1.6 nm^{-1},

corresponding to the intensity maxima for normal and diseased tissue respectively [Kidane, 2000], have been fully corrected for background and beam spectrum using the correction processes described in section 4.4.6. They have not been corrected for attenuation following the analysis of the necessity of an attenuation correction using the images of the breast tissue samples in Set A.

Each set of images follows the same lay-out. The top row shows a transmission image, a binned transmission image to simulate the spatial resolution of the diffraction images and the histopathologically stained tissue slice, removed from the sample holder and oriented such that it matches the x-ray images. The bottom row shows diffraction images at 1.1 nm^{-1} and 1.6 nm^{-1}. The dotted lines on the binned transmission image indicate ROI used for contrast analysis. A full explanation of the histopathological slices is given in Hanby [2004]. The necessary information regarding the grey scale and histopathological stain colour identification of tissue types can be found in table 4.5.

Table 4.5 *Key to grey-scales in figures 4.25 and 4.26.*

Tissue type	***Grey level in transmission image***	***Grey level in diffraction image at 1.1 nm^{-1}***	***Grey level in diffraction image at 1.6 nm^{-1}***	***Histopathology stain colour***
Fat	*Light grey*	*White*	*Black*	*Clear*
Epithelium *(found in walls of ducts and lactiferous sinuses)*	*Not visible against background*	*Not visible against background*	*Not visible against background*	*Blue/purple*
Stroma *(connective tissue)*	*Mid - Dark grey*	*Dark grey/black*	*White/light grey*	*Pink cells with some variation*
Carcinoma	*Dark grey*	*Black*	*White*	*Pink, ordered pleomorphic cells*

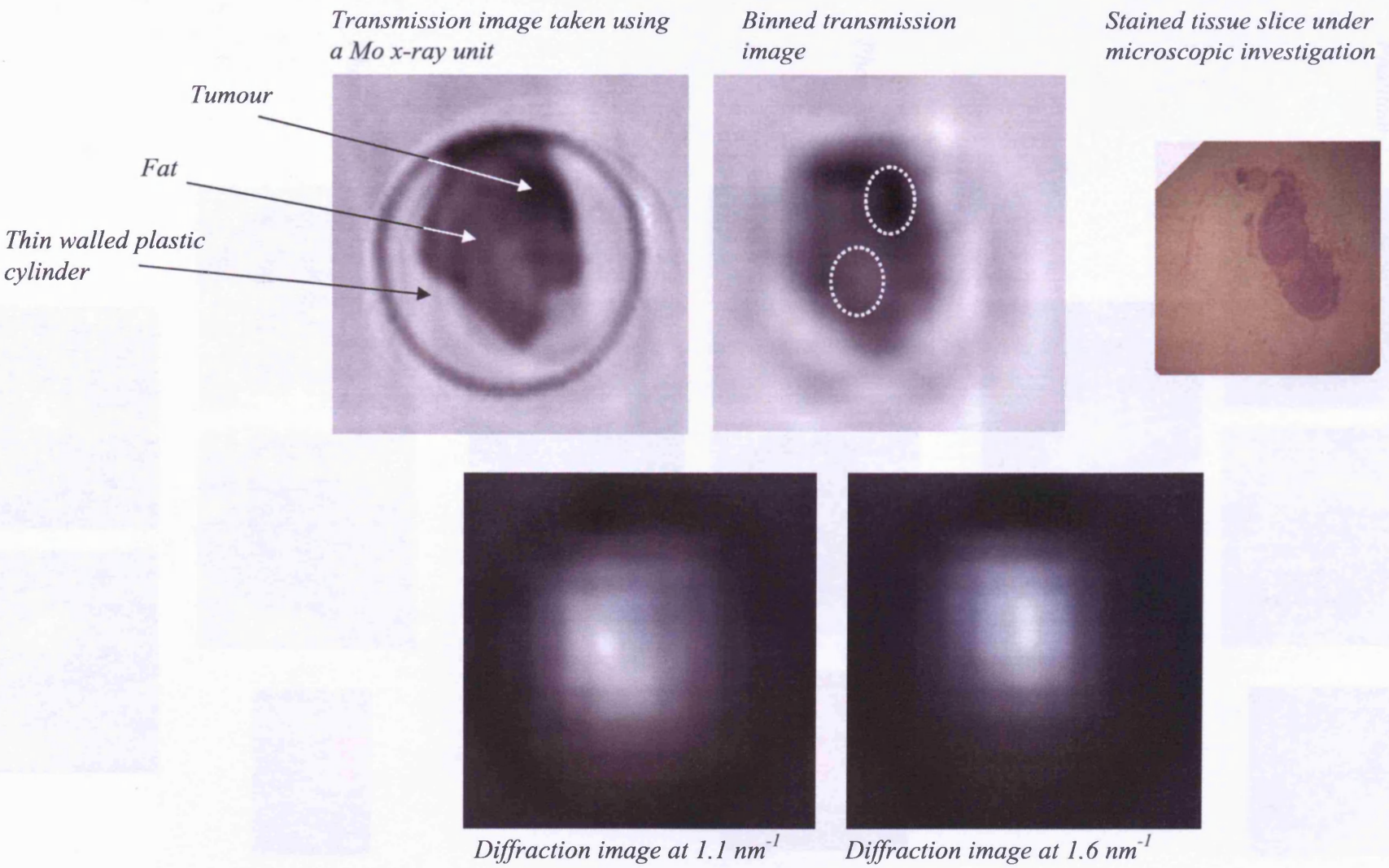

Figure 4.25 *Images of breast tissue sample 1 from Set B. Key to grey scales follows in Table 4.5.*

Phantom 2

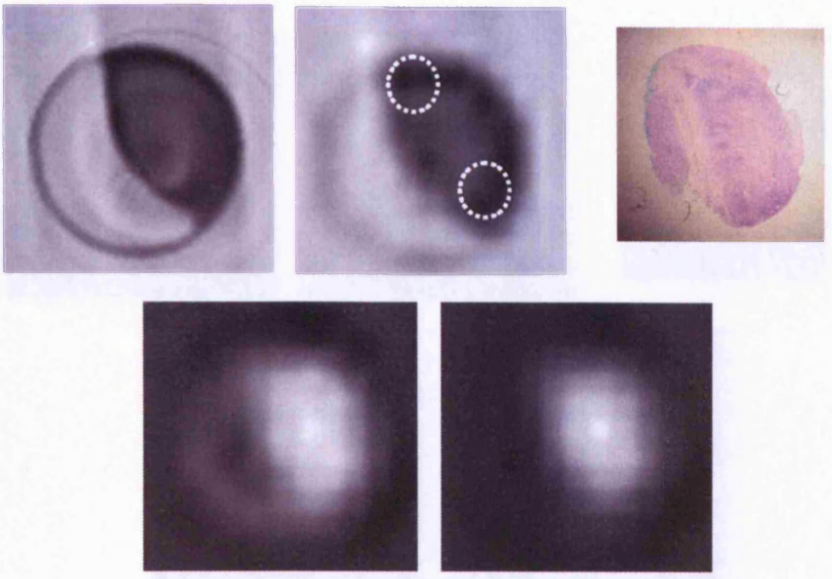

Phantom 3

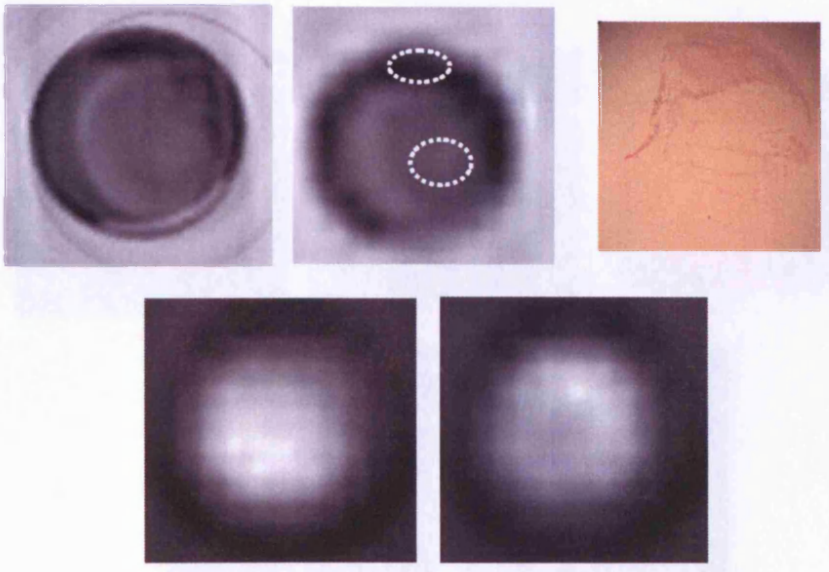

Phantom 4

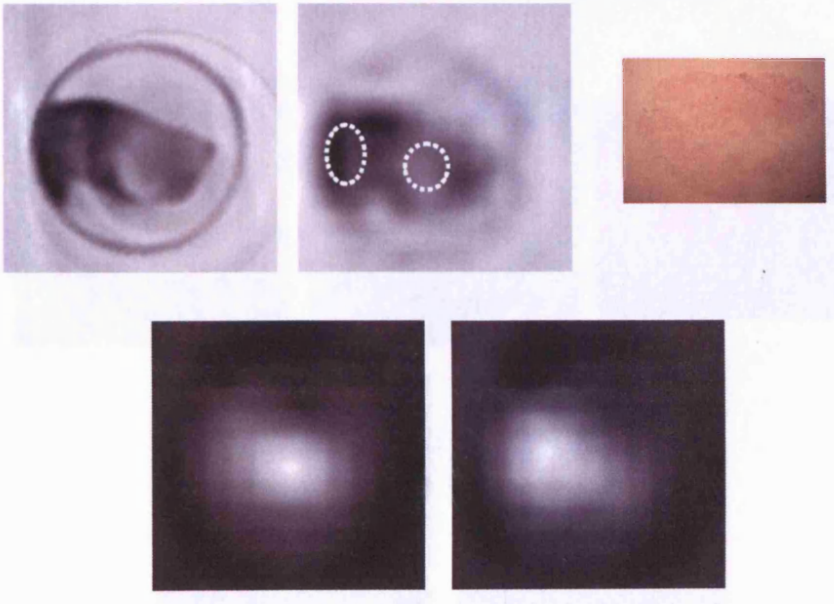

Phantom 5

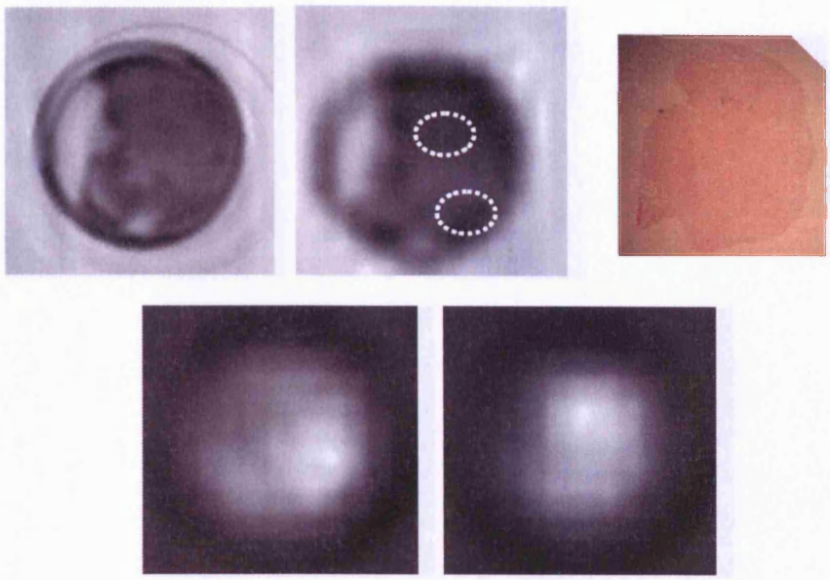

Phantom 6

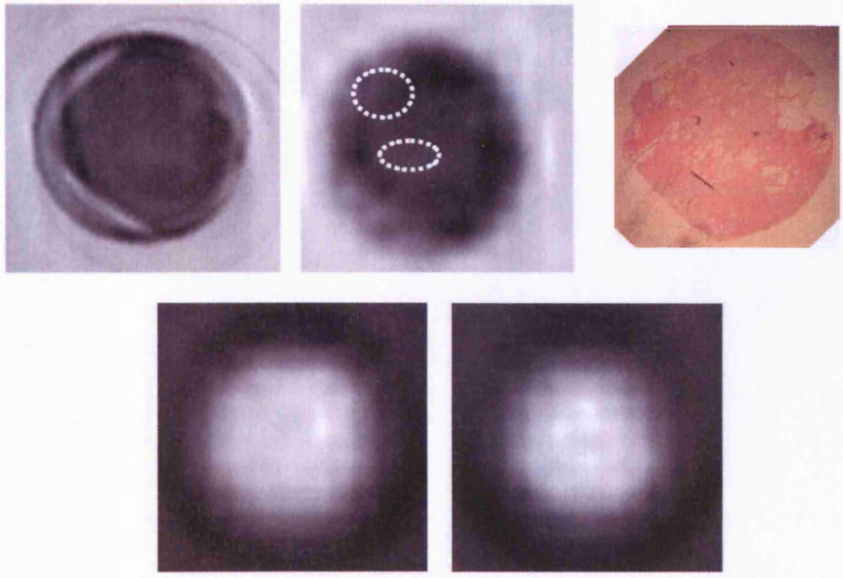

Phantom 7

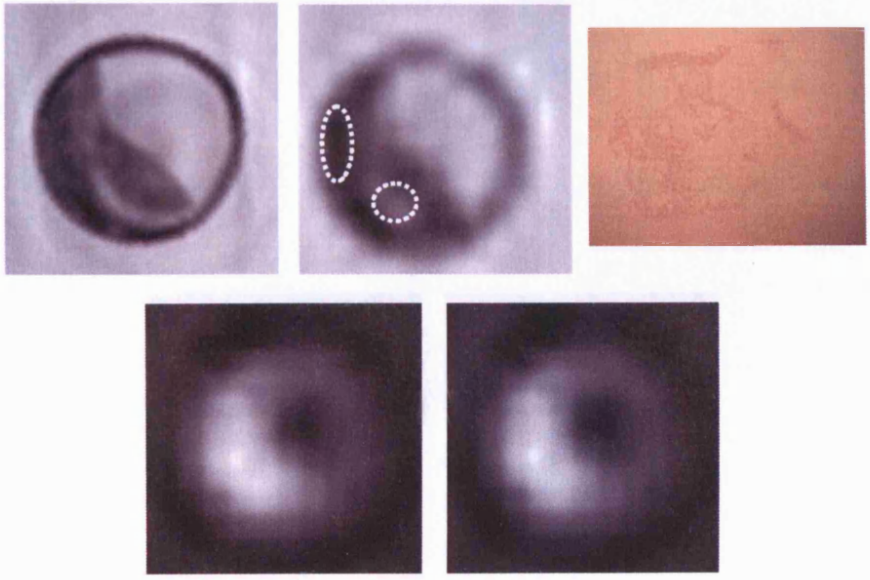

Phantom 8

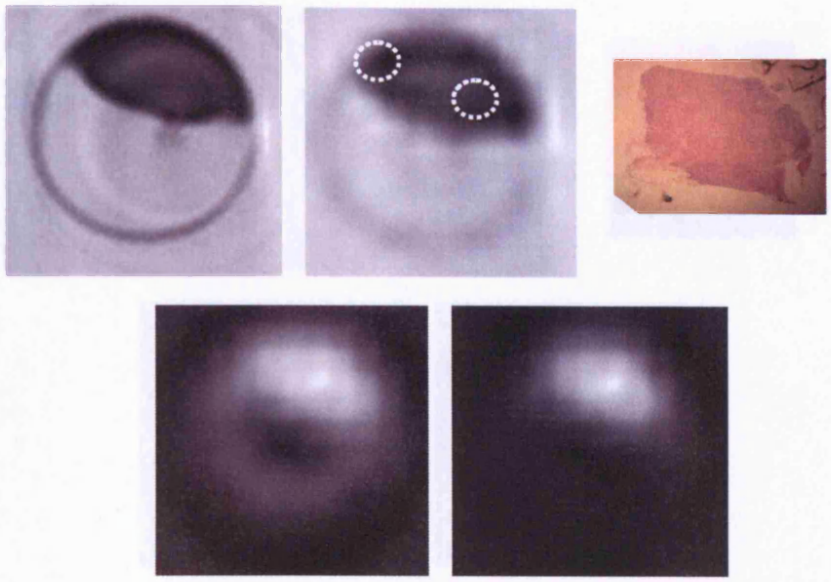

Phantom 9

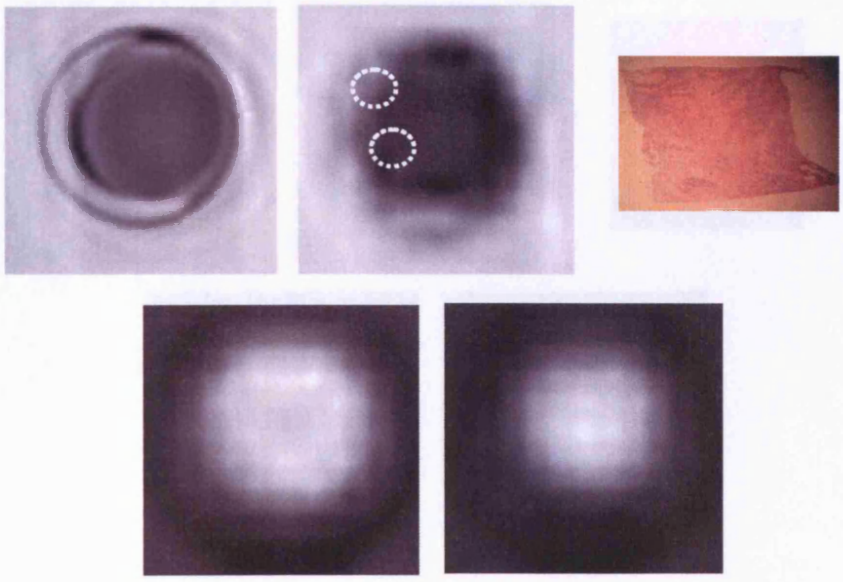

Phantom 10

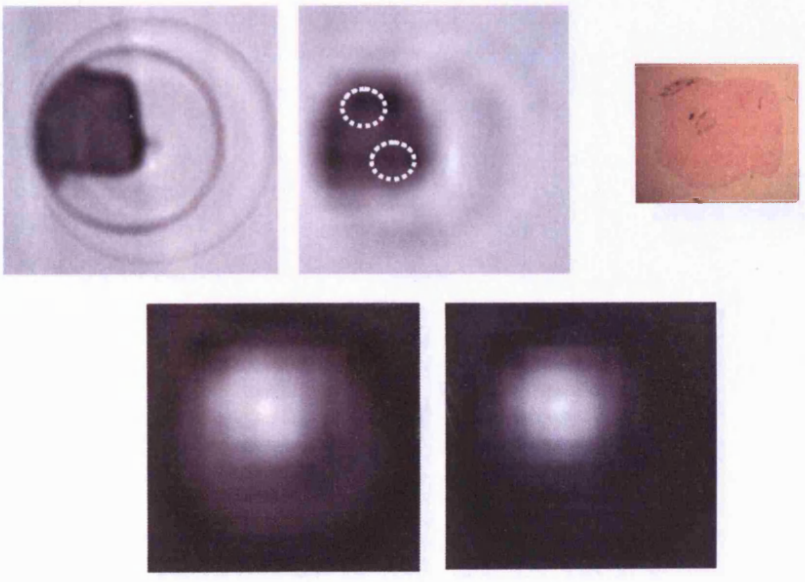

Phantom 11

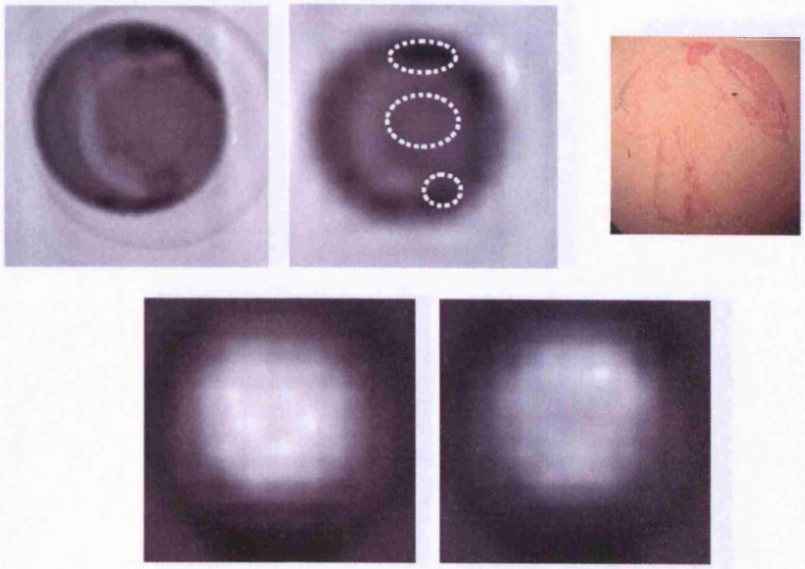

Phantom 12

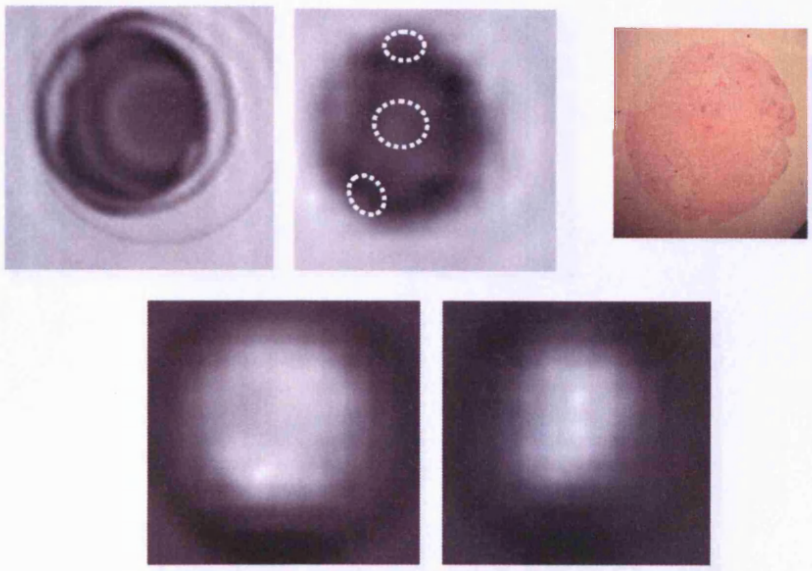

Phantom 13

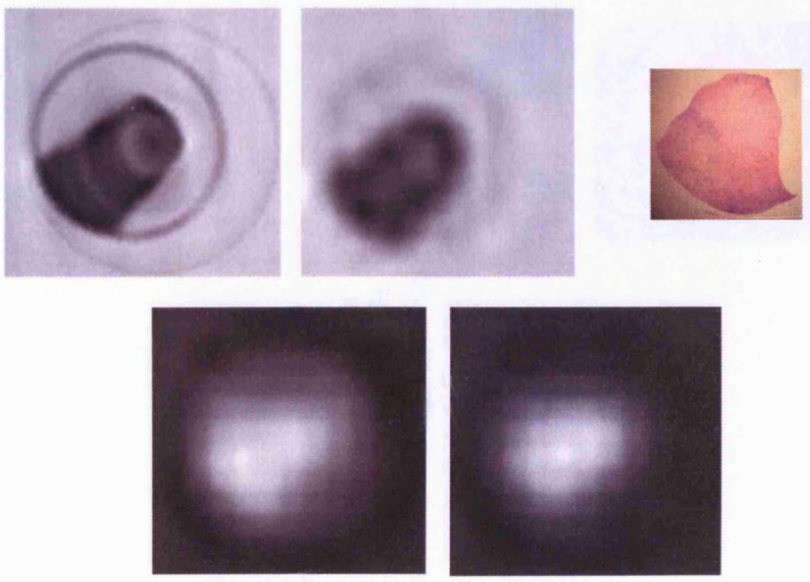

Phantom 14

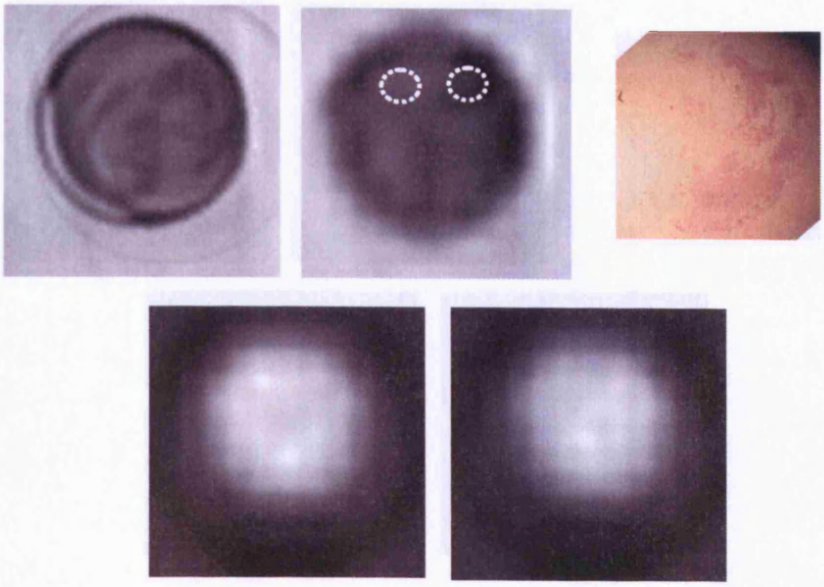

Phantom 15

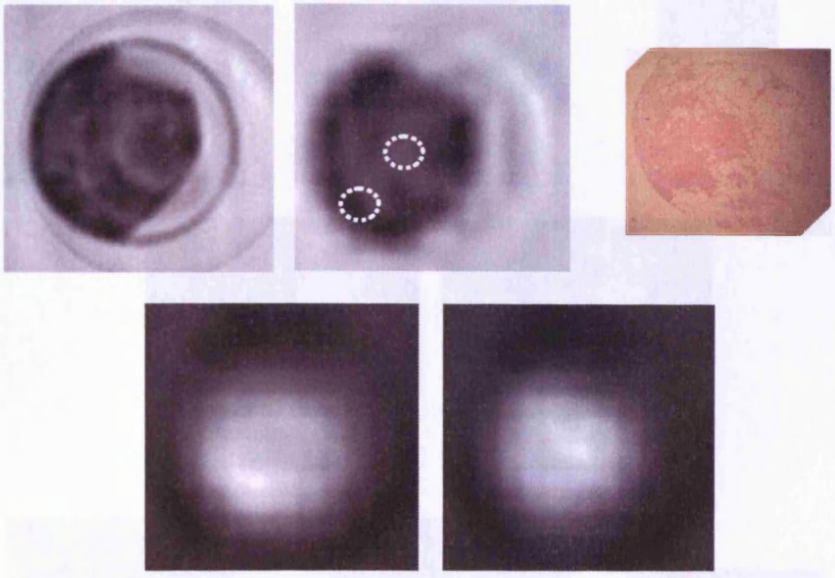

Phantom 16

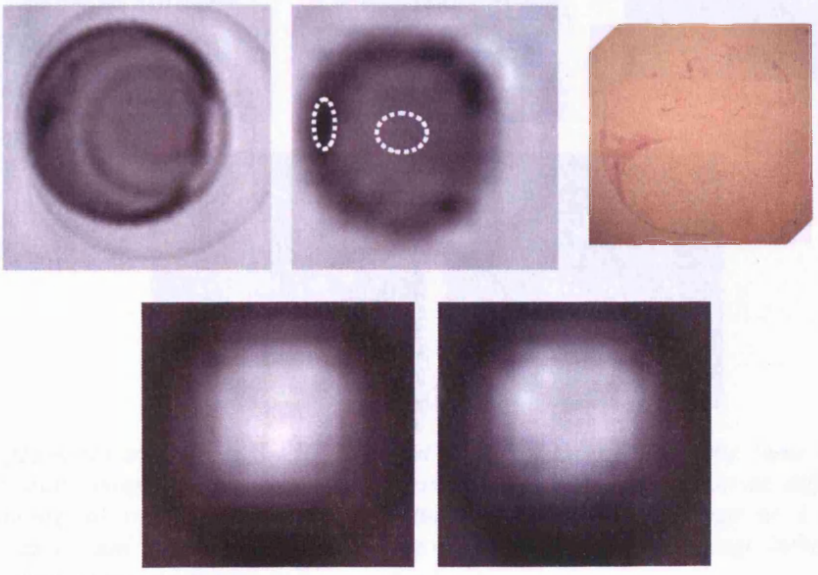

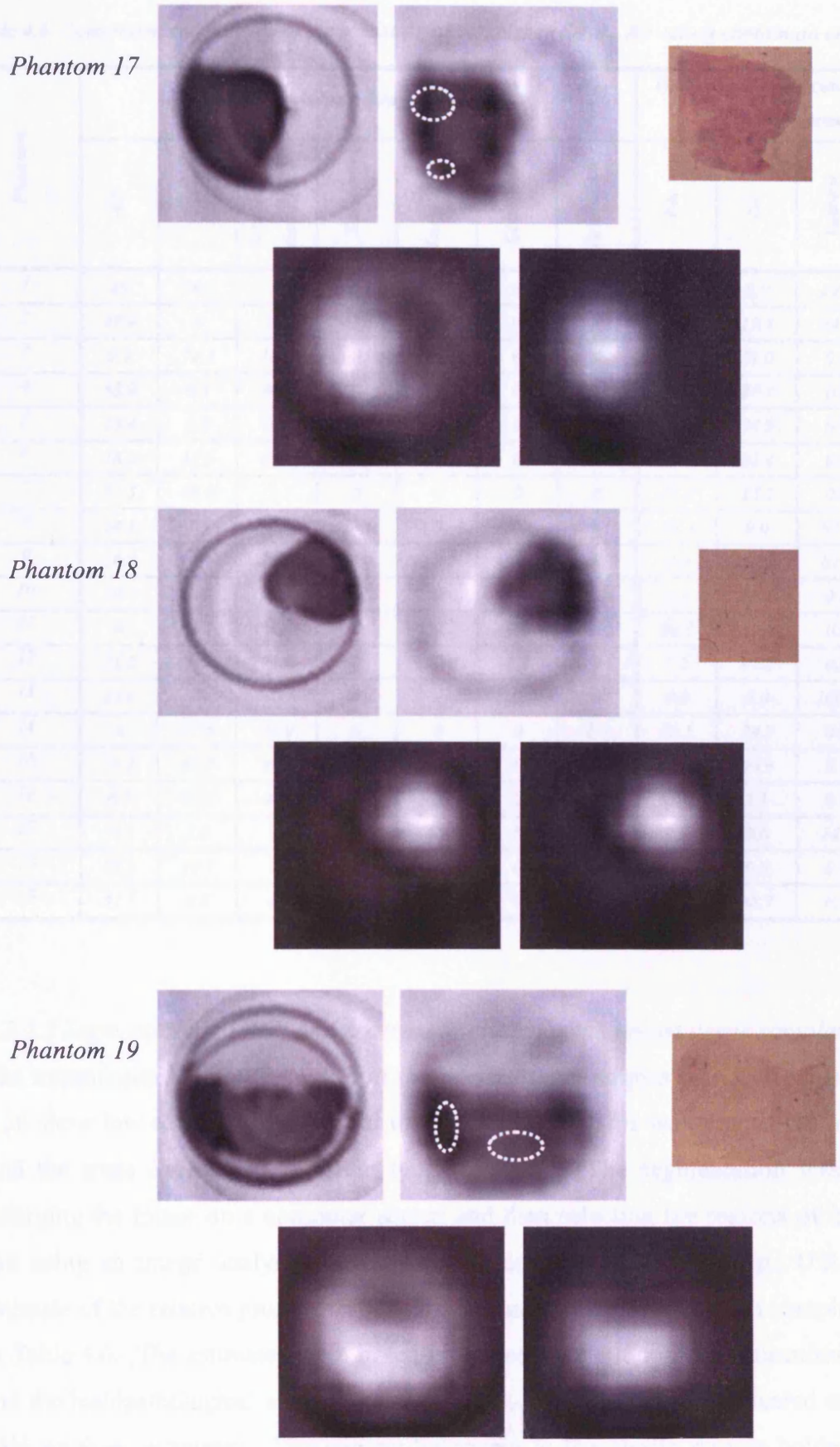

Figure 4.26 *Images of the samples in Set B. Each set of five pictures follows the same lay-out. Top row: Transmission image, Transmission image rebinned to same resolution as diffraction images, Histopathological stained tissue slice. Bottom row: diffraction image at 1.1 nm^{-1}, diffraction image at 1.6 nm^{-1}. The dotted lines on the rebinned transmission image indicate the ROI taken for the contrast measurements.*

Table 4.6 Constituent components of the breast tissue samples in Set B. All values contain an error of ± 3%.

Phantom	Constituents as percentage of total area							Tissue types as percentage of total tissue area			
	Air	Fat	Connective tissue (c.t.)	Tumour	Tumour c.t.	Glandular	Epithelium	Fat	c.t.	Tumour	Other
1	49	36.1	0	14.9	0	0	0	70.8	0.0	29.2	0.0
2	49.9	0	7.6	42.5	0	0	0	0.0	15.2	84.8	0.0
3	9.9	71.2	18.9	0	0	0	0	79.0	21.0	0.0	0.0
4	48.9	6.3	44.8	0	0	0	0	12.3	87.7	0.0	0.0
5	25.4	3.8	70.8	0	0	0	0	5.1	94.9	0.0	0.0
6	18.2	13.6	68.2	0	0	0	0	16.6	83.4	0.0	0.0
7	51.5	35.8	12.7	0	0	0	0	73.8	26.2	0.0	0.0
8	64.1	5.5	0	30.4	0	0	0	15.3	0.0	84.7	0.0
9	26.4	0	28.2	45.4	0	0	0	0.0	38.3	61.7	0.0
10	56.7	1.4	41.6	0	0	0	0.3	3.2	96.1	0.0	0.7
11	0	68.1	31	0	0	0.9	0	68.1	31.0	0.0	0.9
12	21.7	5.7	71.4	0	0	1.2	0	7.3	91.2	0.0	1.5
13	53.4	0	0	46.6	0	0	0	0.0	0.0	100.0	0.0
14	8	67.6	22.9	0	0	0	1.5	73.5	24.9	0.0	1.6
15	26.1	42.7	30.2	0	0	0	1	57.8	40.9	0.0	1.4
16	6.5	87.7	4.8	0	0	0	1	93.8	5.1	0.0	1.1
17	57.9	3.9	0	31.3	6.9	0	0	9.3	0.0	74.3	16.4
18	73.3	26.7	0	0	0	0	0	100.0	0.0	0.0	0.0
19	51.5	4.8	43	0	0	0	0.7	9.9	88.7	0.0	1.4

4.5.2.3 Segmentation of ROI and contrast analysis for the breast tissue samples

The transmission microCT images of the breast tissue samples seen in figures 4.25 and 4.26 show low contrast, high spatial resolution detail. This was segmented in order to find the areas covered by different types of tissue. The segmentation was done by enlarging the image on a computer screen and then selecting the regions of interest by eye using an image analysis drawing tool (Scion Image, Scion Corp., U.S.A.). An estimate of the relative proportions of tissues (and air) making up each sample is given in Table 4.6. The estimates were based on the segmentation of the transmission image and the histopathological analysis of the tissues. Repeat analysis indicated an error of ±3% on these estimates. The content belonging to the plastic sample holder was not included. The table shows that the main components of the samples were fat and connective tissue with occasional large quantities of tumour. Other tissue types

(glandular and epithelial) formed just a small part of the samples except for sample 17 where there was a high quantity of cancerous connective tissue (sarcoma) as well as carcinoma.

The contrast in a transmission image is mainly due to the photoelectric effect, a phenomenon dependent on the atomic number and density of a material. As the tissues found naturally in the breast have similar atomic numbers and densities, the image contrast in the transmission images seen in figures 4.25 and 4.26 is low and individual tissue type identification is not reliable. The diffraction microCT images offer low spatial resolution, high contrast images of the tissue sections, with a limited possibility of individual tissue type identification. The contrast in these images is due to a combination of the density and the coherent scatter characteristics of the tissues; therefore for tissues of similar densities, the contrast is almost entirely due to the coherent scatter coefficients of the individual tissue types. Previous work has indicated that images taken at a momentum transfer value of 1.1 nm^{-1} should highlight normal fatty/fibroglandular tissue, whilst those taken at 1.6 nm^{-1} should highlight diseased, and possibly dense fibroglandular, tissue. The segmentation of the images of the samples allowed them to be categorised by percentage tissue type, as identified by the pathologist. It also allowed comparison of the contrast between tissue types for the different imaging modalities. Values of contrast for the samples in figures 4.25 and 4.26 are given in table 4.7 and a summary of the average tissue contrasts is given in table 4.8. The errors on the contrast in table 4.7 were found using equation 3.1. The areas used to find the contrast values were highlighted in figures 2.25 and 2.26 by dotted lines.

Precise segmentation of the tissue types was difficult for some samples as the different types of cells often intermingle, so although a good estimate of the proportion of the sample containing a certain type of cell may be made, it can prove difficult to choose an adequate region of interest containing predominantly that cell type for contrast analysis purposes. This segmentation problem may explain why the contrast between identical tissue types is much worse in some images than in others. This intermingling also means that, as the size of the scatter data voxels are significantly larger than the size of the transmission data voxels, the diffraction signal for these intermingled portions of

tissues will be an average of the different cell types present in the voxel, rather than relating to a single cell type.

Table 4.7 *Values of contrast for images of samples in set B. Error calculated using equation 3.1.*

Phantom	Tissues involved (% of total tissue)	Image	Contrast (%)	Error in fractional contrast value (%)	Comments
1	Fat (70.8) Tumour (29.2)	Transmission	56.4	2.1	
		Diff at 1.1 nm^{-1}	36.4	0.8	
		Diff at 1.6 nm^{-1}	20.8	0.7	
2	Tumour (84.8) c.t. (15.2)	Transmission	5.4	1.2	c.t. interspersed throughout tumour, so contrast may not give true value
		Diff at 1.1 nm^{-1}	9.4	0.7	
		Diff at 1.6 nm^{-1}	14.3	1.1	
3	Fat (79.0) c.t (21.0)	Transmission	12.0	1.7	
		Diff at 1.1 nm^{-1}	26.2	0.9	
		Diff at 1.6 nm^{-1}	21.4	0.8	
4	Fat (12.3) c.t. (87.7)	Transmission	35.4	2.3	Only a small amount of fat present, so contrast ROI may not be accurate.
		Diff at 1.1 nm^{-1}	28.8	1.8	
		Diff at 1.6 nm^{-1}	26.6	1.0	
5	Fat (5.1) c.t. (94.9)	Transmission	21.1	0.7	Almost no fat in sample, so high level on error on specification of tissue type in ROI.
		Diff at 1.1 nm^{-1}	13.3	0.6	
		Diff at 1.6 nm^{-1}	22.2	0.9	
6	Fat (16.6) c.t. (83.4)	Transmission	11.0	0.6	Fat interspersed throughout c.t., so ROI may not be completely fat/c.t.
		Diff at 1.1 nm^{-1}	2.1	0.3	
		Diff at 1.6 nm^{-1}	0.1	0.2	
7	Fat (73.8) c.t. (26.2)	Transmission	22.5	1.2	c.t. interspersed throughout fat, so c.t. ROI may contain some fat.
		Diff at 1.1 nm^{-1}	0.5	1.0	
		Diff at 1.6 nm^{-1}	11.0	1.4	
8	Fat (15.3) Tumour (84.7)	Transmission	8.7	3.1	
		Diff at 1.1 nm^{-1}	2.5	1.1	
		Diff at 1.6 nm^{-1}	2.7	1.1	
9	Tumour (61.7 c.t. (38.3)	Transmission	5.7	0.2	
		Diff at 1.1 nm^{-1}	4.4	0.2	
		Diff at 1.6 nm^{-1}	2.9	0.3	
10	Fat (3.2 c.t. (96.1)	Transmission	2.8	0.9	Only a very small amount of fat, so ROI may not contain pure fat.
		Diff at 1.1 nm^{-1}	8.5	0.7	
		Diff at 1.6 nm^{-1}	16.5	1.5	
11	Fat (68.1) c.t (31.0)	Transmission	55.3	1.6	Contrast between fat (in middle) and large cap of c.t. at top of image.
		Diff at 1.1 nm^{-1}	21.7	0.6	
		Diff at 1.6 nm^{-1}	5.7	0.3	
11	Fat (68.1) c.t (31.0)	Transmission	25.0	1.0	Contrast between fat and small bit of c.t., also containing some glandular tissue
		Diff at 1.1 nm^{-1}	26.2	1.0	
		Diff at 1.6 nm^{-1}	22.2	1.3	

12	Fat (7.3) c.t. (91.2)	Transmission	27.9	1.4	Contrast between c.t (middle). and small amount of fat at top of image.
		Diff at 1.1 nm^{-1}	2.2	0.6	
		Diff at 1.6 nm^{-1}	27.1	1.1	
12	Fat (7.3) c.t (91.2).	Transmission	19.6	1.4	Contrast between c.t. and larger amount of fat at bottom of image.
		Diff at 1.1 nm^{-1}	7.4	1.0	
		Diff at 1.6 nm^{-1}	31.2	1.3	
14	Fat (73.5) c.t.(24.9)	Transmission	26.6	0.7	c.t. also contains epithelium of a large lactiferous duct.
		Diff at 1.1 nm^{-1}	2.1	0.3	
		Diff at 1.6 nm^{-1}	0.1	1.0	
15	Fat (57.8) c.t.(40.9)	Transmission	38.8	2.8	Fat is interspersed with some c.t.
		Diff at 1.1 nm^{-1}	2.1	0.8	
		Diff at 1.6 nm^{-1}	29.5	1.4	
16	Fat (93.8) c.t.(5.1)	Transmission	40.8	1.3	
		Diff at 1.1 nm^{-1}	44.7	0.9	
		Diff at 1.6 nm^{-1}	41.1	1.1	
17	Tumour (74.3) fat (9.3)	Transmission	1.7	1.1	Tumour contains carcinoma and sarcoma.
		Diff at 1.1 nm^{-1}	23.3	0.8	
		Diff at 1.6 nm^{-1}	33.2	1.0	
19	Fat (9.9) c.t (88.7)	Transmission	13.3	2.8	Small amount of fat spread amongst c.t., so fat ROI may contain c.t.
		Diff at 1.1 nm^{-1}	7.5	0.5	
		Diff at 1.6 nm^{-1}	2.1	1.2	

Table 4.8 *Summary of mean contrast and error values for different tissue types for each imaging technique.*

Tissue types	***Image***	***Contrast (%)***	***Error in fractional contrast value(%)***
Fat/tumour	Transmission	22.3	2.1
	Diffraction at 1.1 nm^{-1}	20.7	0.9
	Diffraction at 1.6 nm^{-1}	18.9	0.9
Fat/c.t.	Transmission	25.1	0.7
	Diffraction at 1.1 nm^{-1}	13.8	0.5
	Diffraction at 1.6 nm^{-1}	18.3	0.7
c.t./tumour	Transmission	5.6	1.5
	Diffraction at 1.1 nm^{-1}	6.9	0.8
	Diffraction at 1.6 nm^{-1}	8.6	1.0

It can be observed from Table 4.7 that the transmission image contrast is higher than the raw diffraction contrast in many of the data sets. This is contradictory to previous work which shows that a much higher level of contrast will result from diffraction imaging, however it must be noted that partial volume effects play a significant role in the diffraction microCT data acquisition and these work to reduce the apparent contrast of the images. Nevertheless, the aim of a DEBI breast tissue imaging system would be to use the diffraction images in conjunction with transmission images. Therefore any contrast that these images show would be used in addition to the contrast already seen in the transmission images.

Table 4.8 shows the mean contrast and error values for the three main constituents of the samples, fat, connective tissue and tumour. Three of the samples show fat/tumour contrast, two show connective tissue/tumour contrast and twelve show connective tissue/fat contrast, with two contrast values being obtained from samples 11 and 12.

A key result highlighted by this data is that both the diffraction data sets - 1.1 nm^{-1} and 1.6 nm^{-1} - showed a higher connective tissue/tumour contrast than the transmission data, although the 1.1 nm^{-1} data lies just inside the bounds of error. The densities of these two tissue types are very similar, resulting in poor transmission contrast. This also means that the contrast seen in the diffraction images is almost entirely due to the coherent scatter coefficients of the two tissues thereby demonstrating the additional information that this technique produces. The increased contrast between connective tissue and tumour in the diffraction images is significant as one of the major problems in diagnosis of breast cancer through transmission mammograms is the lack of discrimination between highly fibrous areas of the breast and carcinoma as both tissue types are very dense and contain very low proportions of fat. The contrast resulting from the diffraction data at 1.6 nm^{-1} is almost 30% higher than the contrast obtained using the transmission data.

The transmission images have the highest level of fat/tumour contrast, however the error on this value is twice that seen for the diffraction contrast and within errors, the transmission value can be considered equal to that of the diffraction image formed at 1.1 nm^{-1}.

The highest fat/connective tissue contrast can be found in the transmission images. The reduction in contrast in the diffraction images compared to the transmission image will be partly due to partial volume effects coming into play in the acquisition of the diffraction data. The system characterisation work using plastic phantoms described in section 4.5.2.1 showed that the diffraction system's spatial resolution is no better than 2 mm. The diameter of the sample holders was 7 mm. The histology images of the samples, which were only a few millimetres in size, frequently show fat and connective tissue cells intermingling and so the diffraction images will show averaged values of the signals from these two tissue types due to the limiting spatial resolution. This voxel effect hypothesis could be tested in future by using collimation in the experiment that

creates a smaller scatter voxel, however this would mean a significant increase in the data acquisition times.

4.5.2.4 Diffraction profiles

One of the prime motivations of this work was the identification of diffraction profiles of pure tissue components, along with the correlation of diffraction profiles of various tissue samples with their histopathological profiles. This would enable a detailed understanding of the tissue sample from its diffraction profile. Previous data has been compromised slightly by uncertainties in the sample purity and composition, whereas for the samples used in this work, that information is known (within the accuracy afforded by the histopathological and segmentation methods used).

Diffraction profiles for the samples were obtained using the technique described in section 4.4.7.1. Each set of diffraction microCT data contained 200 views of the sample and the live time for each spectrum acquisition was 4 seconds. Therefore the total live time for each diffraction profile was 800 seconds, or 13 minutes and 20 seconds. The diffraction profiles were corrected to remove the signal due to the plastic sample holder and to correct for the variation of intensity with energy for the incident x-ray beam. Self-attenuation of the signal by the sample was not taken into account as the tissue samples are not symmetric within the holders and there is a varying amount of air within the beam depending on the orientation of the sample within the beam. This correction could be done by considering the photon path through the centre of the transmission image of the sample at each sample rotation.

It can be seen from Table 4.6 that sample 13 was exclusively tumour and sample 18 exclusively fat (disregarding air). The spectra for these two samples were therefore considered to be pure tumour and fat signatures that the shape of the other samples' profiles could be compared to. The purest connective tissue sample was number 10, where 96.1% of the tissue content was connective tissue and the rest was fat (3.7%) and epithelium (0.7%). This sample's signal was used as the measure for the connective tissue profile. These three signatures are shown in figure 4.27 plotted as relative count rate against momentum transfer. The x-axis error bars will be the same size for all data sets, but have been shown for just the fat set for ease of viewing the plot. A conversion of the y-axis values to the differential linear scatter coefficient per solid angle can be

found in Kidane [2000]; it assumes that at high momentum transfer values, the measured data will approach form factors calculated using the independent atomic model (IAM). The conversion is carried out by fully correcting the data for the samples' self-attenuation and variations in volume and then normalising it, using the higher momentum transfer values, to the IAM form factor values.

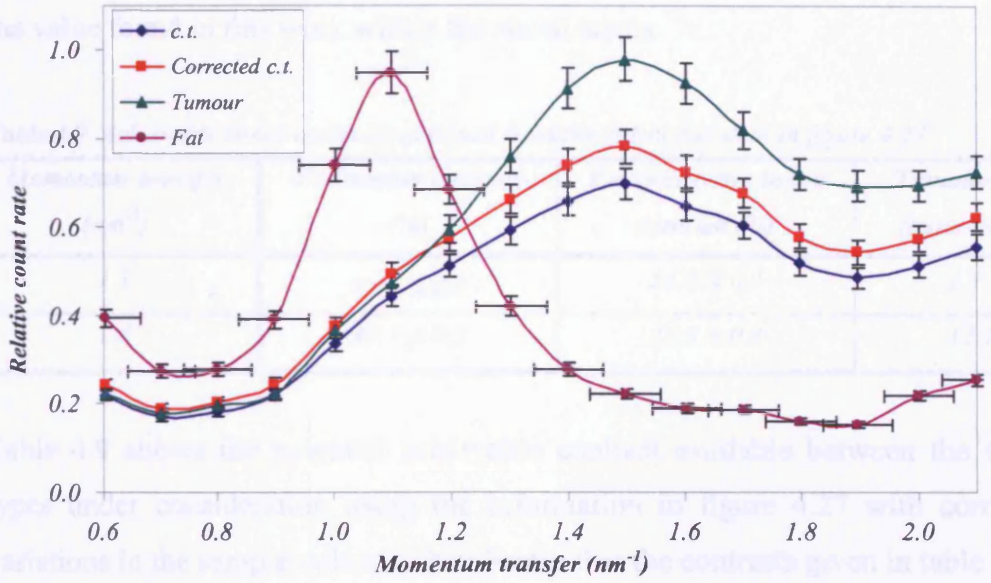

Figure 4.27 *Diffraction signatures from pure fat, pure carcinoma, 96% pure connective tissue and 96% pure connective tissue corrected for volume of sample.*

The fat sample filled just 26.7% of the sample holder, the connective tissue sample filled 43.3% and the tumour filled 46.6%. Figure 4.27 shows that the fat sample has a completely differently shaped signature from the other tissue types. The fat volume was also only ~60% of the volume of the other two samples, indicating that if a complete comparison taking into account the volume of each sample were to take place, the fat peak would be almost twice as high as the peaks from the other two samples. Therefore, for all further analysis of the diffraction signatures of the samples, the signals were corrected to take account of the varying tissue volumes present within the sample holder.

It can be seen from figure 4.27 that the shapes of the signals due to connective tissue and tumour are similar, but their intensities vary. In order to confirm that this is a true phenomenon and not due to the different ratios of tissue and air found in the samples, the signal from the connective tissue was multiplied by a factor that normalised the volume of connective tissue in sample 10 to the volume of tumour in sample 13. This

volume corrected signature is also shown in the figure. It raises the connective tissue signal a little, but it still lies statistically lower than the tumour signal. Another feature of the plot is that the peaks for the carcinoma and connective tissue appear to both occur at a momentum transfer of closer to 1.5 ± 0.06 nm^{-1}, whereas Kidane *et. al.* [1999] showed the carcinoma peak lay at 1.57 ±0.14 nm^{-1} and the connective tissue peak at 1.44 ±0.06 nm^{-1}, however both of these previous values can be assumed to be equal to the value found in this work within the stated errors.

Table 4.9 *Achievable tissue contrasts obtained from the diffraction data in figure 4.27*

Momentum transfer (nm^{-1})	***Fat/tumour contrast (%)***	***Fat/connective tissue contrast (%)***	***Tumour/connective tissue contrast (%)***
1.1	*55.6 ±0.3*	*54.0 ± 0.3*	*2.3 ± 0.02*
1.6	*47.1 ±0.3*	*37.2 ±0.3*	*12.1 ±0.1*

Table 4.9 shows the potential achievable contrast available between the three tissue types under consideration using the information in figure 4.27 with corrections for variations in the sample volume. It indicates that the contrasts given in table 4.8 are less than half the expected values for the fat/tumour and fat/connective tissue contrasts. This can be considered to be mainly due to the difficulties of selecting regions of interest where no significant intermingling of the tissues has occurred. Nevertheless, the tumour/connective tissue contrast is much lower than the fat contrasts in table 4.8 and this ties in well with the results seen in table 4.9.

Samples consisting of a mixture of different tissue types show signature spectra that are a combination of the pure spectra, as can be seen in figure 4.28. This figure shows spectra for pure samples and for samples that are 71% fat and 29% tumour, 38% connective tissue and 62% tumour, and 58% fat and 41% connective tissue. It can be seen, particularly in the cases where fat is involved, that, within statistical error, the mixture spectrum shows the shape of both of the constituent components to different extents. This property will be used to attempt identification of the components of tissue present in a sample.

0.66 nm^{-1} wide windows centred on 1.1 nm^{-1} and 1.5 nm^{-1} were taken for all sample signatures and the total signal within each window found. Figure 4.29 shows these total signal values for the samples plotted against the proportion of a given tissue type in the

sample. The plots are grouped to indicate the predominant tissue type (i.e. forms more than 50%) seen in each sample. The vertical error bars are negligible, whilst the horizontal bars indicate an error on the percentage proportion of tissue type of 3%.

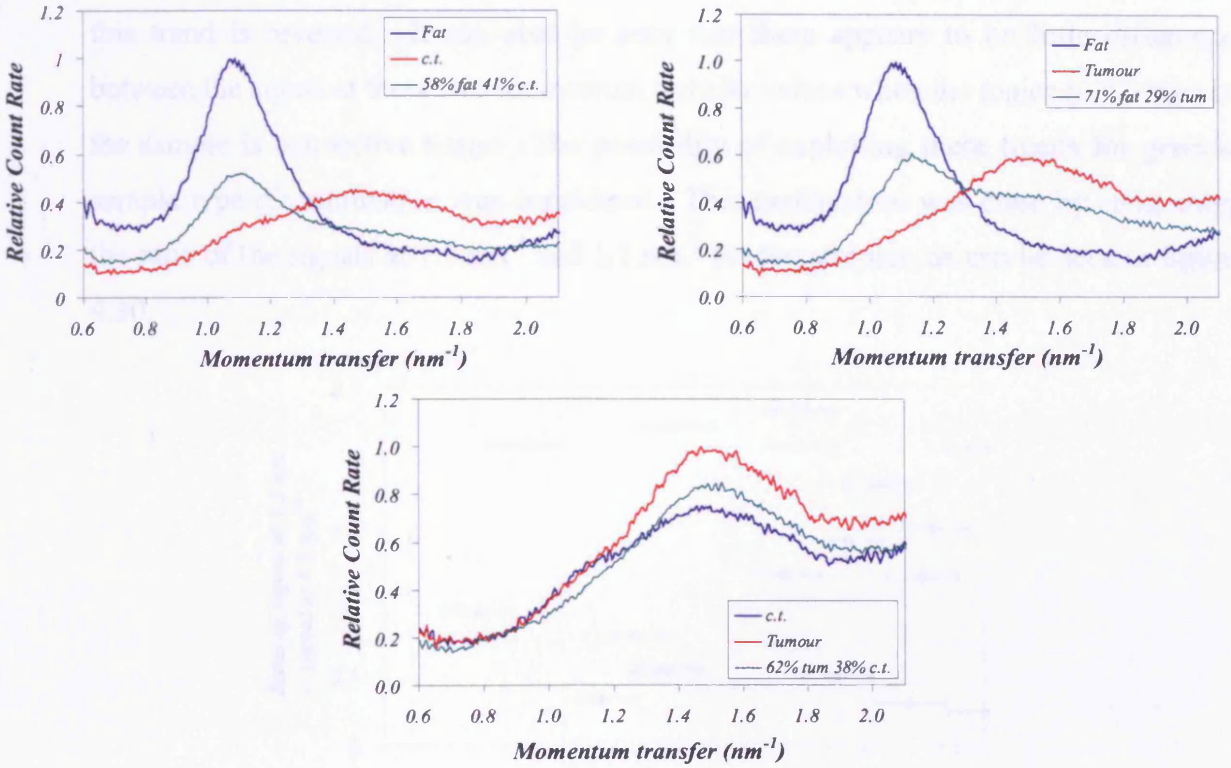

Figure 4.28 *Scatter signatures of samples containing a mixture of tissue types.*

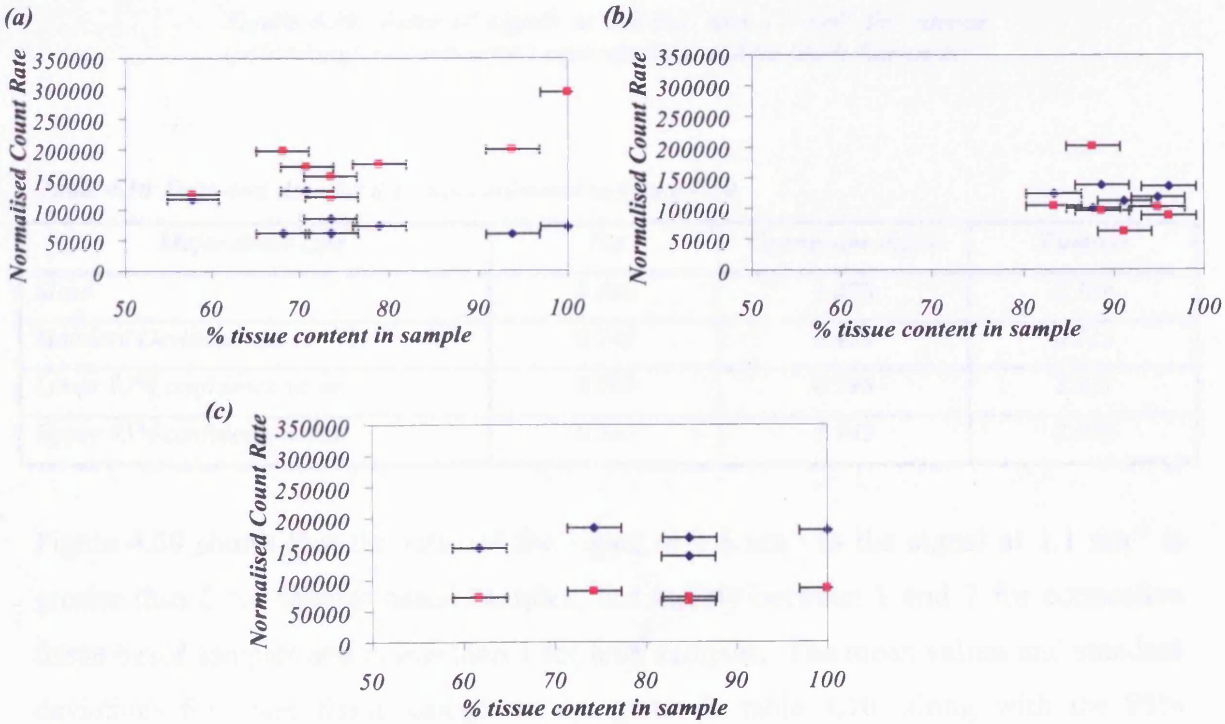

Figure 4.29 *Variation of diffraction signal intensity with % tissue type for (a) fat, (b) connective tissue, (c) tumour. Light squares indicate values for 1.1 nm^{-1} and dark diamonds indicate those for 1.5 nm^{-1}.*

Figure 4.29 shows that, despite errors on the amount of the major tissue present in each sample, definite trends, which can also be inferred from figures 4.27 and 4.28, appear which are dependent on tissue type. When a sample is predominantly fat, the signal at 1.1 nm^{-1} is higher than that at 1.5 nm^{-1} and when the sample is predominantly tumour this trend is reversed. It can also be seen that there appears to be little difference between the signal at these two momentum transfer values when the major tissue type in the sample is connective tissue. The possibility of exploiting these trends for general sample type discrimination was considered. This exploitation was done by comparing the ratio of the signals at 1.5 nm^{-1} and 1.1 nm^{-1} for the samples, as can be seen in figure 4.30.

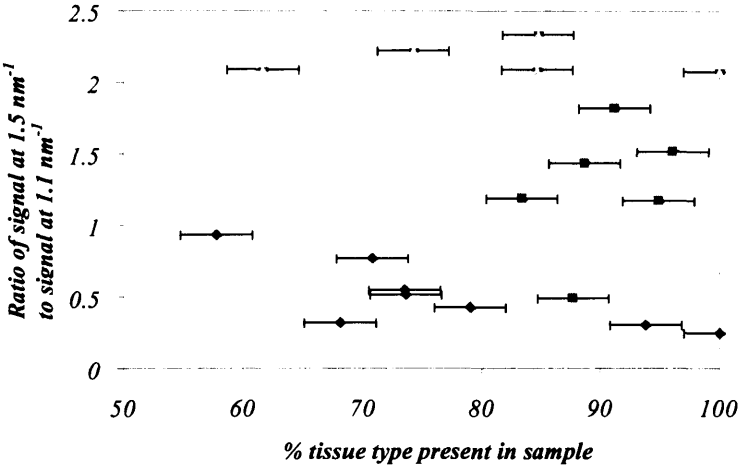

Figure 4.30 *Ratio of signals at 1.5 nm^{-1} and 1.1 nm^{-1} for tumour (pale triangles), connective tissue (squares) and fat (dark diamonds).*

Table 4.10 *Statistical data for the ratios indicated in figure 4.30.*

Major tissue type	*Fat*	*Connective tissue*	*Tumour*
Mean	*0.506*	*1.270*	*2.164*
Standard Deviation	*0.241*	*0.450*	*0.115*
Lower 95% confidence value	*0.305*	*0.798*	*2.021*
Upper 95% confidence value	*0.707*	*1.743*	*2.306*

Figure 4.30 shows that the ratio of the signal at 1.5 nm^{-1} to the signal at 1.1 nm^{-1} is greater than 2 for tumour based samples, lies mainly between 1 and 2 for connective tissue based samples and is less than 1 for fatty samples. The mean values and standard deviations for these tissue categories are given in table 4.10, along with the 95% confidence levels on the means which, due to the small sampling statistics of the data,

were calculated based on a Student's t – distribution [Frodesen *et. al.*, 1979; CUP, 1989].

The 95% confidence levels on the mean values of the distributions of the ratios for the three tissue types do not overlap, indicating that there is a strong possibility that these ratios can be used as an indicator of the major tissue type present in a sample. This was confirmed statistically by using a t-test to assess whether there was a significant difference between the populations that the three sample groups were taken from. The results of this comparison based test are shown in table 4.11. They show that the probability of the samples coming from the same data populations is small – 1% at worst for tumour and connective tissue. This gives significant confidence in using the ratio of the signals at 1.1 nm^{-1} and 1.5 nm^{-1} to indicate the major contributory tissue type in the sample, thus allowing tissue characterisation using diffraction methods alone.

Table 4.11 *t-test results for the comparison of the mean ratio values for the tissue types.*

Major tissue types being compared	***Fat and connective tissue***	***Fat and tumour***	***Tumour and connective tissue***
Degrees of freedom in test	*12*	*11*	*9*
t value	*4.116*	*14.226*	*4.286*
Probability of a null hypothesis standing	*0.2%*	*0.1%*	*1%*

4.6 Conclusions on microCT of small phantoms

The work in this chapter considered two different methods for transmission and diffraction microCT of small phantoms. An L3CCD camera was used in conjunction with a synchrotron radiation source to obtain both transmission and diffraction images and two laboratory based systems were also used; one utilising an amorphous silicon array and a microfocal molybdenum x-ray unit to take transmission images and the other a tungsten x-ray source and an HPGe detector to obtain Spectral Selective Momentum Transfer diffraction images.

Preliminary work was carried out by imaging the breast tissue samples in Set A with the L3CCD camera. This work indicated that the microCT techniques presented a viable

option for imaging small tissue samples and the experiment also highlighted the need for cooling of the samples during imaging in order to preserve the integrity of the pathological markers needed for accurate histopathological analysis of the tissues after imaging. An attenuation correction procedure was used on these images and it was found to make only a very limited difference to the data within them and therefore, as these images were obtained at the lowest x-ray energy used in this work, it was decided that the correction would not need to be applied to all following work in this thesis.

Further to this work, four samples from Set B were imaged using the L3CCD at the synchrotron by Royle *et. al.* [2004]. This time, the resulting images were tied more accurately to the pathological data as the samples were cooled throughout the acquisition and the orientation of the samples was more accurately known.

The samples in Set B were also imaged in the laboratory whilst being cooled to preserve their cellular structures. An amorphous silicon array was used to obtain high spatial resolution transmission images of the samples which were used for tissue type localisation and for comparison with the diffraction images.

The laboratory based diffraction microCT system used an HPGe detector placed behind a collimation system to obtain the signal from tungsten target x-ray photons scattered by the samples into an angle of 6°. The spatial resolution of the system was characterised using plastic test phantoms and the acquisition parameters for the imaging of the breast tissue samples were set using pork and lard human tissue substitute phantoms. The use of a polyenergetic source allowed a complete range of momentum transfer values to be imaged simultaneously. The signal was used both to form a full diffraction spectrum for the samples and to construct diffraction microCT images with a spatial resolution of around 2 mm. This poor spatial resolution meant that partial volume effects were significant in the images, resulting in a poorer image contrast than implied by the samples' total diffraction spectra. This problem can be solved by using more tightly defined collimation in the future, however this would then result in longer acquisition times.

The diffraction spectra obtained in this work correlate with those measured in previous work, however there is a small discrepancy in the situation of the connective tissue and

carcinoma peak signals which can be investigated by further measurements. These spectra allowed a measure of the ultimate achievable contrast with the microCT system to be assessed. This was found to be potentially higher than that found in transmission imaging.

Analysis of the samples' diffraction signatures at selected momentum transfer windows also presented the key result that tissue discrimination using diffraction techniques alone is possible with a probability of 1% or less. The ratio technique described, along with the confidence levels given, needs to be tested by future work using blind trials of unknown samples in order to fully verify its potential in a laboratory situation.

The diffraction microCT has shown that forming images of small tissue samples is possible using this method and the diffraction signatures have shown reliable levels of potential tissue discrimination. Therefore these techniques could be considered as a future biopsy aid, especially if the spatial resolution can be further optimised using finer collimation.

CHAPTER 5

Conclusions

The aim of this thesis has been to investigate the elastic, or coherent, scatter from human breast tissues with a view to incorporating a scatter detector into a standard mammographic unit or creating an x-ray diffraction imaging biopsy tool in the future using a Diffraction Enhanced Breast Imaging (DEBI) technique. An outline of breast tissue pathology and mammography techniques, along with the physical reasoning for using coherent scatter for imaging breast tissues was given in the first, introductory chapter. This chapter also described the effective starting point of the work covered in this thesis.

There have been several studies examining the diffraction signatures of various biological tissues, with breast tissue being measured by groups such as Evans *et. al.* [1991], Kidane *et. al.*, [1999], Lewis *et. al.*, [2000] and Poletti *et. al.*, [2002]. The authors, who considered signals at momentum transfer values between 1.0 and 3.0 nm^{-1}, have all seen differences between the signals for fatty and non-fatty tissues, although this work has been limited by the inhomogeneous nature of the tissue samples. Some initial work was also carried out at UCL to investigate the feasibility of using elastic scatter to form images of life-size breast tissue phantoms [Harris, 2000]. This work was successful and indicated that the technique warranted further investigation. The work in this thesis has therefore been directed towards further analysis of the diffraction signatures of breast tissues, further investigation of the diffraction imaging work illustrated by Harris, and also investigation into using the inelastic properties of tissues to form microCT images of small samples with a view to creating a biopsy aid.

5.1 Diffraction imaging instrumentation

The second chapter of this thesis considered the equipment requirements for obtaining diffraction images of breast tissue. Two techniques may be used for obtaining complete

sets of diffraction data; either an angular dispersive technique or an energy dispersive technique. The collimation and detection needs and practicalities for both techniques were analysed before a decision was made to use an L3CCD with a parallel hole array collimator for angular dispersive imaging and an HPGe detector with a conical collimator for energy dispersive data collection. A more ideal detector that could potentially be utilised for both imaging techniques would be the CDD, however this is not yet commercially available and is currently only a few mm^2 in size.

The L3CCD has been shown to be a photon counting device, so the potential energy resolution of the device was also investigated in this chapter with a view to possible dual energy diffraction imaging in the future. The conclusion of this work was that the Gd_2O_2S:Eu coated L3CCD may well exhibit energy discrimination properties, but they are unquantifiable from the currently available data sets. A new set of images using a range of non-self-attenuating phosphors and a range of monoenergetic sources with energies of 10s of keV should be obtained for clarification of the detector's ability to discriminate between two energies - specifically 18 and 26 keV if the rest of the angular dispersive imaging apparatus is to remain unchanged. The main conclusion of this chapter was however, that although there may be some practical application if energy discrimination of the order of 8 keV can be obtained with the detector, it is by no means essential for the angular dispersive diffraction imaging done in this thesis. These experiments were carried out at a synchrotron radiation source where a dual energy technique utilising x-rays at 18 and 26 keV could not be set up for the experiments.

5.2 Planar diffraction imaging

The following portion of the thesis focussed on diffraction imaging experiments; the third chapter concentrated on planar imaging of large scale phantoms, as originally seen in the work by Harris. Two phantoms were considered in this thesis – one a high contrast Perspex and air phantom and the other a breast tissue phantom. In previous work, images of phantoms were only attained for a single depth within the phantom. The work in this chapter formed images at two depths within each phantom, and the potential was expressed for further depth information to be gained in the future. The images of the high contrast phantom showed large non-uniformities in the diffraction

signal from a uniform layer of the phantom, indicating that the signal was affected by non-uniformly attenuating regions in the phantom. On the basis of this finding, an attenuation correction procedure was proposed that would correct the raw diffraction images to produce images containing purely coherent scatter information. The necessity for the application of this correction in a clinical breast imaging system was also discussed.

Application of the correction resulted in an increase in the uniformity of the high contrast phantom; however the correction was not entirely successful for the breast tissue phantom due to the data acquisition parameters of the equipment used to obtain the transmission image. The grey scale range of the transmission image of the area of interest in the phantom was very narrow due to auto-scaling of the original full-field image by the equipment. Further images for analysis of the correction will need to be taken with a transmission detection system that can offer a full range of grey levels over the area of interest in the phantom.

This attenuation correction also assumed that the x-ray beam path through the tissue for the diffraction data was a straight line following the same path as the transmission image x-rays. This lead to a misregistration of the path due to the fact that the transmission image was taken using a system with fan beam geometry; however this was minimal as the phantoms were placed close to the detector, which lay some distance away from the x-ray source. A larger factor in misregistration occured due to the paths of x-rays scattered close to the front of the phantom deviating significantly from the near-parallel paths in the transmission image. No depth information is available from transmission images and thus a possible solution to this misalignment would be to use the diffraction images themselves to find the depths of densities that can be seen in the transmission images before correction.

Nevertheless, despite an attenuation correction being a requirement for obtaining an image due purely to the coherent scatter characteristics of an object, this work suggested that an attenuation correction may not be necessary for good diagnostic visualisation of breast tissue. The correction had the effect of increasing the diffraction image contrast between normal and cancerous tissue when considering data taken at a momentum transfer value of 1.1 nm^{-1}, but it reduced the contrast for data taken at 1.6 nm^{-1}. This

indicated that a selective correction at specific momentum transfer values may be more beneficial for diagnosis, although this could potentially fail as it would not fully take into account the fact that the diffraction images are formed from data acquired from different depths in the breast, each of which may contain different tissue types.

A secondary aim of this chapter was to examine the spatial resolution offered by the planar diffraction imaging system. The high contrast phantom consisted of a 3 cm thick Perspex block with holes of 1 mm, 2 mm, 4 mm and 8 mm diameter drilled through 1 cm of it. The diffraction images of this phantom clearly showed the 1 mm diameter hole, despite the use of a collimator with dimensions of half this size. The visibility of this feature can be considered very encouraging for the spatial resolution of the planar diffraction imaging system. A reduction in the collimation hole dimensions to increase the spatial resolution of the system could be implemented, but it should be noted that a reduction in the partial volume effects will result in a corresponding increase in the acquisition time due to the reduction of the number of photons reaching the detector. This will also lead to a larger error on the data due to detector pixel non-uniformities and an increase in the experimental alignment time, which is an important issue to consider when undertaking experiments in a time-limited environment, such as a synchrotron beamline.

One of the end aims of the DEBI project is to combine the imaging technique used in these planar diffraction imaging experiments with a standard digital line scan mammography unit [Kidane, 2000] to create high spatial resolution, increased contrast images of the breast. Once a suitable viewing system that will present diagnostically useful information in a user-friendly format is created, the depth information realised by obtaining diffraction images of different slices of the breast may be of benefit to clinicians and will create a third dimension in planar breast imaging.

5.3 MicroCT and diffraction signatures

The fourth chapter of this thesis focussed on the analysis of small tissue samples using microCT techniques with two aims in mind; the first being to analyse the potential of using diffraction microCT as a future biopsy aid and the second being to build on

previous breast tissue diffraction measurements, such as those by Kidane *et. al.* [1999], with a view to quantifying the exact tissue content of individual samples for full characterisation of their diffraction signatures. This work found that sample cooling was necessary in order to fully preserve the cytologic structural integrity of the samples during data acquisition. A cooling system was proposed, designed and constructed, and proved adequate for the further experiments that utilised it, leading to accurate histopathological analysis of the tissue samples.

Maps of the pathological content of these samples were obtained using laboratory and synchrotron based energy and angular dispersive techniques; these were then compared to histopathological analyses of the samples. The diffraction signatures of the samples were also obtained whilst running the laboratory angular dispersive diffraction microCT acquisitions.

Following on from the planar imaging work in the previous chapter, an attenuation correction was applied to the diffraction microCT images taken using 18 keV synchrotron radiation. The correction was found to have only a marginal effect on these images, and there was a possibility that this could have been due to artefacts present in the transmission images used to correct the diffraction data. It can also be expected that as the energy of the x-rays is increased, the differences in attenuation between different breast tissues will decrease; therefore, as this correction was carried out on images formed at the lowest energy used in this work, it can be assumed that the correction will also have an even smaller effect on the remainder of the images in this work. Therefore, as the effect of the correction would be small and may contain errors due to the quality of the transmission images used, it was not applied to the remainder of the images in the thesis.

The diffraction microCT images indicated areas of differing tissue types within the samples at a far lower spatial resolution than the transmission images. The contrast seen in these images was less than predicted mainly due to the partial volume effects created by the poor spatial resolution. Future work may need to utilise smaller CT translation steps with tighter primary collimation in order to fully analyse the realistic potential contrast of this technique, nonetheless this work has shown that diffraction

microCT is a viable option for imaging small tissue types, creating images which can be taken simultaneously with, and used in conjunction with, transmission images.

The diffraction data was also used to form total diffraction profiles for all samples, which were found to compare favourably with published data [Kidane *et. al.*, 1999; Evans *et. al.*, 1991; Poletti *et. al.*, 2002]. The laboratory based microCT images were compared with histopathologically stained slices of the samples in order to assess the contrasts available between differing tissue types and also to segment the tissue types for categorisation of the diffraction profiles. Fatty tissue exhibits a differently shaped signature if compared to both tumour and connective tissue, peaking at 1.1 ± 0.06 nm^{-1}, as opposed to 1.5 ± 0.06 nm^{-1}; also, despite showing the same signal shape, there appears to be a difference in the signal intensity between tumour and connective tissue. These signature shapes were fully classified by tissue type and a statistical analysis showed that they can be used with confidence for categorisation of samples by their main tissue type (fat, connective tissue or tumour).

This thesis has drawn together several aspects of the UCL DEBI project. Work has been executed on the analysis of the instrumentation that will be needed for a clinical system and the raw data corrections that would be used. Work to further the current knowledge on the coherent scatter properties of individual tissue types has also been successfully carried out, along with the construction, commissioning and use of a laboratory based diffraction microCT system for small tissue samples. Each of these aspects of the work has produced conclusions which will benefit future work in this area.

In conclusion, this thesis has shown that with suitable instrumentation, basic tissue discrimination based on the coherent scatter signal from a sample is possible, and that DEBI can be utilised both in planar mammography and in biopsy procedures to create additional information that can be used to aid the diagnosis of disease in breast tissue.

References

L. **Alexander**, H.P. **Klug**, *Basic Aspects Of X-ray Absorption In Quantitative Diffraction Analysis Of Powder Mixtures*, Analytical Chemistry, **20**(10), 886-889, (1948).

D. **Alexiev**, N. Dytlewski, M.I. Reinhard, L. Mo, *Characterisation of single-crystal mercuric iodide*, Nuclear Instruments and Methods in Physics Research A, **517**(1-3), 226-229, (2004).

L.E. **Antonuk**, K.W. Jee, Y. El-Mohri, M. Maolinsky, S. Nassif, X. Rong, Q. Zhao, J.H. Siewerdsen, R.A. Street, K.S. Shah, *Strategies to improve the signal and noise performance of active matrix, flat-panel imagers for diagnostic x-ray applications*, Medical Physics, **27**(2), 289-306, (2000).

F. **Arfelli**, A. Bravin, G. Barbiellini, G. Cantatore, E. Castelli, M. Di Michiel, P. Poropat, R. Rosei, M. Sessa, A.Vacchi, L. Dalla Palma, R. Longo, S. Bernstorff, A. Svoia, G. Tromba, *Digital mammography with synchrotron radiation*, Review of Scientific Instruments, **66**(2), 1325- 1328, (1995).

F. **Arfelli**, G. Barbiellini, V. Bonvicini, A. Bravin, G. Cantatore, E. Castelli, P. Cristaudo, M. Di Michiel, R. Longo, A. Olivo. S. Pani, D. Pontoni, P. Poropat, M. Prest, A. Rashevsky, G. Tromba, A. Vacchi, F. Tomasini, *SYRMEP: an innovative detection system for soft X-rays*, Nuclear Instruments and Methods in Physics Research A, **392**(1-3), 188-191, (1997).

K. **Arisaka**, *New trends in vacuum-based photon detectors*, Nuclear Instruments and Methods in Physics Research A, **442**, 80-90, (2000).

J.E. **Baciak**, Z. **He**, *Long term stability of 1-cm thick pixelated HgI_2 gamma-ray spectrometers*, IEEE Transactions on Nuclear Science, **51**(4), 1886-1894, (2004).

K.M. **Balakrishna**, N. Govinda Nayak, N. Lingappa, K. Siddappa, *K fluorescence yield measurements in rare earth and heavy elements*, Journal of Physics B: Atomic, Molecular and Optical Physics, **27**, 715-720, (1994).

E. **Banks**, G. Reeves, V. Beral, D. Bull, B. Crossley, M. Simmonds, E. Hilton, S. Bailey, N. Barrett, P. Briers, R. English, A. Jackson, E. Knutt, J. Lavelle, L. Rockall, M.G. Wallis, M. Wilson, J. Patnick, *Influence of personal characteristics of individual women on sensitivity and specificity of mammography in the Million Women Study: cohort study*, British Medical Journal, **329**, 477-479, (2004).

R.C. **Barroso**, R.T. Lopes, E.F.O. de Jesus, L.F. Oliveira, *X-ray diffraction microtomography using synchrotron radiation*, Nuclear Instruments and Methods in Physics Research A, **471**(1-2), 75-79, (2001).

M.J. **Berger**, J.H. Hubbell, S.M. Seltzer, J.S. Coursey, D.S. Zucker, *XCOM: Photon Cross Section Database* (version 1.2, used online on 13 Jan 2005), Available at: http://physics.nist.gov/xcom, National Institute of Standards and Technology, Gaithersbury, MD, (1999).

E. **Beuville**, R. Cahn, B. Cederström, M. Danielsson, A. Hall, B. Hasegawa, L. Luo, M. Lundqvist, D. Nygren, E. Oltman, J. Walton, *High Resolution X-ray Imaging Using a Silicon Strip Detector*, IEEE Transactions on Nuclear Science, **45**(6), 3059-3063, (1998).

S.C. **Blankespoor**, X. Wu, K. Kalki, J.K. Brown, H.R. Tang, C.E. Cann, B.H. Hasegawa, *Atteunation Correction of SPECT Using X-Ray CT on an Emission-Transmission CT System: Myocardial Perfustion Assessment*, IEEE Transactions on Nuclear Science, **43**(4), 2263-2274, (1996).

R.G. **Blanks**, S.M. Moss, C.E. McGahan, M.J. Quinn, P.J. Babb, *Effect of NHS breast screening programme on mortality from breast cancer in England and Wales, 1990-8: comparison of observed with predicted mortality*, British Medical Journal, **321**(7262), 665-669, (2000).

S.E. **Bohndiek**, *Tomographic Studies on Diffraction Enhanced Breast Imaging*, Vacation Project Report, (2004).

B.E. **Burke**, J.A. Gregory, A.H. Loomis, M. Lesser, M.W. Bautz, S.E. Kissel, D.D. Rathman, R.M. Osgood III, M.J. Cooper, T.A. Lind, G.R. Ricker, *CCD Soft-X-ray Detectors With Improved High-and Low-Energy Performance*, IEEE Transactions on Nuclear Science, **51**(5), 2322-2327, (2004).

C.L. **Carter**, C. Allen, D.E. Henson, *Relation of tumor size, lymph node status, and survival in 24,740 breast cancer cases*, Cancer, **63**, 181-187, (1989).

A. **Castoldi**, C. Guazzoni, E. Longoni, E. Gatti, P. Rehak, L. Strüder, *Conception and Design Criteria of a Novel Silicon Device for the Measurement of Position and Energy of X Rays*, IEEE Transactions on Nuclear Science, **44**(5), 1724-1732, (1997).

A. **Castoldi**, C. Guazzoni, *A New Position Sensing X-Ray Detector: Working Principle and Experimental Results*, IEEE Transactions on Electron Devices, **46**(2), 329-334, (1999).

A. **Castoldi**, C. Guazzoni, P. Rehak, L. Strüder, *Spectroscopic-Grade X-Ray Imaging up to 100-kHz Frame Rate With Controlled-Drift Detectors*, IEEE Transactions on Nuclear Science, **48**(4), 982-986, (2001).

A. **Castoldi**, G. Cattaneo, A. Galimberti, C. Guazzoni, P, Rehak, L. Strüder, *Room-Temperature 2-D X-ray Imaging With the Controlled Drift Detector*, IEEE Transactions on Nuclear Science, **49**(3), 989-994, (2002).

A. **Castolidi**, A. Galimberti, C. Guazzoni, P. Rehak, L. Strüder, *X-ray imaging and spectroscopy with Controlled-Drift Detectors: experimental results and perspectives*, Nuclear Instruments and Methods in Physics Research A, **512**(1-2), 250-256, (2003).

A. **Castoldi**, A. Galimberti, C. Guazzoni, P. Rehak, L. Strüder, *Towards large area X- and gamma-ray imagers based on Controlled Drift Detectors*, Nuclear Instruments and Methods in Physics Research A, **518**(1-2), 426-428, (2004).

X.F. **Cheng**, J.M. Mao, R. Bush, D.B. Kopans, R.H. Moore, M. Chorlton, *Breast cancer detection by mapping haemoglobin concentration and oxygen saturation*, Applied Optics, **42**(31), 6412-6421, (2003).

M. **Chevalier**, P. Moran, J.I. Ten, T. Cepeda, E. Vano, *Patient dose in digital mammography*, Medical Physics, **31**(9), 2471-2479, (2004).

R. **Choe**, A. Corlu, K. Lee, T. Durduran, S.D. Konecky, M. Grosicka-Koptyra, S.R. Arridge, B.J. Czerniecki, D.L. Fraker, A. DeMichele, B. Chance, M.A. Rosen, A.G. Yodh, *Diffuse optical tomography of breast cancer during neoadjuvant chemotherapy: A case study with comparison to MRI*, Medical Physics, **32**(4), 1128-1239, (2005).

CUP - SMP Advanced Tables, 3rd Edition, *publ.* Cambridge University Press, (1989).

O.S. **Desouky**, W.M. Elshemey, N.S. Selim, A.H. Ashour, *Analysis of low-angle x-ray scattering peaks from lyophilized biological samples*, Physics in Medicine and Biology, **46**(8), 2099-2106, (2001).

W.D. **Dupont**, D.L. **Page**, *Risk factors in women with proliferative breast disease*, New England Journal of Medicine, **312**, 146-151, (1985).

e2v technologies ltd., private communication, (2002).

e2v technologies ltd., *CCD65 Series Ceramic Pack*, product data sheet. Available at: http://e2vtechnologies.com/datasheets/l3vision_ccds/ccd65_series_ceramic_pack.pdf, Downloaded Jan 2003.

Elettra, SYRMEP beamline data, Available online at: http://www.elettra.trieste.it/experiments/beamlines/syrmep/index.html, downloaded January 2005.

I.O. **Ellis**, M. Galea, N. Broughton, A. Locker, R.W. Blamey, C.W. Elston, *Pathological prognostic factors in breast cancer II. Histological Type. Relationship with survival in a large study with long-term follow-up*, Histopathology, **20**, 479-489, (1992).

C.W. **Elston**, I.O. **Ellis**, *Pathological prognostic factors in breast-cancer 1. The value of histological grade in breast-cancer – experience from a large study with long-term follow-up*, Histopathology, **19**(5), 403-410, (1991).

S.H. **Evans**, D.A. Bradley, D.R. Dance, J.E. Bateman, C.H. Jones, *Measurement of small-angle photon scattering for some breast tissues and tissue substitute materials*, Physics in Medicine and Biology, **36**(1), 7-18, (1991).

M. **Fernández**, J. Keyriläinen, R. Serimaa, M. Torkkeli, M.-L. Karjalainen-Lindsberg, M. Tenhunen, W. Thomlinson, V. Urban, P. Suortti, *Small-angle x-ray scattering studies of human breast tissue samples*, Physics in Medicine and Biology, **47**(4), 577-592, (2002).

V.K. **Frantz**, J.W. Pickren, G.W. Melcher, H. Auchincloss, *Incidence of chronic cystic disease in so called 'normal breasts': a study based on 225 postmortem examinations*, Cancer, **4**, 762-783, (1951).

A.G. **Frodesen**, O. Skjeggestad, H. Tøfte, *Probability and statistics in particle physics*, 1st Edition, *publ.* Universitetsforlaget, Oslo, Norway, (1979).

K. **Geraki**, M. Farquharson, D. Bradley, *X-ray fluorescence and energy dispersive X-ray diffraction for the characterisation of breast tissue*, Radiation Physics and Chemistry, **71**(3-4), 969-970, (2004).

G.C. **Giakos**, S. Suryanarayanan, R. Guntupalli, J. Odogba, N. Shah, S. Vedantham, S. Chowdhury, K. Mehta, S. Sumrain, N. Patnekar, A. Moholkar, V. Kumar, R.E. Endorf, *Detective Quantum Efficiency [DQE(0)] of CZT Semiconductor Detectors for Digital Radiography*, IEEE Transactions on Instrumentation and Measurement, **53**(6), 1479-1484, (2004).

M. **Gombia**, A. Tartari, M. Gambaccini, G. Di Domenico, D. Bollini, A. Del Guerra, *Attenuation compensation for breast tissue in combined CT/SPECT devices dedicated to mammography*, Nuclear Instruments and Methods in Physics Research A, **497**(1), 150-156, (2003).

J.A. **Griffiths**, R.D. Speller, G.J. Royle, J.A. Horrocks, A. Olivo, S. Pani, R. Longo, D. Dreossi, S.H. Spencer, M.S. Robbins, D.P. Clifford, A.M. Hanby, *X-ray diffraction CT of excised breast tissue sections: first results from Elettra*, IEEE Nuclear Science Symposium & Medical Imaging Conference Record, Portland, U.S.A., (2003).

J.A. **Griffiths**, Royle G.J., R.D. Speller, J.A. Horrocks, A. Olivo, S. Pani, R. Longo, S.H. Spencer, M.S. Robbins, D.P. Clifford, A.M. Hanby, *Diffraction Enhanced Breast Imaging: assessment of realistic system requirements to improve the diagnostic capabilities of mammography*, IEEE Nuclear Science Symposium & Medical Imaging Conference Record, Portland, U.S.A., (2003).

A.M. **Hanby**, Pathological details of tissue samples, Personal communication, (2004).

G. **Harding**, B. Schreiber, *Coherent X-ray scatter imaging and its applications in biomedical science and industry*, Radiation Physics and Chemistry, **56**(1-2), 229-245, (1999).

E.J. **Harris**, G.J. Royle, R.D. Speller, S. Spencer, W. Suske, *Evaluation of a Novel CCD Camera for Dose Reduction in Digtial Radiography*, IEEE Nuclear Science Symposium & Medical Imaging Conference Record, Lyon, France, 2000, **3**, 23_53-23_58, (2001).

E.J. **Harris**, *Application of a novel CCD technology to medical imaging*, Ph.D. thesis, University of London, (2002).

E.J. **Harris**, G.J. Royle, R.D. Speller, J.A. Griffiths, G. Kidane, A.M. Hanby, *Evaluation of a novel low light level (L3Vision) CCD technology for application to diffraction enhanced breast imaging*, Nuclear Instruments and Methods in Physics Research A, **513**(1-2), 27-31, (2003).

J.C. **Hebden**, H. Veenstra, H. Dehghani, E.M.C. Hilman, M. Schweiger, S.R. Arridge, D.T. Delpy, *Three-dimensional time-resolved optical tomography of a conical breast phantom*, Applied Optics, **40**(19), 3278-3287, (2001).

J.C. **Hebden**, A. Gibson, T. Austin, R.M. Yusof, N. Everdell, D.T. Delpy, S.R. Arridge, J.H. Meek, J.S. Wyatt, *Imaging changes in blood volume and oxygenation in the newborn infant brain using three-dimensional optical tomography*, Physics in Medicine and Biology, **49**(7), 1117-1130, (2004).

R.E. **Hendrick**, *Breast MRI: Physics to Maximise Its Sensitivity and Specificity to Breast Cancer*, Medical Physics, **31**(6), 1737-1737, (2005).

S.R. **Hintz**, D.A. Benaron, A.M. Siegel, A. Zourabian, D.K. Stevenson, D.A. Boas, *Bedside functional imaging of the premature infant brain during passive motor activiation*, Journal of Perinatal Medicine, **29**(4), 335-343, (2001).

D. **Holder** *et. al.*, Internal Communication, Department of Medical Physics & Bioengineering, University College London, (2005).

N. **Houssami**, L. Irwig, C. Loy, *Accuracy of combined breast imaging in young women*, The Breast, **11**, 36-40, (2002).

J.H. **Hubbell**, S.M. **Seltzer**, *Tables of x-ray mass attenuation coeffieicnts and mass energy absorption coefficients*, Version 4.1, National Institute of Standards and Technology, Gaithersbury, MD, U.S.A., Available at: http://physics.nist.gov/xaamdi, (2004).

J.H. **Hubbell**, W.J. Veigele, E.A. Briggs, R.T. Brown, D.T. Cromer, R.J. Howerton, *Atomic form factors, incoherent scattering functions and photon scattering cross-sections*, Journal of Physical Chemistry Reference Data, **4**, 471, (1975).

J. **Hynecek**, *Impactron – A New Solid State Image Intensifier*, IEEE Transactions on Electron Devices, **48**(10), 2238-2241, (2001).

ICRU, *Tissue Substitutes in Radiation Dosimetry and Measurement*, Report 44 of the International Commission on Radiation Units and Measurements, *publ.* Bethesda, MD, U.S.A., (1989).

L. **Irwig**, N. Houssami, C. van Vliet, *New technologies in screening for breast cancer: a systematic review of their accuracy*, British Journal of Cancer, **90**, 2118-2122, (2004).

V. **James**, J. Kearsley, T. Irving, Y. Amemiya, D. Cookson, *Using hair to screen for breast cancer*, Nature, **398**, 33-34, (1999).

R.A. **Jensen**, D.L. Page, W.D. Dupont, L.W. Rogers, *Invasive breast cancer risk in women with sclerosing adenosis*, Cancer, **64**, 1977-1983, (1989).

P. **Jerram**, P. Pool, R. Bell, D. Burt, S. Bowring, S. Spencer, M. Hazelwood, I. Moody, N. Catlett, P. Heyes, *The LLLCCD: Low Light Imaging without the need for an intensifier*, Technical Report, Marconi Technologies ltd. Available from: http://www.marconitech.co.uk/downloads/l3vision/4306a_20.pdf, Downloaded Jan 2001.

H.E. **Johns**, J.R. **Cunningham**, *The Physics of Radiology*, Fourth edition, *publ.* Charles C. Thomas, Springfield, Illinois, U.S.A. (1983).

P.C. **Johns**, M.J. **Yaffe**, *X-ray characterization of normal and neoplastic breast tissues*, Physics in Medicine and Biology, **32**(6), 675-695, (1987).

G.A. **Kastis**, H.B. Barber, H.H. Barrett, S.J. Balzer, D. Lu, D.G. Marks, G. Stevenson, J.M. Woolfenden, M. Appleby, J. Tueller, *Gamma-Ray Imaging Using a CdZnTe Pixel Array and a High-Resolution, Parallel-Hole Collimator*, IEEE Transactions on Nuclear Science, **47**(6), 1923-1927, (2000).

G. **Kidane**, R.D. Speller, G.J. Royle, A.M. Hanby, *X-ray scatter signatures for normal and neoplastic breast tissues*, Physics in Medicine and Biology, **44**(7), 1791-1802, (1999).

G. **Kidane**, *Breast Tissue Characterisation Using Low Angle X-ray Scattering*, Ph.D. Thesis, University of London, (2000).

G.F. **Knoll**, *Radiation Detection And Measurement*, 3rd Edition, *publ.* John Wiley & Sons, Inc., (1999).

J. **Kosanetzky**, B. Knoerr, G. Harding, U. Neitzel, *X-ray diffraction measurements of some plastic materials and body tissues*, Medical Physics, **14**(4), 526-532, (1987).

M. **Kreige**, C.T.M. Brekelmans, C. Boetes, P.E. Besnard, H.M. Zonderland, I.M. Obdeijn, R.A. Manoliu, T. Kok, H. Peterse, M.M.A. Tilanus-Linthorst, S.H. Muller, S. Meijer, J.C. Oosterwijk, L.V.A.M. Beex, R.A.E.M. Tollenaar, H.J. de Koning, E.J.T. Rutgers, J.G.M. Klijn, *Efficacy of MRI and mammography for breast-cancer screening in women with a familial or genetic predisposition*, New England Journal of Medicine, **351**(5), 427-437, (2004).

P. **Lazarev**, M. Paukshto, N. Pelc, A. Sakharova, *Human Tissue X-ray Diffraction: Breast, Brain and Prostate*, Proceedings of the 22nd Annual IEEE EMBS Conference, **4**, 3230-3233, (2000).

R.A. **Lewis**, K.D. Rogers, C.J. Hall, E. Towns-Andrews, S. Slawson, A. Evans, S.E. Pinder, I.O. Ellis, C.R.M. Boggis, A.P. Hufton, D.R. Dance, *Breast cancer diagnosis using scattering X-rays*, Journal of Synchrotron Radiation, **7**, 348-352, (2000).

M. **Liberman**, F. Sampalis, D.S. Mulder, J.S. Sampalis, *Breast cancer diagnosis by scintimammography: a meta-analysis and review of the literature*, Breast Cancer Research and Treatment, **80**, 115-126, (2003).

F. **Livet**, F. Bley, J. Mainville, R. Caudron, S.G.J. Mochrie, E. Geissler, G. Dolino, D. Abernathy, G. Grübel, M. Sutton, *Using direct illumination CCDs as high-resolution area detectors for X-ray scattering*, Nuclear Instruments and Methods in Physics Research A, **451**(3), 596-609, (2000).

J.G. **Mainprize**, N.L. Ford, Shi Yin, T. Tümer, M.J. Yaffe, *A slot-scanned photodiode-array/CCD hybrid detector for digital mammography*, Medical Physics, **29**(2), 214-225, (2002).

A. **Malich**, T. Böhm, M. Facius, I. Kleinteich, M. fleck, D. Sauner, R. Anderson, W.A. Kaiser, *Electrical impedence scanning as a new imaging modality in breast cancer detection – a short review of clinical value on breast application, limitations and perspectives*, Nuclear Instruments and Methods in Physics Research A., **497**(1), 75-81, (2003).

M. **Maolinbay**, Y. El-Mohri, L.E. Antonuk, K.W. Jee, S. Nassif, X. Rong, Q. Zhao, *Additive noise properties of active matrix flat-panel imagers*, Medical Physics, **27**(8), 1841-1854, (2000).

R.W. **McDivett**, J.A. Stevens, N.C. Lee, P.A. Wingo, G.L. Rubin, D. Gersell, *Histologic types of benign breast disease and the risk for breast cancer. The Cancer and Steroid Hormone Study Group*, Cancer, **69**, 1408-1414, (1992).

R.W. **McDivett**, F.W. Stewart, J.W. Berg, *Tumors of the breast*, Chapter in *Atlas of Tumor Pathology, II, publ.* Washington D.C. Armed Forces Institute of Pathology, (1969).

K.M. **Meek**, A.J. Quantock, *The Use of X-ray Scattering Techniques to Determine Corneal Ultrastructure*, Progress in Retinal and Eye Research, **20**(1), 95-137, (2001).

Melcor Corporation, U.S.A., *Product data sheet for SH1.0-95-05L thermo-electric cooling device*, Available online at:
http://www.melcor.com/CENTER%20HOLE%20SERIES/SH1.0-95-05L.PDF,
downloaded June 2004.

Q.R. **Morrissey**, N.R. Waltham, R. Turchetta, M.J. French, D.M. Bagnall, B.M. Al-Hashimi, *Design of a 3 μm pixel linear CMOS sensor for earth observation*, Nuclear Instruments and Methods in Physics Research A, **512**(1-2), 350-357, (2003).

S.M. **Moss**, M. Michel, J. Patnick, L. Johns, R.G. Blanks, J. Chamberlain, *Results of the NHS breast screening programme 1990-1993*, Journal of Medical Screening, **2**, 186-190, (1995).

T.M. **Murad**, G. Contesso, H. Mouriesse, *Papillary tumors of large lactiferous ducts*, Cancer, **48**, 122-133, (1981).

T. **Nishibayashi**, *Description of the UCL* L3CCD, personal communication, (2004).

H.J. **Norris**, H.B. **Taylor**, *Relationship of histological features to behaviour of cystosarcoma phyllodes: analysis of 94 cases*, Cancer, **20**, 2090-2099, (1967).

R.J. **Ott**, J. MacDonald, K. Wells, *The performance of a CCD digital autoradiography imaging system*, Physics in Medicine and Biology, **45**(7), 2011-2027, (2000).

A. **Owens**, H. Andersson, M. Bavdaz, L. van den Berg, A. Peacock, A. Puig, *The hard X-ray response of a large area HgI_2 detector*, Nuclear Instruments and Methods in Physics Research A, **487**(1-2), 90-95, (2002).

D.L. **Page**, T.E. Kidd, W.D. Dupont, J.F. Simpson, L.W. Rogers, *Lobular neoplasia of the breast: higher risk for subsequent invasive cancer predicted by more extensive disease*, Human Pathology, **22**, 1232-1239, (1991).

S. **Pani**, Explanation of microCT reconstruction algorithm, Personal communication, (2005).

D.E. **Peplow**, K. **Verghese**, *Measured molecular coherent scattering form factors of animal tissue, plastics and human breast tissue*, Physics in Medicine and Biology, **43**, 2431-2452, (1998).

M.E. **Poletti**, O.D. Gonçalves, I. Mazzaro, *X-ray scattering from human breast tissues and breast-equivalent materials*, Physics in Medicine and Biology, **47**(1), 47-63, (2002).

M.L. **Prydderch**, N.J. Waltham, R. Turchetta, M.J. French, R. Holt, A. Marshall D. Burt, R. Bell, P. Pool, C. Eyles, H. Mapson-Menard, *A 512 x 512 CMOS Monolithic Active Pixel Sensor with integrated ADCs for space science*, Nuclear Instruments and Methods in Physics Research A, **512**, 358-367, (2003).

M.J. **Quinn**, P.J. Babb, A. Brock, E. Kirby, J. Jones, *Cancer trends in England and Wales 1950-1999, Studies on Medical and Population Subjects No. 66*, Office for National Statistics, U.K., Available at: http://www.statistics.gov.uk/downloads/theme_health/cancertrends_5099.pdf, (2001).

M.J. **Quinn**, S. Rowan, M. Gautrey, *Cancer registrations in England, 2001*, Office for National Statistics, U.K., Available at: http://www.statistics.gov.uk/statbase/Expodata/Spreadsheets/D8397.xls,(2004).

B. **Ramsey**, D.P. Sharma, R. Austin, V. Gostilo, V. Ivanov, A. Loupilov, A. Sokolov, H. Sipila, *Preliminary performance of CdZnTe imaging detector prototypes*, Nuclear Instruments and Methods in Physics Research A, **458**(1-2), 55-61, (2001).

F.D. **Rahusen**, R. Pijpers, P.J. van Diest, R.P. Bleichrodt, H. Torrenga, S. Meijer, *The implementation of the sentinel node biopsy as a routine procedure for patients with breast cancer*, Surgery, **128**(1), 6-12, (2000).

B.I. **Rees**, I.H. Gravelle, L.E. Hughes, *Nipple retraction in duct ectasia*, British Journal of Surgery, **64**, 577-580, (1977).

P. **Riviere**, undergraduate project report, (2004).

A. **Rose**, *Sensitivity performance of the human eye in an absolute scale*, Journal of the Optical Society of America, **38**, 196-208, (1948).

P.P. **Rosen**, J.A. **Urban**, *Coexistent mammary carcinoma and cytosarcoma phyllodes*, Breast, **1**, 9-15, (1975).

R. **Roylance**, P. Gorman, W. Harris, R. Liebmann, D. Barnes, A.M. Hanby, D. Sheer, *Comparative Genomic Hybridization of Breast Tumors Stratified by Histologic Grade Reveals New Insights into the Biological Progression of Breast Cancer*, Cancer Research, **59**, 1433-1436, (1999).

G.J. **Royle**, EGS4 Monte Carlo code, personal communication, (2002).

G.J. **Royle**, R.D. **Speller**, *Quantitative x-ray diffraction analysis of bone and marrow volumes in excised femoral head samples*, Physics in Medicine and Biology, **40**(9), 1487-1498, (1995).

G.J. **Royle**, A. Papenistis, R.D. Speller, G. Hall, G. Iles, M. Raymond, E. Corrin, P.F. van der Stelt, N. Manthos, F.A. Triantis, *Development of a 2D silicon strip detector system for mammographic imaging using particle physics technology*, Nuclear Instruments and Methods in Physics Research A, **493**(3), 176-188, (2002).

G.J. **Royle**, E.J. Harris, R.D. Speller, J.A. Griffiths, A.M. Hanby, *Diffraction enhanced breast imaging: preliminary results from the Elettra synchrotron source*, IEEE Nuclear Science Symposium & Medical Imaging Conference Record, San Diego, U.S.A., 2001, **3**, 1814-1818, (2002).

G.J. **Royle**, S. Pani, R.D. Speller, *Spectral selective momentum transfer imaging of breast tissue*, work carried out under Elettra Proposal Number 2003641, (2004).

A.T. **Sandison**, *A study of surgically removed specimens of breast, with special reference to sclerosing adenosis*, Journal of Clinical Pathology, **11**, 101-109, (1958).

M.G. **Scannavini**, R.D. Speller, G.J. Royle, I. Cullum, M. Raymond, G. Hall, G. Iles, *Design of a Small Laboratory Compton Camera for the Imaging of Positron Emitters*, IEEE Transactions on Nuclear Science, **47**(3), 1155-1162, (2000).

F. **Scoparino**, O. Schillaci, W. Ussof, K. Nordling, R. Capoferro, R. De Vincentis, G. Danieli, R. Ieradi, M. Picardi, R. Tavolaro, A.C. Colella, *A three center study on the diagnostic accuracy of 99mTc-MIBI scintimammography*, Anticancer Research, **17**, 1631-1634, (1997).

L. **Sjöström**, P. Björntorp, J. Vrána, *Microscopic fat cell size measurements on frozen-cut adipose tissue in comparison with automatic determinations of osmium-fixed fat cells*, Journal of Lipid Research, **12**(5), 521-530, (1971).

J.P. **Sloane**, P.A. Trott, S.R. Lakhani, *Biopsy pathology of the breast*, 2nd Edition, Biopsy Pathology Series 24, *publ.* Arnold, London, U.K., (2001).

R.D. **Speller**, *'Blobfinder'*, IDL programme, personal communication, (2002).

R.D. **Speller**, Diffractometer collimation schematic, personal communication, (2003).

R.D. **Speller**, *'L3diffractionCT'*, IDL programme, personal communication (2003(a)).

R.D. **Speller**, S.E. **Bohndick**, *'microCT'*, IDL programme, personal communication (2004).

R.D. **Speller**, J.A. **Horrocks**, *'L3SSMTI'*, IDL programme, personal communication, (2003).

R.D. **Speller**, G.J. **Royle**, *'dPiX CT'*, LabView programme, personal communication (2003).

S.H. **Spencer**, N.J. **Catlett**, *Low Light Level Solid State TV Imaging*, Technical Note, Marconi Technologies ltd., Available at: http://www.marconitech.co.uk/downloads/l3vision/tpnv2_rev.pdf , Downloaded December 2000.

J.S. **Spratt**, *Anatomy of the Breast*, Major Problems in Clinical Surgery, **5**, 1-13, (1979).

St. James' University Hospital, *Use of the Shandon Citadel 2000*, Standard Equipment Operating Procedures, Department of Histopathology and Molecular Pathology, (2002).

A. **Studen**, D. Burdette, E. Chesi, V. Cindro, N.H. Clinthorne, W. Dulinski, J. Fuster, L. Han, H. Kagan, C. Lacasta, G. Llosá, A.C. Marques, N. Malakhov, D. Meier, M. Mikuz, S.J. Park, S. Roe, W.L. Rogers, J. Steinberg, P. Weilhammer, S.J. Wilderman, L. Zhang, D. Zontar, *First coincidences in pre-clinical Compton camera prototype for medical imaging*, Nuclear Instruments and Methods in Physics Research A. **531**(1-2), 258-264, (2004).

A.J. **Surowiec**, S.S. Stanislaw, J.R. Barr, A. Swarup, *Dielectric Properties of Breast Carcinoma and the Surrounding Tissues*, IEEE Transactions on Biomedical Engineering, **35**(4), 257-263, (1988).

A. **Taibi**, A. Del Guerra, M. Gambaccini, M. Marziani, A. Tuffanelli, *Evaluation of a digital X-ray detector based on a phosphor-coated CCD for mammography*, Nuclear Instruments and Methods in Physics Research, **392**(1), 210-213, (1997).

A. **Taibi**, G.J. Royle, R.D. Speller, *A Monte Carlo Simulation Study to Investigate the Potential of Diffraction Enhanced Breast Imaging*, IEEE Transactions in Nuclear Science, **47**(4), 1581-1586, (2000).

I. **Takayanagi**, J. Nakamura, E.R. Fossum, K. Nagashima, T. Kunihoro, H. Yurimoto, *Dark Current Reduction in Stacked-Type CMOS-APS for Charged Particle Imaging*, IEEE Transactions on Electron Devices, **50**(1), 70-76, (2003).

P.F. **van der Stelt**, *The implementation of digital sensors in maxillofacial radiography*, Nuclear Instruments and Methods in Physics Research, **460**(1), 45-49, (2001).

S.R. **Wellings**, H.N. Jensen, R.C. Marcum, *An atlas of subgross pathology of the human breast with special refernce to possible precancerous lesions*, Journal of the National Cancer Institute, **55**, 231-273, (1975).

G. **Whish**, M.Sc. project report, (2004).

L.**Zhang**, W.L. Rogers, N.H. Clinthorpe, *Potential of a Compton camera for high performance scintimammography*, Physics in Medicine and Biology, **49**(4), 617-638, (2004).